The Design of a Carbide-Free Alloy Composition and Heat Treatment Process for Forged Rail Wheel Application in South Africa

Asimenye Kapito

A thesis submitted to the Faculty of Engineering and the Built Environment, University of the Pretoria, in fulfilment of the requirements for the degree of Doctor of Philosophy in Engineering

JOHANNESBURG, February 2019

DECLARATION

I, Asimenye Kapito, declare that this thesis is my own work, except where otherwise acknowledged. It is submitted for the degree of Doctor of Philosophy in Engineering at the University of Pretoria, South Africa. It has not been submitted previously at this, or any other university for any degree or examination.

SIGNATURE

ABSTRACT

This study investigates the carbide-free bainitic steels for forged rail wheel applications in South Africa. This project emanated from the need for durable rail steels by the South African industry, particularly for wheel applications. The pearlitic steels have reached a threshold in their development and bainitic steels have emerged as the third generation of rail steels, particularly the carbide-free bainitic alloys. The addition of high silicon has been found to retard the formation of carbides in bainite, forming what is called carbide-free bainite.

This thesis gives an in-depth literature review on carbide-free and pearlitic steels, their wear properties and failure mechanisms when applied as rail steels. It also gives details on the experimental procedure followed to manufacture and test experimental alloys, as well as the results found. There is also a discussion on the future work to be completed.

In this study a number of carbide-free bainitic alloys were manufactured with the addition of 1 wt% - 2 wt% silicon and other alloying elements, such as carbon, manganese and chromium. A thermodynamic study of the effects of alloying elements showed that the addition of molybdenum, vanadium and boron were beneficial in increasing the hardenability of the alloys. Examination of the bainite using transmission Kikuchi diffraction showed no carbides in the microstructure.

The mechanical properties of the experimental carbide-free alloys were ranked against those of the commercial AAR Class C. The yield and tensile strengths of Alloy F were better than those of the reference. Alloy H showed better elongation and impact properties even though the impact properties of experimental carbide-free alloys was generally poor with high ductile to brittle transition temperatures.

The sliding wear resistance of Alloy I heat treated at 400°C was similar to that of AAR Class B.

In this study a number of alloy compositions and heat treatments were used to produce a carbide-free bainitic microstructure. The three different Alloy Series 1 to 3 studied the carbide-free bainitic microstructure under different test conditions. The carbide-free bainite alloy composition ranges have been developed for forged rail wheel applications for different sets of parameters:

- Series 1 alloys (Alloys A to D) were produced to study the effect of alloying elements and heat treatment (isothermal and continuous cooling) on the carbide-free microstructure.
- Series 2 alloys (Alloys E to H) were used to study the mechanical properties (hardness, tensile and impact) of the carbide-free bainitic microstructure.
- Series 3 (Alloy I) was used to study the wear behaviour of the carbide-free microstructure.

The best performing alloys for the different series tested are summarised in the table below.

Chemical Composition and heat treatment of Alloys for Forged Rail Wheel Application

Alloy	Chemical Composition, wt%								Comment	Heat Treatment
	C	Si	Mn	Cr	Mo	B	V	Al		
A	0.30	1.4	1.9	0.5	0.02	0.003	0.001	0.27	Ideal for isothermal heat treatment	Austenitise at 850 and cool at <0.1°C/s to 380°C
D	0.24	2.0	1.6	0.5	0.18	0.0003	0.20	0.22	Ideal for continuous cooling heat treatment	Austenitise at 950 and cool at >1°C/s to room temperature
F	0.26	1.9	1.4	0.6	0.18	0.0007	0.011	0.009	Ideal for high tensile properties and high hardness	Austenitise at 950°C and cool quickly to 365°C and temper at <400°C
H	0.28	1.0	1.6	0.5	0.23	0.0003	0.025	0.006	Ideal for moderate impact properties	Austenitise at 950°C and cool quickly to 365°C and temper at 200°C
I-400	0.30	1.78	0.71	0.62	0.16	0.002	0.001	0.022	Ideal for good wear resistance-	Austenitise at 1050°C and cool quickly to 400°C

DEDICATION

I would like to dedicate this work to God, my children, Jayden and Ethan, and my parents, Lyson and Atupele Muwila. I love you all dearly and I am so grateful for your unwavering love and support.

2 Timothy 2:15 (KJV)

***Study to shew thyself approved unto God, a workman that needeth not to be ashamed, rightly dividing the word of truth*.**

ACKNOWLEDGEMENTS

I would like to thank the following people and organisations, without which this PhD study would not have been possible:

- My supervisor Prof. Roelf Mostert and co-supervisor Prof. Charles Siyasiya at the University of Pretoria for their continued technical support. Special gratitude to Prof. Stumpf for your wise technical and personal counsel. Thank you to Professor G.T. Van Rooyen for designing and building the rolling/sliding simulation rig.
- Mintek, for technical and financial support. Thank you Mr Joseph Moema and Dr Jones Papo for your support. Special gratitude to Mr Sibusiso Kantwela, Mr Absalom Mabeba, Mr Mbavhalelo Maumela and Mr Lebedike Mampuru for their assistance, as well as Mr Archie Corfield, for scanning electron microscopy (SEM) testing.
- The Department of Science and Technology (DST), Advanced Materials Initiative (AMI)-Ferrous Metals Development Network (FMDN) for their financial support, particularly to attend conferences.
- The Nelson Mandela University, Department of Physics and Centre for HRTEM for transmission electron microscopy (TEM) and transmission Kikuchi diffraction (TKD) analysis. In particular I would like to mention Dr John Westraadt and Prof. Mike Lee for assistance.
- Nuclear Energy Council for South Africa (NECSA) for their neutron diffraction analysis, particularly Ms Zeldah Sentsho and Dr Andrew Venter for their technical assistance.
- The Electron Microscope Unit at the University of Cape Town, particularly Dr Innocent Shuro, for assistance with TEM analysis
- The University of Cambridge, Dr Matthew Peet, for proving the MUCG38 software for thermodynamic analysis
- My family and friend for all their love and support, especially Dr Gabriel Sean Mukucha for pushing me to finish.

TABLE OF CONTENTS

LIST OF FIGURES

LIST OF TABLES

1. Background

This project, on bainitic steels for rail wheel applications, is part of the Ferrous and Base Metals Development Network (FMDN) of the Department of Science and Technology's (DST's) Advanced Metals Initiative (AMI). The FMDN focusses on adding value to ferrous and base metals as well as assisting the ferrous industry in facing its materials related challenges. A major aim of the FMDN is to assist the local ferrous industry to improve its competitiveness. A key focus area of the FMDN is on the development of lightweight and/or durable steels for cost-effective transportation and infrastructure (lightweight steels). This project fits in well with this focus as it aims at the research and development of durable steels for the transport industry.

1.1. The Industrial Problem

There is a government push to shift South Africa's freight from road to rail, cutting both high logistical costs and carbon emissions in the process. In 2012, Transnet, South Africa's state-owned ports and rail company, launched the Market Development Strategy (MDS) [1]. This strategy aims to expand and modernise the country's ports, rail and pipelines infrastructure over a period of seven years to promote economic growth in South Africa. The MDS is a R312.2bn investment programme that will make Transnet, one of the biggest rail freight companies in the world [1]. Rail volumes will increase significantly from ~216 million tons to 343.9 million tons per annum fuelling a strong economy in South Africa. The aim is to lower the cost of doing business in South Africa by increasing efficiency.

The MDS implementation plan has six pillars [1]. The initial plans are to expand and grow the infrastructure and develop skills to run Transnet's business safely and effectively. The last pillar however is to drive research and development of new and cutting edge technologies. This will involve the development of durable materials to withstand the high demand that will be placed on the rail locomotives.

Maintaining railway wagons is costly and Transnet's operating expenses for the year ended 31 March 2016 amounted to R35bn and of this 4% (R1.4bn) was used for material and maintenance (Figure 1) [2] These costs are expected to increase significantly with the MDS programme. The maintenance costs include costs for replacing and maintaining rails and railway wheels.

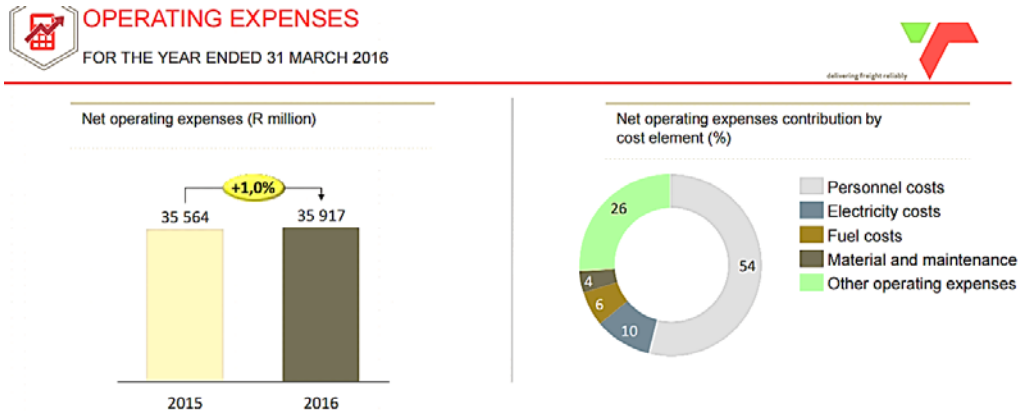

Figure 1. Transnet's operating expenses for the year ended 31 March 2016 [2]

South Africa uses both locally produced and imported railway wheels. Italian forged railway product manufacturer, Lucchini RS, opened a new manufacturing facility in Germiston, Ekurhuleni, South Africa in 2017 [3]. This facility is a R200-million investment and sees the company localise rail wheel machining in the country. South Africa is the first facility to machine forged railway wheels in Africa [3]. There is thus a significant drive in the country to use forged wheels, particularly due to the fact that the forged railway wheel market in South Africa have declined sharply from its boom days of around 60 000 wheels a year [3]. Cast wheels are cheaper that forged wheels but forged wheels have a higher performance level and better mechanical properties [3].

Several workshops and consultative meetings under the AMI-FMDN programme led to the decision that one R&D focus of the programme should be on the development of durable railway wheel steels. Railway wheels are a high consumption item and with the planned increase in tonnages to be transported by freight rail, the railway wheel is in danger of becoming a very costly consumable.

The most effective way to obtain cost effective operation and maintenance of wheels and rails is by having a systems approach, as indicated in Figure 2 [4]. The factors that affect wheel/rail performance are:

- Wheel/rail dynamics
- Rail contact mechanics
- Friction management
- Wheel/rail damage modes
- **Wheel/rail materials**

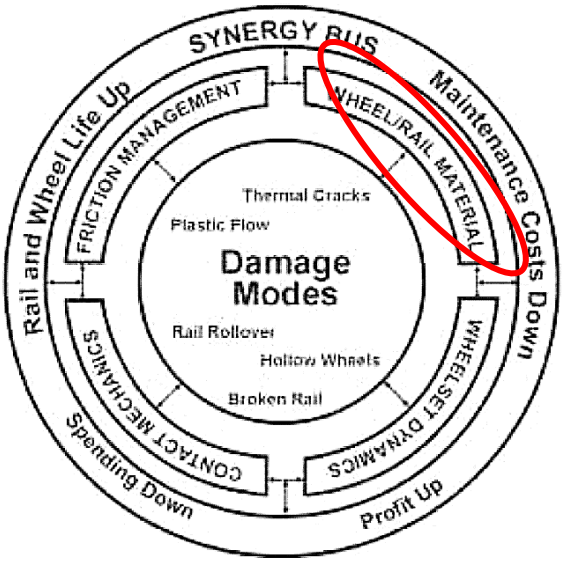

Figure 2. Scheme of systems approach to wheel/rail performance research and development [4]

It is against this backdrop that a project to explore the carbide-free bainitic alloys for rail wheel applications was initiated.

1.2. The Academic Problem: The Design of a Carbide-Free Composition and Heat Treatment Process for Application as a Forged Rail Wheel in South Africa

Carbide-free bainite are novel alloys for rail steels but they are not new in that their research and development has spanned over decades. Rigorous developmental work has been completed particularly in Europe but also elsewhere to understand the thermodynamics, kinetics and properties of these alloys, particularly for rail steel applications.

It is the purpose of this PhD study to use these tools and models available for carbide-free bainitic steels to design and produce a laboratory alloy for a rail wheel for the South African rail transport industry. The objectives of this project is alloy development and the aims are:

- To understand the carbide-free microstructural features that are important in the design of rail wheel steels as well as the differences in pearlitic and carbide-free bainitic rail steels
- To choose appropriate alloy compositions needed to produce carbide-free microstructures based on dilatometry tests as well as thermodynamic modelling using software such as MUCG83

- To produce a number of experimental alloys with a carbide-free bainitic microstructure in the laboratory and determine the possible heat treatment processes to produce a forged wheel
- To test the carbide-free microstructure for tensile, impact and wear properties

- Identify an alloy composition for further development into a forged rail wheel alloy

2. Literature Review

2.1. Pearlitic Steels for Rail Applications

Rail steels are generally made of medium and high-carbon steel with a pearlite microstructure (Figure 3). The alternating plates, or lamella, of cementite and ferrite are ideal for the type of wear experienced in the rail steel during operation [5, 6]. Pearlitic rails are manufactured through melting, casting, forming by hot rolling, heat treatment and roller straightening [7, 8, 9, 10]. Solid wheel steel grades for heavy haul, all over the world, are mainly governed by the Association of American Railroad's (AAR) standards [3, 11]. The main steel grades particularly recommended for heavy haul are also the pearlitic steels [3, 11].

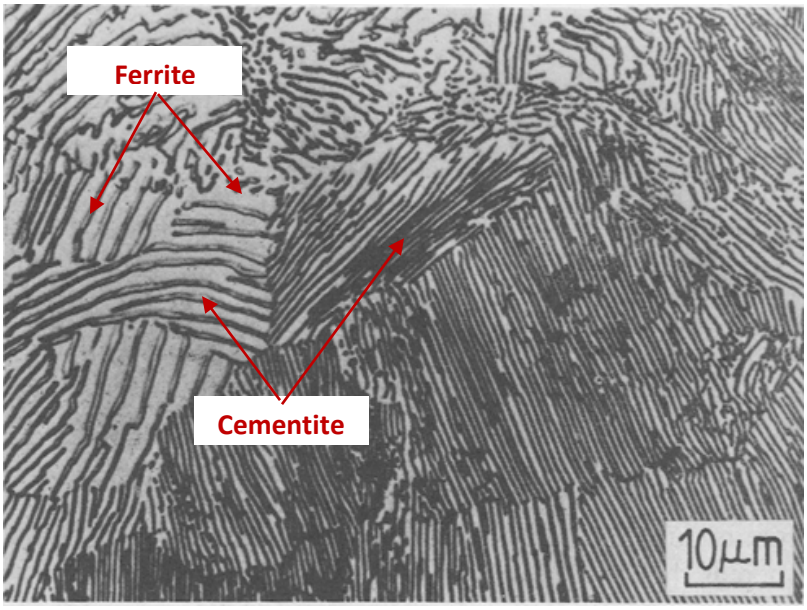

Figure 3. Microstructure of pearlite, a lamellar mixture of ferrite and cementite for a plain carbon eutectoid steel heat treated at 705°C [5]

The pearlite transformation is a discontinuous transformation which takes place in such a manner that the average concentration of solutes within the microstructure on either side of the growth front is the same [12, 13]. In the discontinuous transformation the parent phase can dissociate into two daughter phases through relatively short range diffusion, unlike with normal nucleation and growth of spherical precipitates where diffusion must occur over increasingly longer distances such that the growth rate of the product phase decreases with time. In discontinuous transformations however the growth rate of the pearlite front is linear with time because the short range diffusion path length is constant with time [12, 13]. In the case of pearlite, the parent phase is austenite (γ) and the product phase is ferrite (α)

+ cementite (Fe_3C). The γ-phase differs both in structure and orientation to the pearlite.

To extend the life cycle of rail steels, hardness has been the primary property to exploit, see Figure 4 [6]. The hardness of pearlitic rails is increased by decreasing the interlamellar spacing and increasing alloying elements, such as manganese and chromium but particularly carbon [6].

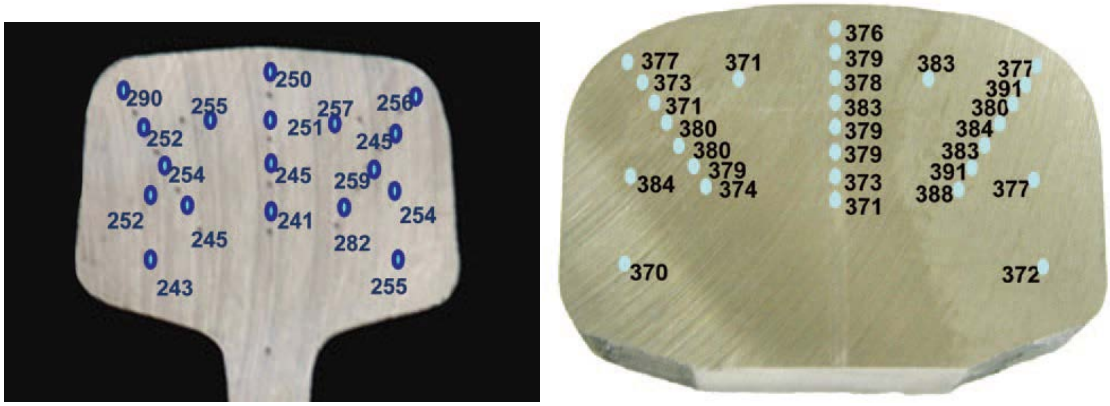

Figure 4. (a) The Brinell hardness profile in the rail head made from steel produced by Henry Bessemer in 1890 with an average hardness of 250 HB. (b) The Brinell hardness profile of a rail head made from modern head hardened steel produced by the electric furnace steelmaking process with an average hardness of 378 HB [6]

In the development of pearlitic rail steel the carbon content has been increased to achieve a 100% pearlitic microstructure, this also increased the strength of the steel [14] but will have a somewhat negative effect on the fracture toughness or ductility of the steel. Carbon provides the large volume fraction of cementite in the pearlite needed for hardness and strength [6]. Hypereutectoid steels, with carbon contents greater than 0.8 wt%, were avoided in the past because of the formation of proeutectoid cementite on prior austenite grain boundaries which provides an easy path for crack propagation, thereby embrittling the steel [6]. Using faster cooling rates and alloying with silicon, however, has allowed hypereutectoid steels with 1wt% carbon to be used on tracks today, see Figure 5 [1]. The proeutectoid cementite is difficult to eliminate but it can be avoided by cooling the steel quickly from the austenitic region to a temperature in the Hultgren triangle, provided the carbon concentration also lies in this triangle. An explanation of the Hultgren triangle will follow later in this section. The proeutectoid cementite can be minimised to avoid a continuous network by breaking it up into units similar to that of the pearlite, giving a higher hardness (~400HB surface hardness) and improved wear resistance [6].

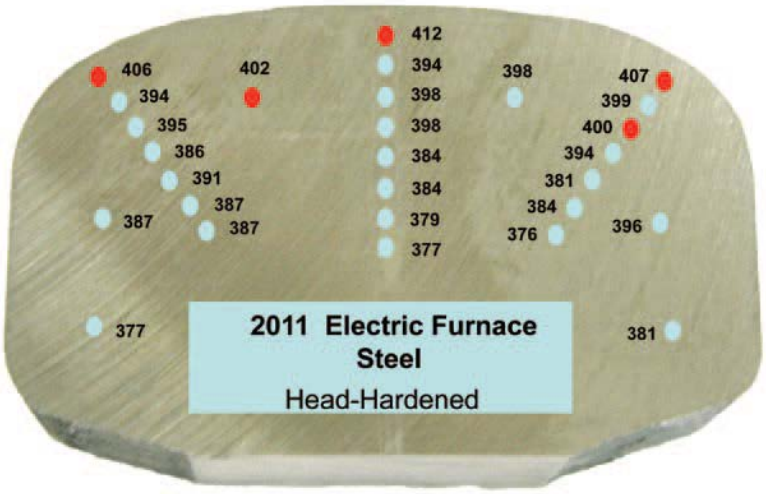

Figure 5. The typical hardness profile of a rail head made from hypereutectoid steel with an average hardness of 390 HB [6]

Further developments of pearlitic rail steels have led to refinement of the pearlite microstructure such that rails with tensile strengths of 1000MPa-1200MPa can be achieved [14]. The yield strength and tensile strength of pearlitic steels increase as the interlamellar spacing decreases while the elongation then decreases [14]. For example, under equilibrium conditions (727°C) the eutectoid reaction for a 0.77wt%C steel is as follows [6]:

$$\gamma(0.77\ at\%C) \rightarrow \alpha(0.02\ wt\%\ C) + Fe_3C\ (6.67\ wt\%\ C) \qquad \textit{Equation 1}$$

From this equation it can be seen that the process of diffusion must eventually redistribute 0.77wt% carbon from austenite between the ferrite and cementite to form a pearlite structure with cementite of 6.67 wt% C and ferrite of 0.02 wt% C (Figure 6) [6].

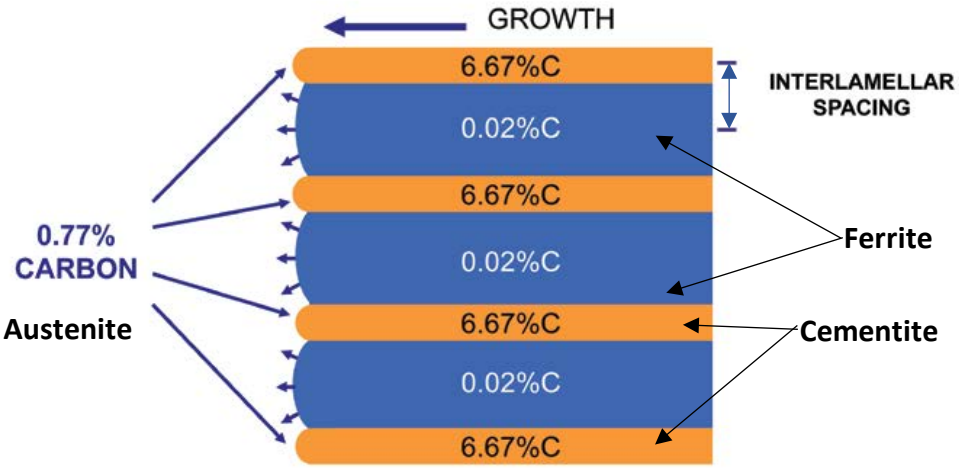

Figure 6. The redistribution of carbon (C) at the growth front during the pearlite transformation [6]

The growth of pearlite occurs with various gradients in the carbon (C) concentration (C_0 to C_5) at the growth front as shown in Figure 7 [15, 16]. The arrows show the directions of the concentration gradients and the interlamellar spacing is defined as d. Hultgren defined these carbon concentration at the growth front of pearlite on the equilibrium Fe - C phase diagram, see Figure 8. For example, for an eutectoid steel (0.8 wt% C) transformed at a temperature of T_2, the carbon concentrations parallel to the growth front can be defined, according to Hultgren as follows [15, 16]:

C_o = Original concentration of carbon in the austenite

C_1 = %C in the ferrite at equilibrium with Fe_3C

C_2 = %C in the ferrite at metastable equilibrium with austenite

C_3 = %C in austenite at metastable equilibrium with Fe_3C

C_4 = %C in austenite at metastable equilibrium with ferrite

C_5 = Equilibrium composition of Carbon in Fe_3C

In the cross hatched area (Figure 8), pearlite may form directly in the austenite [15, 16]. Outside of this area pro-eutectoid ferrite (to the left) or pro-eutectoid cementite (to the right) will always form first before pearlite will form. The carbon concentration gradient of significance in the pearlite transformation is the one that is parallel to the growth front i.e. C4 - C3. This is the concentration gradient that determines the growth rate of pearlite. Full equilibrium does not exist at the growth front because of the concentration gradients at the growth front. The concentrations then that are read off the Hultgren extrapolations (off the dotted lines of the phase diagram in Figure 8), are defined as being in metastable equilibrium [15, 16]. The concentrations that are read off the phase diagram's full lines, however, are equilibrium concentrations and these concentrations do not lead to concentration gradients and are achieved far behind the growth front [15, 16]. All of the concentrations are temperature dependent except for C_o and C_5. There is also no concentration gradient of carbon in the Fe_3C lamella as Fe_3C, according to the equilibrium phase diagram, has no solid solubility for carbon or iron [15, 16]. In practice the concentrations of C_2, C_3 and C_4 are only achieved approximately near the growth front.

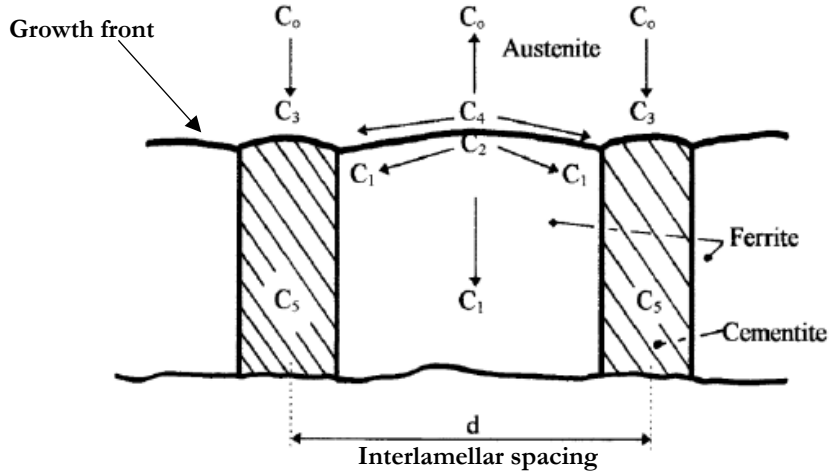

Figure 7. Concentrations and concentration gradients at and near the growth front of pearlite in a Fe – C steel. The interlamellar spacing is defined as d [15, 16]

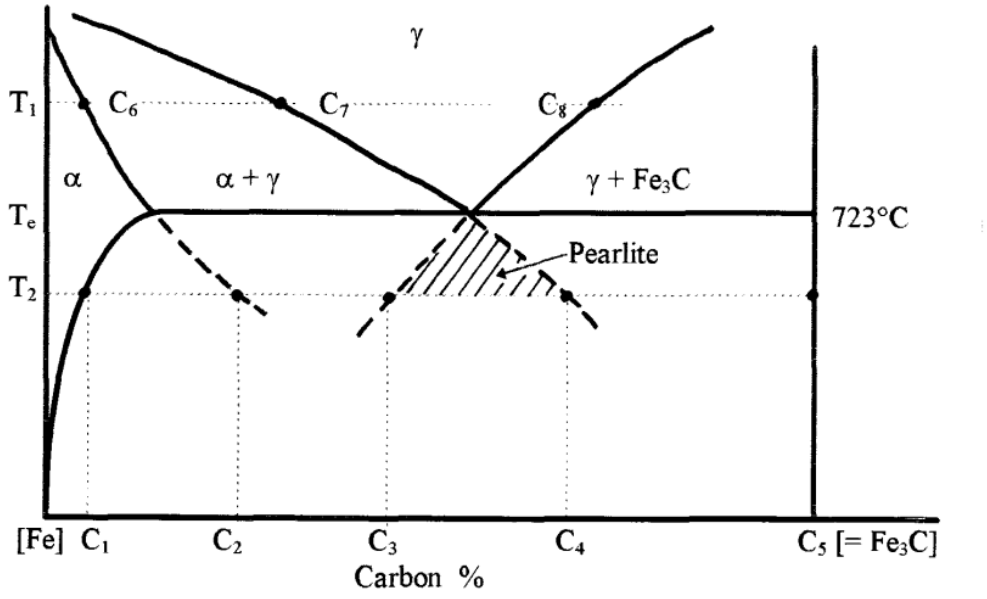

*Figure 8. (a) The Fe – C phase diagram with the Hultgren extrapolations on which various compositions above and below the eutectoid temperature T_e are defined. Note the cross hatched area within the Hultgren extrapolation in which pearlite can form directly. T_1 and T_2 are transformation temperatures, γ is austenite, α is ferrite and Fe_3C is cementite [*15, 16*]*

Figure 9 shows the concentration of carbon (C) lengthwise through the ferrite and a cementite lamella respectively as the pearlite grows into the austenite. There is a small gradient of carbon, C_2 at the ferrite interface which does not exist at the interface through the cementite.

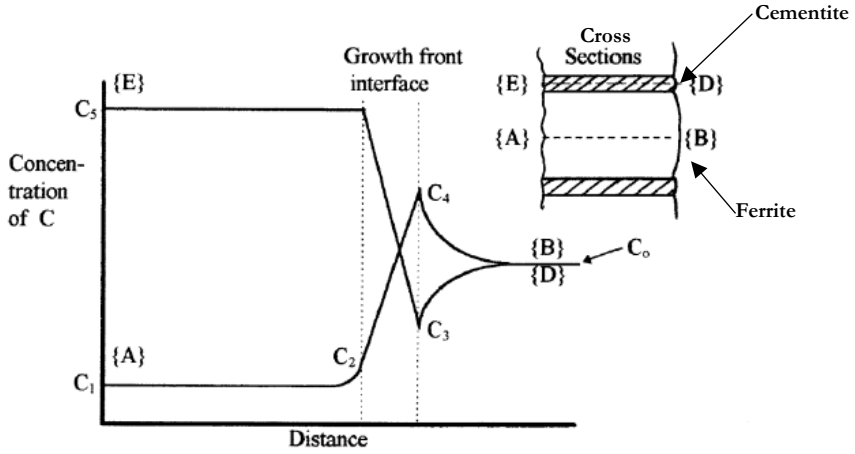

Figure 9. Concentration of carbon (C) lengthwise raced through the cross sections of the ferrite (A/B) and cementite (E/D) lamella respectively. Note the presence of the C2 small gradient at the ferrite interface, such a gradient does not exist in the trace at the interface through the cementite [15, 16]. A and E are regions in the ferrite and cementite respectively, away from the growth front, in already formed pearlite, D and B are regions in the cementite and ferrite in the pearlite just ahead of the growth front

Figure 10 shows the volume fraction of pearlite formed in slowly cooled plain carbon steel, as a function of the carbon content [15, 16]. From the figure it can be seen that100% pearlite can be achieved with 0.8 wt% carbon in the steel. At lower carbon contents (< 0.8 wt%) the formation of pro-eutectoid ferrite is favoured together with pearlite. At carbon contents >0.8 wt% pro-eutectoid cementite forms together with pearlite in the steel. The highlighted region is the 'Hultgren triangle', where pearlite will form in the alloy with slow cooling.

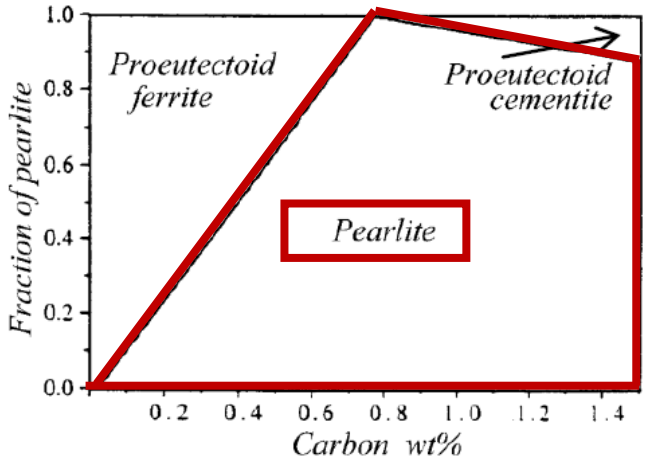

Figure 10. The volume fraction of pearlite in slowly cooled plain carbon steel, as a function of the carbon content [15, 16]

The growth of pearlite is co-operative and a lamellar structure of ferrite and cementite is formed [15, 16]. If one considers a hypereutectoid steel, with a carbon concentration >0.8 wt%, for example, the first nucleus to form on the austenite grain boundary is cementite [15, 16]. On either side of the nucleus, the austenite will become depleted in carbon because of the carbon uptake by the cementite nucleus. This will continue until the carbon concentration in the austenite reaches the critical value required for the formation of a ferrite nucleus, according to the Hultgren extrapolations [15, 16].The carbon now starts to build up in the austenite next to the ferrite lamella because of the low solubility of ferrite for carbon. This will proceed until the critical concentration for the nucleation of a cementite lamella is reached once more, and the process repeats itself [15, 16].It is clear therefore that the diffusion of carbon plays a vital role in the transformation of pearlite and the carbon is constantly being redistributed between the ferrite and cementite to form pearlite.

The cooperative growth of ferrite and cementite also depends on how fast the carbon can diffuse. At slow cooling rates (small undercooling, close to the equilibrium temperature) from the eutectoid temperature, carbon has sufficient time to diffuse and form coarse pearlite with a large interlamellar spacing [6]. At higher cooling rates, however, the carbon atoms need to diffuse faster in order to keep up with the coupled growth and the diffusion distance becomes shorter, in order for the carbon to distribute properly, and the interlamellar spacing becomes finer [6]. This is why rail steels are often made using the head-hardening process (Figure 11) where accelerated cooling, with water sprays, cools the hot steel [6]. The optimum cooling path is related to the percentage carbon in the steel and the Hultgren triangle, and must be tailored to the particular rail composition and process and a study of the continuous cooling transformation (CCT) diagram is essential in this case.

(a) (b)

Figure 11. Rails being processed in an in-line head-hardening process: (a) rails from the rail mill in queue to enter the head-hardening machine and (b) a rail passing by water sprays that cool the rail to achieve the ideal cooling path [6]

Figure 12 is an example of a continuous cooling diagram for a pearlitic rail steel showing the different phases that will form for a combination of different temperatures, time and cooling paths. A number of different cooling paths (A to D) can be used to cool rail steels and these will result in different microstructures [17]. Path A shows a very slow cooling rate that if used to cool the steel forms a fully pearlitic microstructure as both the pearlite start (P_s) and pearlite finish (P_f) lines are crossed. Path C shows a faster cooling rate that crosses the P_s, bainite start (B_s) and bainite finish (B_f) transformation boundaries yielding a mixed microstructure of pearlite and bainite. If the very fast cooling Path D is chosen then martensite forms as the path crosses the martensite start (M_s) and finish (M_f) temperatures. Path B represents an accelerated/interrupted cooling rate where the steel is rapidly cooled, for example by an air-water mist spray, to the pearlite start temperature located just above the bainite start temperature [17], high cooling rates are then applied up to the pearlite finish boundary, which should lie within the Hultgren triangle. This is followed by slow air cooling to ambient temperatures [17]. This cooling process and the heat of transformation produce a uniform and almost constant temperature profile throughout the cross-section of the rail and this yields a fine pearlitic microstructure with high hardness and wear resistance.

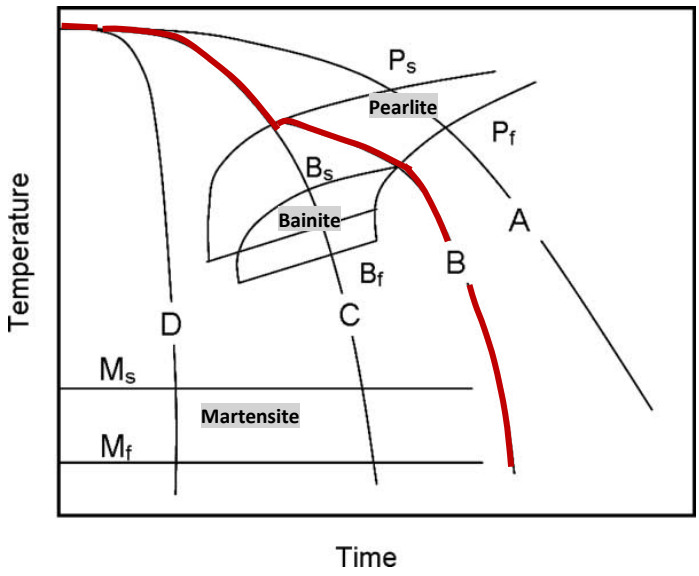

Figure 12. The effect of different cooling profiles (A to D) on the final microstructure for eutectoid steel [17]. In this figure, the pearlite (P_s) bainite (B_s) and martensite (M_s) start and their finish temperatures (P_f, B_f, M_f) are shown

There are three variants of rail hardening that exist, i.e. conventional heat treatment, off-line and in-line head hardening processes [17, 18, 19, 20]. In the conventional heat treatment process the entire rail is reheated to austenitising temperatures and then quenched in oil to produce fine pearlite [17]. Tempering is needed to remove residual stresses formed during quenching. This process is costly. In off-line head hardening only the head of rail is austenitised by induction or flame heating followed by accelerated cooling with air-water mist to form fine pearlite [17, 21]. In this process, there are significant variations in the microstructure of the rail and hence its properties. Residual stresses also form during heat treatment and the process is costly [17]. In on-line head hardening the heat of the hot-rolling process and controlled cooling throughout the rolling process is used to provide the elevated temperature to the rail [17, 21, 22, 23, 24]. This produces a uniform microstructure and hence uniform properties of the rail [17]. This process is the most cost-effective of the accelerated cooling processes developed thus far and is tailored for every producer to achieve the desired properties in the rail steel.

To achieve a fine pearlite microstructure in the steel two methods can be used: the addition of alloying elements and applying accelerated cooling to the steel [14]. These effects can be explained by studying the continuous cooling transformation (CTT) diagrams of the Grade 900 rail steel (Figure 13). The CCT diagram shows the different phases formed in the steel during continuous cooling. It is useful to predict the microstructure of the steel after heat treatment.

Grade 900 rail steel is a high carbon steel that forms 100% coarse pearlite, and has an average tensile strength of 900 MPa [14]. When chromium is added to the Grade 900 steel, its tensile strength increases to 1100MPa and this grade of steel is called Grade 1100. In Figure 13, the CCT diagram shows that the addition of chromium to Grade 900 steel, shifts the austenite to pearlite transformation curve to the right, i.e to longer times, and also to lower temperatures, making it possible to use air (slow) cooling to form fine pearlite with a narrow interlamellar spacing. Another possibility to form fine pearlite is to accelerate the cooling of the Grade 900 steel. This shifts the CCT diagram of the steel to the left and fine pearlite can form, but with higher tensile strength of about 1100MPa (Figure 14) [14]. This is how head hardened steels are formed.

Figure 15 shows that a fine pearlitic spacing results in a steel with higher hardness and yield strength [25]. To achieve fine pearlite spacings the addition of alloying elements and/or the use of accelerated cooling can be used.

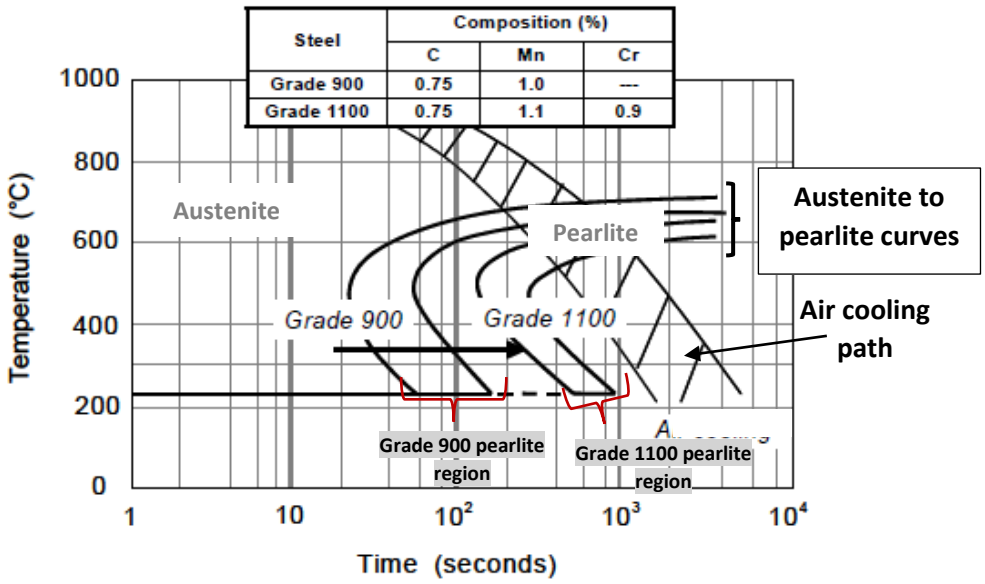

Figure 13. The continuous cooling transformation (CCT) diagram for Grade 900 rail steel showing the shifting of the Grade 900 rail steel's austenite to pearlite transformation curve to the right, due to the addition of chromium. This allows for the formation of fine pearlite with air cooling [14]

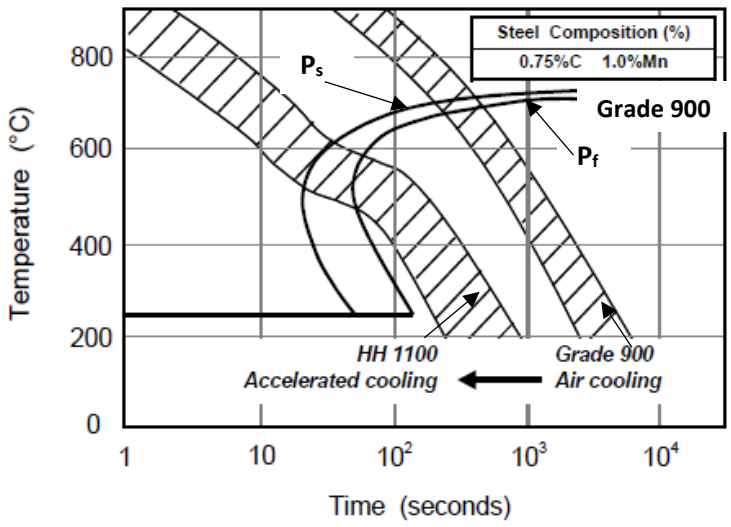

Figure 14. The continuous cooling transformation (CCT) diagram for Grade 900 rail steel showing the accelerated cooling path that is required to form fine pearlite. HH stands for head hardening [14]. P_s is the pearlite start and P_f the pearlite finish temperatures

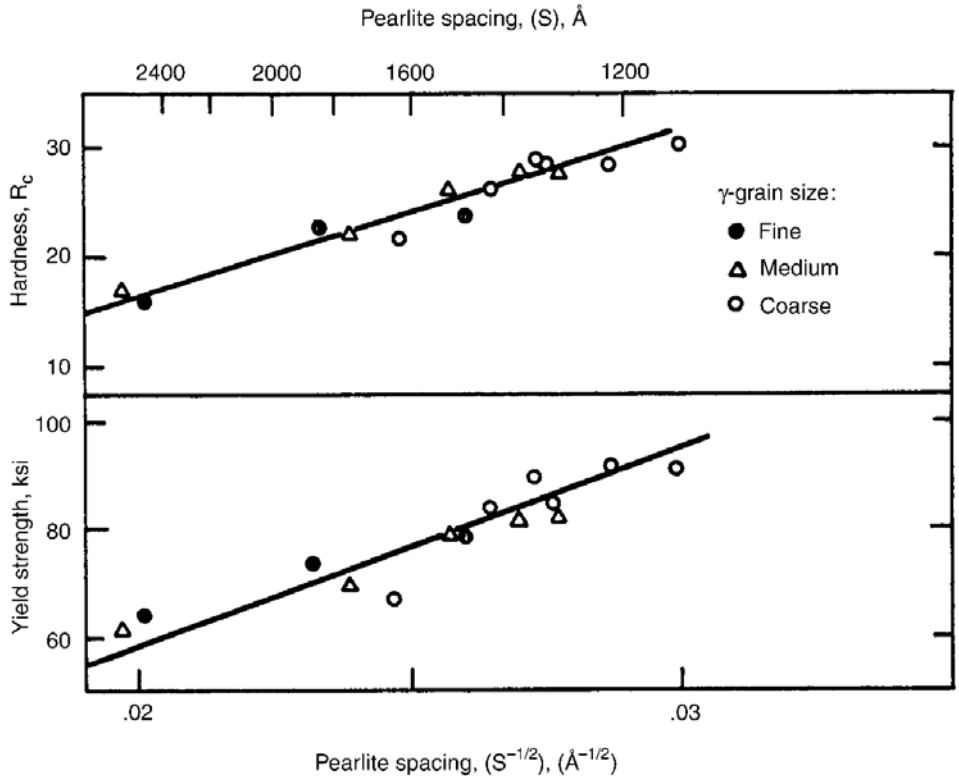

Figure 15. Hardness and yield strength as a function of pearlite interlamellar spacing in fully pearlitic microstructures [25], (γ=is austenite)

Figure 16 shows the historical development of rail steels and it is clear that the tensile strength of the rail steels has increased continuously over the years [26]. This is mainly due to an increase in the hardness of the rails, to reduce the wear rate, and also due to the development of technologies in the steel making process

[26]. In Figure 16, R200, R260, R320Cr and R350HT are names for pearlitic rail steels grades, developed over the years, with Brinell hardness of 200BHN, 260BHN, 320BHN and 350BHN respectively. Figure 16 also shows the steel named Dobain®, a specially heat-treated bainitic high-grade steel developed in Europe in the 2000's for rail steel applications.

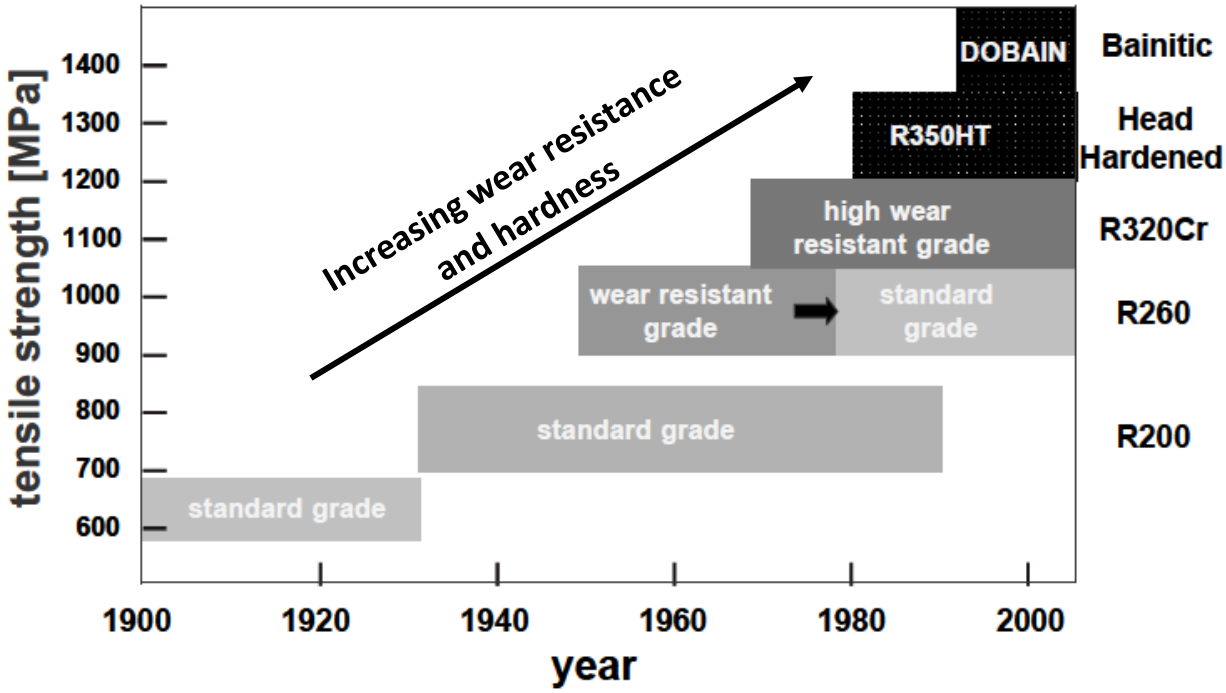

Figure 16. Trends in the development of rail steels from the 1900's to 2000's showing the different grades of steel developed with an increase in tensile strength and hardness [26]

2.2. Pearlitic Steels for Rail Wheel Applications

The railway wheel has different parts, hub (1), centre (2), rim (3) with flange (4), each having different functions, and their properties are determined by their chemical composition, forming process and heat treatment, see Figure 17 [27].

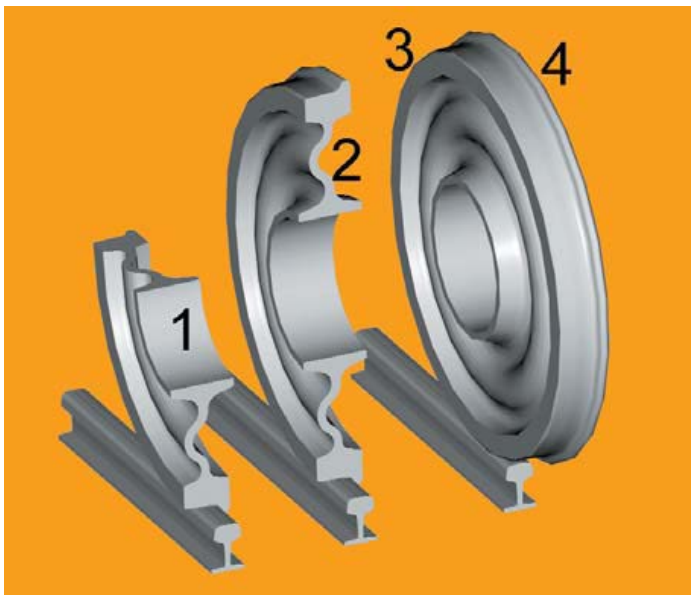

Figure 17. Functional parts of a railway wheel: hub (1), centre (2), rim (3) with flange (4) [27]

Around the world both cast and forged wheels are manufactured from hypo-eutectoid steel with an average of 0.65 wt% C as shown in Table 1 [28]. These wheels are heat treated to have a fully pearlitic microstructure. North America, China and Sweden have their own chemical composition specifications which the majority of the other countries adopt [28]. Though the chemical compositions are similar, the production technologies are different. For instance some countries adopt the Griffin casting technology which uses a graphite block to cast the wheels whilst other foundries use only resin sand moulding [28]. Wheel forging technology has been used for centuries to manufacture rail wheels [28]. In South Africa cast and forged wheels are produced based on the North American chemical composition and the specified mechanical properties are given in Table 2. No yield strength properties are specified in the standard.

Cast wheels are heavier than the forged wheels because by design the forged wheels are smaller in size [28]. Tables 3 and 4 give a more comprehensive summary of the composition and properties of rail steels used globally [29].

Table 1. Chemical compositions of railway wheels around the world (in wt%) [28]. No yield strength properties are specified in the standard

Elements Wt%	North America	Australia	South Africa	China	Russia	Sweden
C	0.57 – 0.67	0.57 – 0.67	0.57 – 0.67	0.55 – 0.65	0.55 – 0.65	0.67 – 0.72
Mn	0.60 – 0.90	0.60 – 1.00	0.60 – 0.90	0.50 – 0.85	0.60 – 0.90	0.73 – 0.85
Si	0.15 - 1.00	0.15 max	0.15 – 1.00	0.17 – 0.37	0.22 – 0.45	0.20 – 0.40
S	0.050 max.	0.050 max.	0.050 max.	0.040 max.	0.045 max.	0.020 max.
P	0.050 max	0.050 max	0.050 max	0.035 max	0.035 max	0.025 max

Table 2. Transnet specification of mechanical properties for railway wheels [28].

Wheel Rim			**Wheel Web**	
UTS (MPa)	% Elongation	Hardness (HB)	UTS (MPa)	% Elongation
>900	>8	277-341	650 – 950	Not specified

Table 3. Summary of Chemical compositions of rail wheel steels used around the world [29].

STANDARD	COUNTRY OF ORIGIN	GRADE	CARBON % (MAX)	SILICON % (MAX)	MANG. % (MAX)	PHOS. % (MAX)	SULP. % (MAX)	CHROME % (MAX)	COPPER % (MAX)	MOLYB. % (MAX)	NICKEL % (MAX)	VAN. % (MAX)	CR+MO+NI % (MAX)	HYDROGEN PPM (MAX)	
														CAT1	CAT2
JIS E5402	JAPAN	C44	0.46	0.40	0.90	0.040	0.040	0.30	0.30	0.08	0.30	0.05	N/S	N/S	N/S
AAR M107*	N.AMERICA	L	0.47	0.15/1.00	0.60/0.90	0.030	0.005/0.040	0.25	0.35	0.10	0.25	0.04	N/S	N/S	N/S
BS5892:PT3	UK	R6T	0.48	0.40	0.75	0.040	0.040	0.30	0.30	0.08	0.30	0.05	0.60	2.0#	2.0#
EN13262	EUROPE	ER6	0.48	0.40	0.75	0.020	0.015	0.30	0.30	0.08	0.30	0.06	0.50	2.0	2.5
JIS E5402	JAPAN	C48	0.50	0.40	0.90	0.040	0.040	0.30	0.30	0.08	0.30	0.05	N/S	N/S	N/S
GOST 10791	RUSSIA	GRADE 1	0.44/0.52	0.40/0.65	0.80/1.20	0.035	0.030	0.30	0.30	0.08	0.30	0.08/0.15	N/S	2.0	2.0
BS5892:PT3	UK	R7T	0.52	0.40	0.80	0.040	0.040	0.30	0.30	0.08	0.30	0.05	0.60	2.0#	2.0#
EN13262	EUROPE	ER7	0.52	0.40	0.80	0.020	0.015	0.30	0.30	0.08	0.30	0.06	0.50	2.0	2.5
IRSS	INDIA	R19	0.52	0.15/0.40	0.60/0.80	0.030	0.030	0.25	0.28	0.06	0.25	0.05	0.50	3.0	3.0
JIS E5402	JAPAN	C51	0.54	0.40	0.90	0.040	0.040	0.30	0.30	0.08	0.30	0.05	N/S	N/S	N/S
VALDUNES	FRANCE	R8TUCS	0.54	0.30/1.10	0.60/1.10	0.020	0.005/0.020	0.30/0.50	0.30	0.08	0.30	0.06	0.65	2.0	2.5
FSR	FINLAND	ER8MOD	0.52/0.56	0.90/1.10	0.90/1.10	0.015	0.006	0.30	0.10	0.08	0.30	0.08	0.05	2.0	2.0
LUCCHINI	ITALY	SUPERLOS	0.49/0.56	0.60/1.10	0.60/1.10	0.015	0.020	0.30	0.30	0.08	0.30	0.08	0.05	1.8	1.8
BS5892:PT3	**UK**	**R8T**	**0.56**	**0.40**	**0.80**	**0.040**	**0.040**	**0.30**	**0.30**	**0.08**	**0.30**	**0.05**	**0.60**	**2.0#**	**2.0#**
EN13262	EUROPE	ER8	0.56	0.40	0.80	0.020	0.015	0.30	0.30	0.08	0.30	0.06	0.50	2.0	2.5
AAR M107*	N.AMERICA	A	0.47/0.57	0.15/1.00	0.60/0.90	0.030	0.005/0.040	0.25	0.35	0.10	0.25	0.04	N/S	N/S	N/S
JIS E5402	JAPAN	C55	0.58	0.40	0.90	0.040	0.040	0.30	0.30	0.08	0.30	0.05	N/S	N/S	N/S
BS5892:PT3	UK	R9T	0.60	0.40	0.80	0.040	0.040	0.30	0.30	0.08	0.30	0.05	0.60	2.0#	2.0#
EN13262	EUROPE	ER9	0.60	0.40	0.80	0.020	0.015	0.30	0.30	0.08	0.30	0.06	0.50	2.0	2.5
GOST 10791	RUSSIA	GRADE 2	0.55/0.65	0.22/0.45	0.50/0.90	0.035	0.030	0.30	0.30	0.08	0.30	0.10	N/S	2.0	2.0
TB/T 2708	CHINA	CL60	0.55/0.65	0.17/0.37	0.50/0.80	0.040	0.040	0.25	0.25	N/S	0.25	N/S	0.50	N/S	N/S
GOST 10791	RUSSIA	GRADE 3	0.58/0.67	0.22/0.45	0.50/0.90	0.035	0.030	0.30	0.30	0.08	0.30	0.08/0.15	N/S	2.0	2.0
JIS E5402	JAPAN	C64	0.67	0.40	0.90	0.040	0.040	0.30	0.30	0.08	0.30	0.05	N/S	N/S	N/S
AAR M107*	N.AMERICA	B	0.57/0.67	0.15/1.00	0.60/0.90	0.030	0.005/0.040	0.25	0.35	0.10	0.25	0.04	N/S	N/S	N/S
IRSS	INDIA	R34	0.57/0.67	0.15 MIN	0.60/0.90	0.030	0.030	0.25	0.28	0.06	0.25	0.05	0.50	2.5	2.5
AAR M107*	N.AMERICA	C	0.67/0.77	0.15/1.00	0.60/0.90	0.030	0.005/0.040	0.25	0.35	0.10	0.25	0.04	N/S	N/S	N/S
JIS E5402	JAPAN	C74	0.77	0.40	0.90	0.040	0.040	0.30	0.30	0.08	0.30	0.05	N/S	N/S	N/S

LIMITS SPECIFIED ARE MAXIMUM UNLESS SPECIFIED OTHERWISE

2PPM LEVEL AS REQUIRED BY RAILWAY GROUP STANDARD GM/RT2466

* AAR SPECIFICATION ALSO HAS AL 0.060 MAX, TITANIUM 0.03 MAX AND NIOBIUM 0.05 MAX.

Table 4. Summary of the mechanical properties of rail wheel steels used around the world [29].

STANDARD	COUNTRY OF ORIGIN	GRADE	YIELD N/MM2 *	UTS N/MM2	A % (MIN)	Z % (MIN)	CHARPY U 20°C J. (AV) (MIN)	CHARPY V -20°C J. (AV) (MIN)	CHARPY V -40°C J. (AV) (MIN)	FRACTURE TOUGHNESS N/MM2√M	CLEANLINESS REQUIREMENT	ULTRASONIC STANDARD DEFECT LEVEL		BRINELL HARDNESS HB	
												CAT1	CAT2	CAT1	CAT2
JIS E5402	JAPAN	C44	N/S	770-890	15	N/S	15	N/S	N/S	N/S	NO	N/S		197-277	
AAR M107	N.AMERICA	L	N/S	N/S	N/S	N/S	N/S	N/S	N/S	N/S	YES	1.6MM		197-277	
BS5892:PT3	UK	R6T	N/S	770-890	15	N/S	15	N/S	N/S	N/S	NO	2MM#		229-262	
EN13262	EUROPE	ER6	500 MIN	780-900	15	N/S	17	12	N/S	100 MIN	YES	1MM	2 OR 3MM$	225 MIN	
JIS E5402	JAPAN	C48	N/S	820-940	14	N/S	15	10	N/S	N/S	NO	N/S		235-285	
BS5892:PT3	UK	R7T	N/S	820-940	14	N/S	15	N/S	N/S	N/S	NO	2MM#		241-277	
EN13262	EUROPE	ER7	520 MIN	820-940	14	N/S	17	10	N/S	80 MIN	YES	1MM	2 OR 3MM$	245 MIN	235 MIN
IRSS	INDIA	R19	410 MIN	820-940	14	N/S	15	N/S	N/S	N/S	NO	3.2MM		241-277	
JIS E5402	JAPAN	C51	N/S	860-980	13	N/S	15	N/S	N/S	N/S	NO	N/S		248-302	
BS5892:PT3	**UK**	**R8T**	**N/S**	**860-980**	**13**	**N/S**	**15**	**N/S**	**N/S**	**N/S**	**NO**	**2MM#**		**255-285**	
EN13262	EUROPE	ER8	540 MIN	860-980	13	N/S	17	10	N/S	N/S	YES	1MM	2 OR 3MM$	245 MIN	
GOST 10791	RUSSIA	GRADE 1	N/S	880-1080	12	21	30	N/S	N/S	N/S	YES	YES		248 MIN	
FSR	FINLAND	ER8MOD	530 MIN	860-980	13	50 MIN	15	10	N/S	N/S	YES	2MM		250 MIN	
VALDUNES	FRANCE	R8TUCS	600 MIN	920-1000	13	40 MIN	17	10	N/S	N/S	YES	1MM	2 OR 3MM$	265 MIN	
IT MET R103	ITALY	SUPERLOS	600 MIN	900-1000	16	45 MIN	22	12	10	85 MIN	YES	1MM	2 MM	265 MIN	
AAR M107	N.AMERICA	A	N/S	N/S	N/S	N/S	N/S	N/S	N/S	N/S	YES	1.6MM		255-321	
JIS E5402	JAPAN	C55	N/S	900-1050	12	N/S	12	N/S	N/S	N/S	NO	N/S		255-311	
BS5892:PT3	UK	R9T	N/S	900-1050	12	N/S	10	N/S	N/S	N/S	NO	2MM#		262-311	
EN13262	EUROPE	ER9	580 MIN	900-1050	12	N/S	13	8	N/S	N/S	YES	1MM	2 OR 3MM$	255 MIN	
GOST 10791	RUSSIA	GRADE 2	N/S	910-1110	8	14	20	N/S	N/S	N/S	YES	YES		255 MIN	
TB/T 2708	CHINA	CL60	N/S	910 MIN	10	14	16	N/S	N/S	N/S	YES	YES		265-320	
GOST 10791	RUSSIA	GRADE 3	N/S	980-1130	8	14	16	N/S	N/S	N/S	YES	YES		285 MIN	
JIS E5402	JAPAN	C64	N/S	940-1140	11	N/S	10	N/S	N/S	N/S	NO	N/S		277-341	
AAR M107	N.AMERICA	B	N/S	N/S	N/S	N/S	N/S	N/S	N/S	N/S	YES	1.6MM		300-341	
IRSS	INDIA	R34	N/S	N/S	N/S	N/S	8	N/S	N/S	N/S	NO	3.2MM		300-341	
AAR M107	N.AMERICA	C	N/S	N/S	N/S	N/S	N/S	N/S	N/S	N/S	YES	1.6MM		321-363	
JIS E5402	JAPAN	C74	N/S	1040-1240	9	N/S	8	N/S	N/S	N/S	NO	N/S		293-363	

N/S = NOT SPECIFIED

UTS = ULTIMATE TENSILE STRENGTH

A = ELONGATION Z = REDUCTION OF AREA

MECHANICAL PROPERTIES OF RIM QUOTED ONLY

* WHEN NO DISTINCT YIELD IS OBSERVED THE 0.2% PROOF STRESS IS REPORTED

2MM LEVEL AS REQUIRED BY RAILWAY GROUP STANDARD GM/RT2466

$ ACTUAL STANDARD DEFECT LEVEL REQUIRED DEPENDENT UPON DESIGN APPLICATION

CAT1 IS PREFERRED OPTION FOR TRAINS WITH SPEED ABOVE 125MPH (200KM/H)

2.2.1. Manufacture of Cast Railroad Wheels

The casting method used for manufacturing steel wheels in South Africa, is the bottom pressure casting process, wherein the molten steel under pressure is forced upwards into a machined graphite mould, see Figure 18 [30, 31, 32]. The graphite moulds are precision-machined to ensure all wheels are cast to the same dimensions and tolerances [30, 31, 32]. Railway scrap is used as raw materials.

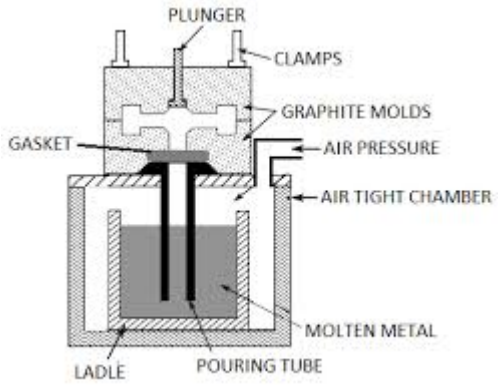

Figure 18. Chamber used for the controlled pressure pouring process [32]

In the controlled pressure pouring process the molten metal is poured into a ladle in a chamber. The chamber has an air tight cover with a ceramic pouring tube attached. The chamber has an air tight cover to prevent oxidation and thus produces very clean steel [30, 31, 32]. Compressed air is forced into the chamber, pushing the molten steel through the pouring tube and into the graphite mould positioned on top of the tube. The molten metal thus fills the mould from the bottom to form the wheel and after allowing for a pre-determined setting time the mould is removed. The wheel is cast to close tolerances because the molten metal is forced into the mould at a controlled rate [30, 31, 32]. This minimizes the amount of machining required.

After casting, the wheels are typically normalised to remove undesired residual stress that remain in the wheels. The wheels are then rim quenched with water spray on the tread surface using equipment similar to that shown in Figure 19 [27, 33]. Rim quenching the wheel increases the strength level of the steel, improves wear resistance and induces a desirable compressive residual hoop stress in the rim. These compressive stresses are known to help prevent the formation of rim fatigue cracks in service and thus are important to wheel life and safety. Following quenching, the wheels are placed in a tempering furnace and then the wheels are air cooled.

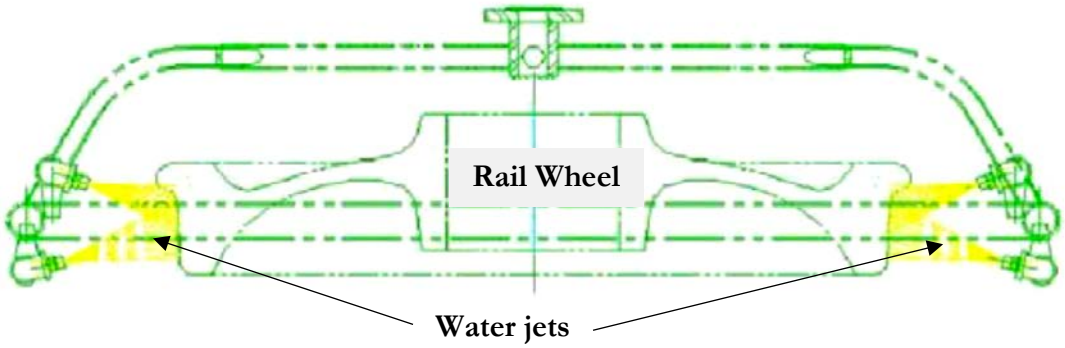

Figure 19. A wheel quenching equipment [33]

Figure 20 is a schematic showing the cross-section of a wheel rim with residual circumferential stresses that formed from the rim quenching process [34, 35]. These stresses are negative compressive stresses and exist within an allowable maximum (σ_{max}) and minimum (σ_{min}) range. The allowable stresses, according to the EN13262:2004 Standard, for the rim near the surface of the tread is required to be in the range of -80 N/mm^2 to -150 N/mm^2. These stresses should decrease away from the rim surface and should be zero at a depth of between 35 mm and 50 mm [35].

When the water spray quenches the hot austenitic wheel rim, the rim cools and shrinks inward and transforms to pearlite [34]. However, the steel below the quenched region is still hot and has a reduced yield strength [34]. The inner parts of the rim and the plate are compressed by the cooled outer rim and localised yielding occurs. When the entire wheel cools and shrinks, the inner rim and plate are now smaller than they there were originally because of the compressive yielding [34]. They however try to fit into a larger space, resulting in the lower part of the rim and plate being in tension, while the outer portion of the rim is in compression, helping to prevent the formation of fatigue cracks [34].

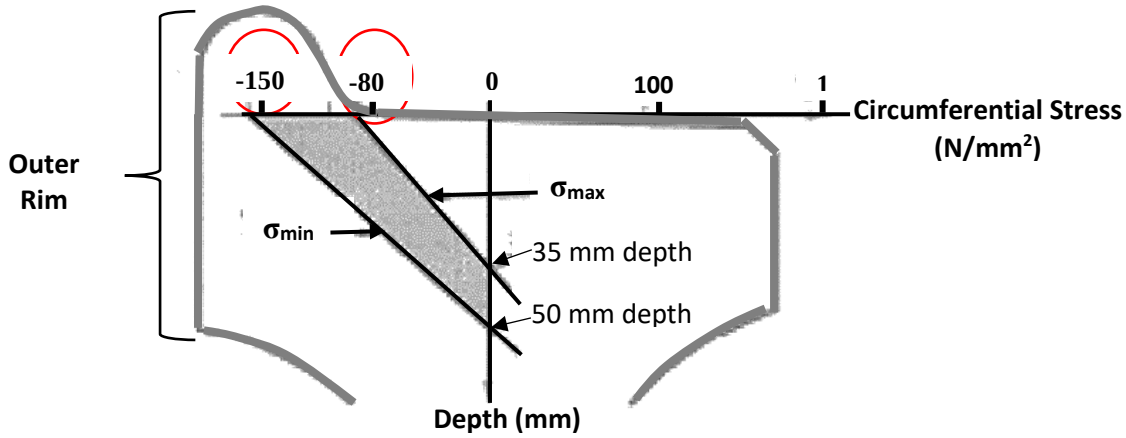

Figure 20. A schematic showing the cross section of a wheel rim showing the allowable ranges for the circumferential stresses, according to the EN13262:2004 Standard, for a rail steel. The level of compressive circumferential stresses near the surface of the tread is required to be in the range of 80 N/mm^2 to 150 N/mm^2. These stresses are required to be zero at a depth of between 35 mm and 50 mm [35]

The casting process inherently produces micro-shrinkage porosity particularly in the absence of degassing [28]. The South African cast wheel manufacturer does not have a degassing facility. The presence of porosity reduces the fracture toughness of the material [28]. For the South African Railways, the inclusion content in wagon wheels are to be determined according to ASTM E45-05 which sets an inclusion limit such that the steel conforms to a quality that is not more severe than types sulphide ≤2, 5; alumina≤2, 5; and globular≤2, 5 for the heavy and thin series [28].

Railway wheels suffer from centreline porosity due to macrosegregation and shrinkage, see Figure 21 [36, 37, 38]. This porosity is common in the continuous casting manufacturing process and occurs at the center of the bloom. A fully columnar structure is not desired since it increases segregation on the centreline [39]. Solute enriched liquid can thus flow through the centreline and solidify as central segregation even if the original structure is of equiaxed type [39]. Centreline porosity can also occur by internal solidification shrinkage that promote a flow of carbon-enriched steel in the final solidification region in the centre of the cast material

This centreline porosity affects the mechanical properties of the steel negatively. The most popular combative method has been the use of Electro Magnetic Stirring (EMS) of the liquid steel by which the equiaxed crystal increase [38].

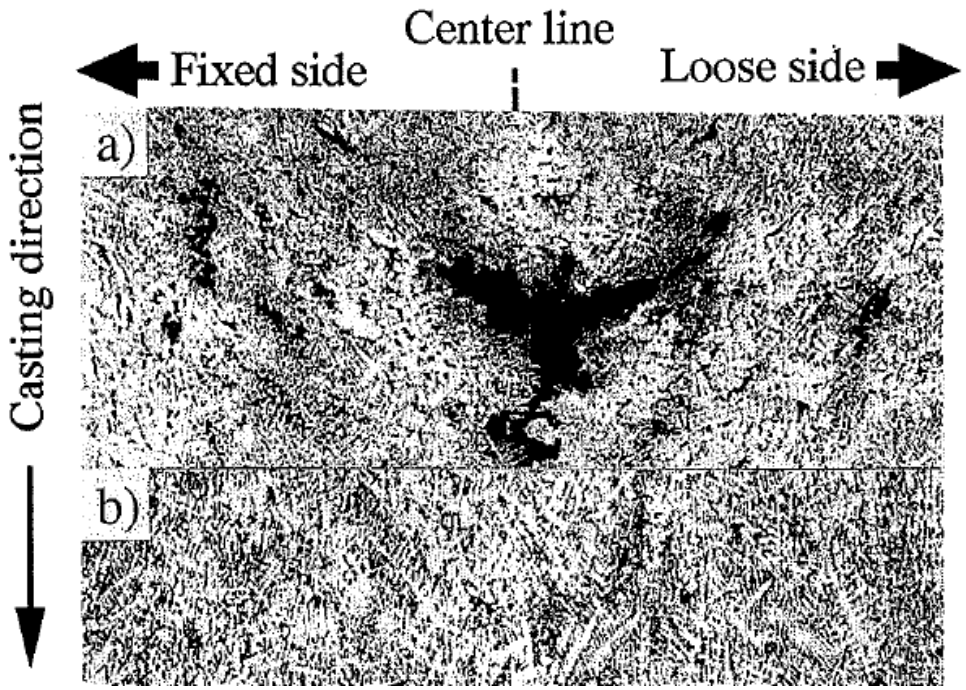

Figure 21. Solidification structure of forged bloom in the casting direction [36]

2.2.2. Manufacture of Forged Rail Wheels

The typical manufacturing process for forged wheels includes the steps shown in Figure 22 [40, 41, 42]. Wheel forging involves the shaping of a hot billet into a wheel shaped die by applying localised compressive forces amounting to 10 tons [28]. The forging is normally carried out above the austenizing temperature ranging between 871°C and 1200°C. The forging process is followed by rolling and a rim quenching heat treatment. The wheel is austenitised at □830°C in, followed by a water quench of the wheel rim [28]. The wheel is then tempered at □450°C [28]. After tempering the wheels can be sand blasted and machined in preparation for shipment.

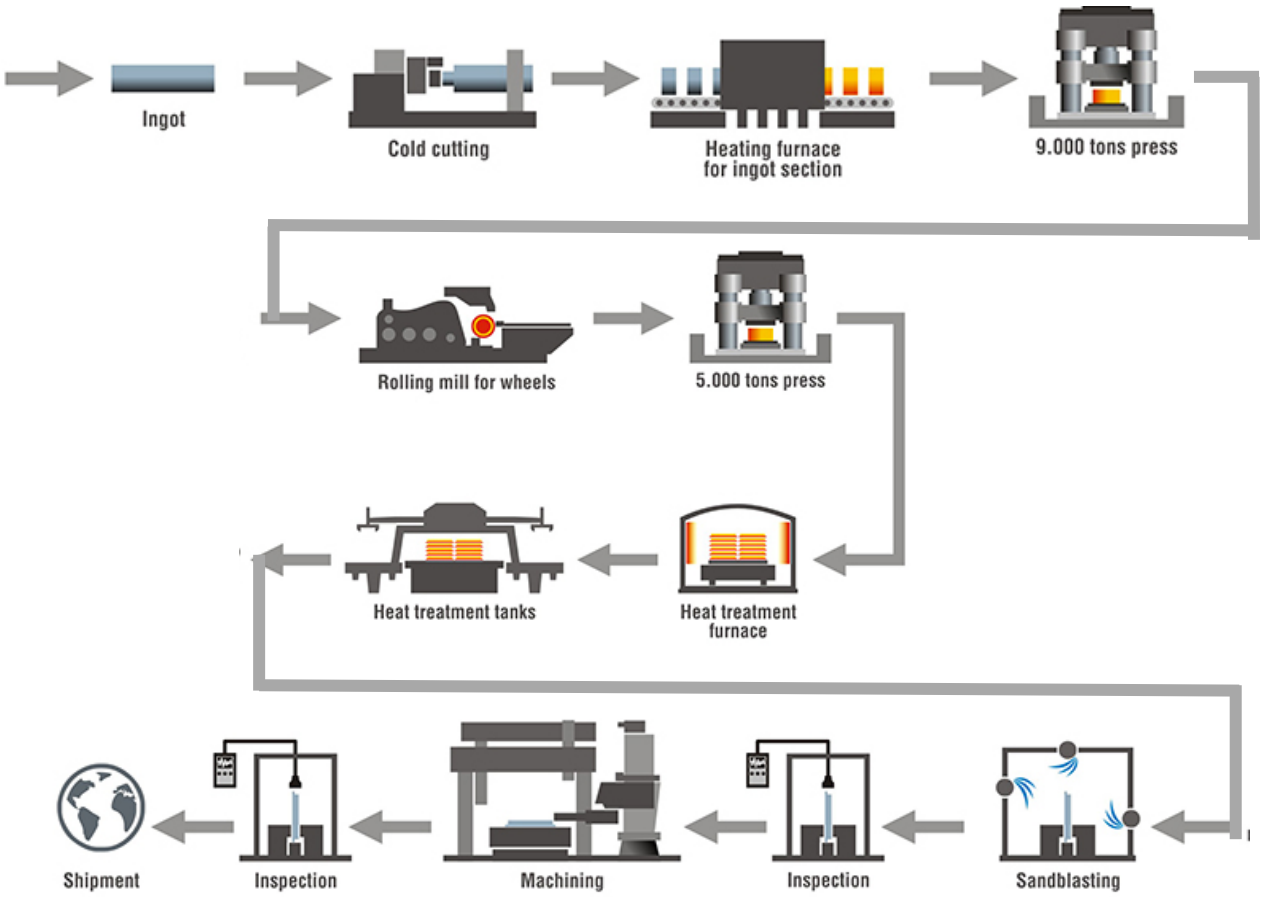

Figure 22. Schematic showing the typical steps used to manufacture forged wheels at Lucchini, Italy [40]

2.2.3. Rim Quenched Forged and Cast Wheels

Rim quenching as previously discussed is a heat treatment process where, after austenitising the rim is sprayed with water for some minutes before air cooling. Cast and forged wheel both are given a rim quenching heat treatment process, followed by tempering. This allows for the development of a hardened rim under compression and increases the strength of the rim. The temperature distribution through a typical solid wheel at the end of rim quenching has been estimated using finite element modelling (FEM) [33, 43]. For an ideal heat treatment, as shown in Figure 23, at the end of the quenching process, the minimum temperature occurs on the tread surface and is approximately 427°F (218°C), heating up towards the centre of the wheel up to 1444°F (784°C).

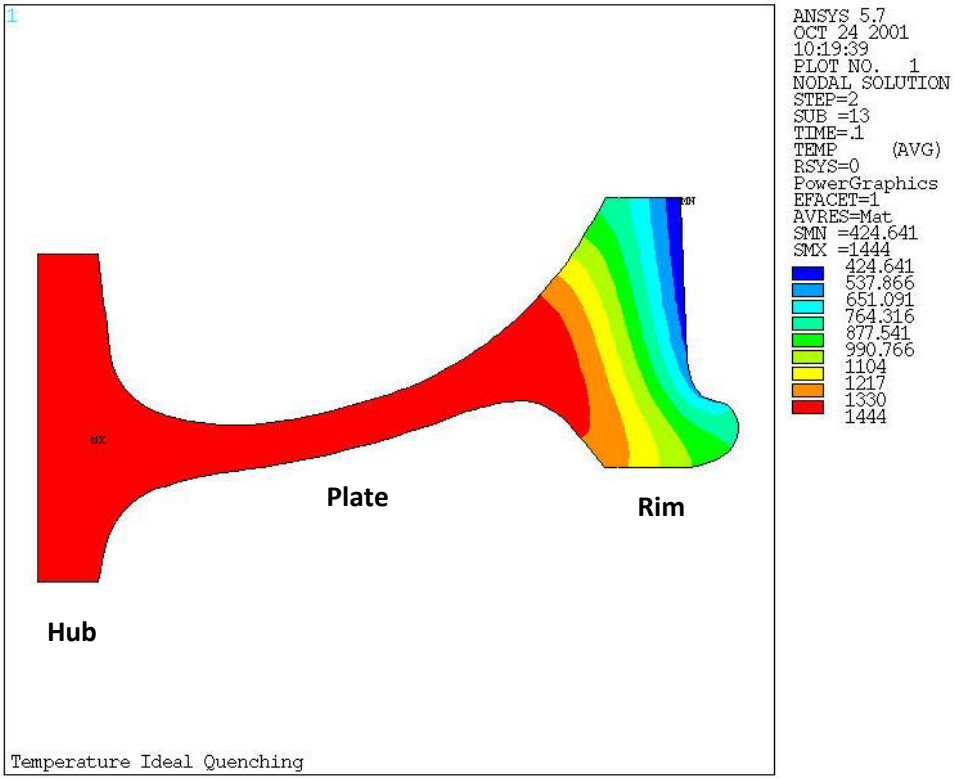

Figure 23. The temperature distribution in a rail wheel at the end of an ideal rim quenching procedure. The temperatures are measured in Fahrenheit [°F] [33]

Figure 24 shows the temperature-time profile taken over 60s of three nodes (on the rim, plate and hub of the wheel), using FEM, beginning at the initial temperature of 920 °C through the quenching process [44]. It can be seen that the temperature in the rim and hub decrease much slower than that in the plate, which characteristic for a wheel is quenching. The rim and hub are significantly thicker than the center piece.

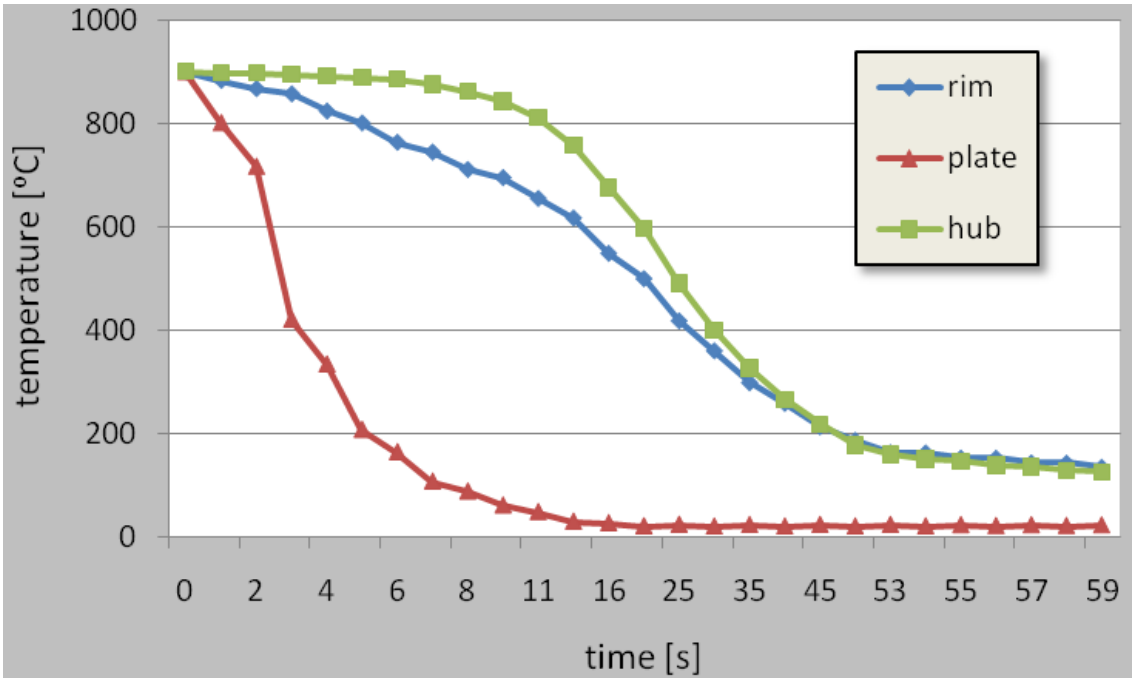

Figure 24. Node temperature over time on the rim, plate and hub during rim quenching [44]

Figure 25 shows a time temperature transition (TTT) diagram for an unalloyed steel with approximately 0.5wt.% carbon [27]. Three cooling paths 1-3 and their corresponding micrographs are also shown. The desired cooling path for rim quenching would be somewhat to the left of path 2 (0.2°C/min or 0.0042°C/sec), crossing the pearlite region, producing a minimum volume fraction of ferrite and leaving the bainite and martensite region untouched [27].

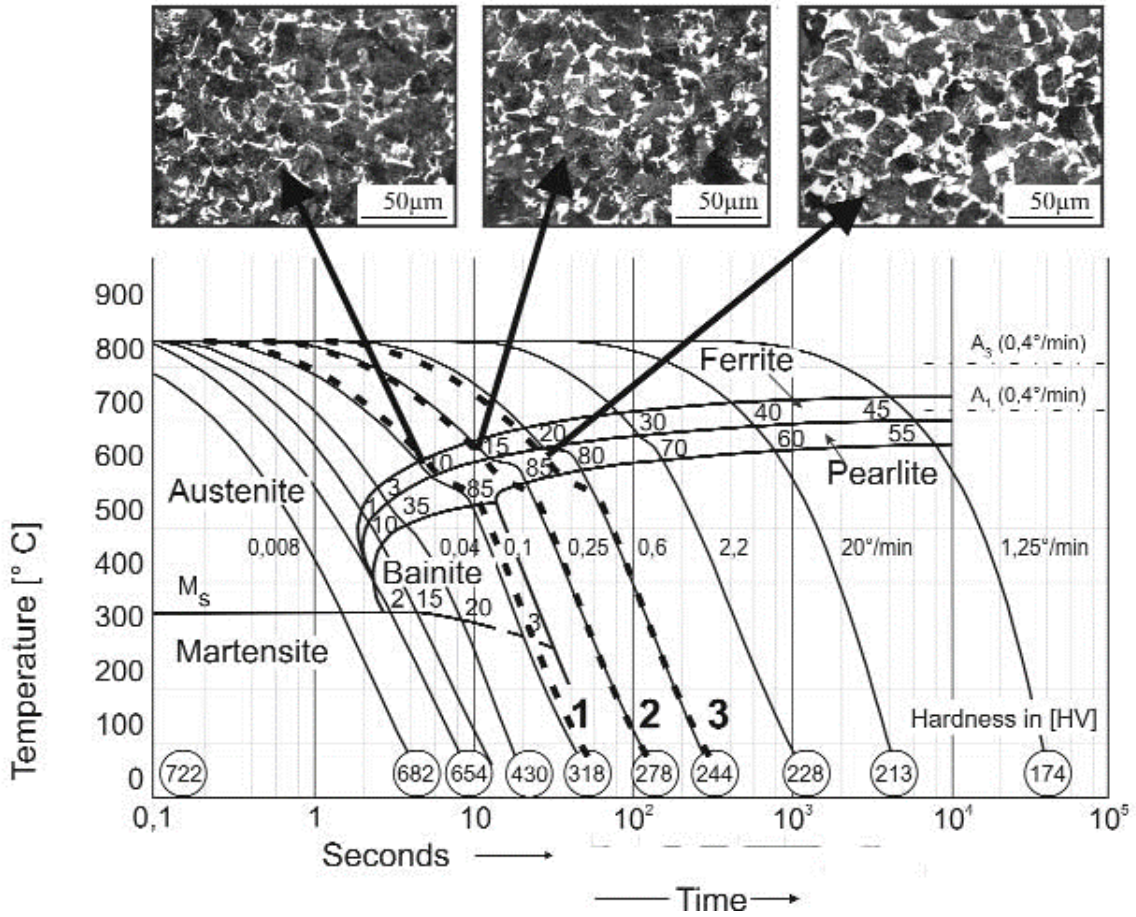

Figure 25. Time Temperature Transition diagram for an unalloyed steel with approximately 0.5 wt.% carbon with different cooling paths (1-3) and the corresponding micrographs [27].

A ferrite-pearlite solid wheel was given a rim chilling treatment consisting of heating the wheel up to 875°C, placing it in a circular tank where the water can flow only around the rim, maintaining it here for a time of 19 minutes and after that leaving it to cool in calm air [45]. The rim chilling was followed by tempering at about 515°C for a time of 5 hours. A CCT diagram was drawn for the different regions of the wheel after heat treatment, but before tempering, see Figure 26a [45]. Figure 26b shows the cooling paths for the different regions a to e and their corresponding microstructures after chilling. The rim edge formed a thin layer of martensite due to faster cooling rates, this is usually machined off. A large portion of the rim comprised bainite-ferrite-pearlite microstructures whereas the hub was pearlite-ferrite.

The estimated cooling rates for Paths a to e are:

- Path a ~65°C/s
- Path b ~60°C/s
- Path c ~5°C/s
- Path d ~0.3°C/s
- Path e ~0.2°C/s

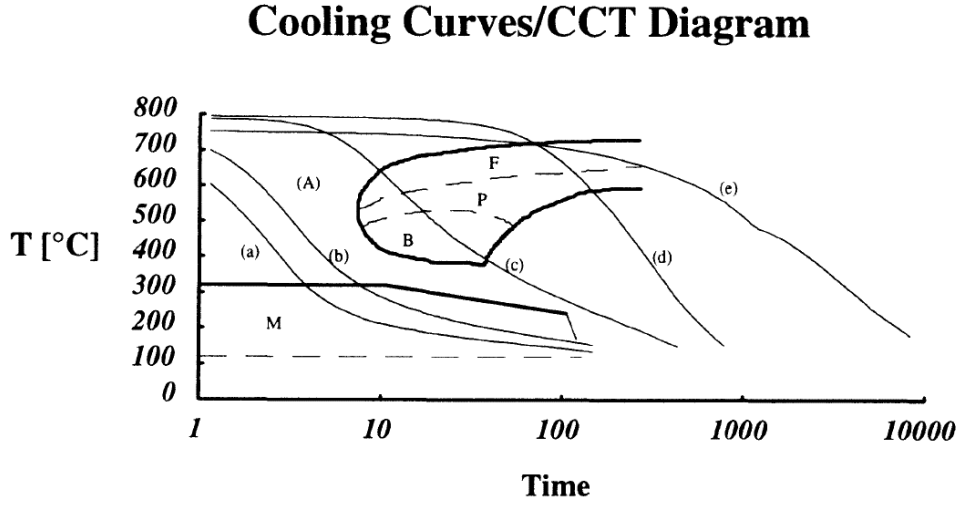

(a)

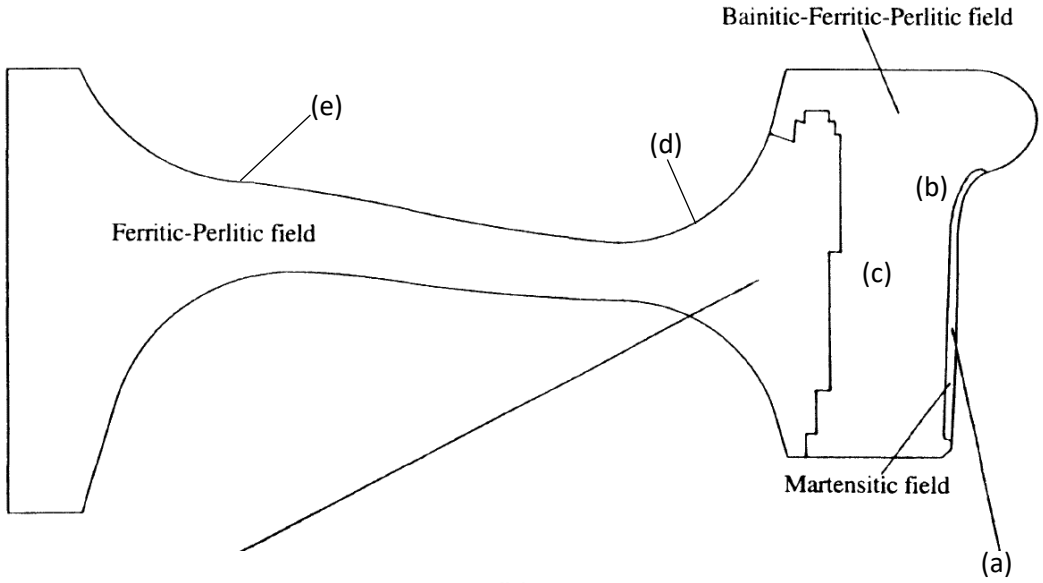

(b)

Figure 26. (a) Numerical cooling curves and CCT diagram of the material, (b) Microstructure map after chilling after chilling of a ferrite-pearlite solid wheel [45].

2.3. The Minimum Pearlite Interlamellar Spacing (d)

The interlamellar spacing in the tread of the wheels is minimises to maximise the strength and hardness properties. Pearlite grows in a lamellar structure with the pearlite spacing (d) defined as the perpendicular distance across two consecutive lamellae, see Figure 27 [46]. The measurements of interlamellar spacing is generally measured using the scanning electron microscope (SEM) or the transmission electron microscope (TEM), except if it is very coarse and light microscopy can be used [46]. The proper sectioning plane also needs to be determined for correct analysis [46]. Even when the pearlite is formed isothermally, yielding a minimal spacing range, the sectioning plane can cut through the pearlite colonies at all possible orientations relative to the lamellae thus giving the appearance of a greater diversity of spacing measurements than are actually present [46]. As the sectioning plane deviates more and more from being perpendicular to the lamellae in a colony, the apparent spacing and the apparent interlamellar spacing increases [46]. The actual thickness of the cementite lamella is purely a function of the lever rule on the Fe-C phase diagram i.e. the percentage carbon.

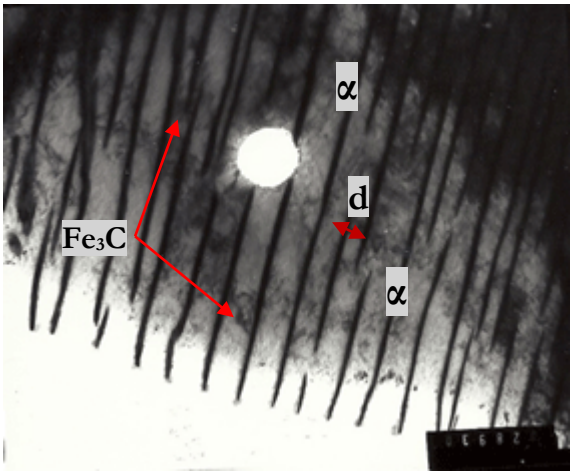

Figure 27. transmission electron microscopy (TEM) micrograph of a thin foil rotated under the beam until the cementite lamellae were parallel to the electron beam to measure the true pearlite spacing (d) at 22 000X. α is ferrite and Fe_3C is cementite [46]

The interlamellar spacing can be determined using direct surface measurements on a polished and etched sample using the lineal intercept method [47]. A line of known length is drawn randomly across a number of pearlite lamellae and the interlamellar spacing is calculated using the line intercept method as an average for a number of

lines. To account for the orientation effects a conversion factor is used as shown in Equation 2, where $\bar{d}$ is the pearlite spacing (after conversion) and d_p is the actual measured pearlite spacing

$$\bar{d} = 2d_p \qquad \textit{Equation 2}$$

There is a thermodynamic limit to the minimum pearlite spacing that can be achieved after transformation from austenite as shown in Equation 3 [48].

$$d_{min} = \frac{2\gamma_{SF}T_e}{\Delta H_V} \times \frac{1}{\Delta T} \qquad \textit{Equation 3}$$

The minimum pearlite spacing decreases with a decrease in transformation temperatures. The actual pearlite spacing (d_p) that is achievable with the current accelerated cooling methods is very close to d_{min}. The real or actual pearlite spacing (d_p) is always greater than the theoretical minimum spacing d_{min}, i.e. $d_p \geq d_{min}$. This limits the further development of pearlitic steels with finer pearlitic spacings. This has led to the search of alternative rail microstructures such as bainite. Additionally higher hardness pearlitic steel will result in higher strength but lower ductility.

2.4. Failure of Railway Wheels

In the past 50 years in North America, the pearlitic rail steels have undergone extensive improvements in their microstructures and properties, see Figure 28 [49]. In this figure, which is an Fe-C diagram, it is shown that the carbon content of the pearlitic rail steels has increased from about 0.4 wt% in the 1960s to >0.8 wt% in the 2000s to date. This has allowed for an increase in the hardness of the steels from a lower 248 BHN to >400BHN. The microstructure of the steel has remained pearlitic but with a reduced ferrite content and refined structure. In the 60s and 70s pearlitic rail steels failed mainly due to general wear and rolling contact fatigue (RCF) [49]. Today, however, the addition of carbon and improved heat treatment processes has allowed for the formation of a refined pearlite microstructure with a hardness >400 HBN. The major failure experienced by pearlitic rail steels today is caused by RCF [49]. This type of failure will be will be discussed in detail in the following sections. .

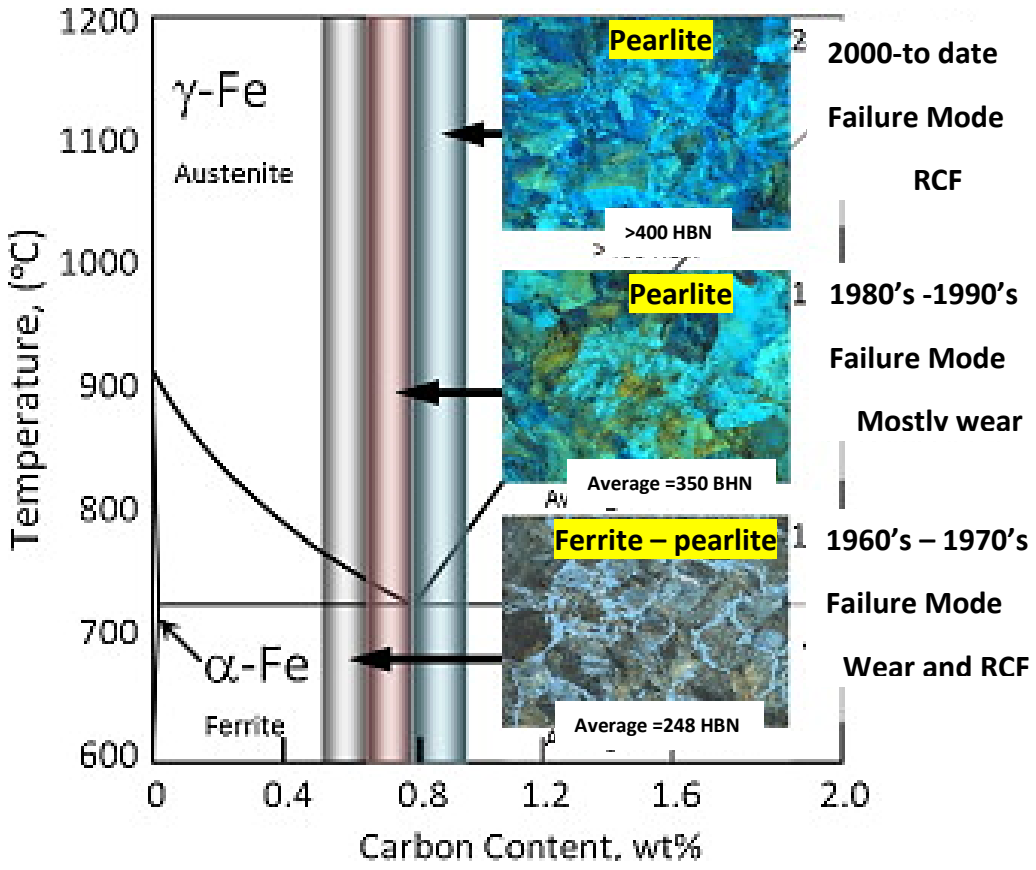

Figure 28. 50 year evolution of rail steel metallurgy for heavy haul use in North America [49]. RCF = rolling contact fatigue, HBN is Brinell hardness

Railway wheels are the most stressed components of the railway vehicle as they carry the axle load (up to 25 tonnes and more), guide the train on the track and transfer acceleration, and deceleration, forces to the rails [27]. They are subject to damage as they do this.

A significant cost for the heavy haul industry results from the damage of railroad wheels in the wheel tread, which often needs unexpected reprofiling to a deep thickness of the tread in order to remove any damage in the form of bruise marks or fatigue cracks. This is one of the most important reasons for the drastic reduction of the total life cycle (TLC) of the wheel itself [11]. Damage on the tread caused by fatigue can also be dangerous if it causes the detachment of small parts of the wheel with consequences both on the suspension, on the vehicle bearings and on the railway infrastructure [11].

The damage on the surface in rails and wheels occurs due to rolling contact fatigue (RCF) through the initiation of fatigue cracks [50].These cracks may lead to the loss of a part of the wheel or rail [51]. Rolling contact fatigue is a family of damage phenomena that appear in railway steels [50, 51]. This damage is caused by

repeated overstressing of the surface or subsurface by a significant number of intense wheel-rail contact cycles [11, 50]. The process is also known as ratcheting [11]. Heavy loading causes deformation to occur at the rail/wheel contact in the direction of the applied traction [50]. The deformation accumulates and each incremental deformation ratchets the surface layer. Eventually, after additional cycles, the steel fractures forming a surface crack [50].

The key processes that govern RCF are crack initiation and propagation [50]. The magnitude and position of the crack-initiating stresses depend on the contact geometry, load and friction conditions [50]. Under high friction conditions (dry conditions), shear stresses are large but very shallow and cracks propagate only about 3mm deep [50]. Under low friction conditions (wet conditions) the peak shear stresses decrease but extend deeper into the rail material, i.e. typically to a depth of between 7 to 15mm [50].

In the contact zone, plastic deformation occurs combined with residual stresses and strain hardening. At high load levels, each new load cycle increases the plasticity and eventually the accumulated deformation exceeds the ductility of the material and ratcheting occurs [51]. Subsurface cracks are initiated below the tread at certain material imperfections such as non-metallic inclusions or as shear cracking of the pearlitic microstructure usually between 3 and 5mm below the running surface where the largest shear stress occurs [51]. The initiation of subsurface cracks requires very high loads and these can propagate parallel or at an inclined angle to the wheel surface [51]. At a certain point they may branch towards the surface and/or in a radial direction. Subsurface induced cracking allows for a larger crack to grow before spalling and are thus more dangerous than surface induced cracks [51].

Shelling (Figure 29) is the term given to the process of material losses from the wheel tread following the establishment of a fatigue network of cracks while spalling is material loss due to thermal input caused from braking, whether from shoe braking or wheelset sliding [11].

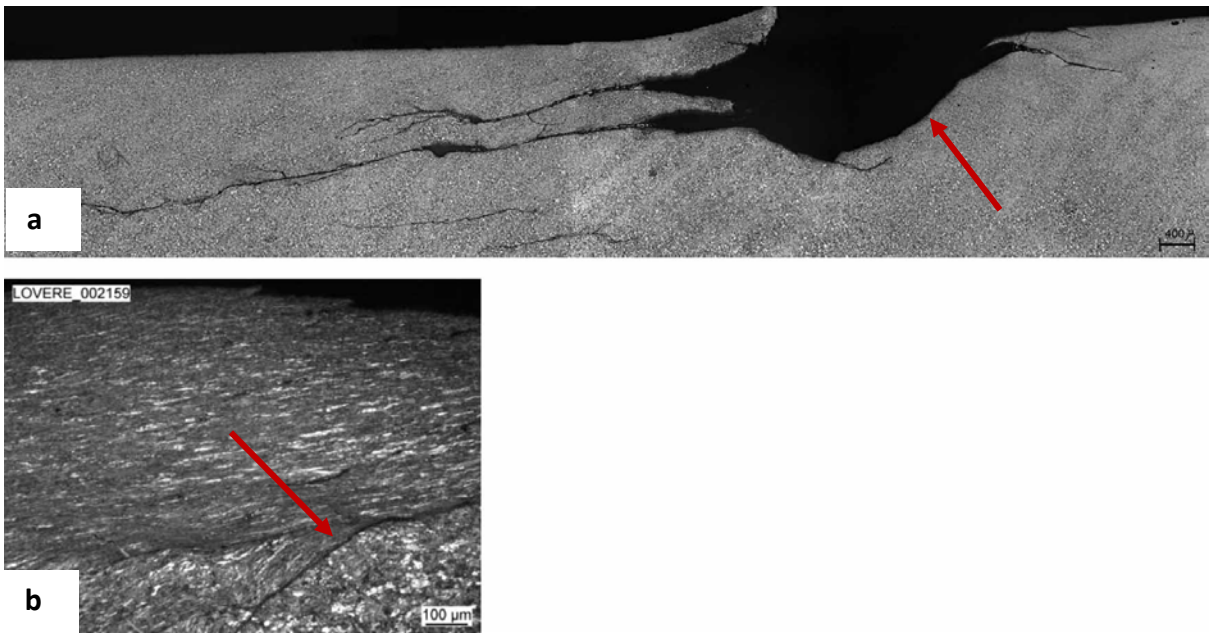

Figure 29. (a) Transversal section of typical rolling contact fatigue (RCF) damage on the tread of solid wheels, (b) severe plastic deformation with subsurface-initiated cracks. This is an example of shelling [11]

The initiation of surface cracks in wheels can be due to cyclic thermal loads, which arise during braking [51]. The braked wheel tread is subjected to periodic heating due to friction with the brakeshoe and subsequent cooling, for example see Figure 30 [51]. In Figure 30 the heating and cooling experienced by the tread of two block-braked wheels over a 500 second period in service is shown. In these wheels temperatures of □400°C are reached during slowing down and braking.

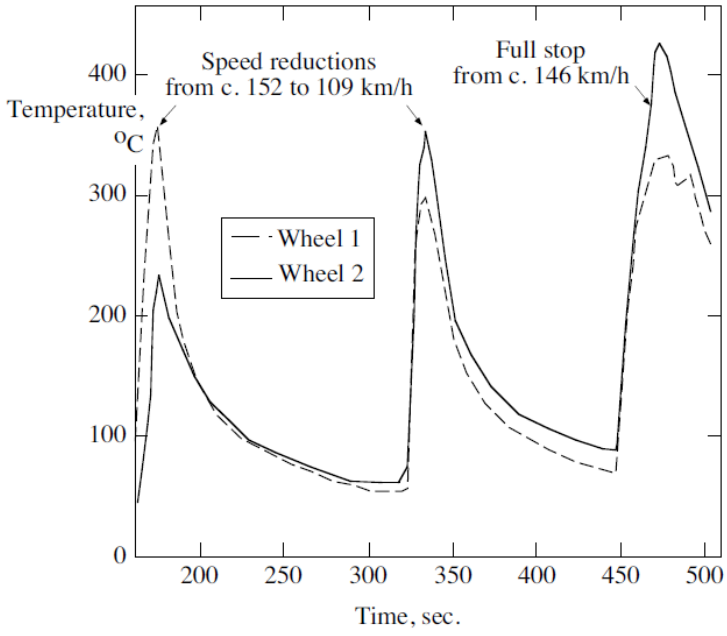

Figure 30. Periodic heating and cooling of the tread of a block-braked wheel [51]

The heating and the cooling occur non-uniformly along the circumference of the wheel, concentrating on the so-called hot spots where the temperature increase can be as high at 540°C and thermal stresses up to 465MPa. In some instances the local temperature can reach much higher values in the austenitic region, above the A_{c3} temperature, forming austenite that cools into brittle martensite. The local transformation of pearlite to austenite and then martensite can occur with local thermal expansion and residual stresses forming in the wheel rim [51]. Cracks originate at these highly stressed regions, and sometimes grow some millimetres into the wheel material before deviating to the surface, causing spalling [51]. They may, however, propagate in the radial direction, damaging the whole wheel section [51]. The brittle martensite formed in heavy haul railway wheels has a peculiar characteristic in that it is present as a thin surface layer known as a 'white layer' (Figure 31) [11].

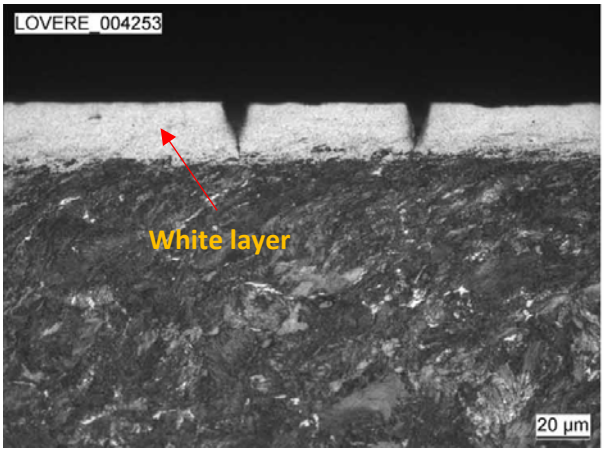

Figure 31. Appearance of brittle martensite ('white layer') [11]

Generally for a given hardness level, pearlitic steels have a higher resistance to RCF than common bainitic steels and the RCF resistance increases with increasing hardness [50]. The strength of steel in shear is understood to be the main factor that controls resistance to rolling contact fatigue in rail steel [50]. In particular, it is the shear yield strength developed in the work-hardened surface layers that is critical, and different microstructures work-harden at different rates [50]. Work hardening leads to a local increase in flow strength resulting in the material being able to accommodate higher strains elastically, before deforming [52].

Laboratory tests have shown bainitic steels work-harden less than pearlitic steels under rolling contact conditions [50]. Thus, while bainitic steels may have higher bulk strength than pearlitic steels, pearlitic steels are likely to develop work-

hardened layers with greater strength. The shear yield strength (K) is easily measured in the laboratory and is estimated as follows [50]:

$K \approx \frac{H}{6}$ *[50]* *where H = hardness in Vickers* *Equation 4*

2.4.1. Wheel Failures in South Africa

The major failure mode for many years for freight wheels in South Africa has been deep shelling/spalling due to casting defects and spread rim failures due to wheel-rail contact problems [28]. The wheels also fail by fatigue originating from micro-shrinkage porosity [28]. [28]. In South Africa there has been a number of reported wheel related derailments between January 2008 and December 2014, particularly on the coal line, as shown in Table 5 [28]. The maximum load of Jumbo wagons on the coal line is 104 t, or 26 t per axle. Three, of the 16 reported failures, were forged wheels and thirteen were cast wheels.

Excessive hollow wheel wear, wear that exceeds 2mm metal loss in the center of the wheel tread, was experienced by forged wheels used on the coal line [28]. Usually these wheels are maintained every two years but between February 2011 and August 2012, the hollow wear was so excessive that premature maintenance of the forged wheels was required. There was no evidence of excessive wear on the cast wheels [28]. The forged wheel failures were due to arc strike and pitting corrosion.

Table 5. Wheel related derailment in South Africa between year 2008 and 2014 [28]

Report no.	Place of derailment	Date of derailment	Type of wheel	Root cause
MV215	Intshamazi	2008-04-15	Cast	Inconclusive evidence
MV570	Empangeni	2008-07-23	Cast	Rim spread
MW335	Sentrarand	2009-05-19	Cast	Mechanical damage
MW287	Vanderbijlpark	2009-07-06	Cast	Shrinkage porosity/ casting defect
MX243	Lydenburg	2010-06-19	Cast	Shrinkage porosity/ casting defect
MY179	Newcastle	2011-03-04	Cast	Stress raiser/ corrosion
MY254	Biljkor	2011-05-01	Cast	Metallurgical notch cause by martensite
MX015	Meyerton	2011-09-08	Cast	Plastic deformation
MY537	Belfast	2011-10-15	Cast	Mechanical damage related
MY255	Dikgale	2012-07-11	Cast	Thermal cracks that initiated on the thread
BBG0620	Kaydale	2013-06-24	Cast	Mechanical damage related
BBF9093	Coal line	2013-07-15	Forged	Weld arc that became stress raiser
TA656	Piet Retief	2013-07-27	Cast	Residual stresses/ matensite
TB 012	Ore line	2014-02-01	Forged	Pitting corrosion
TB 145	Sentrarand	2014-04-14	Cast	Shrinkage porosity
TB 612	Orex	2014-08-19	Forged	Pitting corrosion

2.5. Bainite

The bainite transformation can generally be divided into two stages: the stage of nucleation and growth of ferrite laths/plates and the stage of carbon redistribution which can lead to the precipitation of carbides [52, 53, 54]. The ferrite plates nucleate at the austenite grain boundaries. [55]. There are many types of bainite that can form such as columnar, granular, inverse, upper and lower bainite [53, 55, 56, 57]. Bainite is therefore defined as a non-equilibrium phase comprising ferrite plates and carbides [55-68].

The ferrite plates are typically ~10μm in length and 0.2μm thick [53, 55]. The plates grow in groups called sheaves and tend to adopt almost the same crystallographic orientation within a sheaf [53, 54, 55, 67, 69]. The sheaves of ferrite are separated by regions of residual phases of retained austenite, martensite or cementite [55]. These residual phases form subsequent to the growth of the ferrite. The plates within the sheaves have a Kurdjumov-Sachs (KS) crystallographic orientation relationship with the parent austenite: $\{111\}_\gamma // \{011\}_\alpha$ and $<011>_\gamma // <110>_\alpha$ [53, 55]. The platelets in a sheaf may not be completely isolated from one another by the

residual phase but may have a low misorientation grain boundary along the surfaces where the platelets come in contact [55].

The most common forms of bainite found are upper and lower bainite. Upper bainite has very coarse interlath cementite stringers decorating the heavily dislocated ferrite plates (Figure 32a) and forms at higher temperatures than lower bainite [56-68]. The continuity of the carbides in upper bainite depends on the carbon concentration. Inter-lath stringers of cementite in upper bainite impart low impact strength to the steel and is generally avoided. In lower bainite, ε-carbide ($Fe_{2.4}C$) particles form inside the bainite laths while some cementite (Fe_3C) from the remaining carbon may form between heavily dislocated ferrite plates (Figure 32b). The lower temperatures at which lower bainite forms provides an opportunity for some of the carbon to precipitate in the supersaturated ferrite, due to the higher undercooling and a slower carbon diffusion rate [53, 55, 56]. The carbides in lower bainite generally adopt a unique habit plane variant in the ferrite: 55°- 65° angle relative to the long axis of the ferrite plate [53, 55, 56].

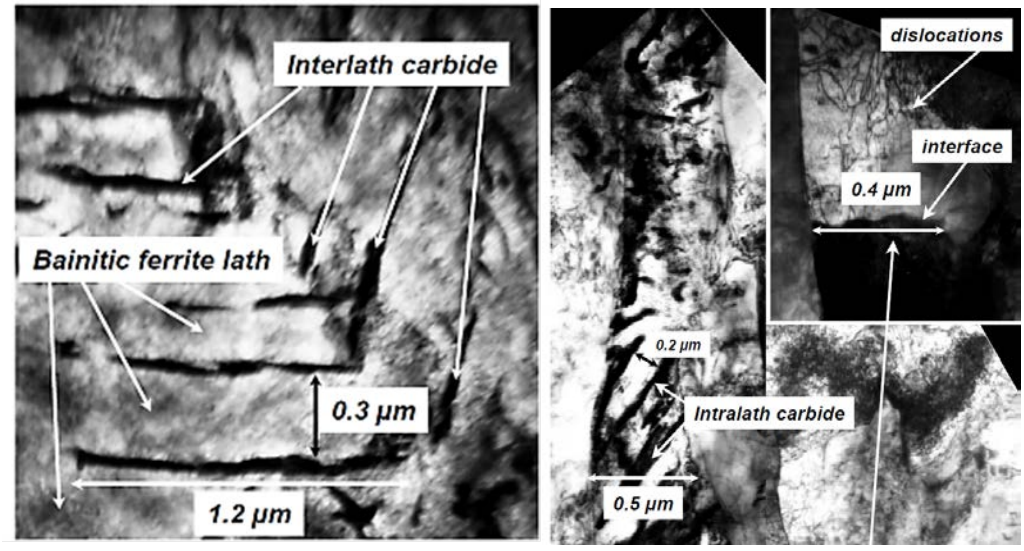

(a) (b)

Figure 32. Transmission electron micrograph (TEM) of (a) upper bainite showing interlath carbides with two different crystallographic variants and (b) lower bainite with intralath carbides and dislocation debris [52]

If carbon redistribution is rapid at high temperatures, i.e. if the carbon diffusion process dominates, the cementite does not precipitate within the ferrite platelets and upper bainite forms [53, 55, 69]. If carbide precipitation is rapid within the ferrite plate or if there is a high carbon saturation in the ferrite at lower temperatures, all the

carbon cannot easily be rejected from the ferrite and lower bainite forms. Figure 33 is an illustration of the differences between upper and lower bainite [53, 55].

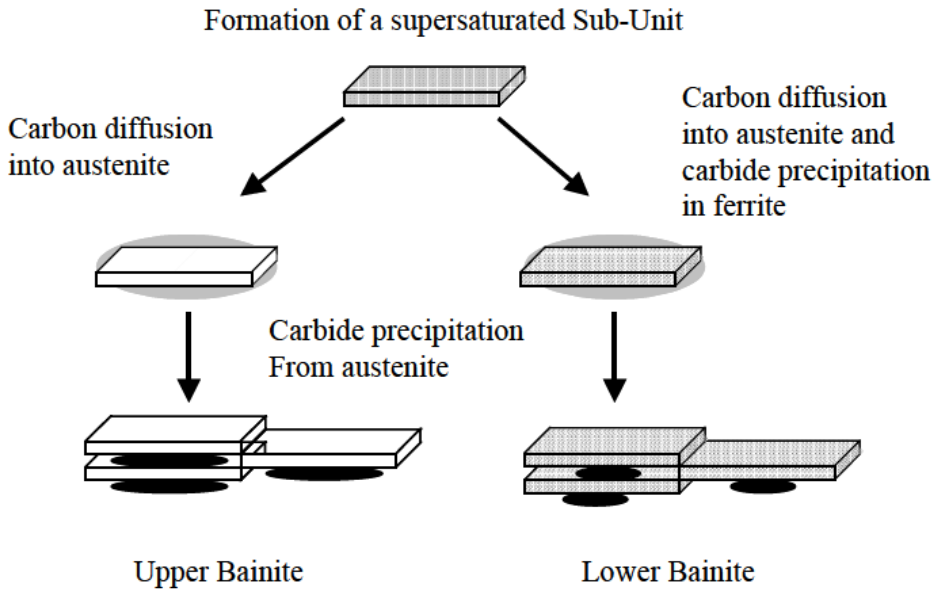

Figure 33. An illustration of the differences between upper and lower bainite [52, 53]

There has been much debate on the mechanism of formation of bainite, whether it is reconstructive (diffusion) or displacive. The diffusion model for the growth of bainite is briefly discussed in the following section.

2.5.1. Diffusional Model for the Growth of Bainite

Pure iron, in the form of austenite, can be transformed into equiaxed grains of ferrite via diffusion of atoms, when the atoms of austenite redistribute into the new lattice structure of ferrite. The flow of atoms occurs in a way which minimises the strain energy of transformation and sufficient time for diffusion is required for the transformation to occur. This kind of transformation is said to occur via a reconstructive mechanism [70].

According to the diffusion theory, bainite is said to nucleate and grow via a reconstructive mechanism [71]. Bainite nucleation is considered to occur by the spontaneous dissociation of specific dislocation defects already present in the parent phase [3]. The ferrite plate of the bainite is considered to form over the whole bainitic temperature range by a diffusion controlled movement of ledges, similar to that for the formation of Widmanstätten pro-eutectoid ferrite [72, 73]. The growth rate of bainite is greater in the edgewise direction, i.e. lengthening of the subunits dominates over thickening [71]. This results in the formation and propagation of

ledges. Cementite and ferrite are thought to grow simultaneously and co-operatively [71].

The bainite reaction is assumed to proceed until the carbon content of the retained austenite reaches the equilibrium A_{e3} line (Figure 34) [53, 71]. The austenite carbon content after the bainite reaction, has however been found to be defined by the T_0 line, a line between A_{e1} and A_{e3} on the Fe-C phase diagram. A_{e1} is the temperature on the Fe-C phase diagram at which austenite begins to form during heating and A_{e3} is the temperature on the Fe-C phase diagram at which transformation of ferrite to austenite is completed during heating, x_{T0} is the carbon concentration at which the α (ferrite) and γ (austenite) free energies are the same, defining the T_0 temperature. The T_0 concept will be discussed in detail in the following section.

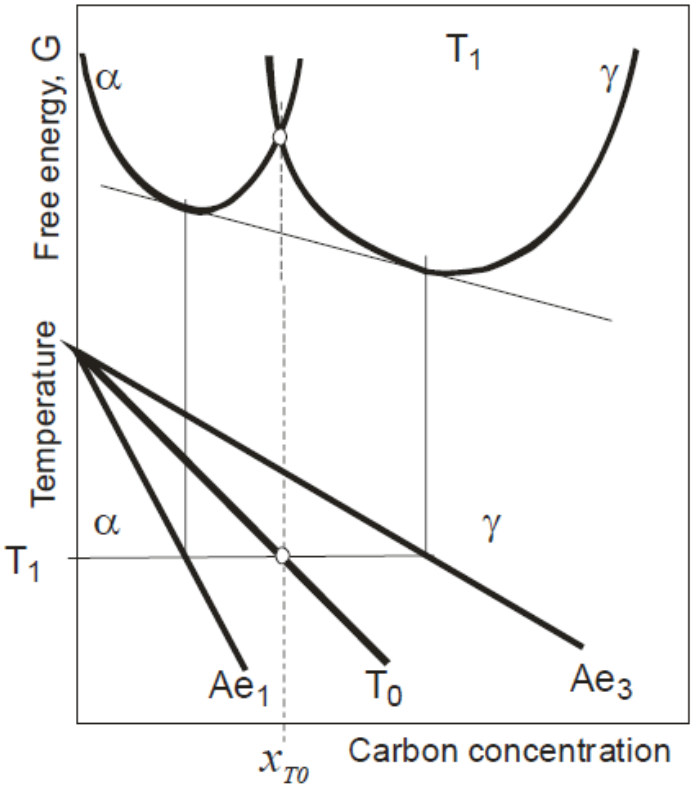

Figure 34. Schematic illustration of the T_0 curve on the phase diagram. α and γ refer to ferrite and austenite respectively. T_1 is the temperature corresponding to the free energy curve, Ae1 is the equilibrium temperature on the Fe-C phase diagram at which austenite begins to form during heating and Ae3 is the equilibrium temperature on the Fe-C phase diagram at which transformation of ferrite to austenite is completed during heating, x_{T0} is the carbon concentration at which the α and γ free energies are the same, α is ferrite and γ is austenite [71]

The carbides are thought to form primarily on the austenitic side of the α/γ interface. This mechanism requires the carbon content of the ferrite to be low and the formation of carbides should occur on the austenite side of the α/γ interface [72, 73]. The process is driven by the solubility of the carbon in the α and γ respectively.

A solute drag model is used to explain the bay in the time-temperature-transformation curve (TTT) at the bainite start (B_s) temperature, while the incomplete reaction characteristics of the bainite transformation are claimed not to be a general phenomenon [72].

Today, however, it is generally agreed that the transformation of bainite is displacive and the focus has shifted to whether carbon diffuses during the formation of bainite or as a result of its formation [53, 54, 74].

2.5.2. Displacive Model for the Growth of Bainite

2.5.2.1. The Shape Deformation - The Invariant Plane Strain

During the phase transformation, when sufficient time is not allowed for diffusion to occur, pure iron can be transformed into bainite when the crystal structure of austenite is changed into that of the product phase by a homogenous deformation of the austenite (the Bain strain) through a displacive mechanism [70]. Figure 35 shows the plastic deformation caused in the adjacent austenite by transformation to bainite [70]. The deformation leads to a change in the shape of the transformed region [70].

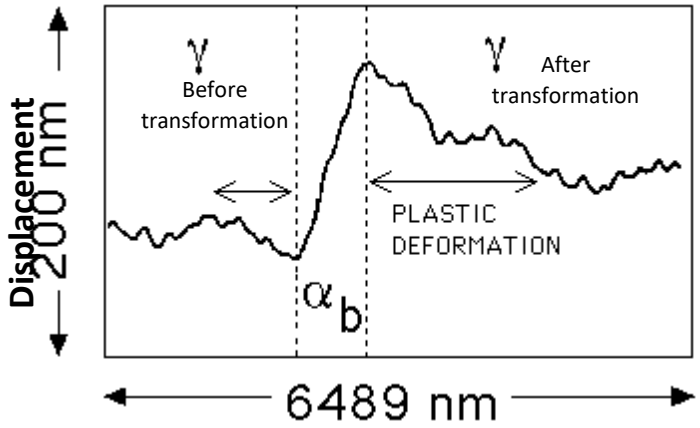

Figure 35. High–resolution atomic–force microscope plot of the displacements caused by the formation of a single sub–unit of bainite. The surface was flat before transformation. Note the plastic deformation caused in the adjacent austenite (γ) after transformation, α_b = bainite ferrite [70]

During the formation of bainite the Bain strain converts the structure of the austenite into the lattice structure of the bainite and the accompanying shape change is called an invariant plane strain (IPS) with a large shear component [70]. The shear strain is caused by the glide of dislocations (conservative motion) on a slip plane and the shear lies in a direction which lies in that plane [75]. The material in the slip plane remains crystalline during the deformation, with no change in the relative positions of atoms on that plane, which is said to be invariant (unchanged) to the shear strain [75]. These shear strains belong to a class known as the invariant-plane strains (IPS) which leave a plane undistorted and unrotated once the dislocations have moved [75].

Figure 36a shows an IPS which is dilatational (δ) and is the type to be expected when a plate shaped precipitate grows diffusionally [75]. This change of shape is due to the volume change accompanying the transformation. Figure 36b shows an IPS corresponding to a simple shear (s) at a constant volume, as in slip or mechanical twinning [75]. The most common IPS is that which combines dilatation and shear, see Figure 36c, and this is representative of the shape deformation accompanying the formation of martensite and bainite, with s~0.22-0.26 and δ~0.02-0.03 (see Table 6) [53, 69, 75, 76]. The IPS reduces the strain energy when compared to the case where the shape deformation is an invariant line strain [70]. s and δ thus have a profound effect on the properties of the steel considering the fact that their magnitudes are much larger than elastic strains in a tensile test (~0.01) [75]. The large strain associated with the transformation cannot be sustained by the austenite and it thus deforms plastically to relieve the strains [76].

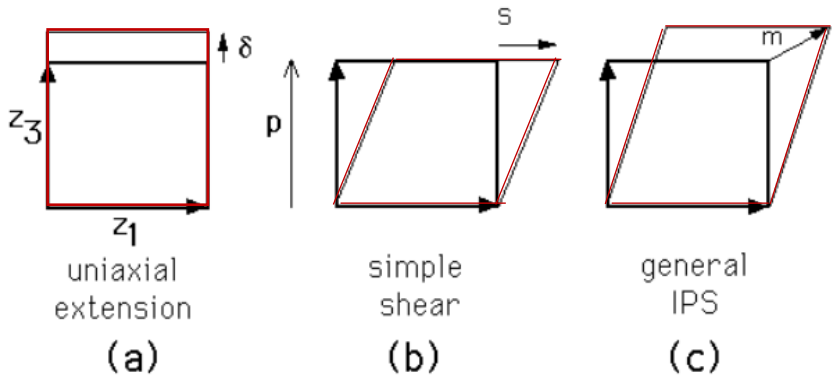

Figure 36. Three kinds of invariant-plane strains. The squares indicate the shape before deformation and the red shapes after deformation. δ, s and m represent the magnitudes of the dilatational strain, shear strain and general displacement respectively. p is a unit vector, the shear strain s is parallel to z_1, whereas δ is parallel to z_3 [75]

Table 6. Approximate values of s and δ for a variety of transformation products in steels [70]

Transformation	s	δ	Morphology
Widmanstätten ferrite	0.36	0.03	Thin plates
Bainite	0.22	0.03	Thin plates
Martensite	0.24	0.03	Thin plates
Allotriomorphic α	0	0.03	irregular
Idiomorphic α	0	0.03	equiaxed

The plastic relaxation of the shape change causes an increase in the dislocation density of bainitic ferrite since any motion of the interface into the deformed austenite will cause the defect structure to be inherited [70]. Thus, although there is considerable scatter in published data, the dislocation density generally decreases as the transformation temperature is increased. An assessed empirical relationship over the temperature range 297°C – 647°C is given by [70]:

$$log_{10}\{\rho_D\} = 9.2840 + \frac{6880.73}{T} + \frac{1780360}{T^2} \qquad \textit{Equation 5}$$

where T is the transformation temperature in Kelvin, and ρ_D is stated in units of m^{-2}. The resulting forest of dislocations block the progress of the glissile interface, halting growth before it reaches the austenite grain boundary.

2.5.2.2. The Thin Plates of Bainite

Due to the fact that large shear strains dominate the displacive transformations of bainite, bainite forms as fine and plate-like microstructures, a shape which minimises the strain energy when the plate is elastically accommodated [76]. A plate shape leads to a finer grain size than an equiaxed grain structure [70].

The elastic strain energy is a retarding energy. In the phase transformation of steel the change in free energy (ΔG) is a sum of the driving forces (undercooling and supersaturation) and the retarding forces (strain and interfacial energies). To minimise ΔG the retarding forces need to be minimised. The equation for calculating the elastic strain energy is as follows [54, 70]:

$$E = \frac{c}{r}\mu(s^2 + \delta^2) \qquad \textit{Equation 6}$$

Where E = Strain Energy, μ = shear modulus, s = shear strain, δ = dilation strain (ΔV), c=thickness of the plate and r = length of the plate. $\frac{c}{r}$ is the shape factor that contributes towards the elastic strain energy value. If the shape of the plate is long (>>>r) and thin (<<< c) then the strain energy is minimised in the austenite, see Figure 37.

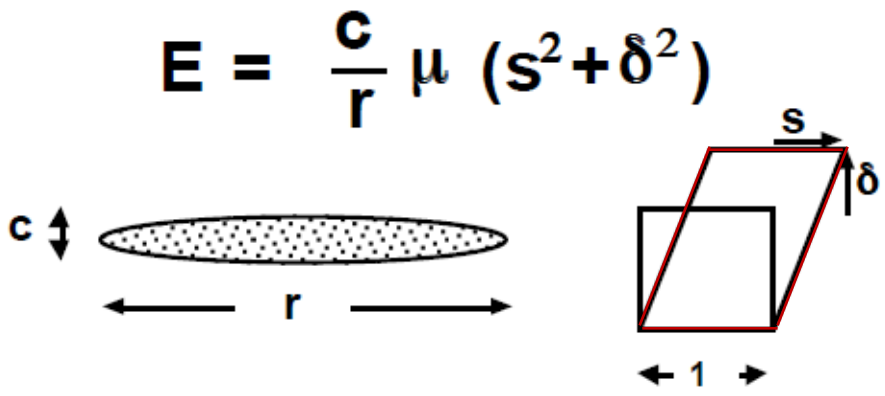

Figure 37. Strain energy per unit volume, E, when the invariant plane strain (IPS) shape deformation is elastically accommodated. μ is the shear modulus of the austenite. The diagram on the right shows how the shape of a unit–cube changes due to the IPS deformation, defined by the dilatational (s) and shear strains, δ and s respectively [70]

2.5.2.3. Stored Energy during the Formation of Bainite

Bainite forms with a stored energy of ~470 $Jmol^{-1}$ relative to allotriomorphic ferrite, this is higher than the stored energy of a severely deformed pure metal [53, 54, 76].

The bainitic microstructure is thus not an equilibrium structure [39]. Table 7 shows the stored energy accompanying different microstructure transformations in steel [75].

Table 7. The stored energy as a function of microstructure, relative to the equilibrium state defined as a mixture of ferrite, cementite and graphite [75]

Phase Mixture in Fe-0.2C-1.5Mn wt.% at 300K	**Stored Energy/ J mol^{-1}**
1. Ferrite, graphite & cementite	0
2. Ferrite & cementite	70
3. Para-equilibrium ferrite & para-equilibrium cementite	385
4. Bainite and para-equilibrium cementite	785
5. Martensite	1214
6. Mechanically alloyed ODS metal	55

The phases in points 1 and 2 of Table 7, involve a partitioning of all elements so as to minimise the free energy. In cases 3–5, the iron and substitutional solutes are configurationally “frozen” (for martensite even the interstitial elements are “frozen” due to the more rapid cooling) [75]. Case 6 refers to an iron-base mechanically alloyed oxide-dispersion strengthened (ODS) sample which has the highest reported stored energy prior to recrystallisation [75].

2.5.2.4. The Glissile Interface of Bainite

The interface accompanying an IPS with a large shear component is semi-coherent, at the parent/product interface, and is therefore glissile [70, 75]. Bainite grows by the advancement of the austenite-bainite interface. The structure of this interface is glissile and can be described as a series of line dislocations whose spacing (D) depends on the b-vector ($\vec{b}$) and angle θ, see Figure 38 [53, 54]. The dislocations accommodate the misfit between the austenite and bainite grains. A glissile interface can move without diffusion, that is, the dislocations can glide with stress because($\vec{b}$) lies outside of the plane of the interface. In sessile interfaces the dislocations need to climb for the interface to move and climb needs vacancies, through the diffusion of atoms, to occur.

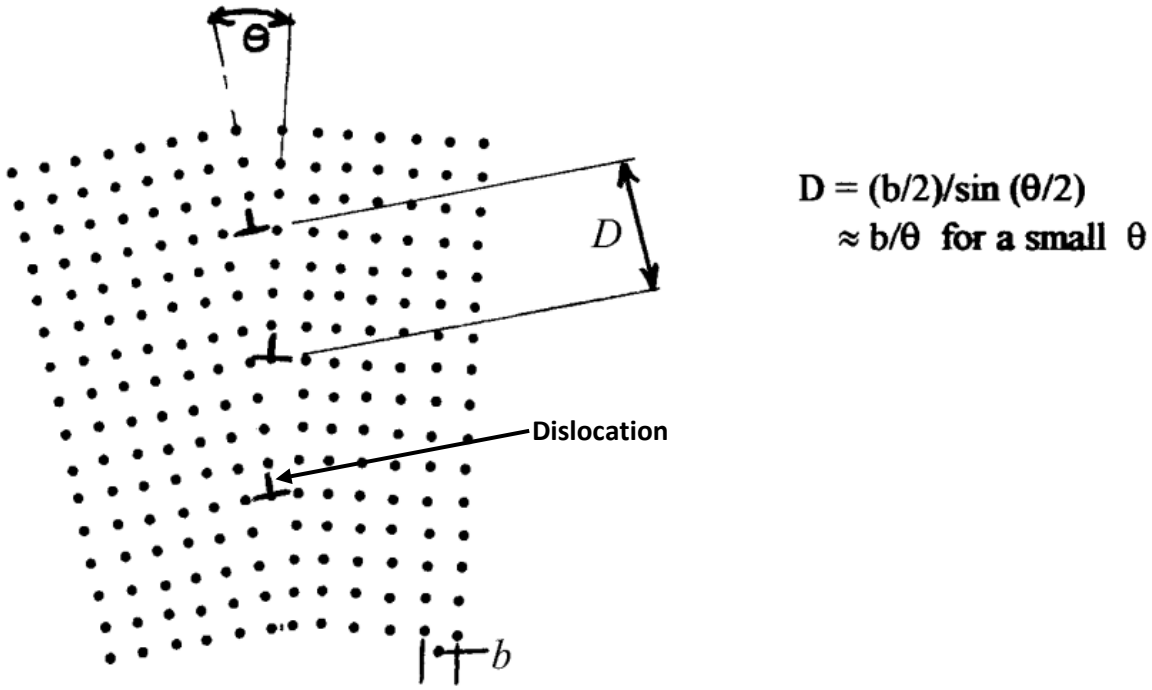

Figure 38. Schematic of a glissile interface with the burgers vector outside the plane of the interface, D is the distance between the dislocations, b is the burgers vector [53, 54]

Dislocation motion is hindered by the presence of other dislocations and because the growth of bainite is accompanied by a large dislocation density in the austenite which opposes the motion of the dislocations in the advancing interface, the growth of bainite is halted [53]. Solid solutions also hinder the motion of dislocations in the interface because there is no diffusion of the alloying elements during transformation.

A glissile interface can glide without the diffusion of substitutional solutes and so the Fe/X atom ratio is constant throughout the transformation, a condition called para-equilibrium (X=solute atom) [53, 55, 70, 76]. Bainitic ferrite thus has the same bulk substitutional content as its parent austenite. It has been verified by experiments that substitutional elements and iron do not diffuse during the bainite transformation [53, 55, 70]. Figure 39, shows that no redistribution of solute nor iron atoms at the austenite-bainite interface occurs [53]. Only the carbon diffuses during transformation and the carbon content after transformation is higher than equilibrium [53].

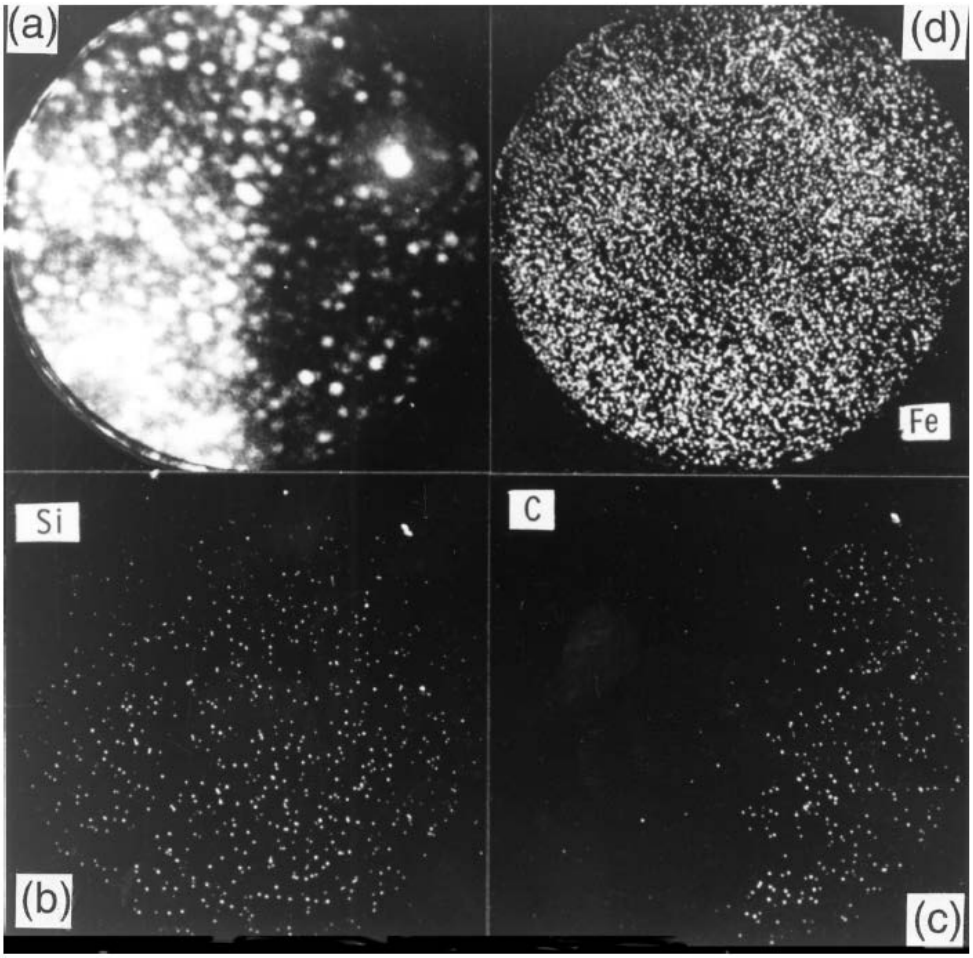

Figure 39. Atom-probe micrographs, taken across an austenite-bainitic ferrite interface in a Fe-C-Si-Mn alloy. The images confirm quantitative data showing the absence of any substitutional atom (iron (Fe) and silicon (Si)) diffusion during transformation. (a) field-ion image (b) corresponding silicon (Si) map (c) corresponding carbon (C) map (d) corresponding iron (Fe) map [53]. The carbon did diffuse during transformation

The substitutional elements in bainite influence the thermodynamics of transformation significantly but not so much the kinetics, since they do not diffuse during transformation [70]. This has consequences on the TTT diagram which can be divided into two C-curves for the bainite reaction, see Figure 40 [70]. The higher temperature C-curve describes the evolution of reconstructive transformations and the lower one, displacive transformations [70]. For example, the addition of the austenite stabilizing substitutional solute, manganese, has a much larger effect on the reconstructive than on the displacive transformation [70]. This is because it may retard transformation both by reducing the thermodynamic driving force and by partitioning between the phases via diffusion during reconstructive transformation, which can become rate-limiting [70].

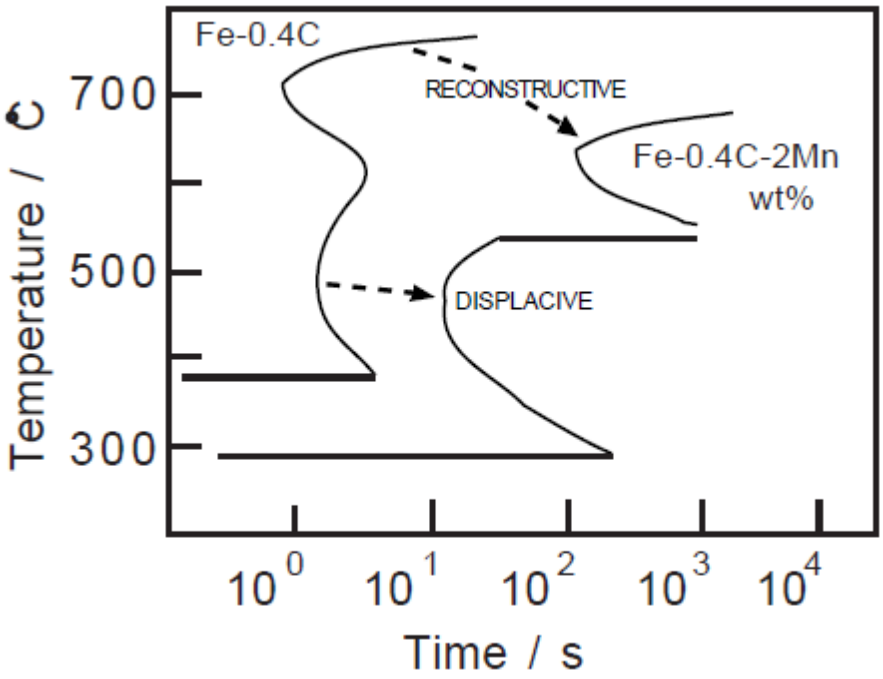

Figure 40. Time temperature transformation (TTT) curves showing that the addition of manganese (Mn) shifts the reconstructive and displacing transformation of the Fe-0.4C-2Mn alloy to the right i.e. longer times. The Mn retards the reconstructive transformation greater than the displacive transformation [70]

2.5.2.5. Dislocations Formed During the Formation of Bainite

Dislocations are created when the shape deformation is accommodated by plastic relaxation of the surrounding austenite [76]. The co-ordinated movement of atoms associated with a displacive transformation cannot be sustained across the austenite grain boundaries, which is not the case in reconstructive transformation [70]. This leads to a refinement of the microstructure. The growing plate then brings itself to a halt before it collides with a hard obstacle such as a grain boundary. This is called the subunit mechanism and in bainite, individual sheaves are made of much smaller plates, each of which grows to a limited size, much smaller than the austenite grain size. The stronger the austenite, i.e. at lower temperatures, the thinner the bainite plates that are formed [53, 70].

At the temperatures where bainite forms, the austenite does not have a high yield strength and cannot support the large shape deformation elastically and thus relaxes by plastic deformation adjacent to the bainite [53, 70]. Dislocation debris forms in the austenite and terminates the bainite transformation completely. Bainite formation is thus halted by the plastic deformation of the austenite and a new plate needs to be nucleated for further growth.

At higher temperatures, the austenite is weaker and dynamic recovery is more likely, the plates are thus thicker at elevated transformation temperatures [53, 75]. Figure 41a shows the effect of transformation temperature on the thickness of the bainite plates. From the figure it is clear that transforming at lower temperatures results in thinner plates being formed. Carbide-free alloys (points 1, 2, 3, 4 in Figure 41b) with different plate thicknesses have been produced [75]. It was found that the alloy with the thinnest bainite plates (<40nm, point 4 in Figure 41b) had an ultimate tensile strength of about 2500 MPa. This alloy though showed the lowest fracture toughness. [75]. Displacive transformations are associated with fine length scales and the plate thickness defines the effective grain size of the bainite [75, 77].

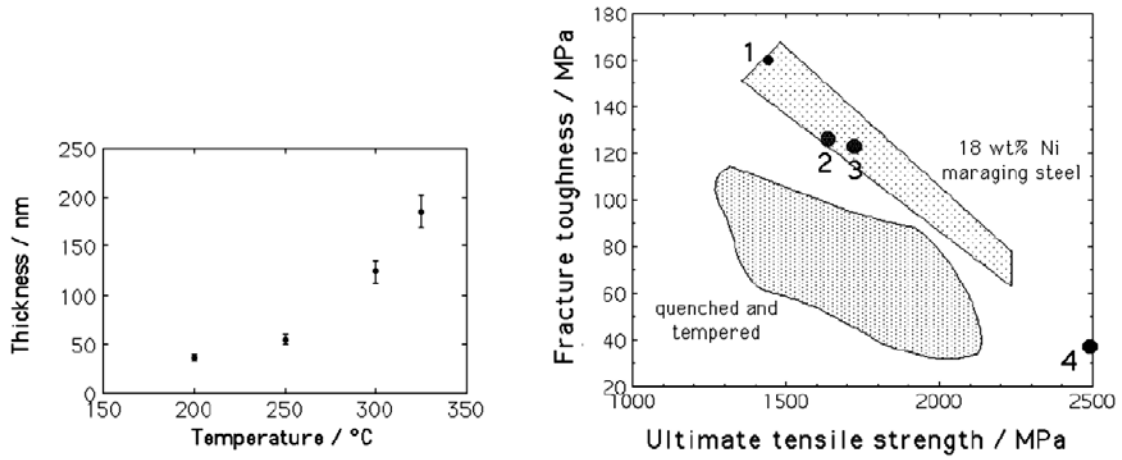

(a) (b)

Figure 41. (a) Stereologically corrected plate thickness of bainite ferrite as a function of the transformation temperature (b) The fracture toughness-ultimate tensile strength of quenched and tempered and 18 wt%, nickel (Ni) maraging steel, points marked 1, 2, 3 and 4 are the results for tested carbide-free bainitic alloys [75]

Dislocations in austenite are inherited in the bainite after transformation, and segregation of carbon at dislocations is expected to bind and hence prevent or hinder the carbon atoms from diffusing out of the ferrite lattice [4, 55]. This explains the high level of carbon that exists in the bainitic ferrite after transformation and the small extent of carbon enrichment detected in the residual austenite. Moreover, the increase in the amount of carbon in bainitic ferrite as the transformation temperature decreases is consistent with the fact that the dislocation density of bainitic ferrite is higher the lower the reaction temperature [4].

2.5.2.6. The Nucleation of New Ferrite Plates

New plates nucleate mostly near the tips of already existing subunits. The bainite transformation is accompanied by large shear stresses and a volume change which causes internal elastic shear stresses and strains in the parent austenite, particularly at the tips of the ferrite plates [53]. These stresses and strains, as well as the accompanying shear deformation, provide an additional driving force for nucleation of bainite and thus assist with the autocatalytic formation of bainite at the tips of existing plates. In addition, the localized carbon content at the tips is the lowest and thus the martensite start (M_S) and bainite start (B_S) temperatures are the highest [52, 53]. This increases the localised driving force for nucleation of new plates/sheaths at the tips. This is called the sub-unit mechanism of transformation [52, 53, 54].

Figure 42 is a schematic representation of the development of a sheaf of upper bainite from individual plates [52]. In step 1, a supersaturated ferrite (α) lath grows into the austenite (γ) accompanied by plastic deformation around the tip. In Step 2, carbon (C) is rejected into the surrounding austenite, reducing the carbon concentration in the vicinity of the tip. A new ferrite lath nucleated and grows from a low carbon area of the tip.

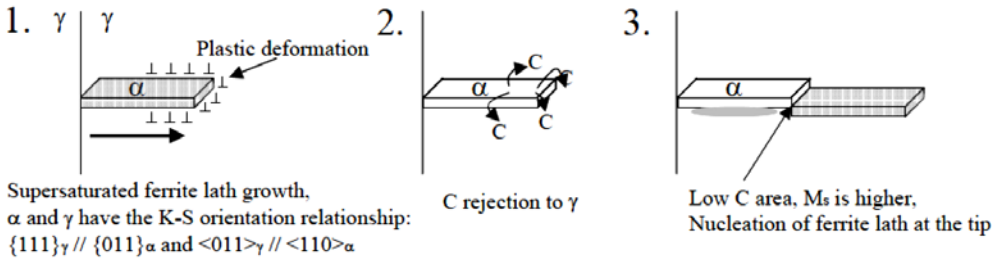

Figure 42. Schematic representation of the development of a sheaf of upper bainite from individual plates [52]

The nucleation of the ferrite platelets is the rate-controlling process for the growth rate of bainite [52, 53]. A decrease in the transformation temperature increases the nucleation rate of ferrite plates due to an increase in the driving force for transformation provided by the larger undercooling [53, 69, 78].

2.5.2.7. The Bainite Start Temperature

A displacive transformation is diffusionless and occurs at high levels of undercooling such as the bainite start temperature (B_S) [52, 53, 54]. The B_S is a well-defined temperature for the start of the bainite transformation and above this temperature, no bainite will form and this temperature has been confirmed for a wide range of

alloy steels [70]. The amount of bainite that forms increases as the transformation temperature is reduced below the B_S temperature during isothermal transformation. The fraction of bainite increases during isothermal transformation at a specific temperature as a sigmoidal function of time, reaching an asymptotic limit which does not change on prolonged heat treatment even when substantial quantities of austenite remain untransformed (Figure 43) [55, 70].

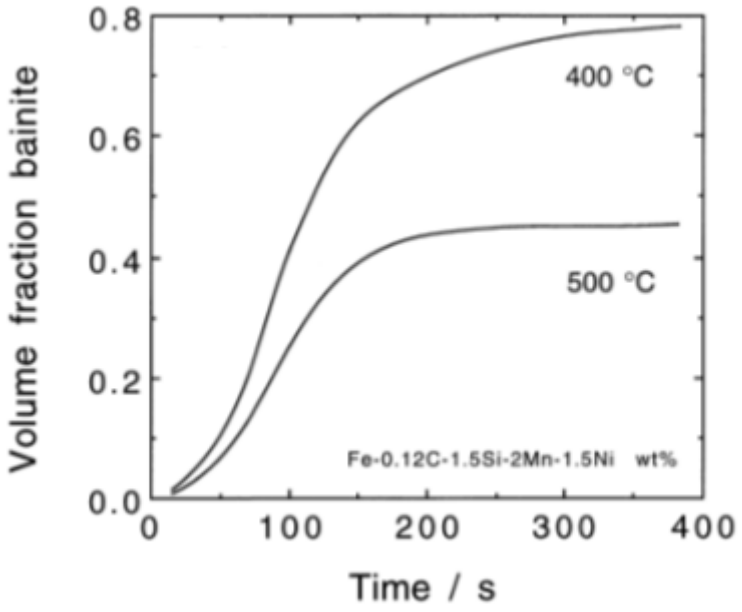

Figure 43. The calculated influence of isothermal transformation temperature on the kinetics of the bainite reaction [55]

2.5.2.8. The Incomplete Reaction Phenomenon

The volume fraction of bainite transformed in the absence of cementite, obeys the incomplete reaction phenomenon [1, 53, 70, 76, 79, 80, 81]. A thermodynamic model was introduced by Bhadeshia *et al*. that estimates the higher percentages of carbon content in the austenite for bainitic transformations at any transformation temperature [76, 79, 80]. The model proposes two lines in the Fe-C phase diagram, called T_0 and T'_0. The T_0 curve represents the locus of all points on a plot of temperature vs carbon concentration where the austenite and ferrite of the same composition have identical Gibbs free energies, without strain (T_0) and with strain (T'_0) - allowing for the stored energy ($400 Jmol^{-1}$) of bainite, see Figure 44 [1, 76, 79]. Due to the stored energy, the T'_0 curve is at lower carbon values than the T_0 curve.

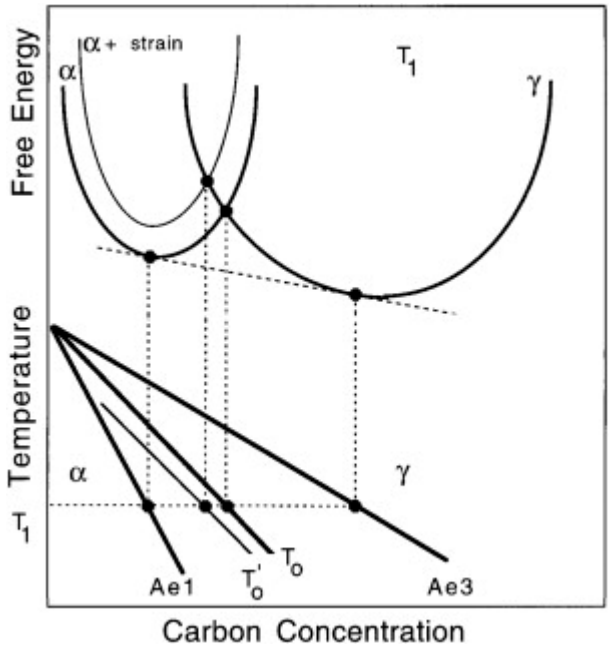

Figure 44. Schematic diagram showing the T_0 (without strain) and T'_0 (with strain) lines and their corresponding free energy curves, plotted against the carbon concentration [79]. A_{e1} is the equilibrium temperature on the Fe-C phase diagram at which austenite begins to form during heating and A_{e3} is the equilibrium temperature on the Fe-C phase diagram at which transformation of ferrite to austenite is completed during heating

The T'_0 lines show the maximum carbon contents of the alloys that limits the formation of bainite at any transformation temperature [76]. It has been found experimentally that the bainite reaction does indeed stop at the T'_0 boundary, see Figure 45 [70]. So, at any temperature, the carbon content of the residual austenite must not exceed that of the T'_0 curve. Transformation ceases before the austenite achieves its equilibrium composition (A_{e3}), this is called the incomplete–reaction phenomenon [70]. This is because at carbon enrichments higher than the value at T'_0 there is no driving force for bainite formation without diffusion as $G^{\alpha}>G^{\gamma}$ and growth of bainite stops.

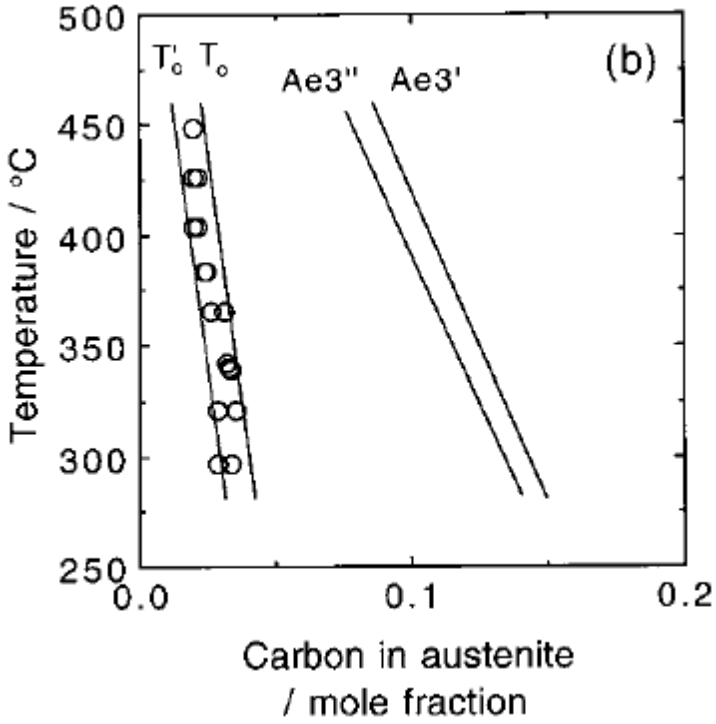

Figure 45. Experimental data (open circles) showing that the growth of bainite stops when the austenite carbon concentration reaches the T_0 curve for an alloy with composition Fe–0.43C–3Mn–2.12Si wt%. The solid lines were calculated using thermodynamic software [53, 70]. Ae3 is the equilibrium temperature on the Fe-C phase diagram at which transformation of ferrite to austenite is completed during equilibrium transformation

The volume fraction of the austenite (V_γ^T) remaining (retained/residual austenite) after the heat treatment of the steel at a particular temperature to form bainite, can be calculated as follows [53, 82]:

$$V_\gamma^T = \frac{x - x_\alpha}{x_{T0} - x_\alpha} \qquad \textit{Equation 7}$$

Where x is the average carbon concentration, x_{T0} is the carbon concentration of the T_0 curve at that temperature, x_α is the carbon concentration of the ferrite.

Upon cooling, some of this retained austenite will transform into martensite and the volume fraction of martensite formed at the temperature is calculated using the equation derived by Koistinen and Marburger, as follows:

$$(1 - V_{\alpha'}) = exp\{-0.011\,(M_s - T)\} \quad \textit{[82]} \qquad \textit{Equation 8}$$

Where $V_{\alpha'}$ = fraction of martensite, M_s = martensite temperature and T is the transformation temperature (°C)

2.5.3. Carbide-Free Bainite

In the recent decades Bhadeshia *et al*. have developed and introduced high silicon, high carbon bainitic steels [1, 70, 72, 73, 76, 79, 80]. It is known that the precipitation of cementite during bainitic transformation can be suppressed by alloying the steel with about 1.5 wt% of silicon [70, 72, 73, 76, 79]. An interesting microstructure results when this silicon–alloyed steel is transformed into upper bainite. The carbon that is rejected into the residual austenite, instead of precipitating as cementite, remains in the austenite and stabilises it down to ambient temperature. The resulting microstructure consists of fine plates of bainitic ferrite separated by carbon–enriched regions of austenite, see Figure 46 [70]. This microstructure is called carbide-free bainite. Silicon is not efficient in suppressing the precipitation of carbides inside the bainite ferrite subunits and lower bainite is frequently observed in steel alloys having high silicon contents.

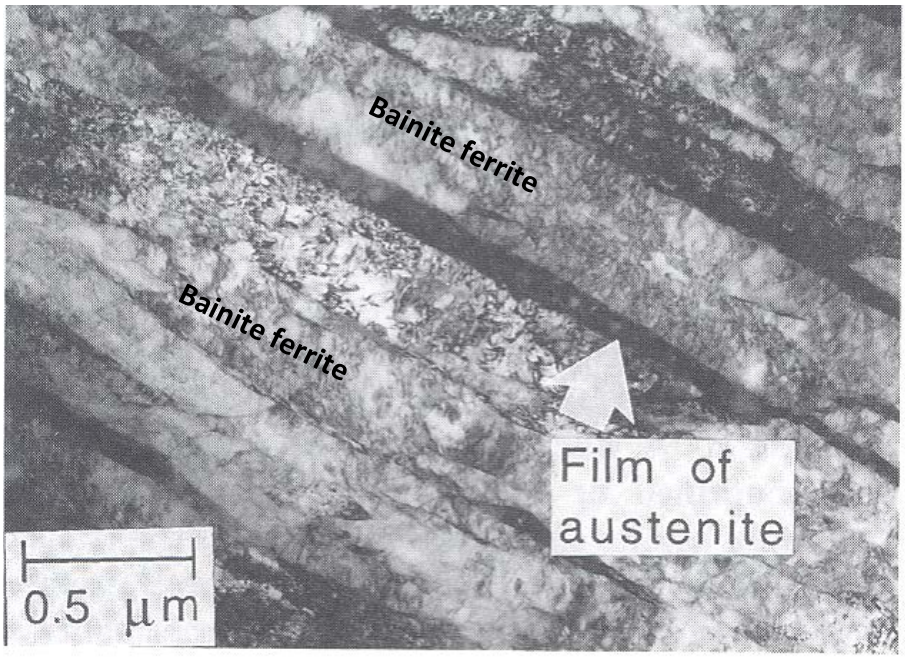

Figure 46. Transmission electron micrograph of a mixture of bainitic ferrite and stable retained austenite [70]

The potential advantages of the mixed microstructure of bainitic ferrite and austenite can be listed as follows [70]:

- Fracture in high–strength steels initiates at the cementite regions and its absence is expected to make the microstructure more resistant to cleavage failure and void formation.
- The bainitic ferrite is almost free of carbon, which is known to embrittle ferritic microstructures.

- The microstructure has an ultrafine grain size giving it strength and toughness. The ferrite plates are less than 1 μm in thickness.
- The ductile films of austenite dispersed between the plates of ferrite have a crack blunting effect. They further add to the toughness by increasing the work of fracture as the austenite is induced to transform to martensite under the influence of the stress field of a propagating crack. This is the TRIP, or transformation–induced plasticity effect.
- The diffusion of hydrogen in austenite is slower than in ferrite. The presence of austenite can therefore improve the hydrogen embrittlement (HE) resistance of the microstructure. The austenite however has a much higher solubility for hydrogen than ferrite and can act as a hydrogen trap. The steel making practice should, therefore, avoid hydrogen uptake.
- The microstructure can be obtained without the use of any expensive alloying additions. All that is required is that the silicon concentration should be large enough to suppress the formation of cementite.

The carbide-free microstructure does not always give the expected good combination of strength and toughness because of the large “blocky” regions of austenite between the sheaves of bainite, see Figure 47 [70]. The thermodynamic limit (T'_0) governing the extent of the bainite transformation needs to be engineered to avoid large quantities of retained austenite in the final microstructure that can transform into untempered, brittle, high carbon, martensite when stress is applied. [1, 76, 80]. The reduction in the large blocks of austenite, or the increase in its stability to martensitic transformation, is controlled by the T'_0 curve of the phase diagram of the steel [1, 70, 76, 80].

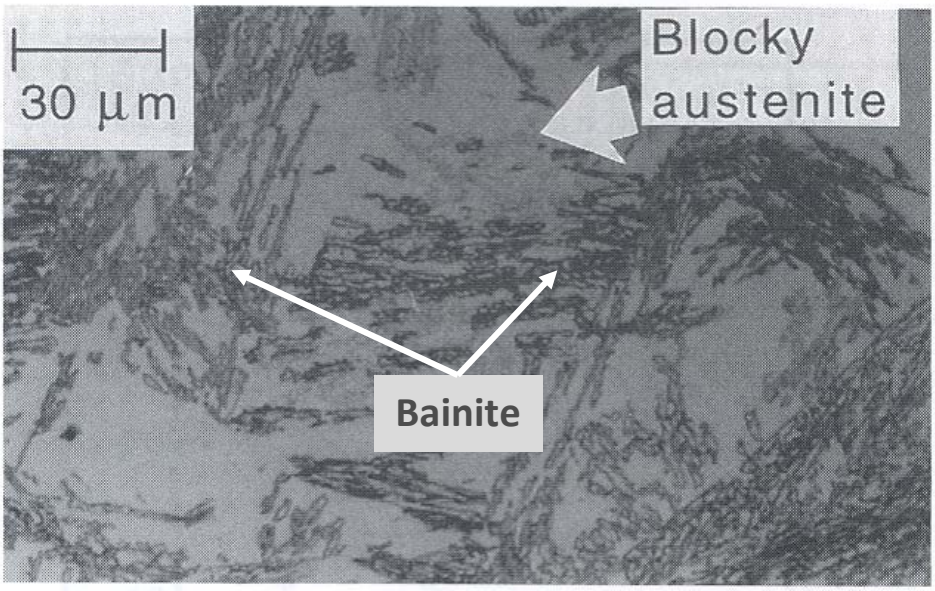

Figure 47. Optical micrograph of upper bainite in a Fe–0.43C–3Mn–2.02Si wt% showing the blocks of retained austenite between sheaves of bainite [70]

The T'_0 curve determines the composition of the austenite at the point where the reaction to bainite stops. By shifting this curve to larger carbon concentrations, both the fraction of bainite that can form, and the carbon concentration of the residual austenite can be increased [1, 70, 76, 80]. Modifications to the T'_0 curve can be achieved by altering the alloy composition. It is therefore necessary to determine the effect of substitutional alloying elements on carbide-free bainite.

2.5.3.1. Alloying Elements in Carbide-Free Bainite

The alloying elements often added to steels have an effect on the TTT diagram of carbide-free bainitic steel [81, 82, 83]. TTT diagrams for these steels can be calculated using developed computer programs, such as the MUCG83 simulator model [84]. The TTT curves for carbide-free bainite consist of two C-curves: The top curve representing the reconstructive transformations, while the lower curve, the displacive transformations. The lower C curve has a flat top at the bainite start temperature (B_s), while the martensite start (M_s) temperature is also calculated. Figure 48, is an example of a TTT diagram that can be drawn by the computer software.

TTT curves can be used to determine the time and temperatures for the bainite transformation at a specific isothermal transformation temperature. In Figure 48, Curve A represents the highest rate of transformation to bainite, Curve B, the lowest rate of bainite transformation and Curve C, the formation of allotriomorphic ferrite [82].

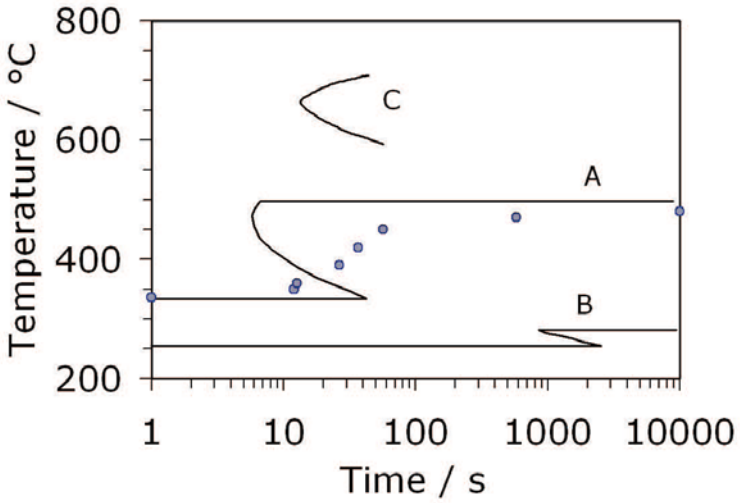

Figure 48. Time transformation temperature diagrams for bainite (A and B) and allotriomorphic ferrite (C). Curves A and B refer to highest and lowest rate of bainite transformation [82]. Curves A, B and C were drawn using thermodynamic software and the dots are actual experimental data for tests conducted on carbide-free bainitic alloys

A higher carbon content leads to higher strength but also stabilises a larger volume fraction of the retained austenite to room temperature [79]. This retained austenite will transform to brittle martensite on impact, making the alloy brittle. The usual carbon contents of carbide-free bainitic alloys is 0.6wt%-0.9wt% but some research has been conducted in low alloy microstructures with 0.1wt% to 0.3wt% carbon [79]. Carbide-free steels with 1.15 wt% carbon have been studied with the removal of manganese from the alloy [79]. Carbon drastically supresses the bainite and martensite transformation temperatures and should be kept low enough to achieve the required rate of reaction but high enough to ensure adequate levels of strength [53].

Adding 2 wt**%** aluminium or cobalt to the alloy drastically reduces the transformation time at the lower temperatures where carbide-free bainite forms [79]. It also decreases the M_s and B_s temperatures, hence the driving force and time for transformation is also reduced [79]. Aluminium retards the cementite precipitation and also accelerates the bainite transformation [53].

Molybdenum additions of ~0.25 wt% are added to avoid austenite grain boundary brittleness. Molybdenum is added to prevent phosphorous segregating to the austenite grain boundaries and causing temper embrittlement [1, 76, 85].

The addition of chromium has been found to decrease the amount of bainite formed, see Figure 49a showing the dilatation (representing the transformation amount) versus time curves formed during the isothermal transformation of low carbon (0.2 wt%), high silicon (1.8 wt%) carbide-free steels. The alloys were transformed at 400°C, 430°C and 450°C [86]. The chromium also hinders the bainitic transformation kinetics i.e the bainite forms at longer times, more so at the higher temperatures (430°C and 450°C) than at the lower temperature of 400°C. The time-temperature-transformation (TTT) curves of the two steels in Figure 49b, which were calculated by software JMatPro, also show that the bainite formation takes longer with the addition of chromium. The delay in the transformation was found to be due to a decrease in the driving force of transformation particularly at higher temperatures [86].

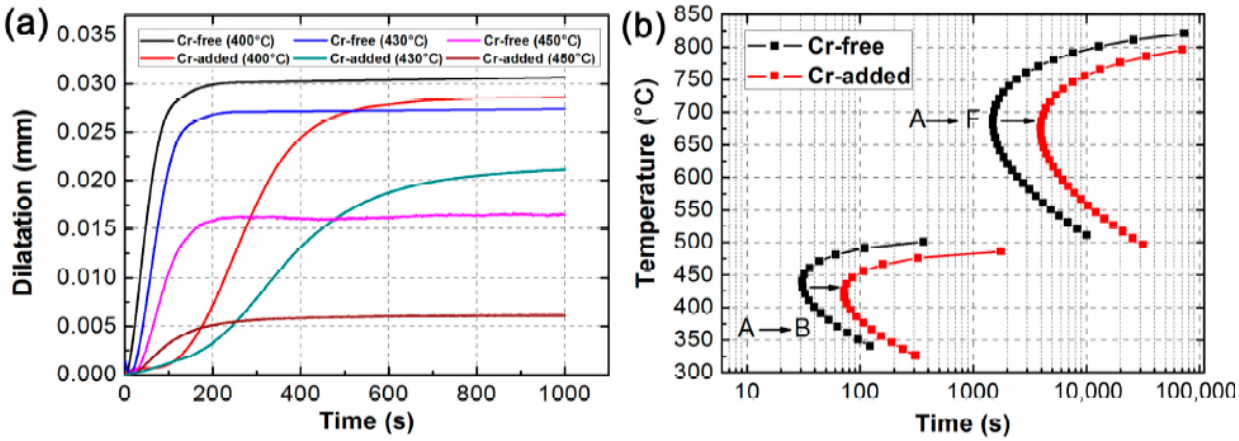

Figure 49. (a) The dilatation versus time during the isothermal holding at 400 °C, 430 °C, and 450 °C of two steels; (b) Calculated time-temperature-transformation (TTT) curves of the Cr-free and Cr added steels showing the start of transformations from austenite A to ferrite F and from austenite to bainite B. It shows that the kinetics of bainitic transformation are hindered by Cr addition. [86]

2.5.3.1.1. The Effect of Silicon in Bainite

Silicon is known to inhibit the precipitation of cementite in bainite [52-88]. In the aerospace industry in the 300M alloy, which contains ~1.6wt% silicon, the rate of cementite precipitation from supersaturated martensite is significantly reduced and silicon also retards the precipitation of cementite from austenite [88].

Silicon does not dissolve in cementite and if by some circumstance the cementite is allowed to absorb the silicon, its formation is retarded [53, 88]. If the silicon is however allowed to partition into the parent phase during growth by diffusion, cementite will form [88]. Diffusion of substitutional elements however is only possible

at elevated temperatures. The formation of bainite occurs at lower temperatures where the mobility of substitutional atoms is limited. The silicon then, once trapped in the cementite lattice during its para-equilibrium growth, will be unable to partition [53, 88]. This drastically reduces the free energy change associated with cementite precipitation, causing a large decrease in the precipitation kinetics of the cementite, i.e. decreasing its growth rate [88].

Calculations done to determine the effect of silicon on cementite precipitation from carbon supersaturated austenite have shown that during equilibrium conditions the fraction of cementite is not influenced by an increase in the silicon content, see Figure 50 [88]. When para-equilibrium conditions exist, however, an increase in silicon decreases the fraction of cementite formed. During para-equilibrium conditions the silicon is inherited and trapped in the cementite lattice but this is not the case during equilibrium conditions [88]. Manganese is not trapped in the cementite lattice during para-equilibrium conditions and thus has no effect on its precipitation kinetics (Figure 50b). This is unusual as the manganese is a carbide former, although a ‘weak’ one.

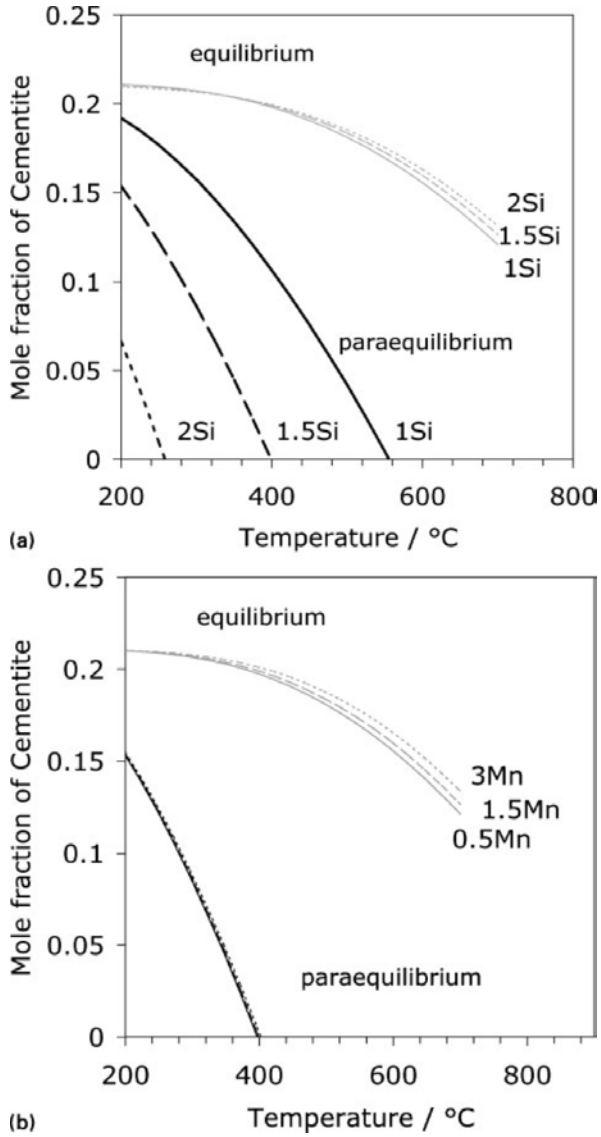

Figure 50. The calculated phase fraction of cementite in equilibrium or para-equilibrium with austenite, in an alloy with base composition Fe–1.2C–1.5Mn–1.5Si (wt-%) with (a) variation of silicon, Si, concentration and (b) variation of manganese, Mn, concentration [88]

Figure 51 shows that the addition of silicon increases the time to transformation for the precipitation of cementite from austenite during para-equilibrium conditions [88]. The change in free energy ΔG, also dramatically decreases with an increase in silicon for the para-equilibrium precipitation of cementite from austenite, when silicon is trapped in the cementite structure [88].

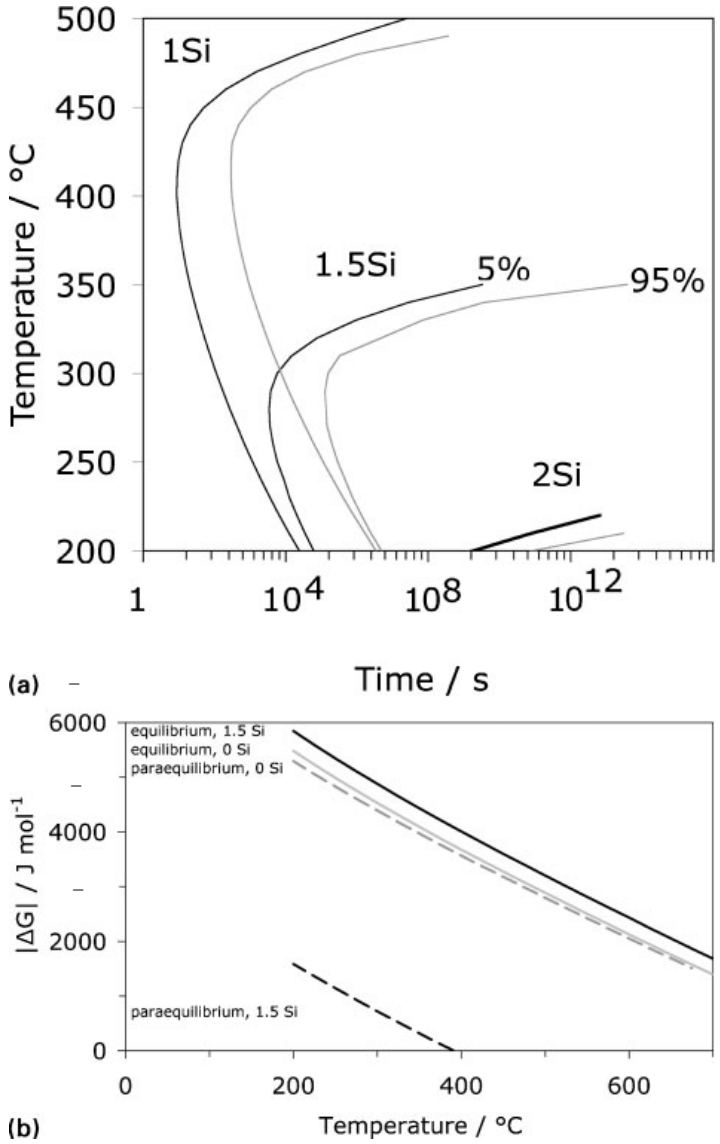

Figure 51. (a) Time temperature precipitation diagram for para-equilibrium cementite in an alloy with a base composition Fe–1.2C–1.5Mn–1.5Si (the percentages represent the portion of cementite precipitation that is completed) and (b) magnitude of free energy change accompanying the γ → γ+θ reaction for both equilibrium and para-equilibrium conditions as a function of the silicon concentration of austenite [88]

2.5.3.1.2. The Effect of Boron in Bainite

The addition of boron (B) to a level of not more than ~0.002 wt. %, is an effective way of isolating the bainite reaction in steels because it retards the ferrite reaction [52]. Boron is an interstitial element that has high diffusivity in austenite [77]. It is believed that boron segregates preferentially to the prior austenite grain boundaries (preferred nucleation sites for ferrite) during cooling [77]. This hinders the heterogeneous nucleation of ferrite on the grain boundaries. For heterogeneous

nucleation to occur on grain boundaries an additional driving force for nucleation (the last term ($A_{gb}\gamma_{gb}$)) in the free energy equation for nucleation as shown below, is established through the removal of a piece of the boundary from the system [89].

$$\Delta G = K1\ \{\Delta G_v + \Delta G_\varepsilon\} + K_2\gamma_{ppt} - A_{gb}\gamma_{gb} \qquad \textit{Equation 9}$$

Where: ΔG = change in free energy of the system, ΔG_v (-) = chemical driving force in a phase transformation, ΔG_ε (+) = strain energy that arises out of the difference in volume between precipitate and solid solution in which it nucleates, γ_{ppt} = the precipitate surface energy, γ_{gb} = grain boundary surface energy, A_{gb} = area of the grain boundary, K_1 and K_2 are constants.

If however through segregation, the austenite grain boundary energy (γ) of the system is sufficiently lowered, the additional driving force for nucleation ($A_{gb}\gamma_{gb}$) becomes less important and grain boundaries do not act as the preferential nucleation sites for ferrite anymore. Boron, therefore, segregates to the grain boundaries, such that the surface energy of the alloy system is lowered sufficiently, making the additional driving force less important and the prior austenite grain boundaries no longer the preferential nucleation sites for ferrite. This retards the ferrite nucleation reaction and drives the ferrite nose to the right on the continuous cooling transformation (CCT) diagram; permitting the bainite reaction to occur at shorter times [52]. Figure 52 illustrates the effect of boron on the austenite-ferrite transformation temperature for a Fe-0.07C-0.03Nb steel [*90*]. In the temperature transformation diagram, at lower temperatures (600°C - 800°C), the start of the ferrite nucleation is shifted to longer times and lower temperatures with the addition of 30ppm boron in the steel. The addition of boron thus retards the ferrite reaction in the steel.

At higher temperatures (>800°C) the start temperature and time for both the boron and no boron steel remains the same. Similarly the addition of boron has no effect on the ferrite finish temperature and time.

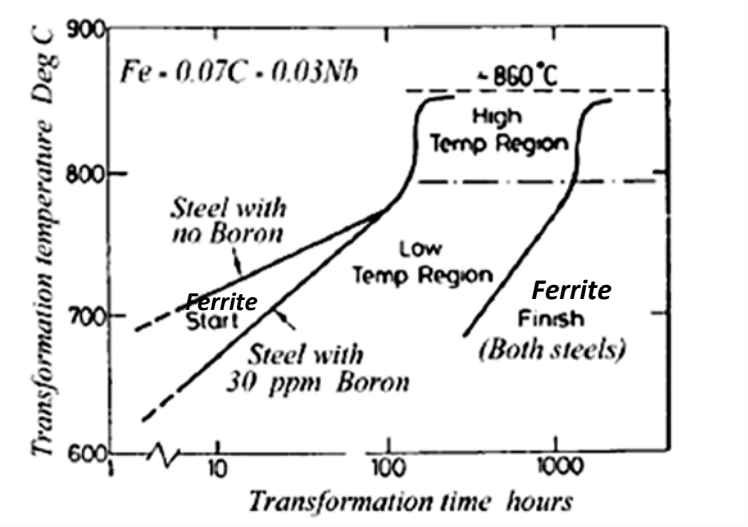

Figure 52. Effect of Boron on the TTT curve of a Fe-0.07C-0.03Nb steel showing the effects of boron on the ferrite start and finish curves of the transformation-time-temperature curves for high and low temperature ranges [90]

Boron, although increasing the hardenability of steels, reacts easily with impurities in the steel, such as nitrogen, to form boron nitrides [*90*]. Only boron in solid solution is effective in retarding the ferrite reaction. When boron nitrides form during solidification the positive effect of boron on the hardenability of the steel is reduced. Strong nitride formers such as titanium and aluminium should be added to the steel to scavenge the nitrogen. Titanium combines more preferentially with nitrogen than with carbon, because the resulting titanium nitride is more stable than the titanium carbide [*90*]. Only when all the N has been 'fixed' as a nitride will the titanium combine with carbon. Titanium must be 3.4 x Nitrogen to fully stabilise the nitrogen in the steel [52]. Excess boron additions induce the precipitation of Fe_2B and $M_{23}(C,B)_6$ borocarbides on the austenite grain boundaries, removing the boron from solution [77].

The addition of molybdenum, further retards the ferrite reaction and Figure 53 illustrates the effects of both boron and molybdenum on facilitating the bainite reaction [52]. Figure 53 is a continuous cooling transformation (CCT) diagram constructed after cooling the steel alloy at different cooling rates between 20°C/s and 0.1°C/s, from the austenitising temperature. A fully bainitic microstructure is obtained for a wide range of cooling rates (20°C/s - 0.1°C/s) over a temperature range of 400°C-550°C The ferrite and pearlite microstructure are found only at the slow cooling rate of 0.1°C/. The martensitic region is below the bainite region. The

dots represent the bainite start and martensite start temperatures calculated for the different cooling rates

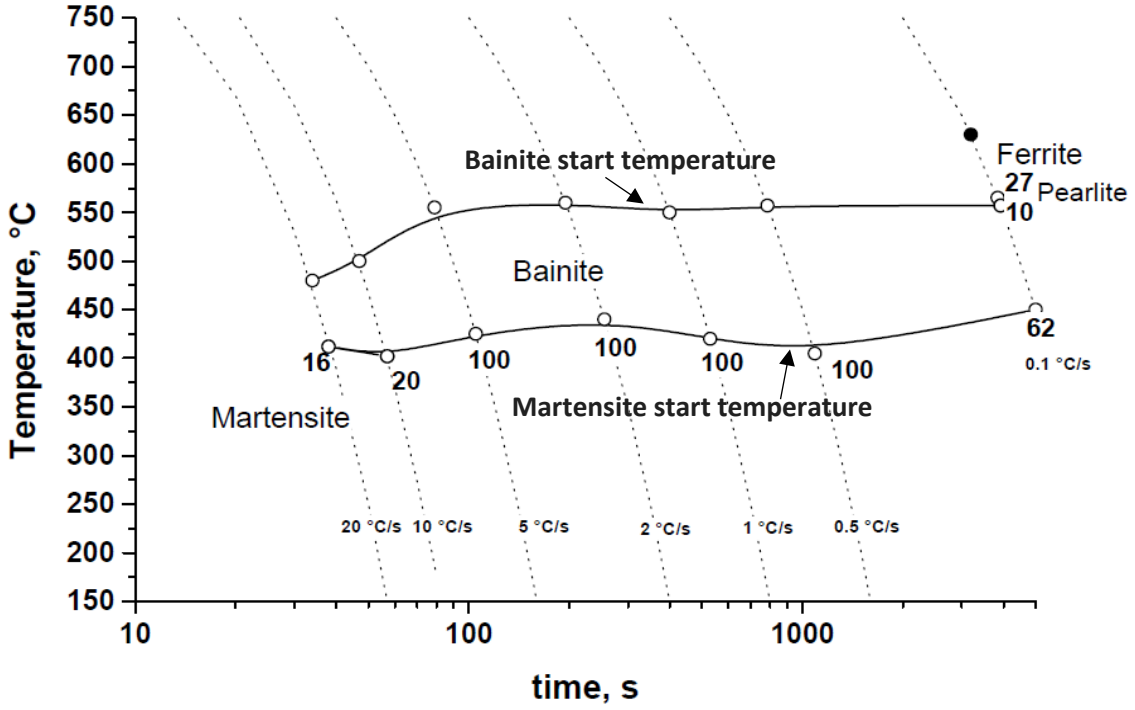

.

Figure 53. CCT Diagram for 0.17C, 1.6Mn-0.2Mo steel with 25ppm soluble B constructed after cooling the steel at different cooling rates between 20°C/s and 0.1°C/s, from the austenitising temperature. A fully bainitic microstructure is obtained for a wide range of cooling rates (20°C/s - 0.1°C/s) over a temperature range of 400°C-550°C [52]. The dots represent the bainite start and martensite start temperatures calculated for the different cooling rates

2.5.3.2. Nanobainite

Nanobainite is produced during isothermal transformation if the hardenability of the alloy is controlled so that the transformation temperature is drastically reduced and a microstructure consisting of slender plates of bainitic ferrite is achieved, see Figure 54 [69, 86]. Bainite plates with a thickness of 20nm-40nm are achieved leading to high strengths [80]. This alloy can then be considered as a bulk nanocrystalline material that can be obtained without expensive processing routes [80].

Nanobainite is formed by austenitising and then austempering at a temperature below the B_S for an adequate time for bainite to form. There is no rapid cooling necessary so that residual stresses are avoided and large samples can be heat treated. [77, 79, 80]

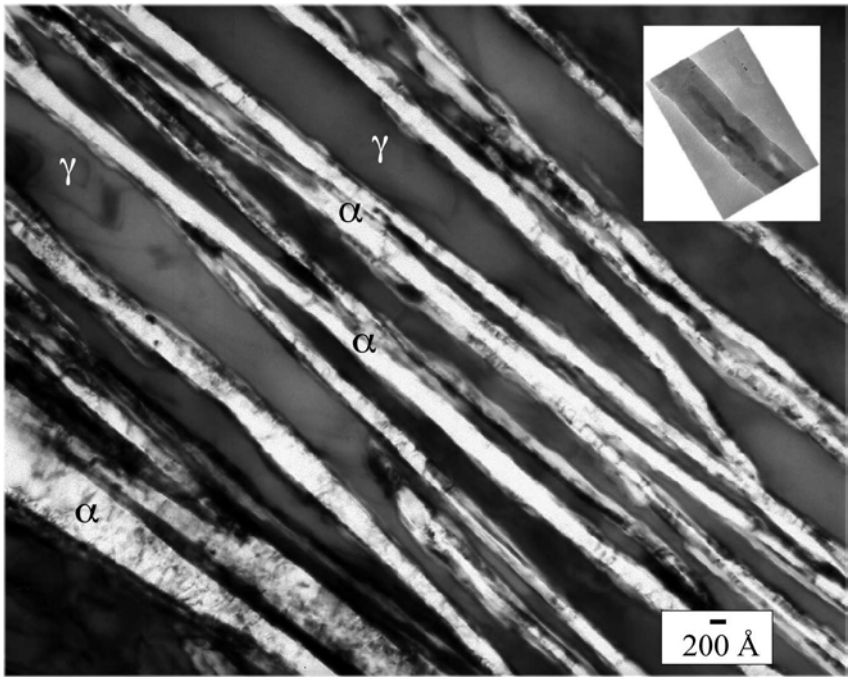

Figure 54. Transmission electron micrograph of a Fe-0.98C-1.46Si-1.89Mn-0.26Mo-1.26Cr-0.09V (wt%) alloy transformed at 200°C for 5 days. [4, 19, 20]. The inset is of a carbon nanotube at the same magnification, [69,86]

In nanobainite the transformation time can take up to 10 days at 125°C and strength values >2000MPa can be achieved (Figure 55a) [69,86]. The low B_s temperature is due to a high carbon content and the addition of manganese and chromium which stabilise the retained austenite to low temperatures [80]. Transforming at very low temperatures has constraints in that the rate determining step of the carbon diffusion is very slow and transformation may take a very long time i.e. months or years [79]. The addition of ~2wt% aluminium/cobalt reduces the transformation time drastically [79]. It has been empirically observed that an optimum austempering temperature of 200°C leads to the finest microstructure [79]. It has been considered that at lower temperatures the bainite sub-units may join and coarsen and it has been proven that if the austenite is strengthened through solid solution or work hardening, finer bainite can form. Ageing for about 2 weeks formed a few cementite particles in the microstructure within the bainite ferrite [80].

Nanobainite alloys have very high strength due to both the Hall-Petch effect and solid solution strengthening [79, 76]. In Figure 55b, virtually all of the elongation is uniform, with hardly any necking. The points plotted in Figure 56 are points that define in each case the strain at which the nanobainite tensile samples failed. A prominent feature is that they all fail when the retained austenite content is reduced to about 10% [77]. This observation can be understood if it is assumed that failure

occurs when the austenite, which is the toughest of all the phases present, becomes geometrically isolated, i.e., it loses percolation, leading to fracture [77]. This is somewhat surprising since the transformation of austenite leads to the formation of very hard, untempered, high–carbon martensite which should be highly susceptible to fracture.

The carbon concentration of the retained austenite before it transforms is between 1wt%–2 wt% [77]. However, a study shows that large amounts of this potentially brittle martensite (7%→27%) can be tolerated in the microstructure before the fraction of austenite reaches the percolation threshold and fracture actually occurs [77]. This is because the tendency of the martensite to crack in a mixed microstructure of austenite and martensite depends on its absolute size and in these mixtures, it is more difficult to crack the fine martensite. [77]. It is the fine scale of the retained austenite in the nanostructured bainitic steels that permits the martensite to be tolerated without endangering their mechanical properties [77].

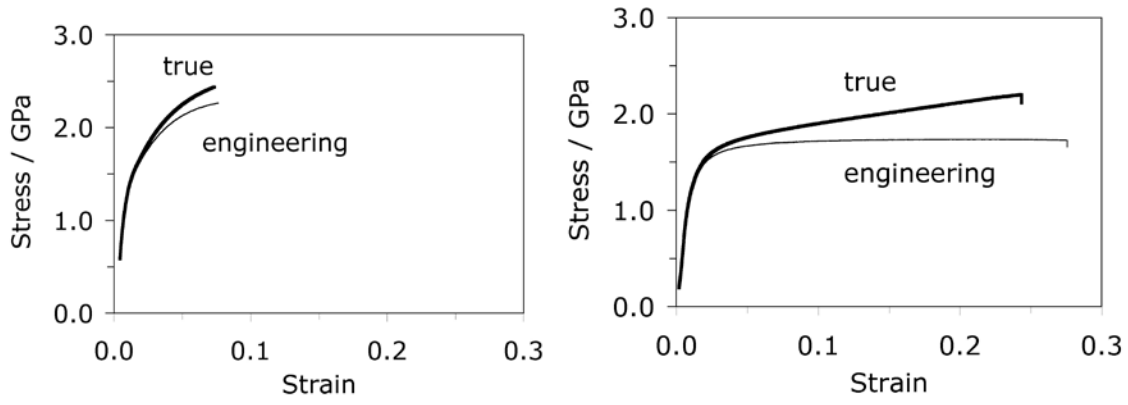

(a) (b)

Figure 55. True and engineering stress–strain curves for an alloy with composition: Fe–0.79C–1.56Si–1.98Mn–0.24Mo–1.01Cr–1.51Co–1.01Al wt%. (a) Bainite generated by transformation at 200°C and (b) bainite generated by transformation at 300°C. Virtually all of the elongation is uniform, with hardly any necking [86]

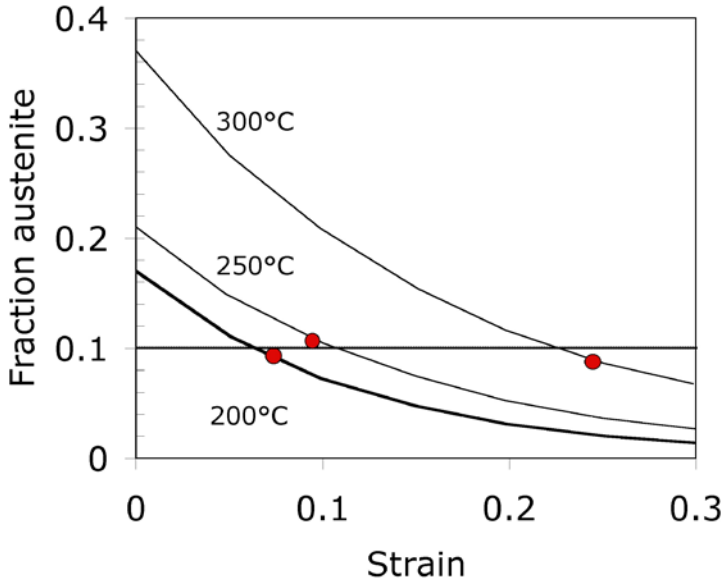

Figure 56. Calculated variations in the fraction of austenite as a function of plastic strain for carbide-free bainitic alloys [86]

2.5.4. Carbide-Free Bainite for Rail Applications

Bainitic steels, inherently, have better toughness, and ductility than the conventional pearlitic steels. Most modern bainitic steels are designed with much reduced carbon and other alloying element concentrations to form very lean alloys [89]. The reduced alloy concentration gives better weldability and improved toughness. The conventional bainitic steels have coarse inter-lath carbides and generally have poorer toughness and wear resistance than the pearlitic rail steels. This has focused attention on the development of carbide-free bainitic steels. The carbide-free bainitic steels have better fatigue properties than the pearlitic steels, accommodating longer crack lengths and growth rates before fracture (Figure 57). They also exhibit higher strength, as indicated in Figure 58.

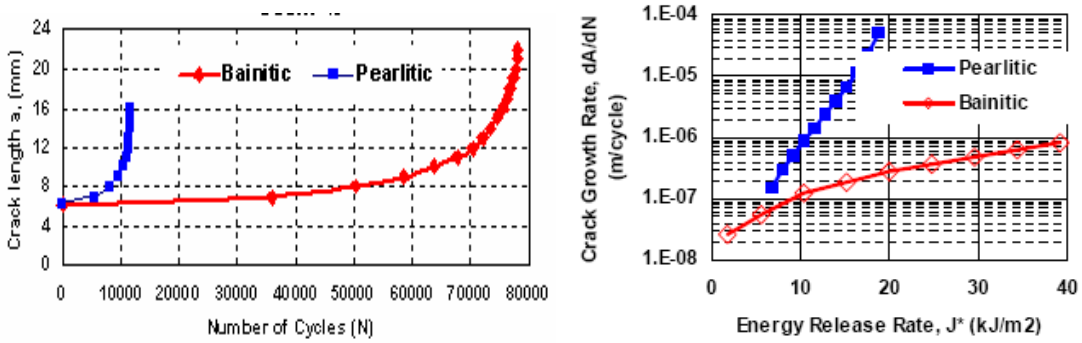

(a) (b)

*Figure 57. (a) Fatigue crack length, a, versus the number of cycles, N [91] and (b) crack growth rate, dA/dN, versus energy release rate, J*for pearlitic and bainitic rail steels [91]*

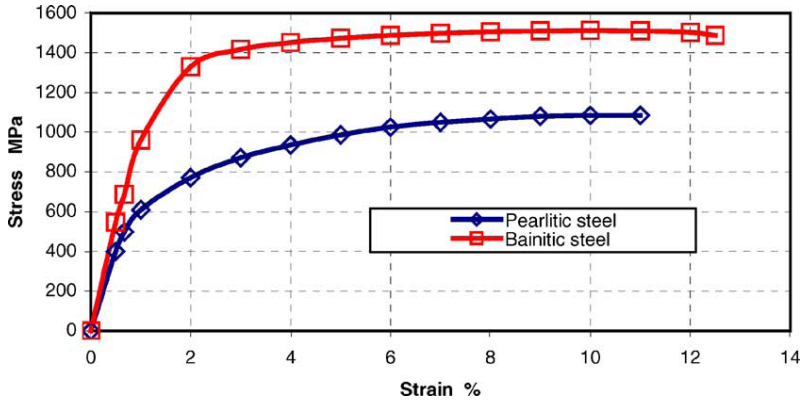

Figure 58. Stress-strain relationships of pearlitic and bainitic rail steels [91]

A number of bainitic steels have been developed for rail applications, see Tables 8 to 11 [34, 92-110]. The B320 and B360 carbide-free bainitic steels have been developed by CORUS in partnership with SNCF, SBB and Eurotunnel [106]. These grades have superior RCF resistance and B360 is slightly harder than B320. B360 is being used by SNCF for movable points of high speed lines because of its high resistance to head checking. Head checking results in cracks which are open towards the rail surface and which occur at a high frequency per metre of rail steel, see Figure 59 [111].

Figure 59. Head check-damaged rail [111]

These bainitic steels were found to be susceptible to tempering during welding and developed a wider heat affected zone (HAZ) than pearlitic steels, leading to differential wear and causing ‘cupping’ in service. This has been eliminated by improving the welding process to create a narrower HAZ.

RB370 and RB390 are Mn-Cr-Mo-V bainitic steels that have been developed by Rolls-Royce, Inc in Poland [66]. RB370 is a low carbon Mn-Cr-Mo-V steel with a minimum head hardness of 370HBW. RB390 has a higher nickel content and is designed for railway frogs or turnouts but can also be used for rails.

Clayton and Jin in collaboration with The Association of American Railroads (AAR) have developed bainitic rail steels designated as the J Alloys (J1, J2, J4, J5 and J6) [91, 100, 101]. The J alloys are bainitic rail steels with low carbon contents, high toughness, high impact and rolling contact fatigue resistance. J6 has a high hardness ~415HBN and good RCF and wear resistance and is comparable to Hadfield steel used to produce rail frogs. J6 had a high RCF resistance because of less surface and subsurface microcracks compared to pearlitic steels. J6, however, despite its higher hardness and RCF resistance, showed poorer wear resistance than conventional pearlitic steels in large scale field testing. The ability of pearlitic steels to work harden with increased contact stress allows them to offer improved wear performance.

Carbide-free rails are in service in the Swiss and French railway lines with chemical composition and mechanical properties as shown in Tables 8 and 10 [69]. Novokuznetsk Metallurgical Combine in Russia has developed bainitic rail steel alloys, É1 and É2 [102]. These steels are produced in an electric arc furnace, normalized at 870°C to improve strength, and tempered at 350°- 460°C to improve toughness and ductility.

British Steel has a patent on bainitic rail steels developed by inventors Bhadeshia and Vijay that can be used to manufacture rail track, wheels, railway points and crossings and crane rails [103]. The microstructure is composed of bainitic ferrite, retained austenite and high carbon martensite. This alloy is produced by hot rolling (~1000°C) and natural continuous cooling in air or by accelerated cooling. The alloy has good RCF and rolling contact wear resistance and can be flash butt welded.

Nippon Steel has invented a high strength, low alloy, bainitic rail steel with good fatigue resistance [104]. Nippon steel also filed another patent on bainitic rail steels (AU 737977 B2 [105]) where the fatigue and wear resistance was improved by

controlling the size and the area occupied by carbides in the microstructure [105]. In this invention it was discovered that for optimum wear resistance the longer axis of the carbide must be between 100 nm - 1000nm and that the area occupied by carbides must be between 20% - 40%. A minimum depth of carbides up to 20mm from the rail corners and the top surface of the rail head are also required.

2.5.5. Carbide-Free Bainite for Rail Wheel Applications

The literature study has shown that the study of carbide-free bainitic wheel alloys has been concentrated in China and testwork has been conducted mainly on forged wheels. A patent on a carbide-free bainitic steel wheel has been filed in china and the steel contains carbon (C): 0.15-0.45%, silicon (Si): 1.00-2.50%, manganese (Mn): 1.20-3.00%, rare earth (RE): 0.001-0.04%, less than or equal to 0.020% of phosphorus (P), and less than or equal to 0.02% of sulphur (S), the remainder being iron and unavoidable residual elements, $3.00\% \leq Si+Mn \leq 5.00\%$ [112].The wheel was produced through smelting, refining, forming and a heat treatment process to produce a carbide-free bainitic structure in the rim.

Zhang and Gu in collaboration with Chinese Railways have developed a novel low – medium carbon Si-Mn-Mo-V carbide-free alloy for forged bainitic steel wheels with a high silicon content and additions of vanadium and molybdenum as microalloying elements [99]. Vanadium and molybdenum were added to achieve fine laths and eliminate temper embrittlement. The microstructure at the rim (up to 55mm below the tread) is carbide-free bainite while at the web and hub it is granular bainite and bainitic ferrite. This steel was used to produce forged and rolled wagon wheels. Slack quenching with water on the tread of the rim section, using a controlled programme that simulated an isothermal heat treatment, was used during heat treatment [99].

Zhang and Gu proposed that austempering is unrealistic to obtain bainite in railway wheels due to their large size and unavailability of heat treatment facilities in industry [99]. The focus was on the properties of the rim and slack quenching was conducted using programmed spray quenching on the tread of the wheel. The wheels were tested on Chinese rail lines and after 180 000 km no shelling, spalling or cracking was found on the tread. The steel was also found to be resistant to hydrogen embrittlement, particularly if the silicon >1 wt% [99].

A carbide-free bainitic wheel alloy has been developed in Italy, MICRALOS. MICRALOS is a bainitic rail steel that has been developed for forged rail wheel

applications by Lucchini Sidermeccanica and LKAB in Italy, for Arctic conditions [89]. For the Arctic, a rail steel which can carry a high axle load with a high resistance to wear, rolling contact fatigue and thermal cracking with a low ductile to brittle transition temperature (DBTT) is required [89]. A steel that is resistant to thermal alteration and the formation of brittle martensite and has a high toughness even at low temperatures, (-40°C to +30°C) is ideal. A special heat treatment process is used to ensure compressive residual stresses on the wheel rim of MICRALOS steel. The microstructure of MICRALOS at the rim is that of tempered martensite and bainite with a very low micro-inclusion content. Field tests showed that the tread wear of the MICRALOS wheel is slightly higher than that of AAR Class C steel, however, MICRALOS did not suffer from thermal nor RCF cracks after 690 000 km (typical operational lives for AAR Class C wheels are 250 000 km-540 000 km).

Table 8. Chemical composition (wt%) of bainitic rail steels

Element	B320	B360	Association of American Railroads (AAR)					Swiss Railway	French Railways	É1	É2
			J1	J2	J4	J5	J6				
C	0.15-0.25	0.25-0.35	0.18	0.12	0.02	0.03	0.23	0.30	0.20	0.40	0.32
S	-	-	-	-	-	-	-	-	-	0.008	0.005
P	-	-	-	-	-	-	-	-	-	0.016	0.017
Mn	1.40-1.70	1.40-1.70	2.01	3.97	2.02	4.04	1.93	1.55	1.55	1.60	1.48
Cr	0.30-0.70	0.30-0.70	1.94	0.02	1.96	0.02	1.84	0.50	0.50	1.20	1.00
Mo	0.10-0.20	0.10-0.20	0.48	0.47	0.48		0.43	0.15	0.15	0.20	0.20
Si	1.00-1.50	1.00-1.50	1.13	0.27	0.27	0.27	1.96	1.25	1.25	1.30	1.21
V	0.10-0.20	0.03 max	-	-	-	-	-	-	0.15	0.11	0.13
Ni	-	-	0.01	0.02	1.93	0.02	0.14	-	-	-	-
Al	-	-	-	-	-	-	0.05	-	-	0.01	0.01
N	-	-	-	-	-	-	-	-	-	0.018	0.010
B	-	-	-	-	-	-	0.005	-	-	-	-
Ti	-	-	-	-	-	-	0.034	-	-	-	-

Table 9. Chemical composition (wt%) of bainitic rail steels (Continued…)

Element	É1	É2	British Steel	Nippon Steel	MICRALOS	Chinese Railways	US 7374622 B2	US 005879474 A	AU 737977B 2
C	0.40	0.32	0.05-0.50	0.15-0.45	0.35	0.21	0.15-0.20	0.05-0.50	0.15-0.45
S	0.008	0.005	-	-	0.015	0.003	-	<0.025	-
P	0.016	0.017	-	-	0.020	0.019	-	-	-
Mn	1.60	1.48	0.05-2.50	0.30-2.00	1.10	1.92	1.00-1.80	0.50-2.50	0.20-3.00
Cr	1.20	1.00	0.25-2.50	0.50-3.00	0.35	0.03	1.50-2.50	0.25-2.50	0.20-3.00
Ni	-	-	<3.00	-	0.50	0.22			
Mo	0.20	0.20	<1.00	0.10-0.60	0.55	0.30	0.40-0.70	<1.00	0.01-1.00
Si	1.30	1.21	0.50-3.00	0.15-2.00	-	1.53	1.00-1.60	1.00-3.00	0.10-2.00
V	0.11	0.13	<0.50	0.03-0.30	-	0.10	-	<0.50	0.01-0.30
Cu	-	-	<3.00	0.05-0.50	-	0.03	-	<3.00	0.05-0.50
Ni	-	-		0.05-4.00	-	0.22	1.50-5.00	<3.00Ni	0.05-4.00
Al	0.01	0.01			-	-	-	-	-
N	0.018	0.010			-	-	-	-	-
B	-	-	<0.005	0.0005-0.0050	-	-	0.0025-0.0005	<0.005	0.0001-0.0050
Ti	-	-	<0.10	0.01-0.05	-	-	-	<0.10	0.01-0.05
Nb	-	-	-	0.01-0.05	-	-	-	-	0.005-0.050

Table 10. Mechanical properties of bainitic rail steels

Property	B320	B360	RB370	RB390	Association of American Railroads (AAR)				Swiss Railway	French Railways	É1	É2
					J1	J2	J4	J6				
YS0.2% (MPa)	800	850	843-858	825-832	846	830	721	992	-	-	1130-1170	880-890
UTS (MPa)	1100	1200	1197-1211	1347-1353	1360	1151	945	1433	>1200	>1100	1420-1490	1270-1290
A (%)	14	13	12-14	13-14	14	16	18	9	>13	>14	4-5	15-17
Z (%)	-	-	39-43	43-49	39	55	69	19	-	-	10-13	25-33
KCU (J)	-	-	31-36	73-80	-	-	-	-	-	-	-	-
KV (J) (°C)	-	-	28-34	33-38	-	-	-	11(-20) 18 (-40)	-	-	-	-
Hardness (HB)	320	360	371-378	390-398	40 HRC	37 HRC	28 HRC	415	360-390	320-340	415-429	363-375
K_{Ic} (°C)	-	-	52-55 40-42 (-20)	91-92 61-63 (-20)	-	-	-	150	-	-	-	-

Table 11. Mechanical properties of bainitic rail steels (Continued..)

Property	British Steel	Nippon Steel	Micralos		Si-Mn-Mo-V	US 7374622B2	US 005879474A
			Rim	Web	Rim		
YS0.2% (MPa)	730-1230	-	1135	1040	955	≤1100	730-1230
UTS (MPa)	1250-1600	-	1215	1160	1020	≤1400	1250-1600
A (%)	14-17	-	15	15	19	-	-
Z (%)	40-55	-	50	50	51.5	-	-
KCU (J)	-	-	34	-	-	-	-
KV (J) (°C)	20-39 (-20)		34 (-20) 33 (-40)	-	312		20-39 (-20)
Hardness (HB)	400-500 H_V	321-422 H_V	386	-	78		390-500 H_v
K_{Ic} (°C)	45-60 (-20)				91 (-20)		
K_{max}, (MPa.√m)					163.8		
Wear	3-36 (750 N/mm2) (mg/m)	1.24-3.10 g/500 000 revolutions					

2.6. Mechanical Properties of Carbide-Free Alloys

Two low carbon alloys isothermally heat treated at 400°C, 430°C, 450°C were tested for tensile properties and the results given in Table 12 [86]. The alloys contained 0.2 wt% C, 1.8wt% Si, 2 wt% Mn, 0.2 wt% Mo and only one alloy had an addition of 1wt% Cr, the other was Cr-free. The steels were cast into 50kg ingots using a vacuum furnace, hot rolled and then air cooled to room temperature [86]. The alloys were heat treated in an instrument that tests the thermal-mechanical properties of metal called a Gleeble, by austenitising at 1000°C (15min) and then cooled at 30°C/s to isothemal temperatures of 400°C, 430°C, 450°C, respectively, and then the cooled to room temperature at 20°C/s.

Figure 60 shows the engineering stress-strain curves for the alloys and it shows that at lower transformation temperatures (400°C) the Cr-added steel shows lower yield strength than the Cr-free steel, but the tensile strength and elongation of the Cr-added steel is higher [86]. This improved elongation and strength has been attributed to higher contents of the retained austenite in the Cr-steel resulting in the TRIP effect. Generally the yield and tensile strengths increase with increasing transformation temperatures but the elongation decreases. The retained austenite also decreases with higher transformation temperatures. The carbide-free alloys can attain an elongation to failure of 13% even with low retained austenite values of ~4% [86].

Table 12. The Tensile and retained austenite (V_γ) results of two carbide-free steels formed using austempering. YS, yield strength, TS, tensile strength, TE, total elongation, PSE, product of strength and elongation, (V_γ, is the carbon content of the retained austenite. [86]

Steel	YS (MPa)	TS (MPa)	TE (%)	PSE (GPa%)	V_γ (vol. %)	C_γ (wt.%)
Cr-free (400°C)	772±16	977±36	15.8±0.3	15.4±0.79	6.3±1.1	1.18±0.11
Cr-added (400°C)	649±16	1083±16	18.3±0.4	19.8±0.52	10.1±0.7	1.14±0.08
Cr-free (430°C)	620±15	986±13	18.5±0.3	18.2±0.55	4.0±0.2	1.13±0.06
Cr-added (430°C)	786±20	1185±26	11.7±0.9	13.9±0.98	4.8±0.3	0.99±0.03
Cr-free (450°C)	795±17	1051±19	13.6±0.6	14.3±0.42	3.6±0.4	0.96±0.05
Cr-added (450°C)	1050±21	1263±23	5.7±0.3	7.2±0.58	2.8±0.2	0.71±0.03

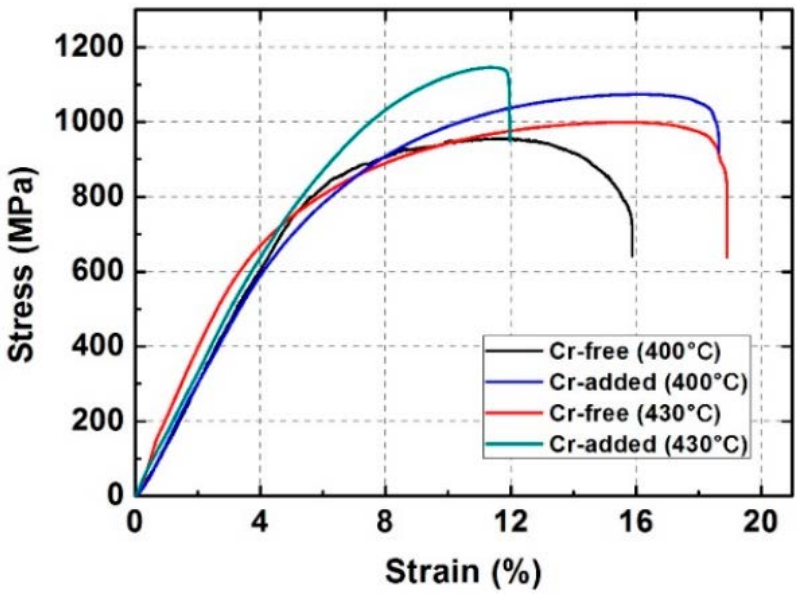

Figure 60. Typical comparison of the engineering strain-stress curves between the Cr-Free and Cr-added steels treated by austempering [86]

The mechanical properties of isothermally heat treated carbide-free bainite have been found to be a strong function of the bainite, retained austenite and martensite [113]. A carbide-free alloy with a composition of 0.34C–1.52Mn–1.48Si–0.93Ni–1.15Cr–0.40Mo–0.71Al (wt%) was produced in a vacuum furnace and forged with a forging ratio in the sample of about 6 [114]. The samples were austenitised at 930°C for 45 min. To obtain different bainite morphologies continuous cooling (CC), single isothermal holding (SIH) and two-stage isothermal holding (TIH) were used [114]. Figure 61 shows the impact toughness vs tensile strength results obtained where upper bainite (UB) was found to have high tensile strength but low impact toughness, lower bainite (LB) showed lower tensile strengths but higher impact properties while low temperature bainite (LTB) showed high strength and impact toughness properties [114].

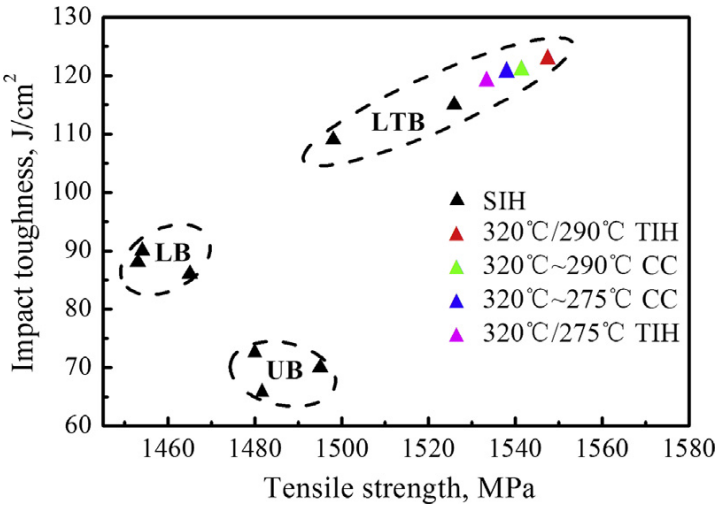

Figure 61. Distribution of tensile strength and impact toughness of different bainite morphologies in 34MnSiCrAlNiMo steel [113]. Lower temperature bainite (LTB), lower bainite (LB) and upper bainite (UB).

2.6.1. The Effect of Banding on the Mechanical Properties of Carbide-Free Bainitic Steels

Chemical segregation in steel making can cause microstructural banding resulting in mechanical properties dependent on the banding orientation [61]. Chemical inhomogeneity develops during solidification when elements with a low partitioning ratio are ejected into the interdendritic regions causing areas of high solute concentration [61]. Subsequent deformation produces a segregated microstructure aligned with the deformation direction [61]. This inhomogeneity in substitutional alloying elements affects the local transformation behaviour of the material. Solute rich areas stabilize austenite so that during cooling the solute lean areas transform first [61].

It is known that manganese is prone to segregate in steel [61]. High concentrations of manganese, chromium and silicon tend to segregate during solidification, staying in the solution within the liquid, thus leading to enriched and depleted regions in the microstructure during subsequent cooling [60, 62]. Further thermomechanical treatments, such as hot rolling, will result in a banded microstructure with alternate bands of different phases or micro-constituents, such is the case of the bands of martensite in a bainitic matrix [60].

This banding is undesirable because it introduces texture in the microstructure and anisotropy in the mechanical properties depending on the severity of the banding. For

example, if martensitic bands exist then there is a decrease in the toughness within the band, but an increase in the hardness [60]. Figure 62 is an example of a severely banded structure with a volume fraction of bands of 0.19±0.06 calculated using light optical microscopy [60, 62]. The investigated steel grade comprises 0.23C-0.97Si-1.55Mn-1.55Cr-0.14Mo-0.15S (wt%). The steel was conventionally hot rolled into 40mm bars, air cooled □2 C/s. The high manganese and chromium were added to increase hardenability and avoid ferrite-pearlite formation before bainitic transformation and high silicon was added to prevent cementite formation [60]. It was found that the microstructure within and without the bands is the same but the banded and unbanded microstructure showed a difference in the resistance to etching [60]. Electron probe microanalysis showed that the bands were enriched in chromium, silicon and molybdenum but depleted in manganese, see Figures 63 and 64 [60, 62]. The B_s and M_s temperatures of the banded and unbanded regions were different due to their different chemical compositions, as shown in Table 13 [60].

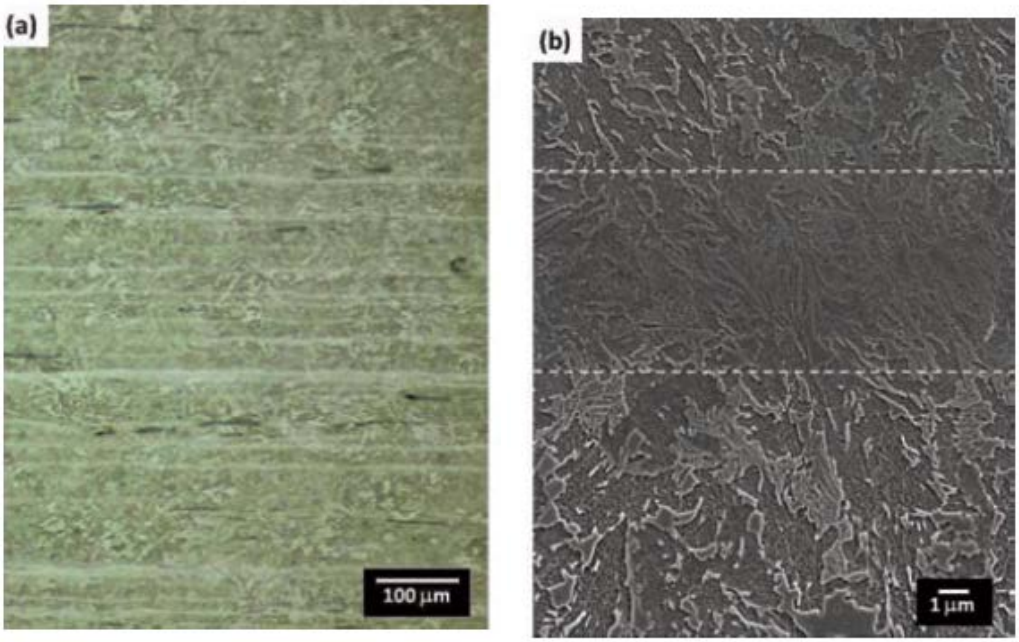

Figure 62. (a) Light optical microscopy and (b) secondary electron SEM micrographs of a longitudinal sample after standard etching to reveal the presence of bands in a bainitic matrix. The dashed lines in the SEM micrograph show the banded region. The invested steel grade is 0.23C-0.97Si-1.55Mn-1.55Cr-0.14Mo-0.15S (wt%). The steel was hot rolled into 40mm bars, air cooled □2 C/s.

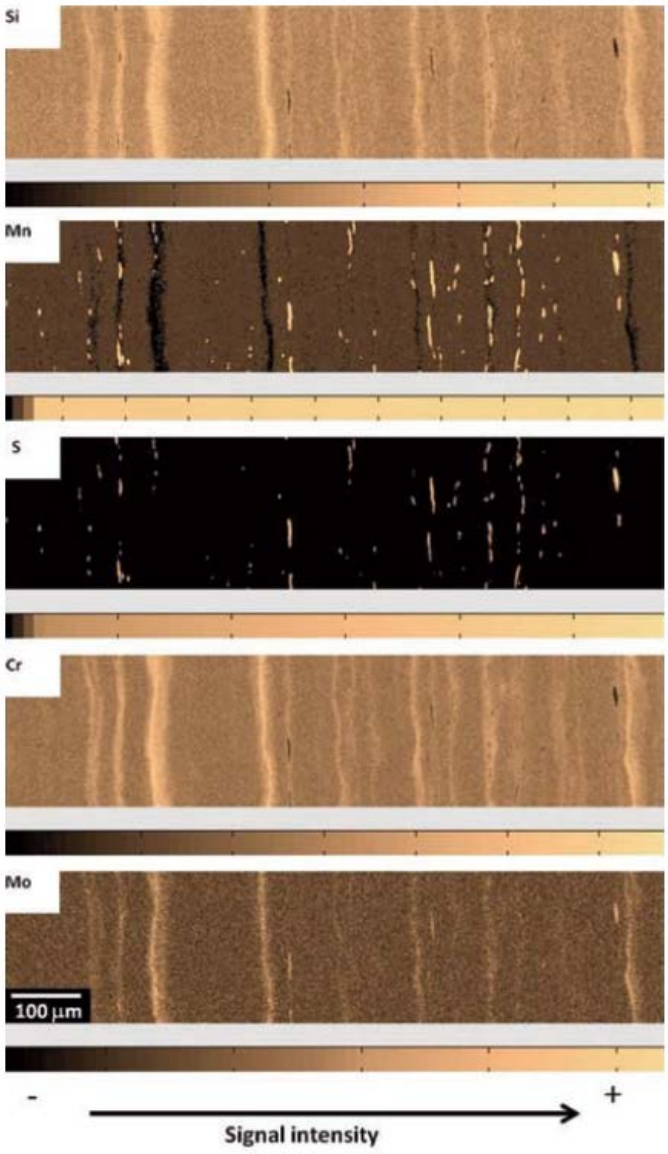

Figure 63. Electron probe microanalysis (EPMA) maps showing the signal intensity detected for Cr, Si, Mo, Mn and Si, which is proportional to their wt%. Most inclusions are found to be MnS. [60]

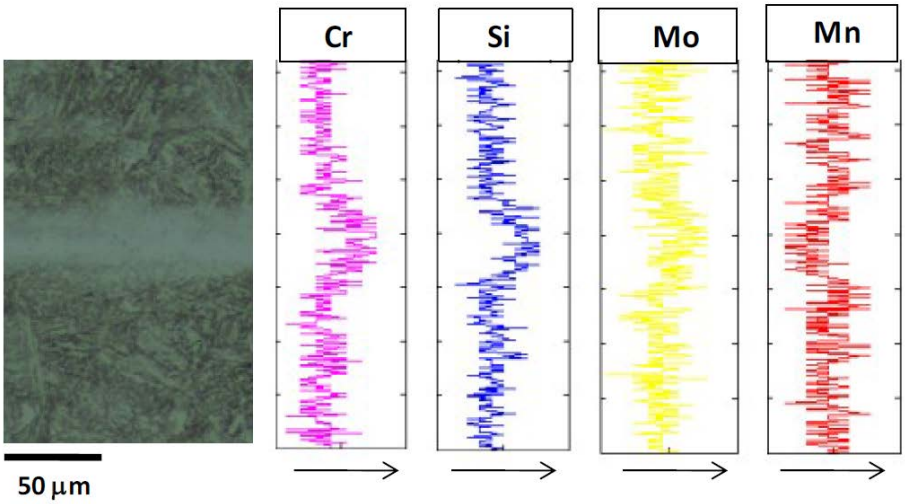

Figure 64. EDS qualitative profiles after scanning in smart-map mode and the corresponding light optical micrograph of the same area confirming the presence of a chemical band [62]

Table 13. B_s and M_s temperatures calculated for the chemical composition of the matrix and banded region [60]

	B_s (°C)	**M_s (°C)**
matrix	505	370
band	495	365

Banded and unbanded carbide-free bainite was tested for tensile properties with a composition of 0.4C-2.8Mn-1.8Si (Figure 65). The alloys were transformed at different times, isothermally, to get different fractions of bainite in the microstructure, the lower times producing less bainite but more martensite in the microstructure [5]. The results show that the banded and unbanded structures had similar deformation behaviour. The alloys with the higher martensite content however showed the higher tensile strength values but lowest elongation [5].

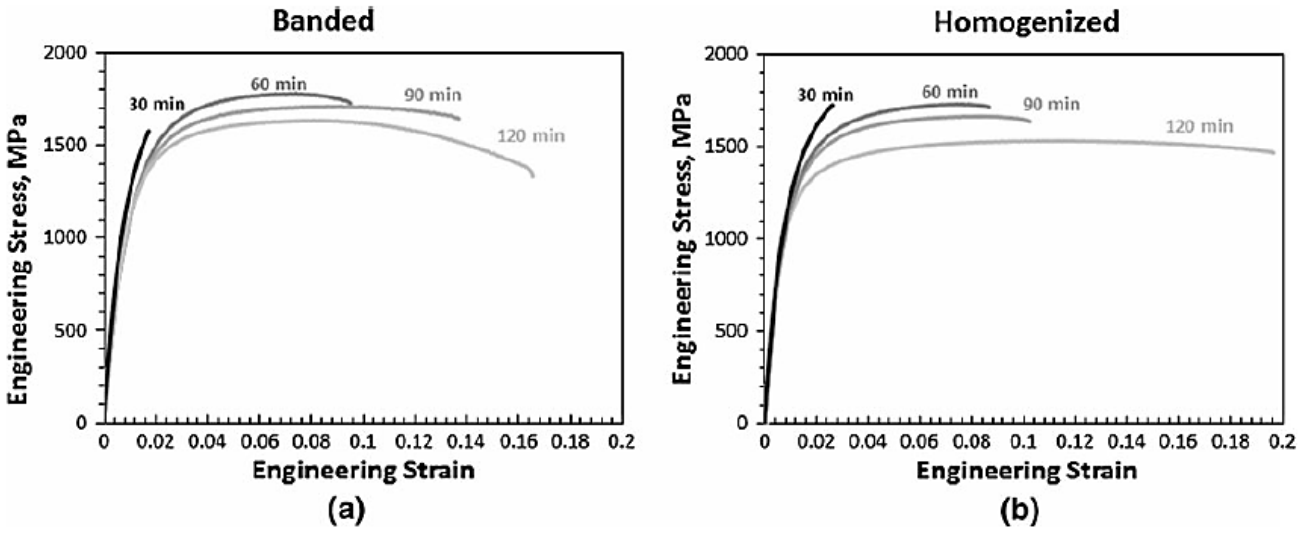

Figure 65. Effect of the bainitic transformation time on the engineering stress-strain curves of (a) banded and (b) unbanded steels [5].

2.7. Wear of Rail Steels

When two surfaces are gently brought together, contact will initially occur only at a few points, called asperities [115]. If the load increases, a larger number of asperities come into contact. These asperities support the normal load on the surface and generate any frictional forces which act between the surfaces [115].

The hertz theory for an idealised case of a single asperity loaded against a rigid plane surface (Figure 66) under a normal load *w*, gives a contact area of radius a as follows:

$$a = \left(\frac{3wr}{4E}\right)^{1/3} \qquad \textit{Equation 10}$$

Where *r* is the radius of the sphere, E is the elastic modulus, *w* is the load and *a* is the radius of the contact circle

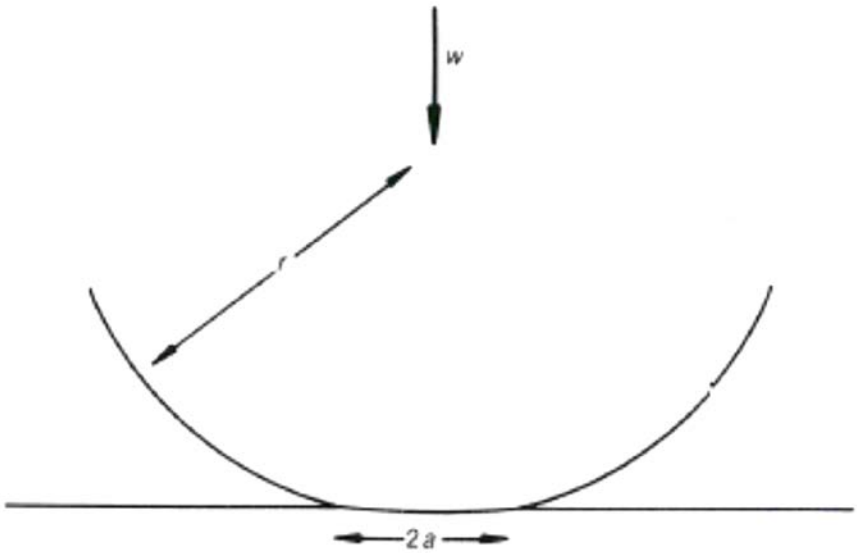

Figure 66. Elastic deformation of a sphere of radius r, pressed against a plane surface under a load w. The radius of the contact circle is a [115]

For this case, in which the deformation is purely elastic, the stress is not uniform over the circular contact, but has a maximum at the centre and falls to zero at the edges, see Figure 67 [115]. The maximum stress at the centre of the contact circle is 3/2 times the mean pressure [115]. The maximum shear stress occurs at a depth of about 0.47a and plastic flow occurs first at this point when the yield criterion is satisfied [115].

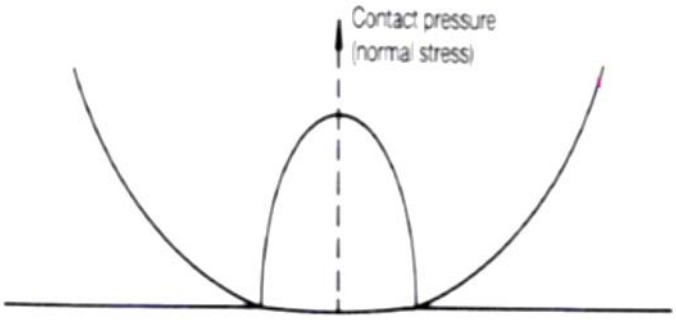

Figure 67. The distribution of normal stress (contact stress) under a sphere loaded elastically against a plane [115]

2.7.1. Friction Force

Friction is a force that resists the motion of one body over another during sliding and rolling motion [115]. In ideal rolling and sliding, a tangential force (F), which is equal to the frictional force, is required to move a body over a stationary counterface as shown

in Figure 68 [115]. The ratio between the frictional force and the normal load (W) is the coefficient of friction, μ [115]:

$$\mu = \frac{F}{W} \qquad \textit{Equation 11}$$

For most common materials sliding in air, μ lies between a narrow range of ~0.1 to 1.0 μ and depends heavily on the test conditions, the microstructure, composition and load.

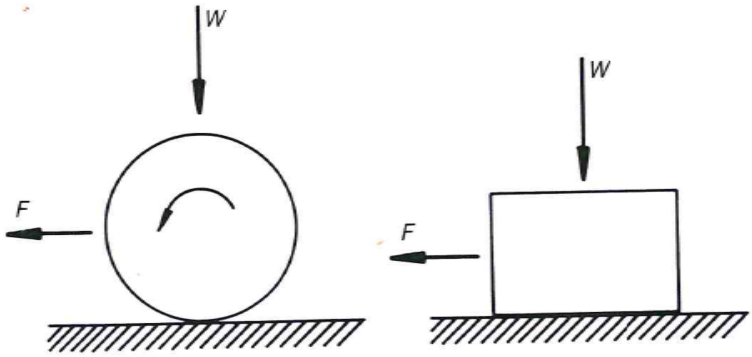

(a) *(b)*

Figure 68. A friction force, F, is needed to cause motion by (a) rolling and (b) sliding [115]

For steel sliding on steel in air, μ typically is high at low loads and decreases to a lower value at higher loads, see Figure 69 [115].

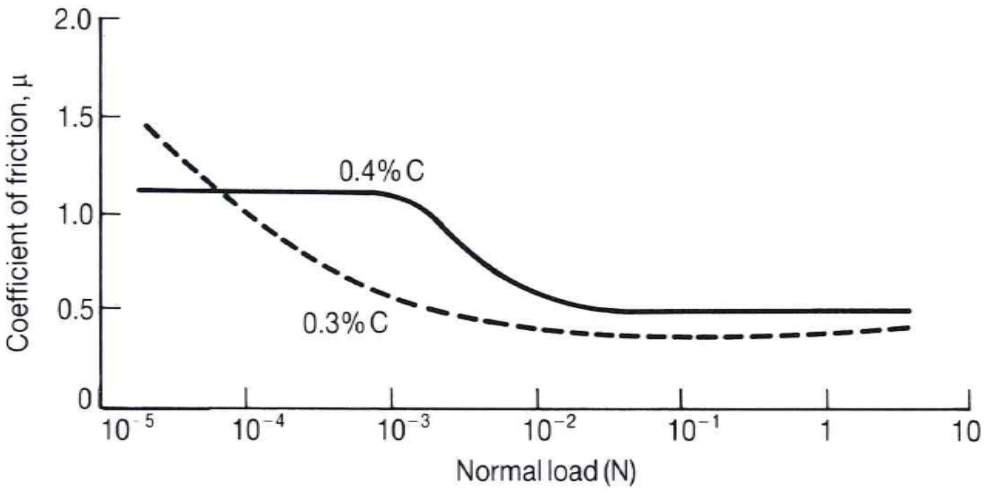

Figure 69. The variation of the coefficient of friction with normal load for steels sliding against themselves in air, unlubricated. Results are shown for two different plain carbon steels, with carbon contents of 0.4% (full curve) and 0.3% (broken curve) [115]

The important mechanical stresses are the normal stress acting at the surface of each sliding body and the shear stress at and below the surface [115]. For systems where $\mu < 0.3$, the maximum shear stress and associated plastic flow is below the surface [115]. This is typical of lubricated systems. If $\mu > 0.3$ then the maximum shear stress is at the surface.

2.8. Lab Scale Wear Tests to Predict Wheel Wear

There are a number of methods available to test for the wear of rail/wheel steels, however no standard test method to perform wear testing and represent the wear data is available [116]. This makes comparison of wear data from different test rigs difficult. The different ways in which wear of rail/wheel steels has been conducted is through [116]:

- field testing in actual environments
- simulated field experiments on specially built test tracks
- Full-scale laboratory testing
- Twin-disc laboratory testing
- Pin-on-disc laboratory testing

The wheel /rail contact is quite complex because of the large variety of loading conditions and contact geometries that exist and the many different rail and wheel profiles available [116]. The contact area between the wheel and rail is thus always changing, as well as the forces exerted. Conditions in the contact area are also affected by natural lubricants such as humidity, precipitation, and leaves [116]. In addition man-made lubricants are also applied to the rail to reduce wear [116]. All these influencing factors work synergistically to determine the wear behaviour of the wheel and rail.

The advantage of laboratory tests is that they are conducted under extremely controlled test conditions but allow for accurate measurements of wear rates [116]. The contact geometry is simplified and the actual operating environments are unachievable. However, their test specimens are easy to manufacture and the tests are cheap to run. The data from the laboratory tests can be used to model the wear process, provided the wear co-efficients are measured [116]. One way to model wear, using data from a pin-on-disc or twin disc tribometer, is through using the Archard adhesive wear equation, as follows [116]:

$V = k\,\frac{Pl}{h}$ where *P* is load, *l* is sliding distance, *k* is the friction co-efficient, and *h* is hardness

The second way to model wear [116], using data from twin disc measurements, is by relating the material loss to energy in the contact area using the Tγ wear value, where T is the tractive force (normal force x traction co-efficient) and γ is the creep in the contact (relative velocity of the wheel and rail divided by the velocity of vehicle).

Figure 70 shows the wear maps attained for an RT8 rail wheel material against 900A rail material after twin-disc and pin-on-disc tests [116]. In these maps the regimes of wear are defined depending on the parameters indicated on the axes [116]. The wear co-efficient can be integrated into simulation software, such as Multi-Body Dynamics (MBD) to predict actual wheel/rail wear. In fact, very good correlations were achieved for wear data from laboratory tests and those of full scale conditions using wear co-efficients from laboratory tests and MBD software at Lucchini, Italy [116]. Wear co-efficient Data from twin disc and pin-on-disc test rigs were also found to correlate well with results obtained using the full scale Voestalpine and Lewis & Olofsson rigs [116].

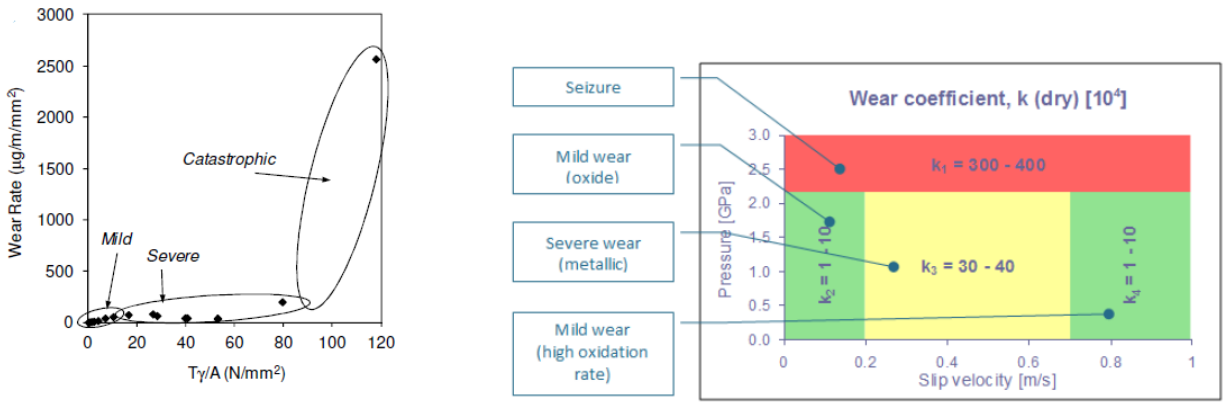

Figure 70. Wear Maps for (a) R8T wheel steel against 900A rail steel after twin disc testing, the Tγ is divided by the contact area, (b) R7 wheel steel against 900A rail steel after pin-on-disc testing [116].

It is stated in ASTM G 99 – 95a: Wear Testing with a Pin-on-Disk Apparatus [117]: that 'the value of any wear test method lies in predicting the relative ranking of material combinations. 'Since the pin-on-disk test method does not attempt to duplicate all the conditions that may be experienced in service (for example; lubrication, load, pressure, contact geometry, removal of wear debris, and presence of corrosive environment),

there is no insurance that the test will predict the wear rate of a given material under conditions differing from those in the test.' The pin-on-disc test is thus a comparative, qualitative test used to rank wear properties of different alloys.

2.9. The Wear of Pearlitic Rail Steels

The resistance to wear of the pearlitic steels reduces with a finer interlamellar spacing and higher hardness as shown in Figures 71 and 72 [25].

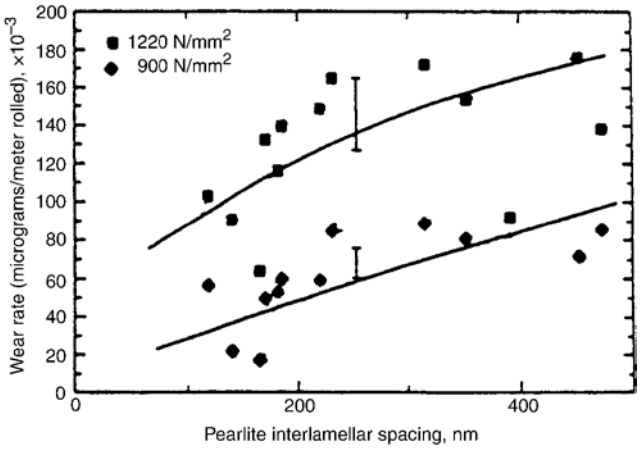

Figure 71. Wear rate as a function of pearlite interlamellar spacing for various rail steels at contact pressures of 1220 N/mm² and 900 N/mm² [25]

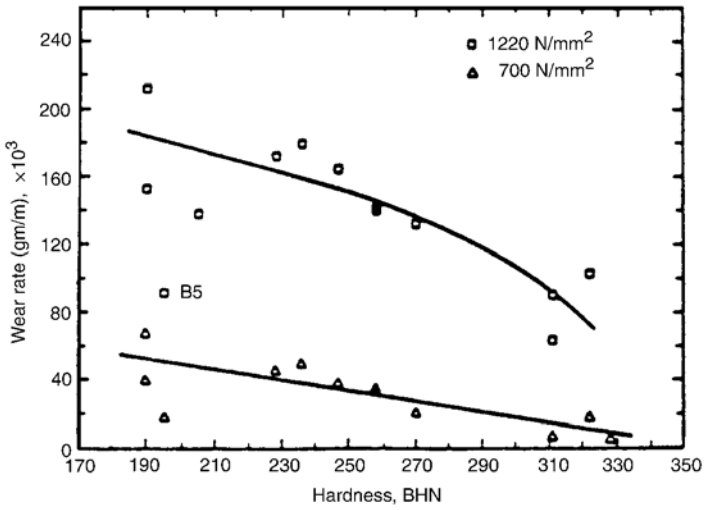

Figure 72. Wear rate as a function of hardness for various rail steels tested at contact pressures of 1220 N/mm² and 700 N/mm² [25]

In the wheel/rail contact both rolling and sliding occur in the contact area [110]. On straight track, the wheel tread is in contact with the rail head (point c in Figure 73) but

in curves the wheel flange may come into contact with the gauge corner of the rail (point d in Figure 73) [110, 113, 118].

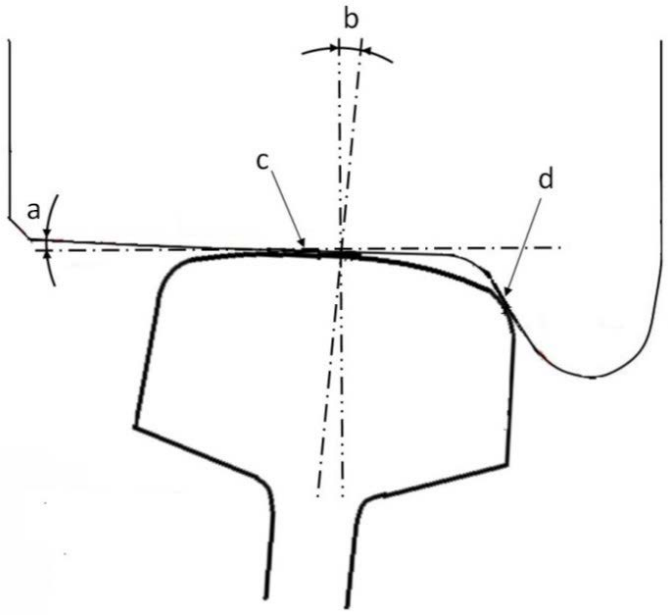

Figure 73. Schematic of wheel–rail contact positions: a = conical wheel profile, b = rail inclination, c = wheel tread–railhead contact and d = wheel flange–rail gauge contact [113]

Since both the wheel and rail materials are hard, the contact area between the wheel and rail is comparatively small, typically $1cm^2$ in size [113]. The size of the contact area varies depending on the position and geometry of the contacting bodies [113]. Railway vehicles are very heavy so the small contact area needs to transfer a very high axle load, causing it to experience very high contact pressures [113]. The contact area can be divided into two regions: the sticking (no slip) and slip regions [110]. With increasing tangential load the slip region increases and the sticking region decreases, resulting in rolling and sliding contact [110]. When the tangential load reaches its saturation value the sticking region disappears and the entire contact area is in a state of pure sliding [110].

In the curves of rail tracks there can be a large sliding component on the contact patch at the gauge corner of the rail head. Due to this sliding, wear occurs in the contact area under the poorly lubricated condition that is typical of the wheel/rail contact area [110]. It has been observed during sliding wear that an increase of the severity of loading (i.e. increase in normal load, sliding velocity or surface temperature) leads at some stage

to a sudden change in wear rate (volume loss per sliding distance) [110]. The wear rate may change from mild wear to severe wear [110].

Mild wear results in a smooth surface, often smoother than the original surface, with minimal plastic deformation and oxide debris [110]. Severe wear results in a rough surface that is usually rougher than the original surface, with extensive plastic deformation and flake-like metallic debris [110].

Figure 74 shows an example of a wear map that has been plotted from wear data after testing under sliding conditions measured using the twin disc apparatus [110]. In this plot the wear rate is plotted as mass loss (μg) per distance tested (m) per area of contact (mm^2). The contact pressure is plotted as Tγ/A, where T is the tractive force (normal force multiplied by coefficient of friction) and γ is the slip (percentage difference in surface speeds between the wheel and rail test specimens) and A is the contact area [110]. The map shows three regions of mild, severe and catastrophic wear.

Figure 75 shows that the wear rate of pearlitic rail steels is decreasing over the years with further developments, standard carbon alloys of 1987 have higher wear rates than the UIC900 alloy produced in 2000 [110]. The wear rate for UIC60 900A (2000) rail is also an order of magnitude lower than that of BS11 (1984). The wear rate was measured using the twin disc apparatus.

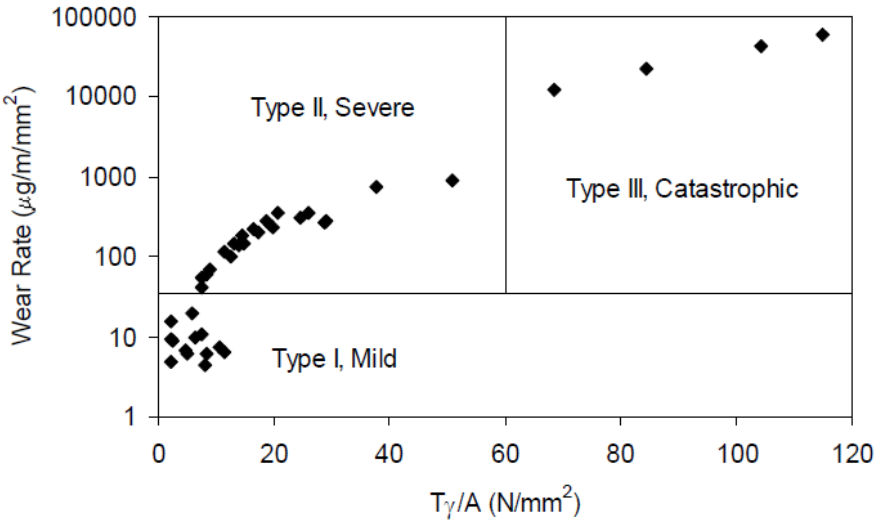

Figure 74. Wear regimes identified during twin disc testing of BS11 rail material vs. Class D tyre material. In this figure the wear rate is plotted as mass loss (μg) per distance tested (m) per area of contact (mm²). The contact pressure is plotted as Tγ/A, where T is the tractive force (normal force multiplied by coefficient of friction) and γ is the slip (percentage difference in surface speeds between the wheel and rail test specimens) and A is the contact area [110].

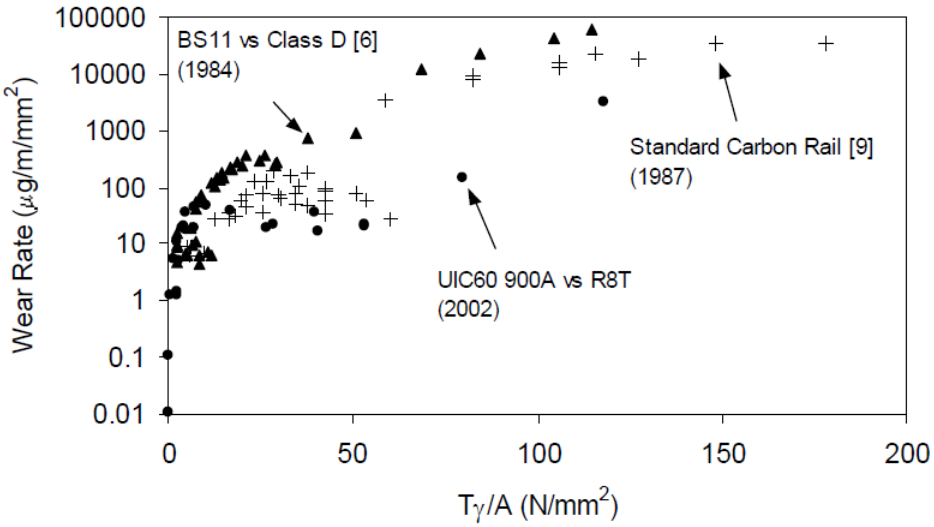

Figure 75. Wear rates resulting from twin disc testing for a number of different material combinations. In this figure the wear rate is plotted as mass loss (μg) per distance tested (m) per area of contact (mm²). The contact pressure is plotted as Tγ/A, where T is the tractive force (normal force multiplied by coefficient of friction) and γ is the slip (percentage difference in surface speeds between the wheel and rail test specimens) and A is the contact area [110].

Previous tests have found wear in the mild region to be dominated by surface oxidation while in the severe and catastrophic regimes the wear was found to be dominated by surface cracking and material loss by spalling [110]. Mild to severe wear is most likely to occur in the wheel tread/rail head contact area and severe to catastrophic in the wheel flange/rail gauge corner contact area [110].

An additional mode of wear called heavy wear has also been identified within the severe wear region where a peak in the wear rate is found, dependent on the operating conditions under consideration, Figure 76 [110].

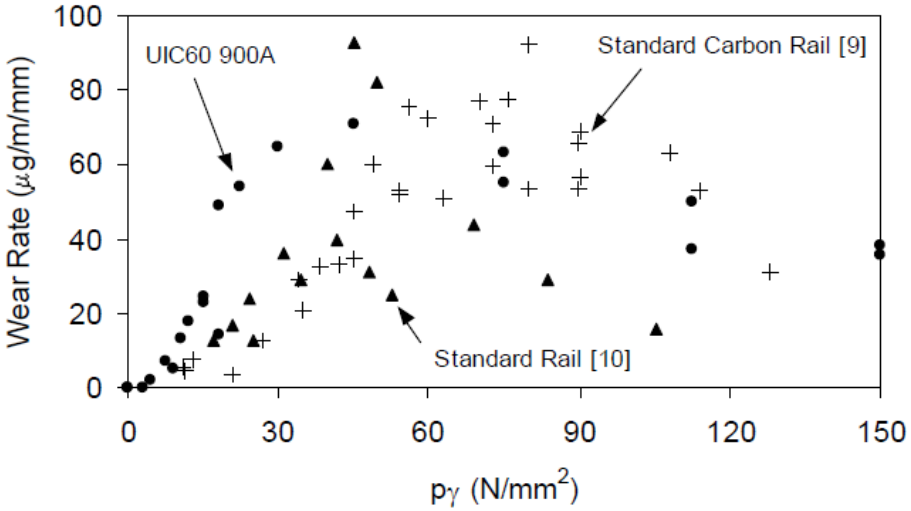

Figure 76. Total wheel and rail wear data in the heavy wear regime. In this figure the wear rate is plotted as mass loss (μg) per distance tested (m) per area of contact (mm^2). P is the normal load (N) and γ is the slip (percentage difference in surface speeds between the wheel and rail test specimens [110]. The wear rate was measured using the twin disc apparatus

Tests have also shown that the transition from severe to catastrophic wear is affected by temperature, [110]. An increase in temperature decreases the yield strength of the material and increases the wear rate.

Wear data for various rail materials under different contact conditions were collected by some researchers and it can be seen in Figure 77 that there is a large amount of data for conditions typically found in the rail head/wheel tread contact area but very little for that in the rail gauge/wheel flange contact area [110, 113]. In the contact area between the wheel tread and rail head, both the contact pressure and sliding velocity

are lower than in the contact area between the wheel flange and rail gauge [110, 113]. Severe contact conditions cause more wear, thus the wheel flange/rail gauge contact is usually lubricated to lower the co-efficient of friction. [113]. The stresses in the rail head/wheel tread contact generally range between 500MPa-1500MPa, while the stresses in the rail gauge/wheel flange contact can reach as high at 2500MPa [110].

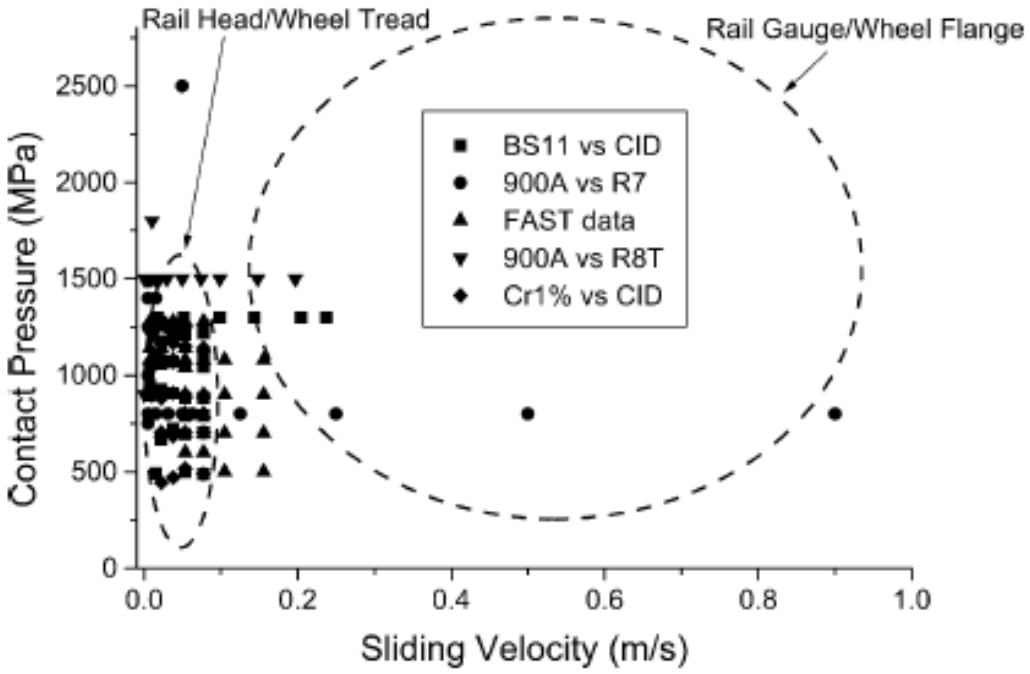

Figure 77. Available rail steel wear data plotted over typical wheel/rail contact conditions [110]

During sliding the wear co-efficient is calculated using Archard's equation as follows [110]:

$$K = \frac{Vh}{Ns} \qquad \textit{Equation 12}$$

where K is the wear coefficient, V the wear volume, N the normal load, *s* the sliding distance and *h* the material hardness. The wear coefficient depends on the sliding velocity, such that a higher sliding velocity results in a higher wear rate [110]. Slip is the percentage difference in surface speeds between the wheel and test specimen [110].

2.10. The Wear of Bainitic Rail Steels

Wear resistance is important in heavy haul rail where high loads are transported [3, 11]. In this case, because steels with a high hardness are required, grinding is used to remove the shallow surface region affected by RCF [97, 111]. Bainitic steels have been studied for their wear behaviour in rolling and sliding conditions and the results have indicated in many instances, that bainite does not in general outperform pearlite with similar hardness and loading conditions [119]. The greater wear resistance of pearlite has been attributed to its ability to deform during rolling and sliding, the ability of the ferrite to work harden and the presence of a significant amount of hard cementite at the wear surface [119]. In contrast, bainite has a smaller fraction of cementite and other residual phases such as martensite and retained austenite complicate its wear response [119].

Figure 78 shows the pin on disc results of a conventional bainitic and pearlitic alloy after pin-on-disc tests using normal loads of 10N, 30N and 50N [120]. The bainite showed wear rates at least two orders of magnitude higher than the pearlitic rail steel. No significant variations in the friction coefficient was found with increases in the normal load. Strain hardening was observed in the pearlitic pins and not in the bainitic ones [120].

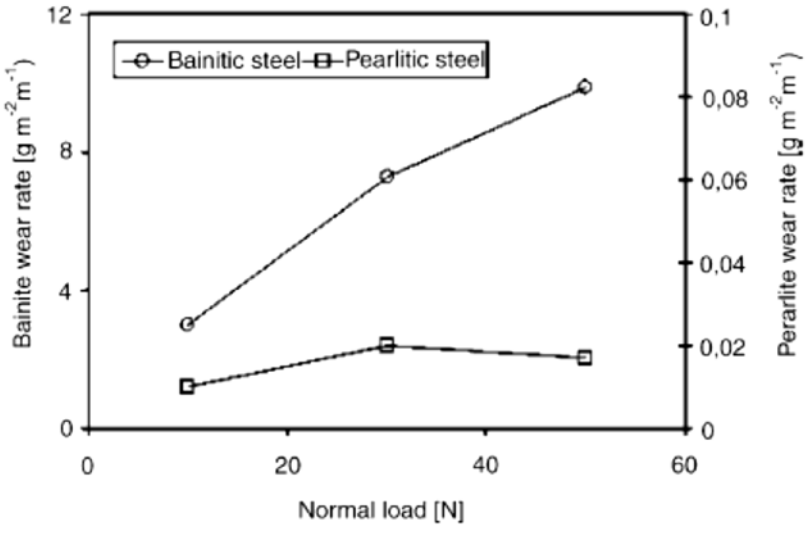

Figure 78. Wear rate as a function of the normal load for pearlitic and bainitic pins [120]

Clayton and Jin performed a number of pin-on-ring tests on different bainitic and pearlitic steels and they found that wear decreased with increasing hardness and that

at a certain hardness the wear rate decreased drastically, see Figure 79 [118]. This is particularly true for pearlitic steels, while the wear of the bainitic steels showed only a small dependency on the hardness.

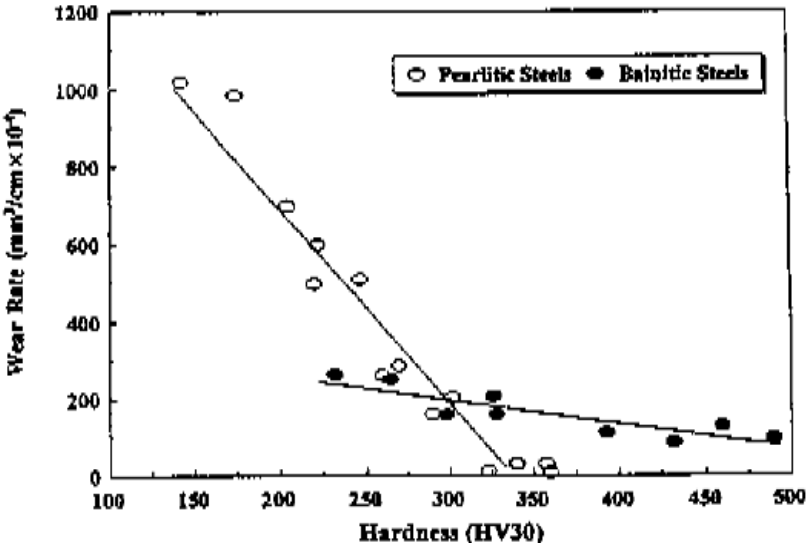

Figure 79. Sliding wear rate versus hardness for bainitic and pearlitic steels [118]

Feng et al [121], conducted pin-on-disc wear tests on carbide-free bainitic and pearlitic alloys under dry sliding conditions and found that the pearlitic steel had a lower wear rate than the bainitic steels [121]. One of their alloys S1, however, with a higher hardness than the pearlitic steel, had a comparable wear resistance to the pearlitic steel, see Figure 80a [121]. The bainitic and pearlitic alloys showed work hardening after testing, see Figure 80b. After testing, the retained austenite had been transformed to martensite in the bainitic S1 alloy and S1 had a lower average coefficient of friction (COF) than the pearlitic alloy at a contact load of 40 MPa [121]. At a contact load of 5MPa the COF for the two alloys was similar. The COF initially increased at shorter sliding distances, but it tended towards steady state values after a longer period of testing.

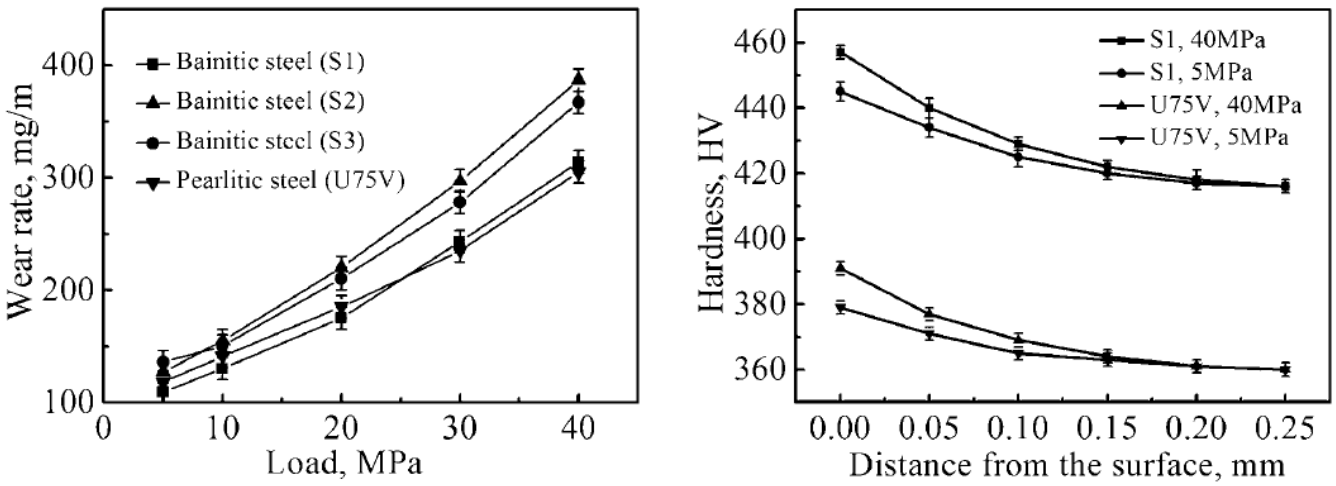

(a) (b)

Figure 80. (a) Variations in wear rate with load for different samples and (b) variations in hardness in the wear sample after wear testing of samples [121]

Tests conducted on carbide-free bainitic alloys with different heat treatments found that the wear rate decreased with increasing hardness under rolling/sliding conditions, see Figure 81 [122]. The near-surface microstructure had suffered large strain with elongations parallel to the sliding direction but with no cracking [122]. A transfer layer was found near the surface, which is much harder than the bulk material. The amount of retained austenite decreased drastically after testing due to transformation to mechanically transformed martensite, showing a work hardening effect in the alloys [122].

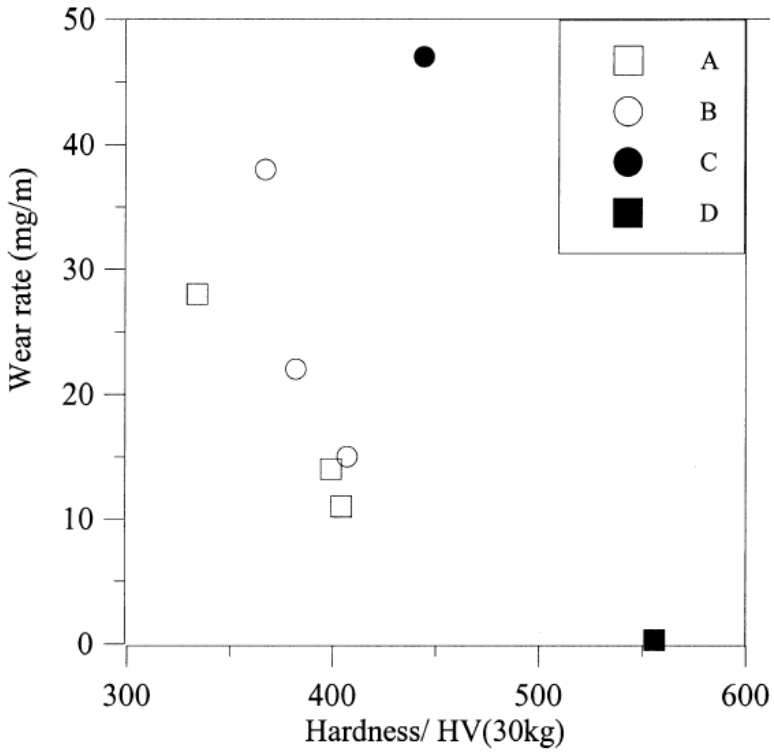

Figure 81. The influence of hardness on rolling/sliding contact wear rates of experimental steels [122]

2.10.1. The Wear of Nanostructured Bainite

A number of wear tests done on nanostructured bainite under rolling and sliding conditions have found this alloy to hold promise for improved wear resistance [119]. Reasons for this include its fine scale microstructure and the retained austenite which prevents crack propagation during sliding [119]. One nanostructured bainite alloy, Bainite200**,** was tested using a twin disc tribometer and even though its hardness was not the highest compared to published data, its wear rate was one of the lowest, see Figure 82 [119].

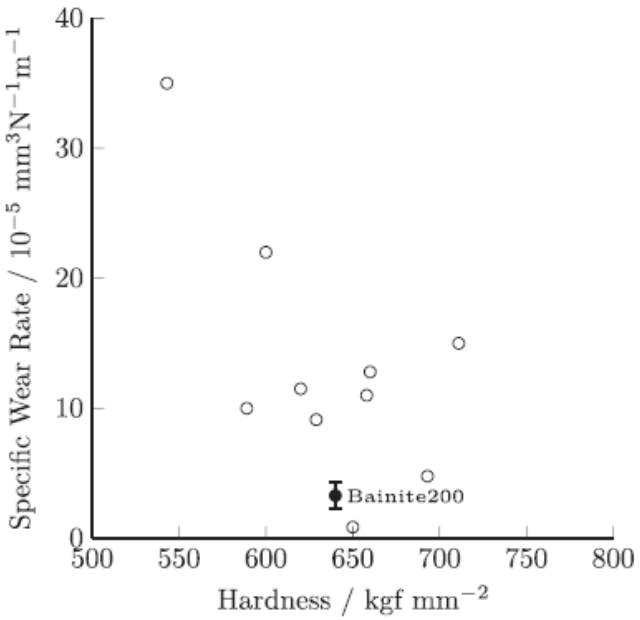

Figure 82. Specific wear recorded for Bainite200 (filled dot with error bars) together with published data on other carbide-free bainitic steels (open dots). All the data is from tests with similar conditions [119]

This alloy showed tracks of wear marks along with ledges protruding from the edges, indicating significant plasticity of the deformed material on the surface (Figure 83a). No wear debris in the form of metallic flakes was found on the surface. The cross-section of the worn surface showed little damage to the nanostructure and the depth of the deformed layer was ≤5μm [119]. A non-etching layer had also formed, see Figure 83b, c. This layer is adherent and continuous. Significant hardening was detected under the surface at a depth of ~40μm-50μm, possibly due to stress induced transformation of the retained austenite into martensite [119]. It was indeed found that the remaining retained austenite decreased by ~40%, indicating mechanical stability of the austenite [119].

Other twin-disc tests under rolling/sliding conditions found that nanobainitic alloys showed much higher wear resistance than other carbide-free bainitic alloys, see Figure 84 [122]. The materials revealed work hardening after wear testing.

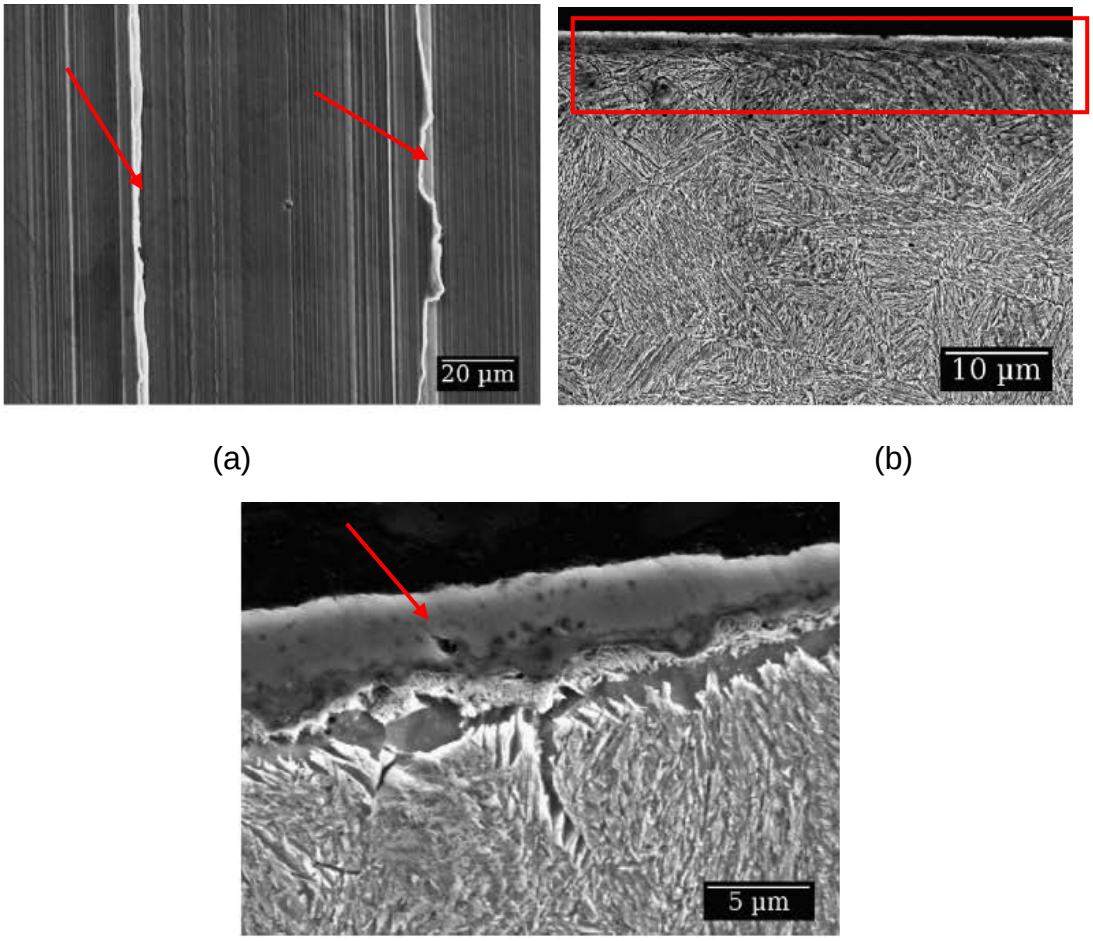

Figure 83. Structure after rolling-sliding (a) showing wear tracks on the surface with ledges indicating plastic deformation of the surface (b) limited subsurface deformation of the microstructure in the direction of rolling/sliding and (c) a very thin non-etching layer on the surface [119]

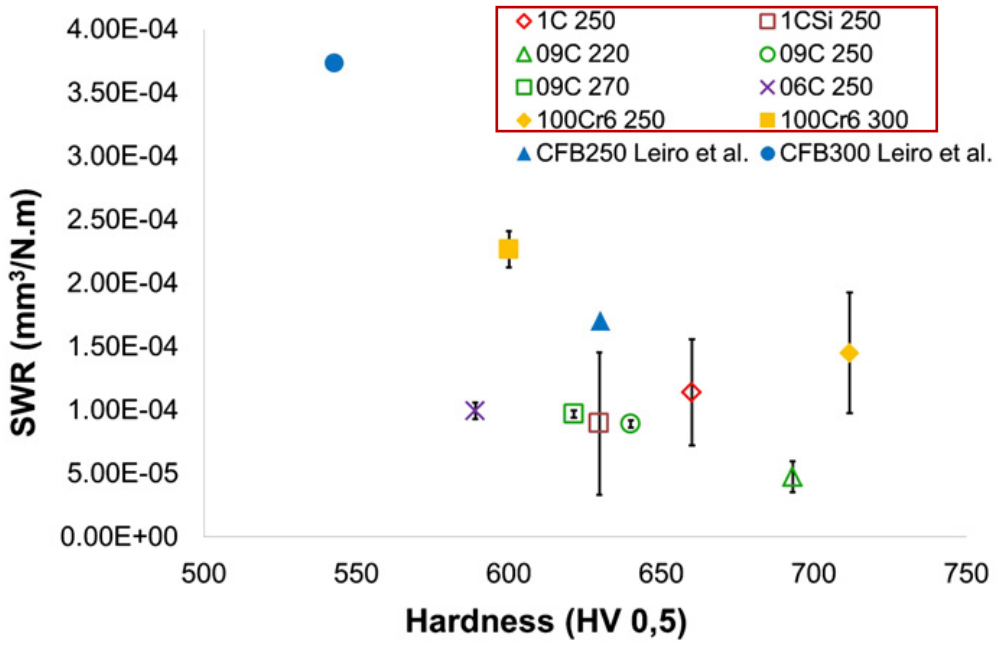

Figure 84. Specific wear rate (SWR) vs. hardness plot of different carbide-free alloys tested under the same conditions [122]

3. Experimental Procedure

This PhD aims to design a carbide-free bainitic alloy composition and heat treatment for forged rail wheel application in South Africa, through alloy development. The alloy development process involves selecting a suitable chemical composition to produce a carbide-free bainite alloy in the laboratory. Modelling software, MUCG83, was used to study the effects of alloying elements on the alloy microstructures and draw the time-temperature-transformation (TTT) diagrams.

A number of experimental alloys were produced for testing, see Table 14. All alloys were manufactured in an induction furnace, in air, forged and hot rolled before heat treatment. All experimental heat treatments were conducted in a salt bath to produce bainite. AAR Class C will be used as the reference alloy in this study, except for the wear testing where AAR Class B will be used as the reference.

Series 1 (Alloys A to D) were carbide-free bainitic alloys produced in the laboratory to the study their microstructural features using optical and electron microscopy. These alloys had varying silicon, manganese, chromium and molybdenum contents. The aluminium content of ~0.2 wt% was not a deliberate addition but a result of the scrap used to produce the alloys. Quench dilatometry was used to draw the continuous cooling transformation (CCT) diagrams to determine the bainite region.

From the results it was found that Alloy D showed the better properties and a new series of Alloys E to H (Series 2) were manufactured with compositions based broadly on Alloy D (C: 0.25±0.5, Mn: 1.5±0.5, Cr: 0.5±0.1, Mo: 0.2±0.05). Series 2 alloys still had varying silicon contents and was produced to test for mechanical properties i.e. tensile testing and impact testing, as well as for the tempering properties. Alloys F showed the better tensile properties while Alloy G showed the better impact properties.

A new high silicon carbide-free Alloy I (Series 3) was produced with a composition based on Alloys F and G (0.28±0.5, Mn: 1.5±0.5, Cr: 0.5±0.1, Mo: 0.2±0.05, Si: 1±1.0). Alloy I was produced to study the wear properties after two different heat treatments, at 400°C and 435°C. The two temperatures were used to produce two different bainite volume fractions.

Phase analysis of the alloys was conducted using optical microscopy, scanning electron microscopy, dilatometry, x-ray diffraction, neutron diffraction and transmission

electron microscopy. Mechanical properties were tested using hardness, tensile and impact testing. The alloys were tested for wear under pure sliding conditions. The techniques used to produce and test the alloys will be discussed in the following section.

Table 14. Experimental matrix for the design a carbide-free bainitic alloy composition and heat treatment for forged rail wheel application

Alloy Series (Pages)	Aim	Alloys	Composition, wt%													Experimental work
			C	Si	Mn	Cr	Mo	B	V	Al	Cu	Ni	S	P	Ti	
Alloys 1 - 8 (pp 89-94)	▪ Study the effects of alloying elements on the TTT diagram of some high silicon alloys	1-8	0.08-0.3	0-2	1-3	0.5-2.0	0.2-0.5	0.005	0.20	0-0.2	0-1	0-0.5	-	-	-	▪ MUCG83 software to draw TTT diagrams and find T'0 curve, Ms, Bs, %bainite
Series 1 Alloys A-D (114-133)	▪ Produce Carbide-free Bainite ▪ Study the transformation of carbide-free structure using MUC83 and dilatometry ▪ Study the structure using optical and electron microscopy after isothermal heating. Continuous cooling produced complex microstructures with many phases so isothermal heat treatment was used instead.	A	0.3	1.4	1.9	0.5	0.02	0.003	0.001	0.27	0.098	0.077	0.021	0.024	0.018	▪ TTT and T'0 diagrams using MUCG83 ▪ Dilatometry to produce CCT curves according to ASTM A1033-10 ▪ Isothermal heat treatment using a salt bath ▪ Optical microscopy to study the microstructures ▪ SEM analysis of bainitic region ▪ TKD and TEM analysis of bainitic region
		B	0.25	1	1.5	0.6	0.02	0.0005	0.002	0.24	0.025	0.048	0.011	0.018	0.004	
		C	0.27	2	0.9	0.7	0	0.002	0.003	0.24	0.045	0.048	0.013	0.02	0.008	
		D	0.24	2	1.6	0.5	0.18	0.0003	0.20	0.22	0.031	0.048	0.01	0.021	0.003	
Series 2 Alloys E-H (140-159)	▪ New alloys produced similar to Alloy D ▪ Test for mechanical properties i.e. tensile testing and impact testing ▪ Study the tempering properties.	E	0.19	0.36	1.41	0.5	0.26	0.0003	0.0074	0.003	0.033	0.056	0.009	0.017	0.0001	▪ Isothermal heat treatment using a salt bath ▪ Optical microscopy to study the microstructures ▪ TKD and TEM analysis of bainitic region ▪ Tensile testing according to ASTM E8 ▪ Charpy V-Notch Impact testing according to ASTM E23 ▪ Tempering treatment in induction furnace ▪ Vickers hardness testing
		F	0.26	1.85	1.37	0.6	0.18	0.0007	0.011	0.009	0.039	0.056	0.01	0.018	0.013	
		G	0.29	1.47	1.38	0.5	0.17	0.0008	0.019	0.018	0.045	0.064	0.011	0.016	0.0008	
		H	0.28	1	1.57	0.5	0.23	0.0003	0.025	0.006	0.059	0.069	0.012	0.024	0.0008	
Series 3 Alloy I (160-176)	▪ To study the wear properties of carbide-free bainitic alloys with 2 different volume fractions of bainite	I-400 I-435	0.3	1.78	0.71	0.62	0.16	0.002	0.001	0.022			0.011	0.018		▪ Dilatometry to produce CCT curves according to ASTM A1033 – 10 ▪ Isothermal heat treatment using a salt bath at 400°C and 435°C ▪ Optical microscopy to study the microstructures ▪ Sliding wear testing ▪ Vickers hardness testing ▪ Ferritescope readings

3.1. Dilatometry Testing

Dilatometry tests were conducted on a *DIL 805 Bähr Thermo Analyser*, quench dilatometer (see Figure 85) that has the capability of heating and cooling test specimens in a vacuum or helium gas atmosphere. It also has a digital data storage and output device. The dilatometer has a programmable thermal cycle and can continuously measure the specimen temperature and dimensional changes during testing. Dimensional changes are measured along the longitudinal axis but temperature is measured at the centre of the test specimen length by a thermocouple welded to the surface of the specimen. The test specimen is heated inside an induction-heating coil.

Cylindrical samples with dimensions of 5mm diameter and 10mm length were machined and ground with 600 grit silicon carbide paper before welding the thermocouple. Each specimen was tested according to ASTM Standard A1033-10. The specimen was austenitized for 5 minutes before cooling at different cooling rates. Continuous cooling transformation diagrams were drawn according to the standard. The cooling rates were chosen to reveal the bainite region during isothermal cooling. ASTM A1033-10 recommends using 12 cooling rates for producing CCT diagrams but fewer tests were conducted in some instances due to the limitation of samples available for testing.

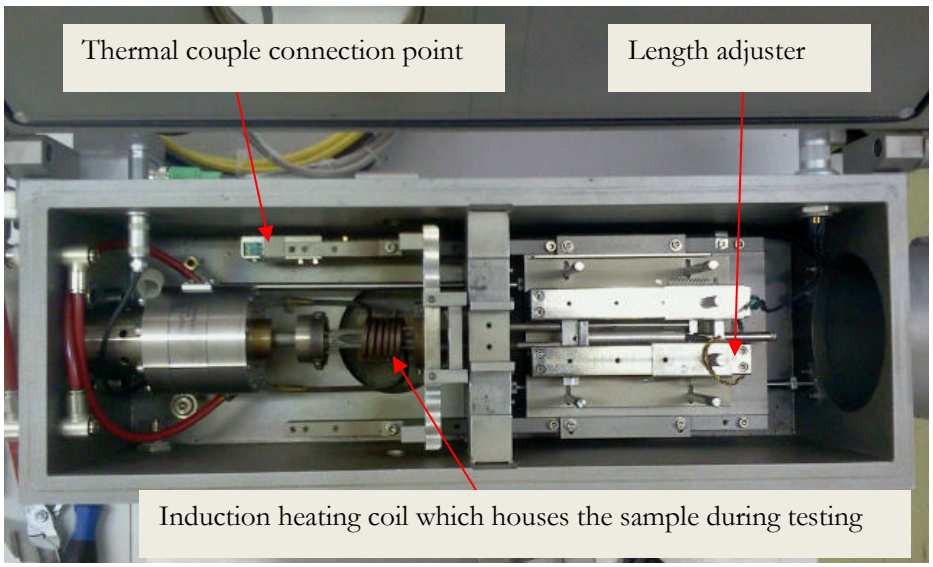

Figure 85. DIL 805 Bahr Thermo Analyser, quench dilatometer

3.2. Neutron Diffraction at the Nuclear Energy Council of South Africa (NECSA)

Samples of 5mm x 5mm x 20mm dimensions were machined and analysed at the *Nuclear Energy Council of South Africa (NECSA)*. Neutron powder diffraction measurements were performed on steel samples to enable chemical phase quantification. The neutron data was analysed using the Rietveld method (least-squares refinement of the calculated/model patterns against the measured data) in conjunction with the software package Topas 4.2, see Figure 86. Contributions from the steel phases martensite and austenite were quantified. The measurement parameters used were:

Diffractometer:	PITSI
Goniometer:	4 position sample changer. Sample rotated continuously
2θ range covered (°):	10 to 115
Detector bank step size (°):	17
Measurement time (min) per step:	10
Wavelength (Å):	1.771
Temperature during measurement:	Room temperature

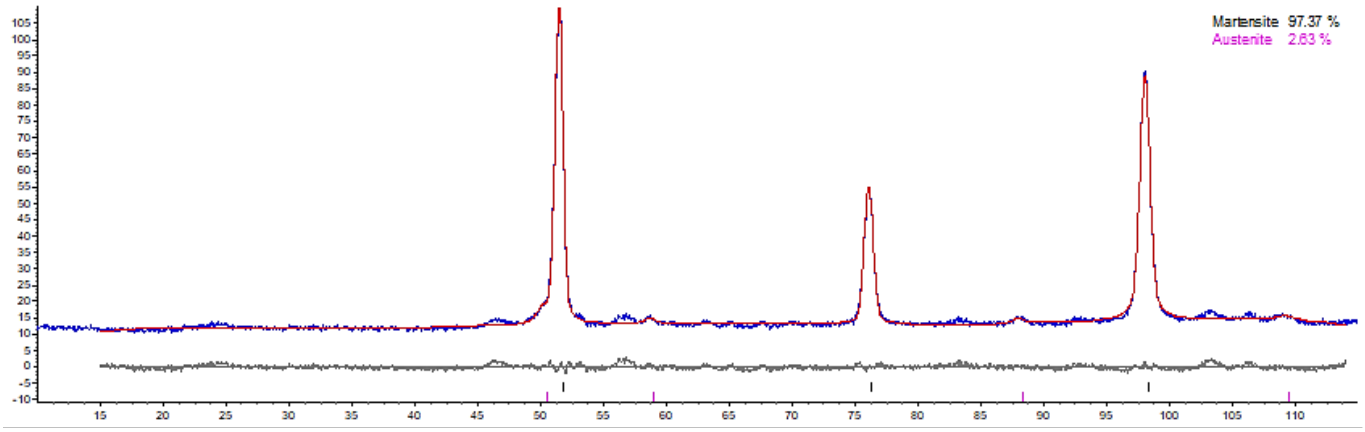

Figure 86. Neutron diffraction graph showing the peaks used to quantify the BCC and FCC phases in the test samples

3.3. Optical Microscopy

Test specimen were taken from the heat treated alloys produced, ground, polished and etched with various chemical etchants to reveal their microstructure. The specimens were analysed with an Olympus DSX510/DSX510i microscope with the ability to capture 3D imaging.

The Fischer Feritscope® MP30 was used as a non-destructive method to measure the ferrite content of the steel samples. Ferrite (bainite and martensite) is magnetic and this instrument measures the magnetism level in the steel.

ImageJ is an open source Java-based image processing programme designed for scientific multidimensional images [125**Error! Reference source not found.**]. It was used in this project to quantify the volume fraction of bainite and martensite in the microstructures.

3.4. Scanning Electron Microscopy (SEM) and EBSD

A *Nova Nano SEM200 High Resolution Scanning Electron Microscope* with a built in EBSD detector was used for analysis. Samples from the different alloys were mounted, ground and polished, up to a 1µm surface finish, and etched deeply with 2 wt% Nital before analysis.

3.5. Transmission Electron Microscopy (TEM) and Transmission Kikuchi Diffraction (TKD)

Focus ion beam scanning electron microscopy (FIBSEM) was used to prepare electron transparent (5x5 µm) lamella for STEM and TKD analysis at the Electron Microscopy Unit at the Nelson Mandela University. Selected area diffraction (SAD) analysis using hollow cone imaging was used to distinguish the different phases in the alloys and the SAD patterns were indexed using JEMS software. Plate thickness measurements were made directly on the TEM micrographs and three measurements were taken per micrograph to establish the plate thickness.

TKD is a method where an electron transparent lamella is analysed using EBSD in the SEM at an angle of 20°. Each phase is coloured differently by this method, depending on its structure, i.e. body centred cubic (BCC) or face centred cubic (FCC). The Transmission Kikuchi Diffraction (tEBSD) is performed on the thin TEM sample,

therefore the interaction volume is roughly a 10x10nm area through the foil thickness. In a bulk EBSD scan this would be roughly 100x100nm in size. No cleaning of the data was made after analysis.

3.6. Tensile Testing

An *Instron 1342 Tensile Tester* was used to tensile test the alloys. Tensile test pieces were prepared in accordance with requirements of ASTM E8. The samples were round and a gauge diameter of 4mm and a gauge length of 16mm.

3.7. Impact Testing

Standard Charpy Impact Test specimens of dimensions 55x10x10mm having a V-notch: 2mm deep, with 45° angle and 0.25mm radius were prepared and tested in accordance with the requirements of ASTM E23. The samples were tested using a *Tinius Olsen* Charpy impact tester at temperatures between -100°C and 200°C in triplicates.

3.8. Dry Sliding Wear Testing

A tribometer was built at the University of Pretoria to test pin and wheel samples for wear in sliding conditions, see Figure 87. For pure sliding conditions, a pin sample is loaded against a flat rotating disc specimen (counterface) such that a circular wear path is carved on the counterface. Different masses are hung on the pin sample carrier to increase the loading on the pin. The kind assistance of Emeritus Professor Gerrit van Rooyen in the design and manufacture of this apparatus is highly appreciated.

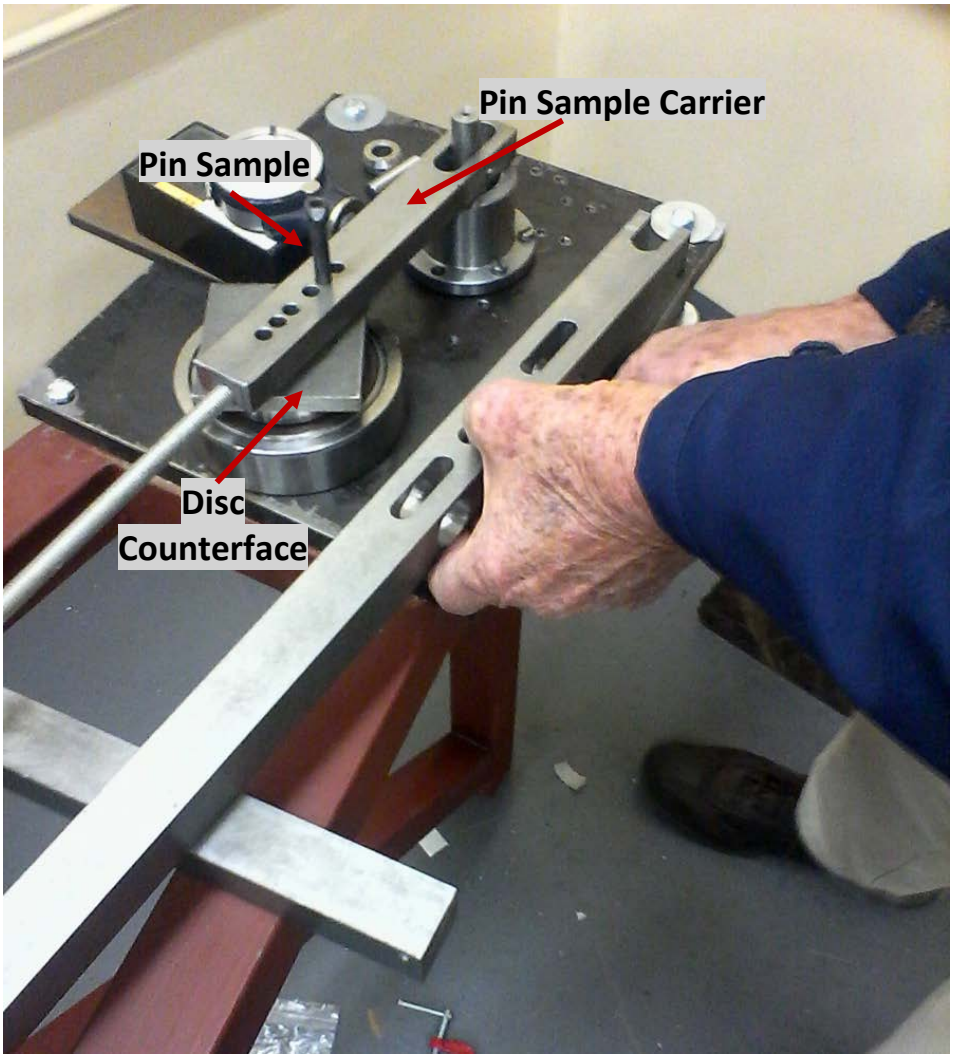

Figure 87. Wear test rig built at the University of Pretoria to test for pure sliding and pure rolling wear

4. Results

4.1. Thermodynamic and Kinetic Analysis of High Silicon Alloys Using MUCG38 Software: The Effect of Alloying Elements on the TTT Curve of High Silicon Alloys

Carbide-free bainite is produced using typical alloying elements, such as carbon (C), manganese (Mn), chromium (Cr) and nickel (Ni). To attain a carbide-free bainitic microstructure a large addition of silicon ≥1 wt% is required. Generally silicon is added as a deoxidiser to the steel melt due to its high affinity for oxygen, which is then removed from the molten metal. Semi-killed steel has a maximum silicon addition of ~0.1wt% whereas fully-killed steel has a maximum silicon addition of ~0.6wt%. In general however commonly produced steels have a low silicon addition of 0.15wt%-0.35wt%.

A number of alloy compositions, as shown in Table 15, were selected to determine the effect of carbon (C), silicon (Si), manganese (Mn), chromium (Cr) and molybdenum (Mo) on their TTT curves.

Table 15. Experimental alloys chosen to study the effect of alloying elements on the TTT curve, using the MUCG83 programme

Alloy	C	Si	Mn	Cr	Mo
1	0.1	2	1.5	0.5	0
2	0.2	2	1.5	0.5	0
3	0.3	2	1.5	0.5	0
4	0.3	2	1.5	0.5	0.5
5	0.3	0	1.5	0.5	0
6	0.3	2	1.5	0.5	1
7	0.3	2	3	0.5	0
8	0.3	2	1.5	1.5	0

The TTT diagrams obtained from the model show an upper and lower c-curve, see Figures 88 to 92. The upper c-curve represents the diffusional transformation (formation of ferrite) and the lower c-curve represents the displacive transformation (formation of bainite). The software also gives the martensite start (M_s) and bainite start (B_s) temperatures.

The increased addition of carbon (Alloys 1 to 3) shifts the upper C-curve of the TTT diagram to the right, retarding the formation of proeutectoid ferrite, see Figure 88. The bainite start temperature (B_S) is also depressed by the increased addition of carbon and the start of the bainite transformation is delayed to longer times. A longer incubation time and lower transformation temperature is thus required with a higher carbon content before bainite can form i.e. a decrease in the driving force for transformation in higher carbon alloys. Increased additions of manganese (Alloy 7), chromium (Alloy 8) and molybdenum (Alloy 4-6) show a similar effect as carbon on the TTT diagram, see Figures 89 to 91. The addition of silicon (Alloy 5), however, promotes the formation of proeutectoid ferrite, shifting the upper TTT curve to the left, see Figure 92. An increased silicon content showed no effect on the B_S temperature nor the time to transformation of the bainite reaction.

Therefore for lower temperature transformations a higher alloying element content is required. Transformation would however also occur at longer times. It is important to consider the combined effect of the alloying elements on the bainite transformation.

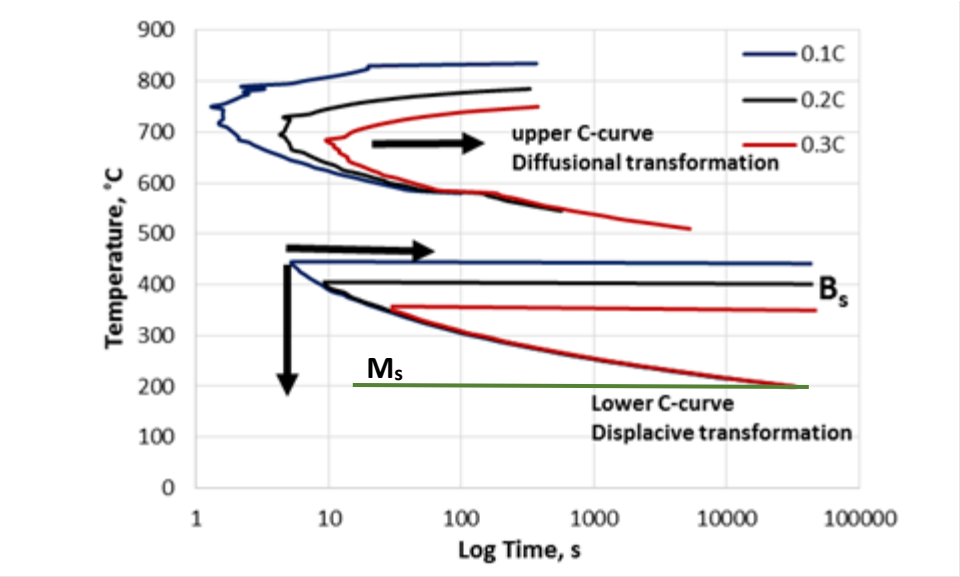

Figure 88. The effect of carbon (C) on the TTT curve of experimental alloy compositions using MUCG83

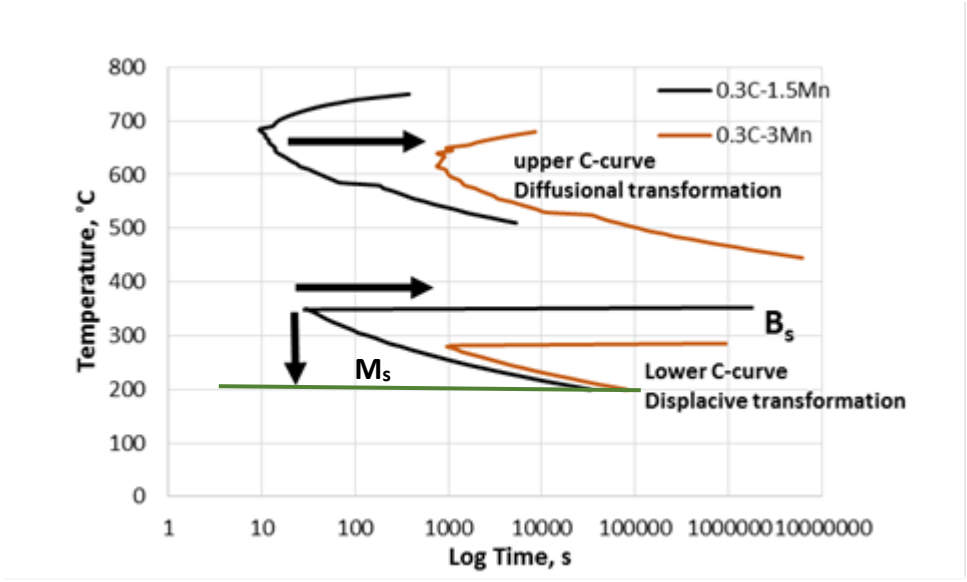

Figure 89. The effect of manganese (Mn) on the TTT curve of experimental alloy compositions using MUCG83

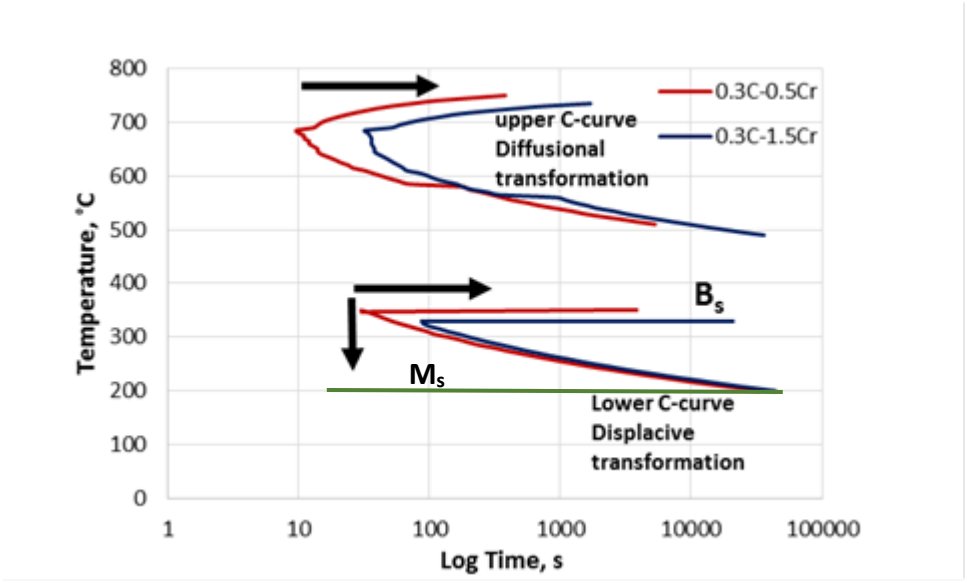

Figure 90. The effect of chromium (Cr) on the TTT curve of experimental alloy compositions using MUCG83

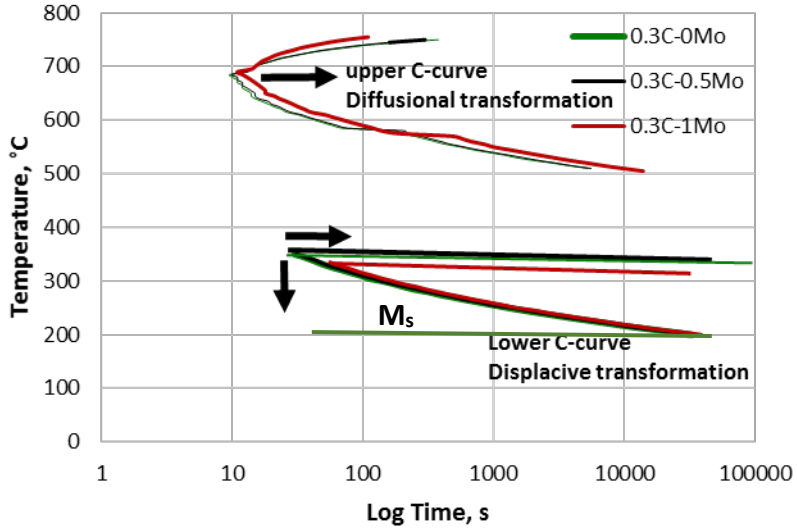

Figure 91. The effect of molybdenum (Mo) on the TTT curve of experimental alloy compositions using MUCG83

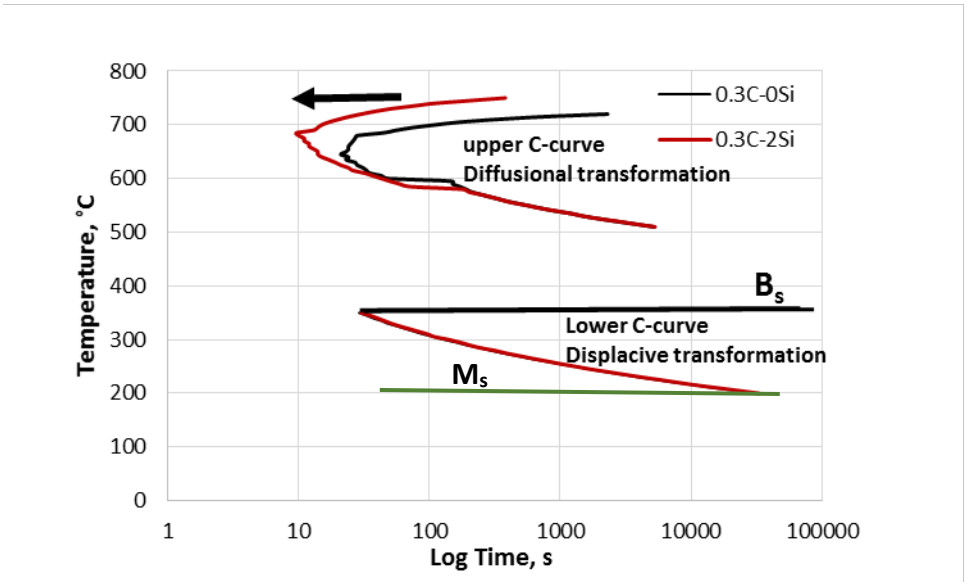

Figure 92. The effect of silicon (Si) on the TTT curve of experimental alloy compositions using MUCG83

4.1.1. The Effect of Alloying Elements on the T'_0 Curve of High Silicon Alloys

It is important to maximize the volume fraction of bainite in carbide-free bainitic alloys using the T'_0 concept. The T'_0, M_s and B_s values of some experimental alloys (Table 16), were calculated using the MUCG83 programme. As previously discussed, the bainite reaction stops when the austenite composition reaches that given by the T'_0 curve during isothermal heat treatment. The volume fraction of the remaining austenite

at a particular temperature after the isothermal heat treatment of the steel, is given by again below:

$$V_{\gamma}^{T} = \frac{x - x_{\alpha}}{x_{T0} - x_{\alpha}}$$

Where x is the average carbon concentration in the steel, x_{T0} is the carbon concentration of the T'$_0$ curve at that temperature, and is given by the T′$_0$ curve calculated using the MUCG83 programme, x_{α} is the carbon concentration of the ferrite, estimated to be 0.03 wt%. Mathematically to decrease the amount of retained austenite formed, and hence maximise the amount of bainite formed, the following needs to be considered:

- The average carbon content of the alloy (x) must be decreased or
- the carbon concentration of the T'$_0$ curve at that temperature (x_{T0}) must be increased

Upon cooling, if the retained austenite does not undergo stabilisation, some of this retained austenite will transform into martensite and the volume fraction of martensite formed is calculated using the derived by Koistinen and Marburger, and again shown below:

$$(1 - V_{\alpha'}) = exp\{-0.011(M_s - T)\}$$

Where $V_{\alpha'}$ = fraction of martensite, M_s = martensite start temperature of unstabilised austenite and T is the transformation temperature (°C).

If however, the retained austenite undergoes thermal stabilisation during bainite formation, the martensite start temperature (M'_s) of the stabilised austenite will be lower than that during single quenching of the steel i.e. $M'_s < M_s$. This will lead to less volume fraction of martensite formed, and more retained austenite in the final microstructure, than without such stabilisation.

For the alloys in Table 16, the transformation temperature was chosen to be ~50°C above the martensite start temperature. Figure 93 shows graphs on the effect of carbon (C), manganese (Mn), aluminium (Al), copper (Cu), nickel (Ni), vanadium (V), silicon (Si) and molybdenum (Mo) on the volume fraction of bainite formed (V_b).

The results of the bainite volume fraction support the fact that lowering the average carbon content of the alloys significantly increases the volume fraction of the bainite

formed. Increasing the additions of manganese, nickel, copper, molybdenum and chromium decreases the volume fraction of bainite formed in the alloys, whereas increasing the additions of aluminium and vanadium increases the volume fraction of bainite formed in the alloys. Notable decreases in the bainite volume fraction occurred at 1 wt% chromium and 1.5 wt% manganese and a notable increase in the bainite volume fraction occurred at 0.5 wt% aluminium. An increase in silicon showed only a small decrease in the bainite volume fraction.

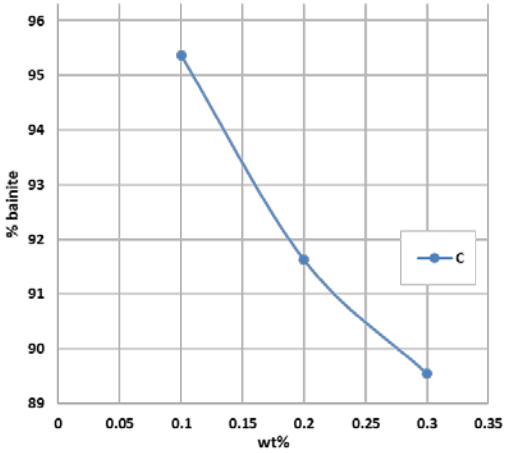

(a)

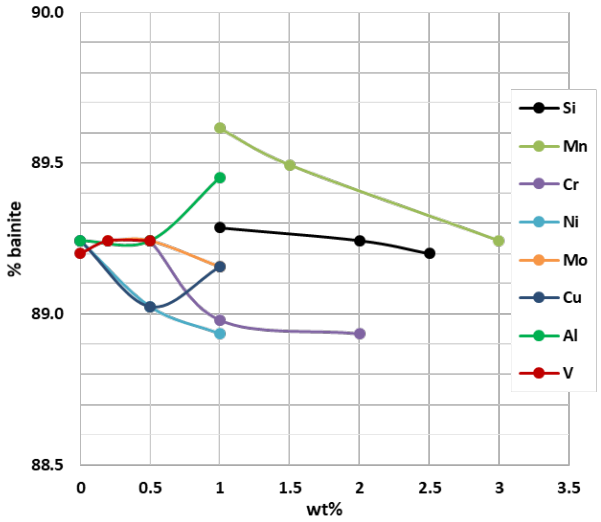

(b)

Figure 93. (a) Effect of increasing carbon and (b) manganese, chromium, silicon, molybdenum, vanadium, nickel, aluminium and copper contents on the on the bainite volume fraction according to the MUCG38 programme

Table 16. The effect of alloying elements on the bainite volume fraction

Alloy	C	si	Mn	Cr	Ni	Mo	Cu	Al	V	Ms	Bs	Ms	Bs	T'0 (mole fraction)	mole%	%RA	%bainite
1	**0.3**	2	3	0.5	0	0.2	0	0	0.2	266	427	298	427	0.0254	2.54	10.76	89.24
2	**0.1**	2	3	0.5	0	0.2	0	0	0.2	369	518	383	481	0.0145	1.45	4.93	95.07
3	**0.08**	2	3	0.5	0	0.2	0	0	0.2	378	527	391	487	0.0133	1.33	3.85	96.15
4	0.3	2	**3**	0.5	0	0.2	0	0	0.2	266	427	298	427	0.0254	2.54	10.76	89.24
5	0.3	2	**1.5**	0.5	0	0.2	0	0	0.2	339	502	344	562	0.0260	2.6	10.51	89.49
6	0.3	2	**1**	0.5	0	0.2	0	0	0.2	364	526	359	607	0.0263	2.63	10.38	89.62
7	0.3	2	3	0.5	0	0.2	0	**0**	0.2	266	427	298	427	0.0254	2.54	10.76	89.24
8	0.3	2	3	0.5	0	0.2	0	**0.5**	0.2	284	446	298	427	0.0254	2.54	10.76	89.24
9	0.3	2	3	0.5	0	0.2	0	**1**	0.2	304	466	298	427	0.0259	2.59	10.55	89.45
10	0.3	2	3	0.5	0	0.2	**0**	0	0.2	266	427	298	427	0.0254	2.54	10.76	89.24
11	0.3	2	3	0.5	0	0.2	**0.5**	0	0.2	259	420	298	427	0.0249	2.49	10.98	89.02
12	0.3	2	3	0.5	0	0.2	**1**	0	0.2	253	412	298	427	0.0252	2.52	10.84	89.16
13	0.3	2	3	0.5	**0**	0.2	0	0	0.2	266	427	298	427	0.0254	2.54	10.76	89.24
14	0.3	2	3	0.5	**0.5**	0.2	0	0	0.2	255	415	289	409	0.0249	2.49	10.98	89.02
15	0.3	2	3	0.5	**1**	0.2	0	0	0.2	245	403	280	390	0.0247	2.47	11.07	88.93
16	0.3	2	3	**0.5**	0	0.2	0	0	0.2	266	427	298	427	0.0254	2.54	10.76	89.24
17	0.3	2	3	**1**	0	0.2	0	0	0.2	253	414	292	392	0.0248	2.48	11.02	88.98
18	0.3	2	3	**2**	0	0.2	0	0	0.2	228	389	280	322	0.0247	2.47	11.07	88.93
19	0.3	2	3	0.5	0	**0.2**	0	0	0.2	266	427	298	427	0.0254	2.54	10.76	89.24
20	0.3	2	3	0.5	0	**0.5**	0	0	0.2	261	423	296	403	0.0254	2.54	10.76	89.24
21	0.3	2	3	0.5	0	**1**	0	0	0.2	254	416	292	361	0.0252	2.52	10.84	89.16
22	0.3	2	3	0.5	0	0.2	0	0	**0**	275	436	298	427	0.0253	2.53	10.80	89.20
23	0.3	2	3	0.5	0	0.2	0	0	**0.2**	266	427	298	427	0.0254	2.54	10.76	89.24
24	0.3	2	3	0.5	0	0.2	0	0	**0.5**	252	414	298	427	0.0254	2.54	10.76	89.24
25	0.3	**1**	3	0.5	0	0.2	0	0	0.2	267	427	306	427	0.0255	2.55	10.71	89.29
26	0.3	**2**	3	0.5	0	0.2	0	0	0.2	266	427	298	427	0.0254	2.54	10.76	89.24
27	0.3	**2.5**	3	0.5	0	0.2	0	0	0.2	265	427	294	427	0.0253	2.53	10.80	89.20

The carbide-free bainite alloys can be produced with common alloying elements used to produce steel i.e. carbon, manganese, chromium and molybdenum. An ideal alloy to maximise bainite volume fraction could contain a balance of these elements and contain:

- 0.1-0.3 wt% C
- 0.5-1 wt% Cr
- 1-1.5 wt% Mn
- 0.5-1 wt% Al
- 0-0.5 wt% Ni
- 0-0.5 wt% Cu
- 0-0.5 wt% Mo
- 1-2 wt% Si
- 0.2-0.5 wt% V

A number of experimental alloys A to D (Series 1) were produced based on this composition range as will be discussed in the following section.

4.2. Series 1 Alloys (Alloys A to D)

Four experimental Alloys A to D were produced with a chemical composition as indicated in Table 17. The alloys have a high silicon content to prevent carbide formation and manganese and chromium were added for hardenability. Boron was added to promote the formation of bainite but was lost during melting in Alloys B and D. As previously discussed, a minimum addition of 2ppm is required to have an effect of transformation. Molybdenum was added to Alloy D for hardenability and vanadium (V) was added for possible grain refinement. The alloy showed a high aluminium content. This was not a deliberate addition but was due to a high aluminium content in the scrap used to produce the alloys. The addition of aluminium in these quantities is not known to affect the formation of bainite negatively. No deliberate additions of copper nor titanium were made of the steel.

Table 17. Chemical composition of bainitic experimental Alloys A to D

Name	Element (wt. %)											
	C	Si	Mn	Cr	Mo	Al	B	P	V	S	Cu	Ti
Alloy A	0.30	1.4	**1.9**	0.5	-	0.30	0.0030	0.024	0.001	0.021	0.098	0.0180
Alloy B	0.25	1.0	1.5	0.6	-	0.20	0.0005	0.018	0.002	0.011	0.025	0.0043
Alloy C	0.27	2.0	0.9	0.7	-	0.20	0.0015	0.020	0.003	0.013	0.045	0.0081
Alloy D	0.24	2.0	1.6	0.5	0.18	0.20	0.0003	0.021	0.20	0.010	0.031	0.0032

4.2.1. TTT Curve of Experimental Alloys Using MUCG83 Software for Alloys A to D

MUCG83 Software was used to produce TTT curves for Alloys A to D, Figure 94. The results show that the alloy composition for Alloy A shifts the upper C-curve the furtherest to the right, than in Alloys B, C and D. This effect is probably do the higher carbon, manganese and boron additions of this alloy. Alloy A also had the lowest bainite start (B_s) temperature probably due to the higher carbon content. Alloy A shows a high hardenability allowing for bainite to be formed over a wide range of cooling rated >0.1°C/s, whilst still avoiding the ferrite curve.

Table 18 shows that B_s, M_s, the cooling rate required to avoid ferrite formation, the volume fraction of bainite ~50° above the M_s temperature and the calculated bainite volume fraction. Alloys A to D. The alloys thus should consist of a mixture of bainite and retained austenite/martensite depending on the stabilisation of the retained austenite during isothermal heat treatment.

Table 18. Bainite start (B_s), martensite start (M_s), transformation time (s) and % bainite for experimental Alloys A to D according to MUCG38

Name	B_s (°C)	M_s (°C)	Cooling rate to avoid ferrite formation
Alloy A	490	330	>0.1°C/s
Alloy B	530	370	>1°C/s
Alloy C	550	390	>100°C/s
Alloy D	530	370	>5°C/s

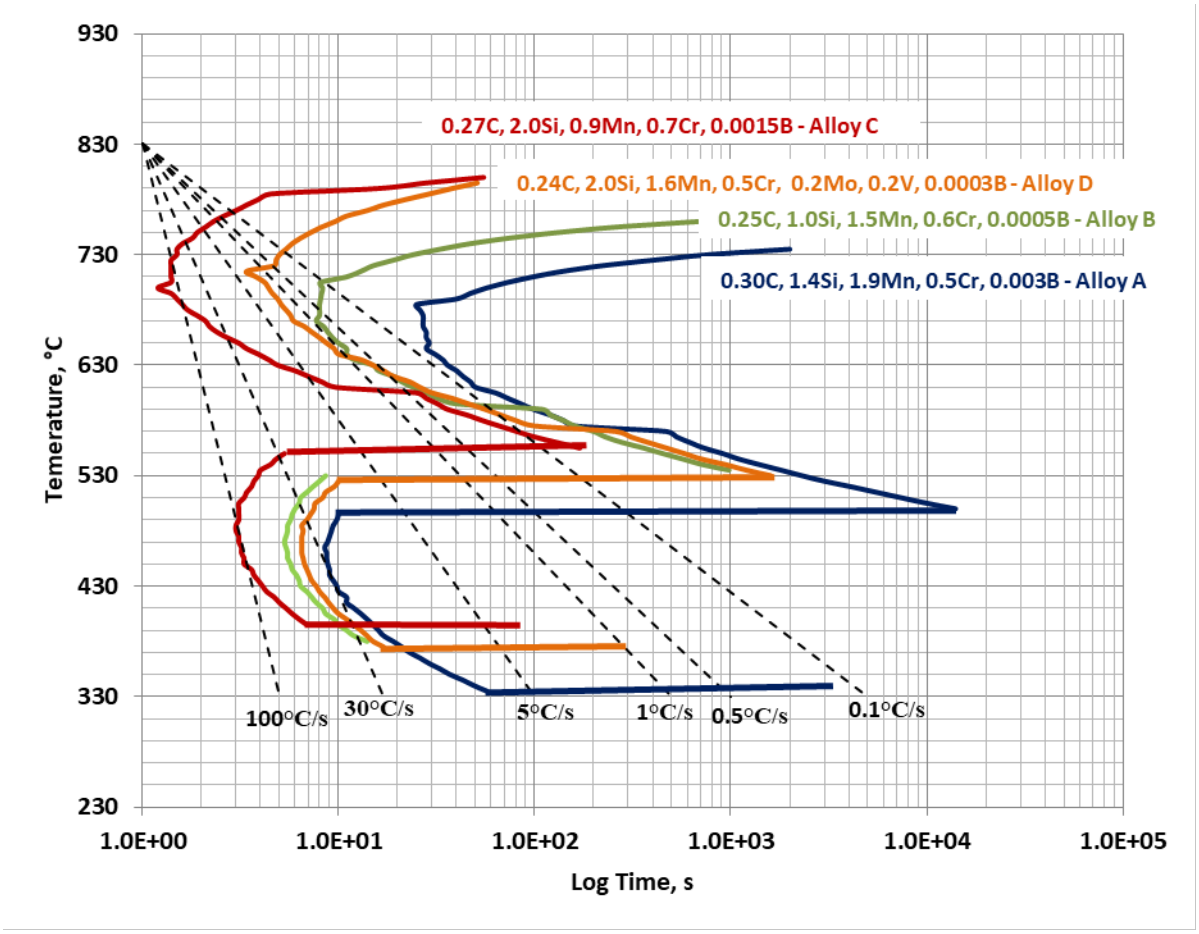

Figure 94. TTT curves for Alloys A to D determined using MUCG83 software

Figure 95 shows the T'_0 calculated for Alloys A to D, where the T'_0 curve shows the maximum carbon content of the austenite that limits the formation of bainite at any transformation temperature. The maximum carbon concentration of the austenite increases with a decrease in transformation temperature, thus a higher volume fraction of bainite can be formed if lower transformation temperatures are used. The T'_0 curve is also affected by the chemical composition. From the results it can be seen that the composition for Alloy C is predicted to have the T'_0 curve shifted to the right, i.e. higher values than Alloys B to D. For Alloy C, the formation of bainite will stop later than in the other alloys because a higher carbon concentration of the austenite is needed to halt the bainite reaction than in Alloys A, B and D. Alloy C then can achieve a higher bainite volume fraction at a given transformation temperature above the M_s. The opposite is true for Alloy A, whose T'_0 curve occurs at lower maximum carbon concentrations.

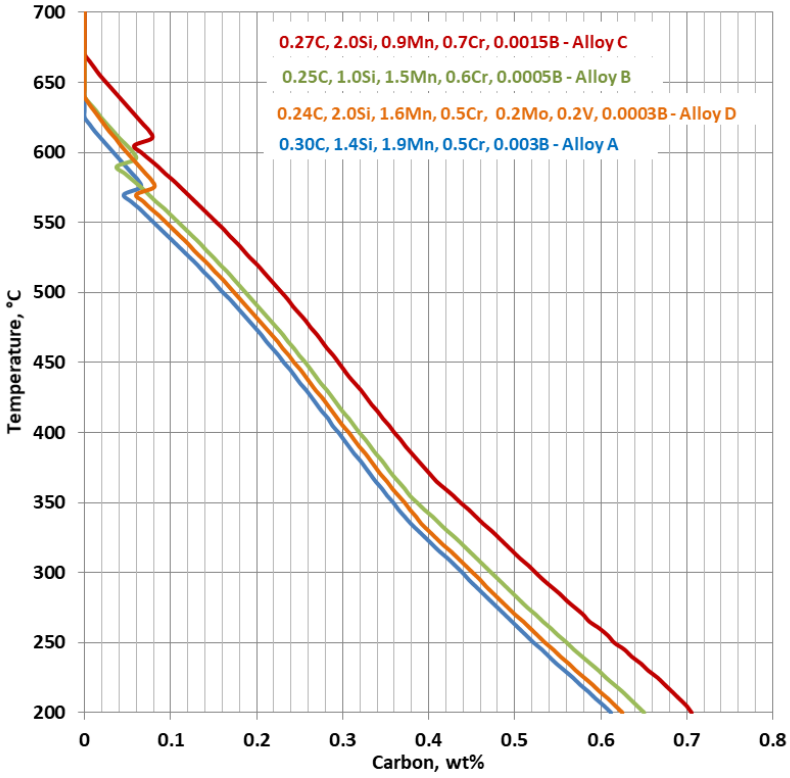

Figure 95. T'_0 curves for Alloys A to D determined using MUCG83 software

Alloy A has the highest hardenability but Alloy C shows, according to MUCG83, that it will form the highest volume fraction of bainite. Alloy C however requires very high cooling rates to avoid ferrite formation, thus Alloy A is better suited for the formation of large components, such as rail wheels, that take longer to cool after heat treatment.

4.3. **Dilatometry**

Dilatometry is technique that is used to study phase transformations in a steel during continuous cooling. Continuous cooling transformation (CCT) diagrams can be drawn with this technique as a map to show the phases to expect after heat treatment at certain cooling rates and temperatures. In this method, a steel specimen is austenitised and then cooled continuously at different rates and its transformation measured as strain. The heating and cooling of test specimens is done in a vacuum or helium gas atmosphere.

The phase transformations occurring in experimental Alloys A to D were calculated using dilatometry. The transformation temperatures were determined by drawing tangents at points where the slope of the cooling/heating curves deviate from linearity. For example, the A_{c1} and A_{c3} temperatures for Alloy D were calculated from deviations

from linearity of the heating curve, see Figure 96. The ferrite start (F_s) and ferrite finish (F_f), pearlite start (P_s), pearlite finish (P_f), martensite start (M_s) and martensite finish (M_f) and bainite start (B_s) temperatures were calculated from deviations from linearity of the cooling curve.

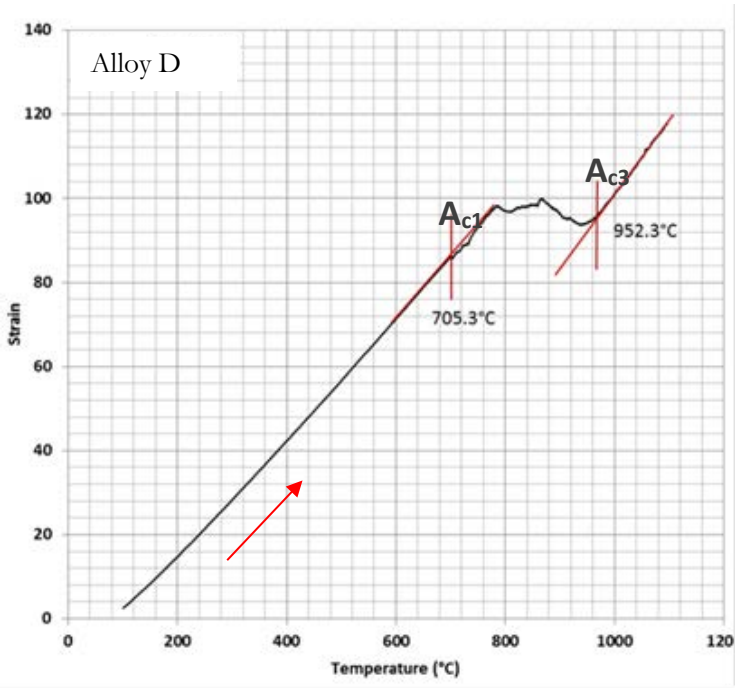

Figure 96. Heating curve for Alloy D at 0.01°C/s to determine the A_{c1} and A_{c3} temperatures

After testing, cross-sections of the dilatometry samples were etched with 2% Nital to reveal the microstructures, see Figures 97 to 101. Different microstructures were formed at the different cooling rates. The microstructures that were found in the alloys are: ferrite (**F**), pearlite (**P**), bainite (**B**) and martensite (**M**).

In Alloys A to D complex microstructures were formed with a mixture of many phases at the different cooling rates. In these alloys martensite is formed at faster cooling rates between 30°C/s and 5°C/s. At slower cooling rates generally a mixture of bainite and ferrite is found, except for Alloy D where bainite forms at very slow cooling rates <1°C/s. Alloy D also shows titanium nitrides in the microstructure formed during casting. Continuous cooling transformation diagrams were determined from the dilatometry results as will be discussed in the next section.

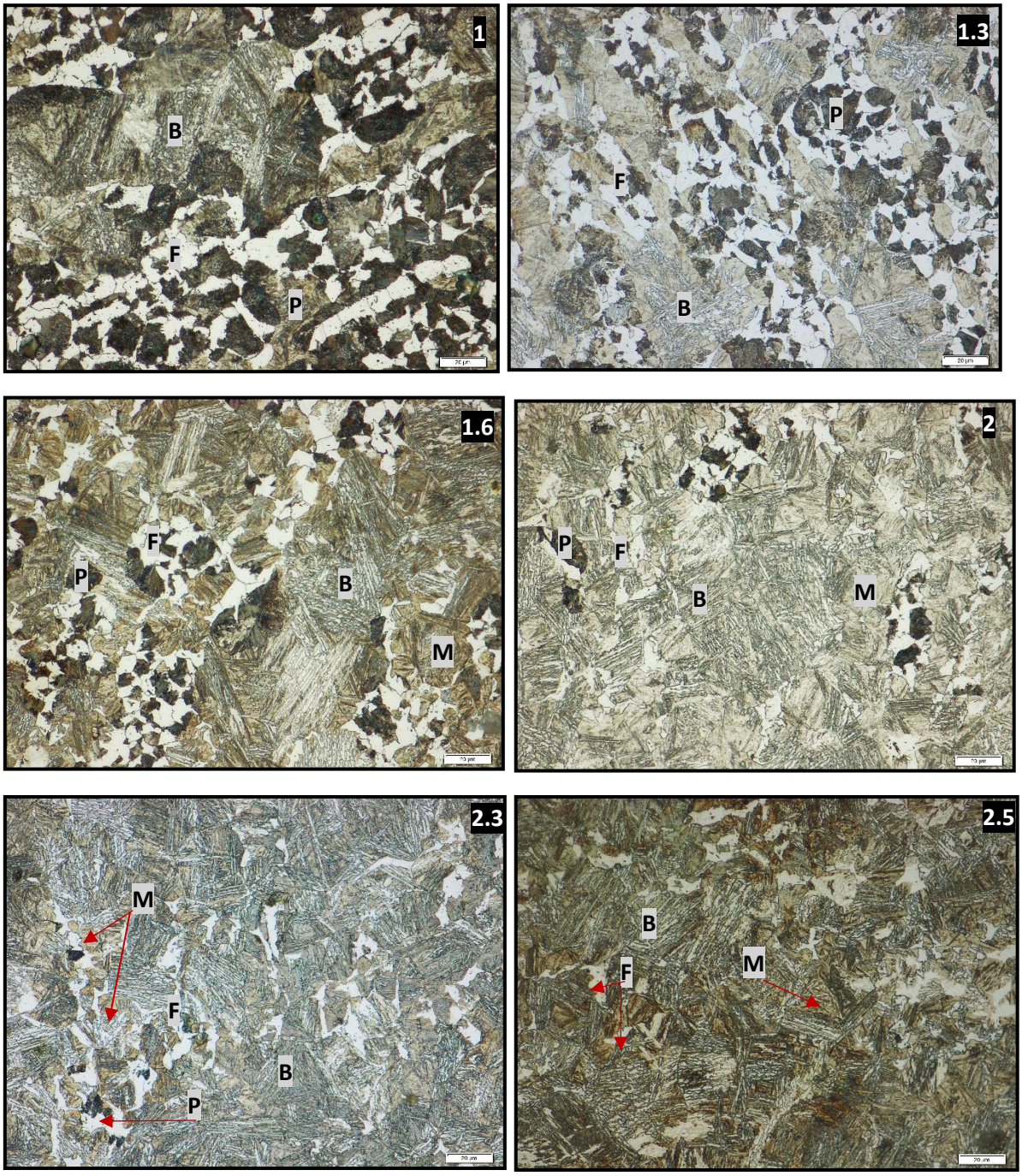

Figure 97. Micrographs for Alloy A after heat treatment in the Bahr Quench Dilatometer at cooling rates between 2.5°C/s and 1°C/s

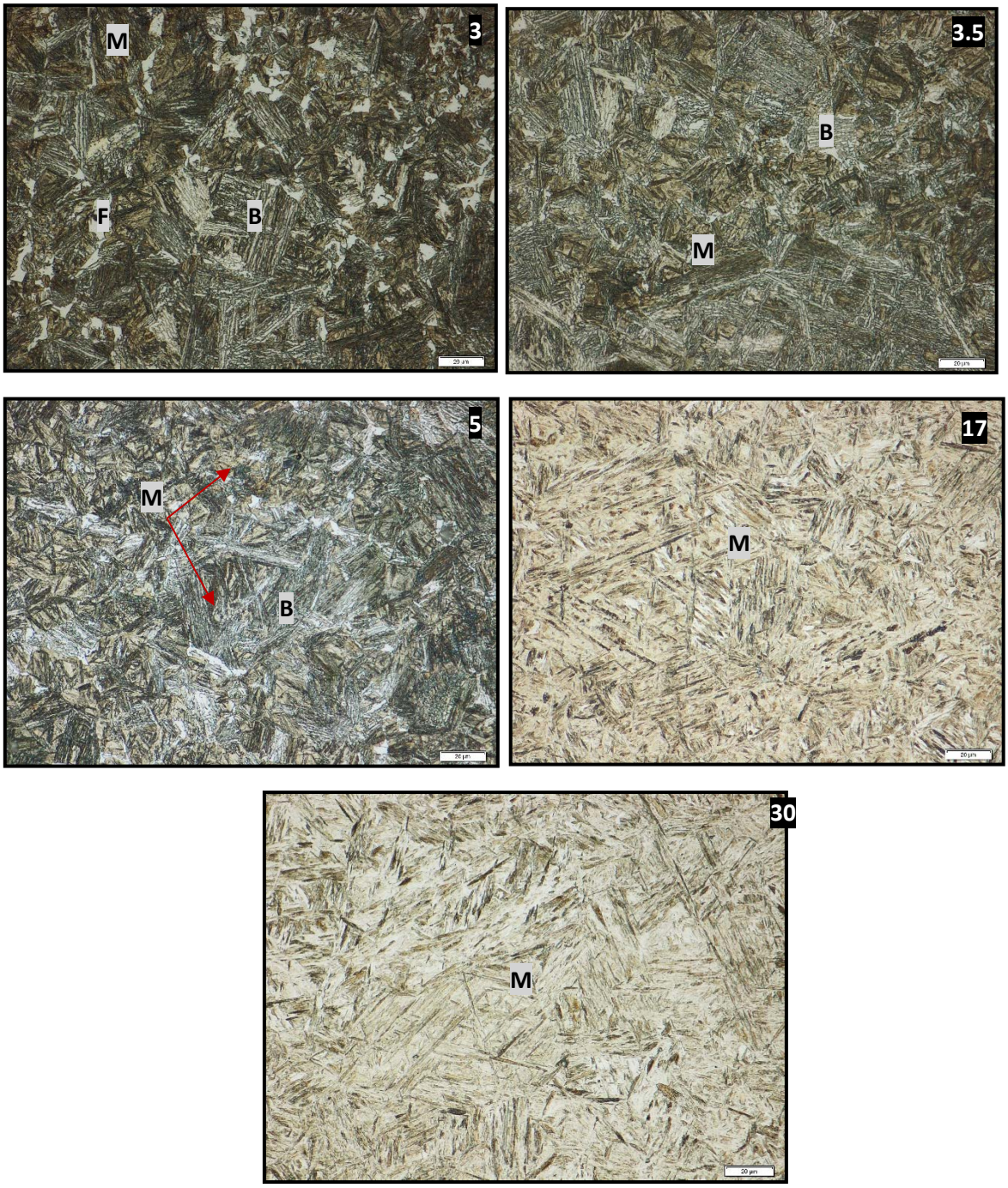

Figure 98. Micrographs for Alloy A after heat treatment in the Bahr Quench Dilatometer at cooling rates between 30°C/s and 3°C/s

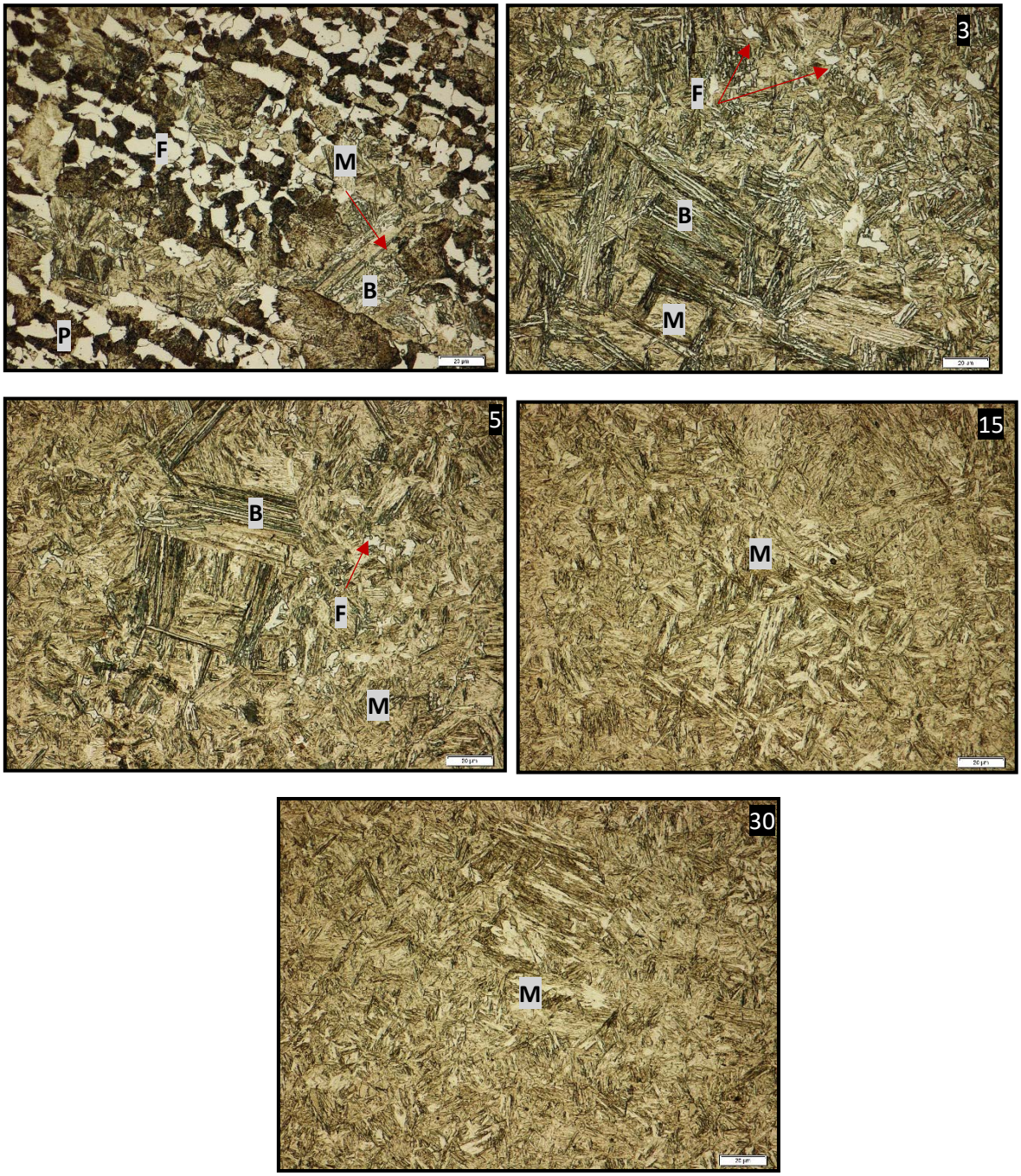

Figure 99. Micrographs for Alloy B after heat treatment in the Bahr Quench Dilatometer at cooling rates between 30°C/s and 1°C/s

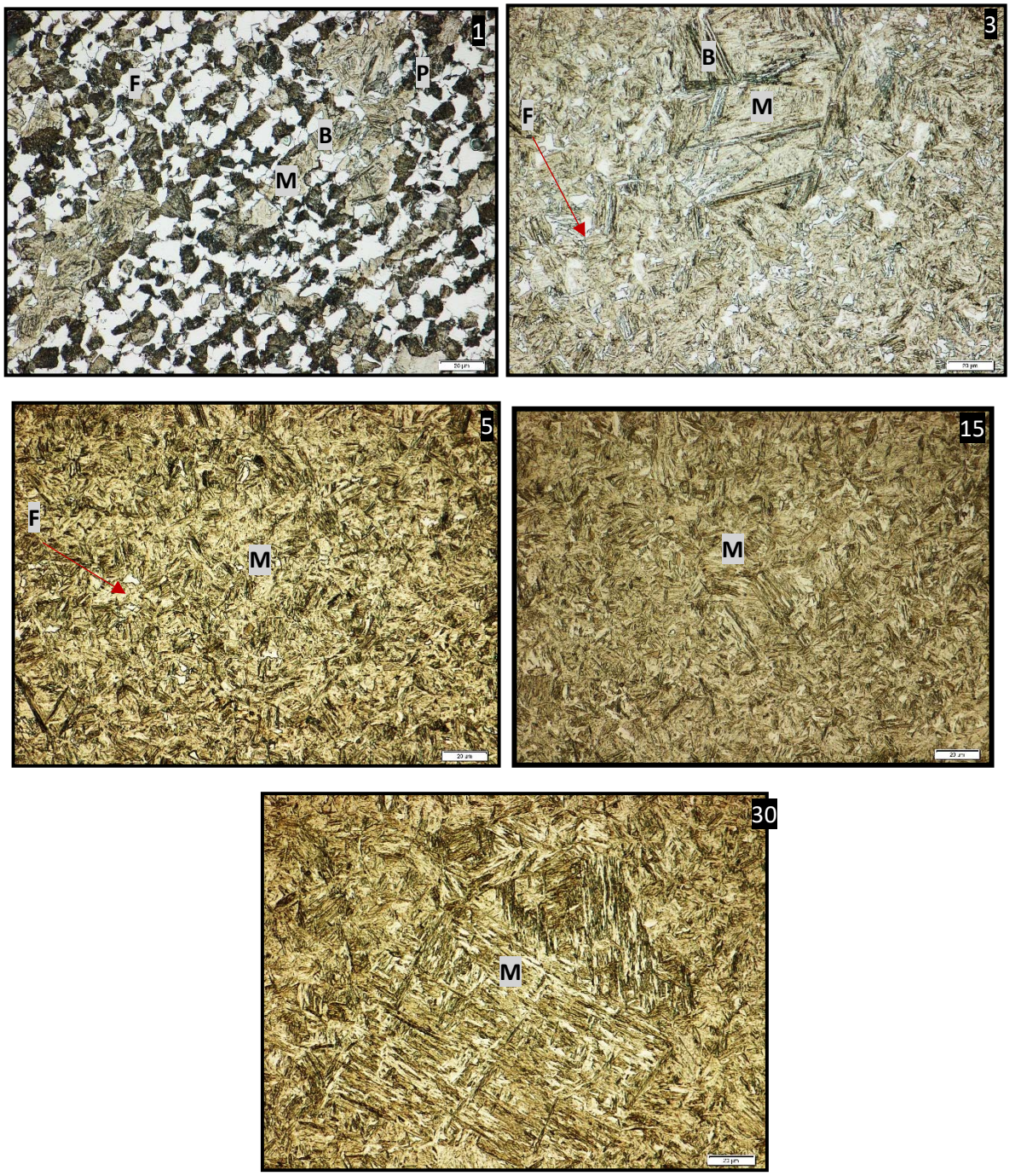

Figure 100. Micrographs for Alloy C after heat treatment in the Bahr Quench Dilatometer at cooling rates between 30°C/s and 1°C/s

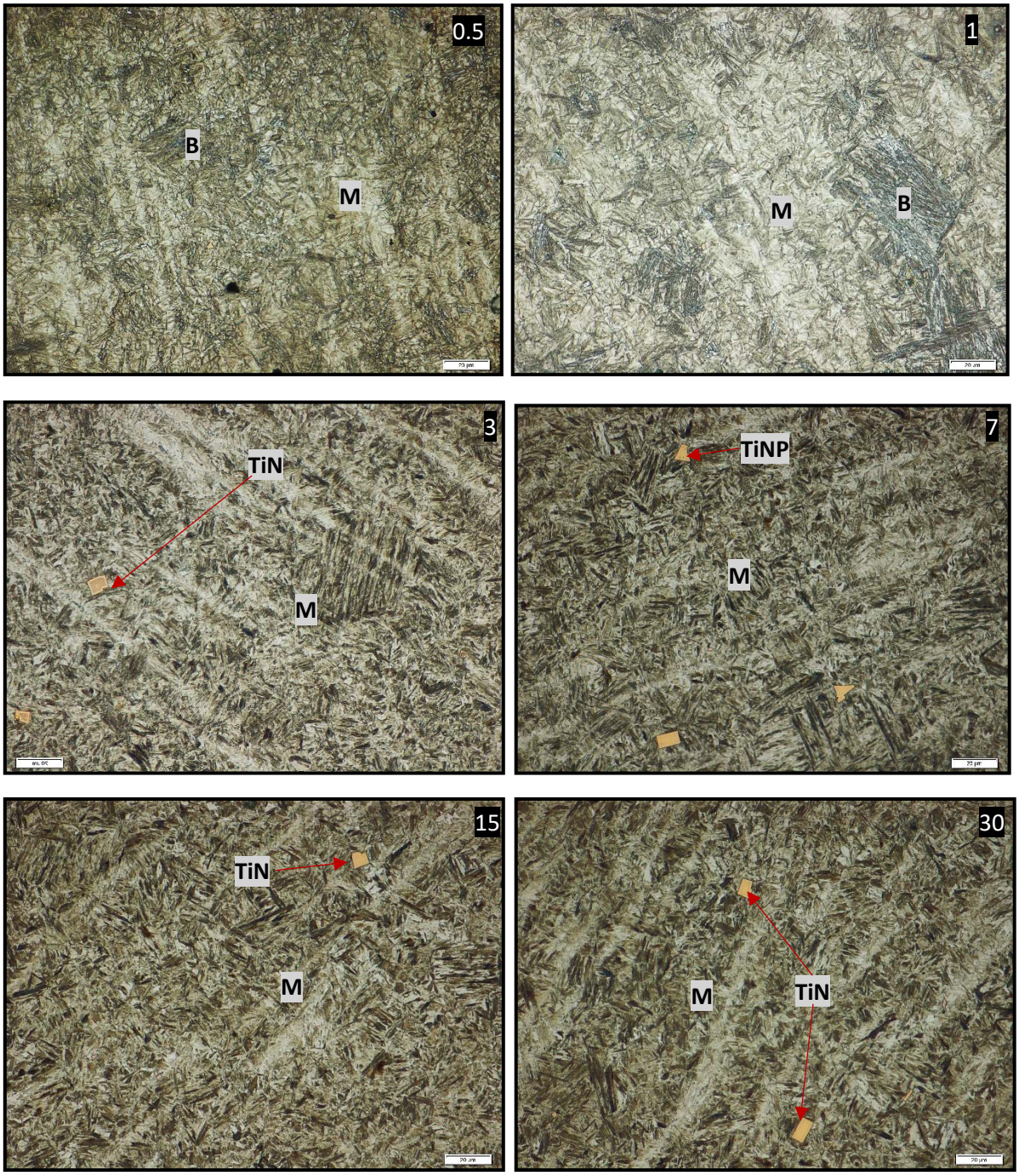

Figure 101. Micrographs for Alloy D after heat treatment in the Bahr Quench Dilatometer at cooling rates between 30°C/s and 1°C/s. The microstructure also shows titanium nitrides (TiN) precipitates.

4.3.1. Continuous Cooling Transformation (CCT) Diagrams for Experimental Alloys A to D

The continuous cooling transformation (CCT) diagrams for experimental Alloys A to D are shown in Figures 102 to 105. The CCT diagrams for Alloys A to C show three phase regions, i.e. the ferrite (F), bainite (B) and martensite (M) regions. In Alloy A the bainite region is isolated from the ferrite region at cooling rates between 5°C/s and 2.5°C/s. The ferrite region has been shifted to the right, most likely due to the additions of 0.003 wt% boron and 1.9 wt% manganese. In Alloys B and C the bainite region is shielded by the ferrite region and bainite. In Alloy D the bainite region has been shifted to the far right and is isolated. The ferrite region has also been shifted even further to the right and no ferrite was formed in the microstructure at very slow cooling rates of 0.5°C/s. Alloy D has very low boron additions, but the combined addition of 0.18 wt% molybdenum and 0.2 wt% vanadium to the steel shifted the ferrite curve to the far right, isolating the bainite curve. The CCT diagrams for Alloys A to D also shows an extensive martensitic region at faster cooling rates.

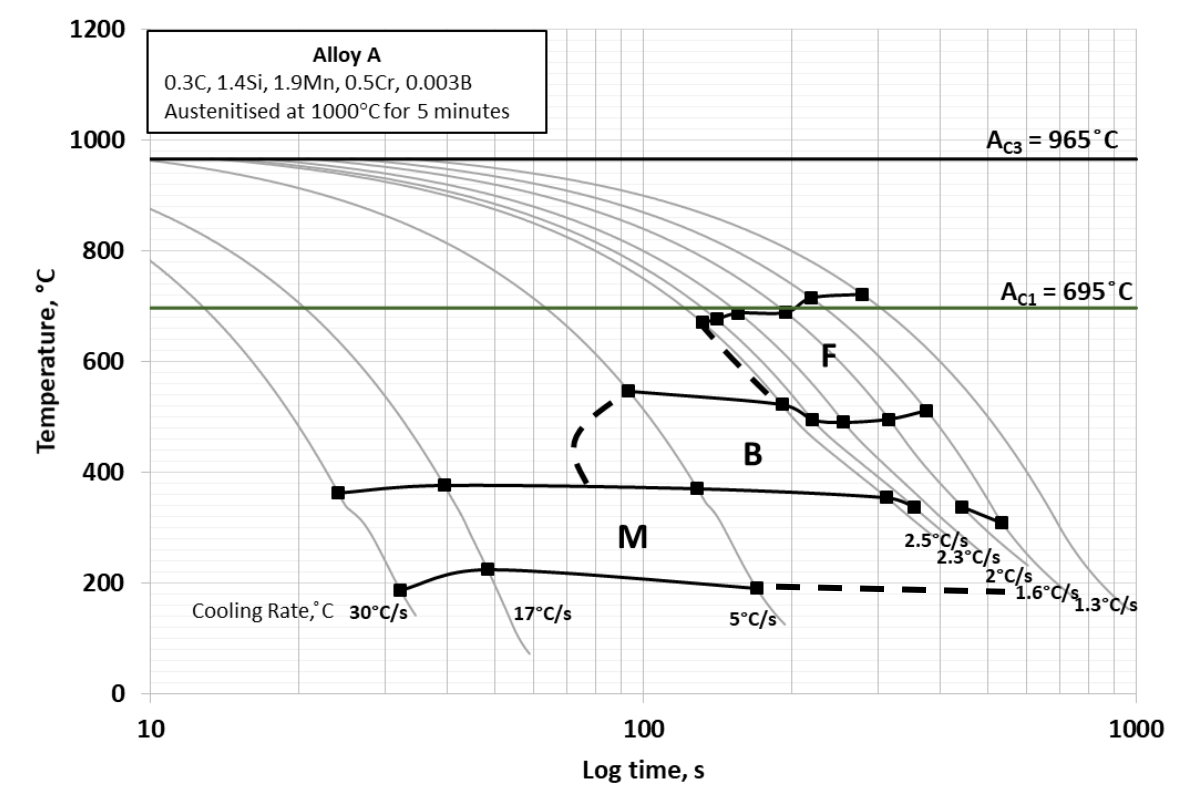

Figure 102. Partial continuous cooling transformation (CCT) diagram for Alloy A showing the martensite (M), bainite (B) and ferrite (F) regions

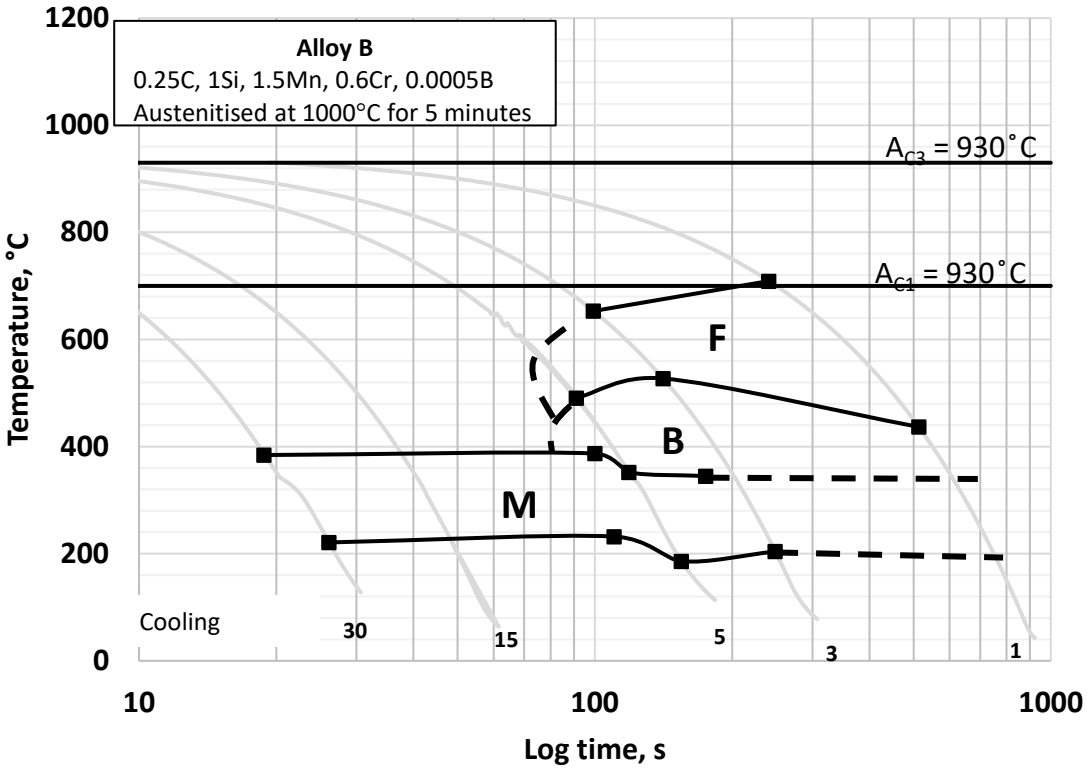

Figure 103. Partial continuous cooling transformation (CCT) diagram for Alloy B showing the martensite (M), bainite (B) and ferrite (F) regions

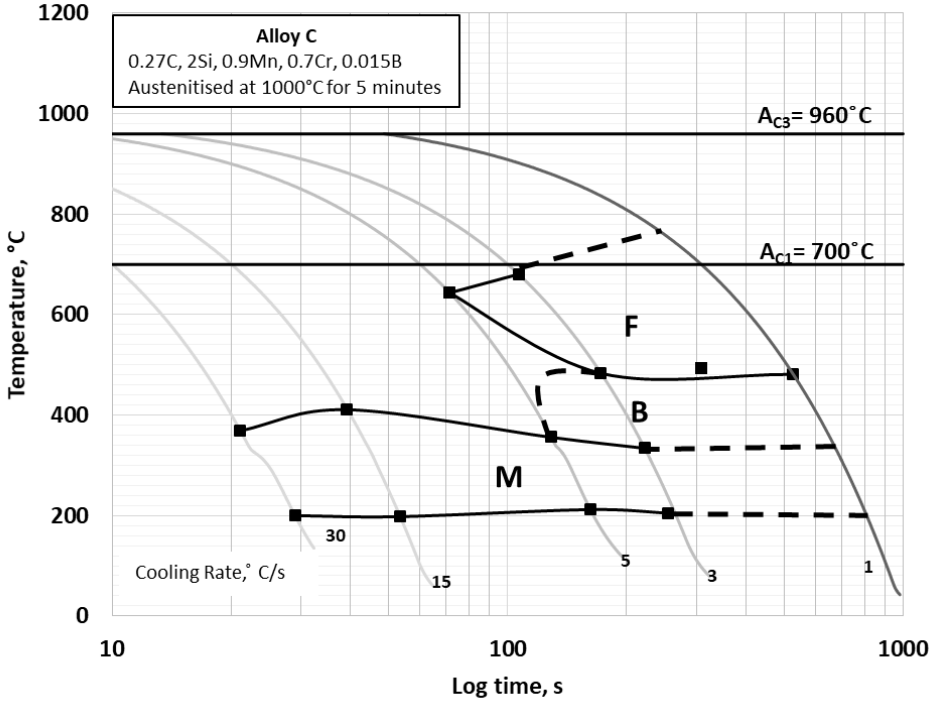

Figure 104. Partial continuous cooling transformation (CCT) diagram for Alloy C showing the martensite (M), bainite (B) and ferrite (F) regions

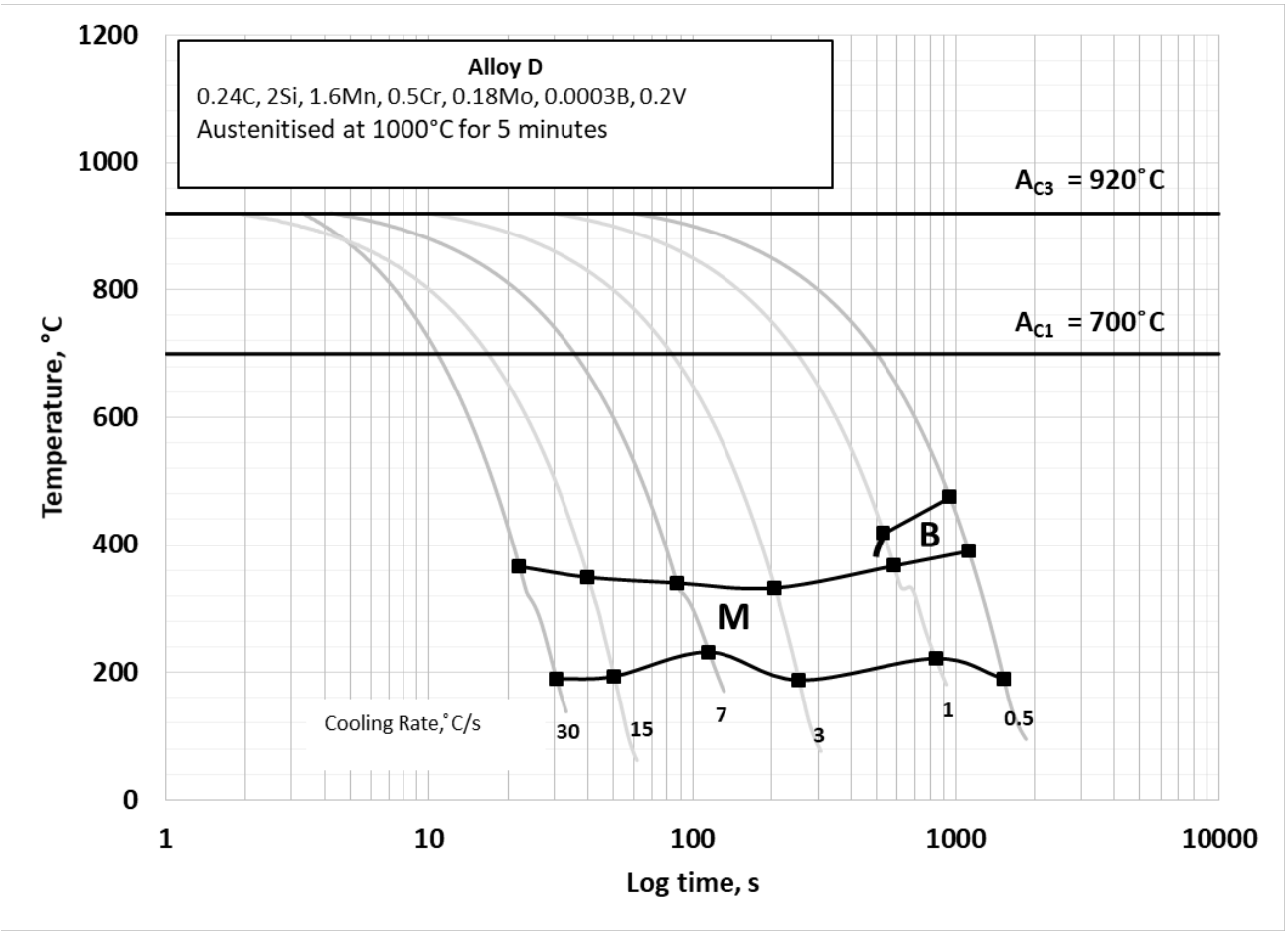

Figure 105. Partial continuous cooling transformation (CCT) diagram for Alloy D showing the martensite (M), bainite (B) and ferrite (F) regions

It was found in literature that the cooling rates experienced by the wheel rim are between 5-60°C/s, with the higher cooling rates experienced closer to the rim surface. Those experienced by the hub are slower at ~0.2C/s. Referring to the CCT diagrams of Alloys A to D, it can be seen that the microstructures given in Table 19 can be expected in the rim and hub of the alloys.

Table 19. Microstructures expected in the Rim and Hub of Alloys A to D according to the CCT results

Alloy	Rim Surface	Rim	Hub	Comment
A	M	B+M	F+P	Need a cooling rate of 2.5-5°C/s to form bainite
B	M	F+B+M	F+P	Largely martenisitic in the hub, bainite region exists shielded by ferrite region at cooling rates >5°C/s
C	M	M	F+P	Bainite region is shielded by ferrite region at cooling rates >5°C/s
D	M	M	B+M	Bainite region occurs at very slow cooling rates <1°C/s

Alloys A and D can be used to form bainite using continuous cooling but the heat treatment needs to be tailored to ensure the use of correct cooling rates. Alloys D is better suited for cooling large wheels.

4.3.1.1. CCT vs TTT diagrams

CCT diagrams can be compared to TTT diagram, even though a TTT diagram is drawn after the steel is cooled isothermally and not continuously. A CCT diagram generally shows longer transformation times and lower transformation temperatures than the TTT diagram. This is evident in Figures 106 to 109 which compares the CCT and TTT diagrams of Alloys A to D. Dilatometry and MUCG38 programme predicts the bainite and ferrite regions to be within similar temperature regions to that of the CCT diagrams (Table 20). The CCT diagrams however shows longer times for the start of the transformation. Dilatometry generally shows somewhat higher M_s and B_s value and much longer transformation start times.

Table 20. Bainite start (B_s), martensite start (M_s) and transformation time (s) for experimental Alloys A to D according to MUCG38 and dilatometry results

Name	MUCG38		Dilatometry		
	B_s (°C)	**M_s (°C)**	**B_s (°C)**	**M_s (°C)**	**Transformation temperature (°C)**
Alloy A	490	330	510	349	380±5
Alloy B	530	370	599	367	380±5
Alloy C	550	390	535	367	380±5
Alloy D	530	370	445	357	380±5

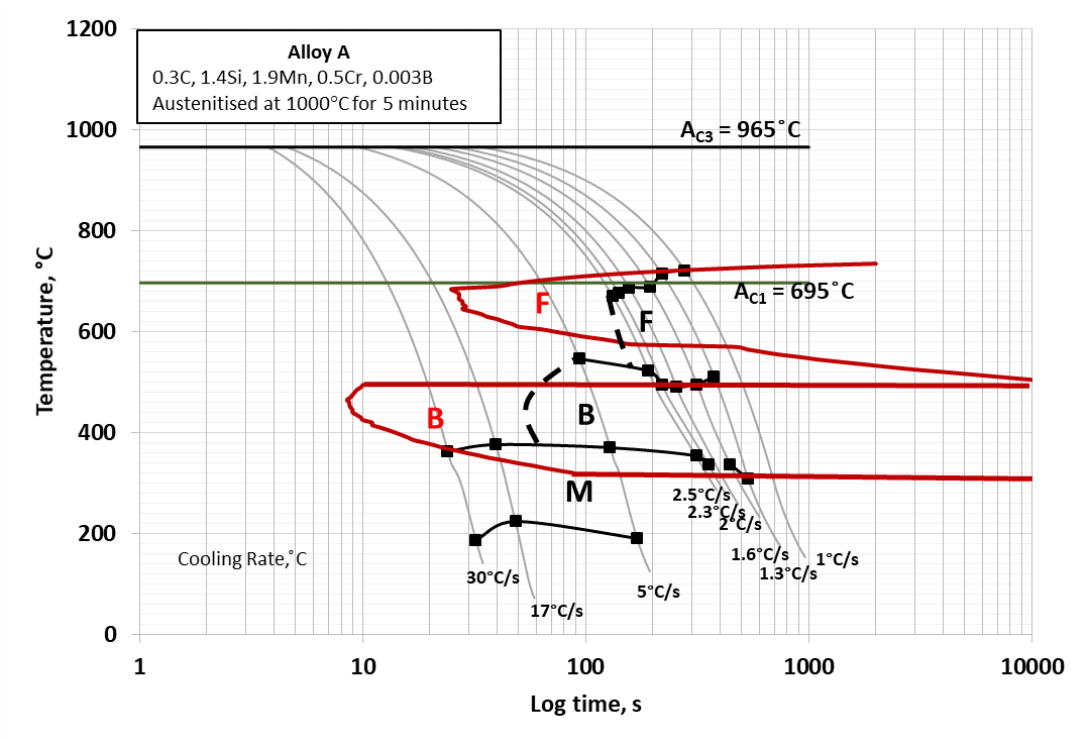

Figure 106. CCT (dilatometry) and TTT (MUCG38) diagrams for Alloy A showing the martensite (M), bainite (B) and ferrite (F) regions

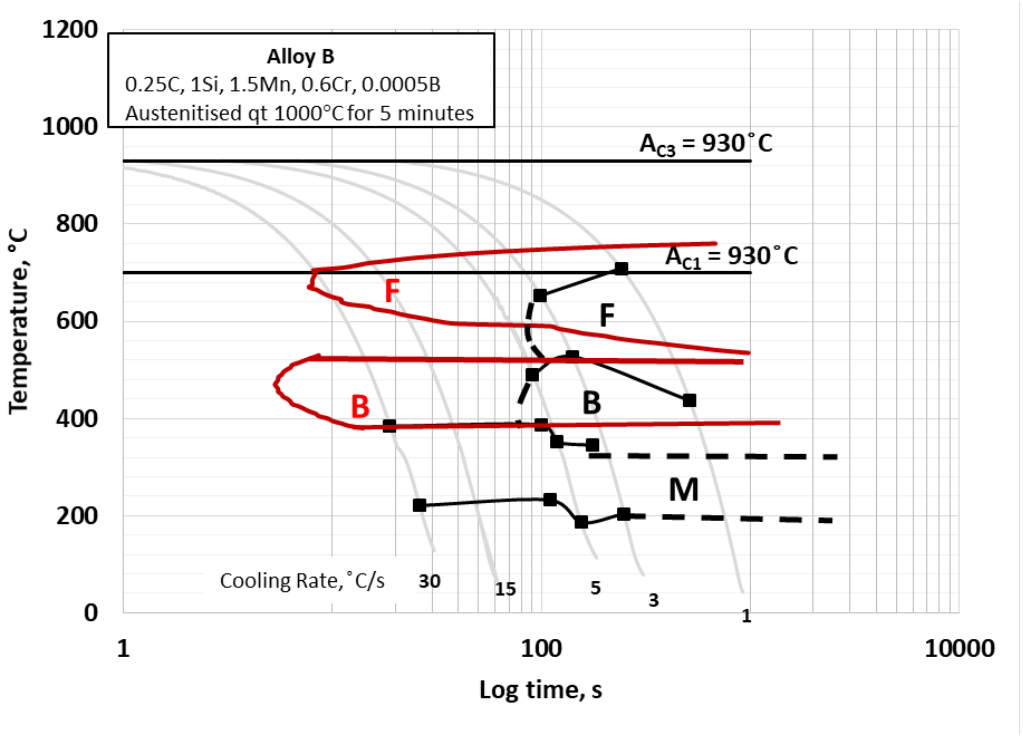

Figure 107. CCT (dilatometry) and TTT (MUCG38) diagrams for Alloy B showing the martensite (M), bainite (B) and ferrite (F) regions

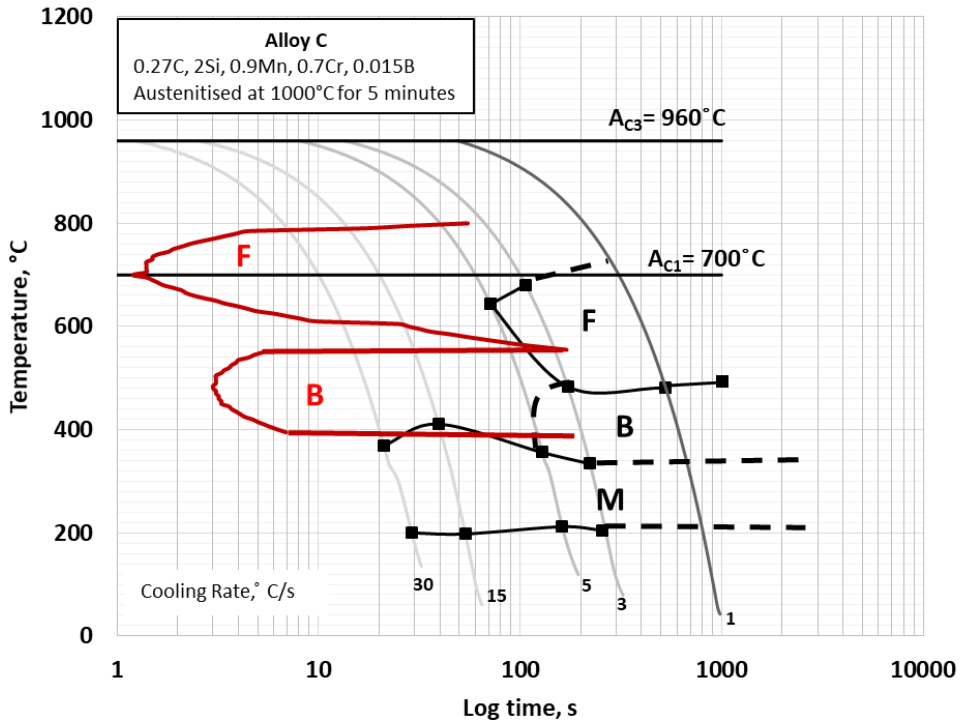

Figure 108. CCT (dilatometry) and TTT (MUCG38) diagrams for Alloy C showing the martensite (M), bainite (B) and ferrite (F) regions

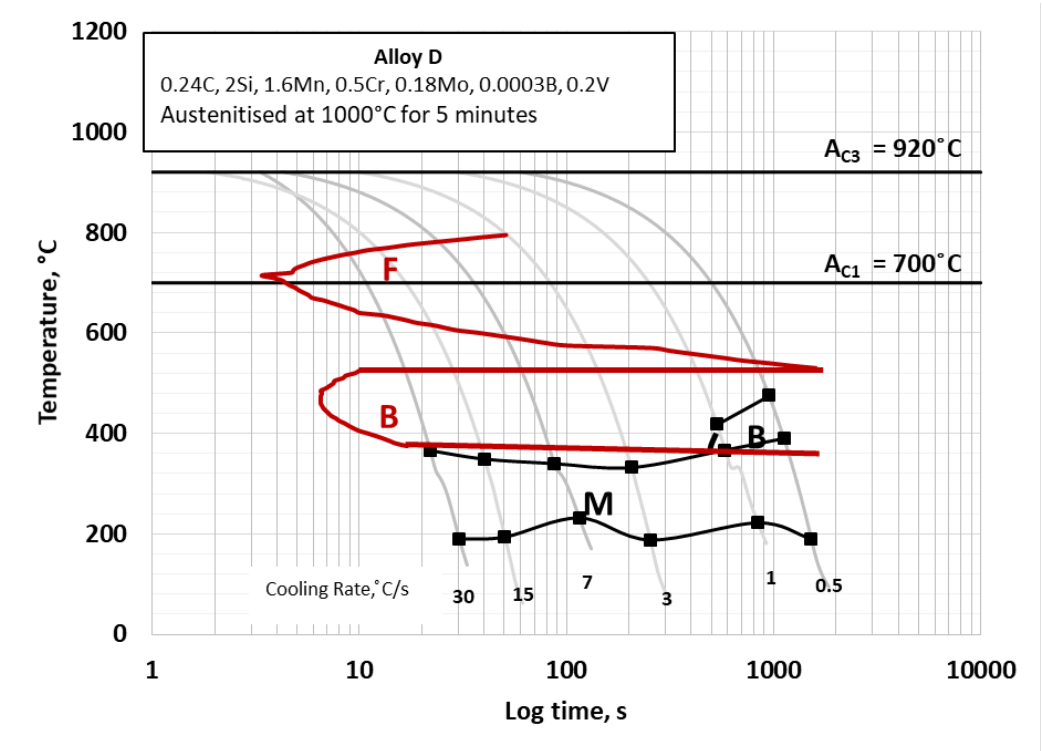

Figure 109. CCT (dilatometry) and TTT (MUCG38) diagrams for Alloy D showing the martensite (M), bainite (B) and ferrite (F) regions

4.4. Isothermal Heat Treatment to Produce Bainite in a Salt bath and Microstructural Analysis

Isothermal heat treatments were conducted on Alloys A to D within the bainitic region. Samples of Alloys A to D were austenitised at temperatures above the A_{C3} temperature in a muffle furnace and then quenched in a salt bath to 380°C for an hour. This temperature was chosen as it was just above the M_S temperature but within the bainite region.

After heat treatment the microstructures of the alloys were examined with an optical microscope and, as expected, showed a mixture of bainite (B) and martensite (M) (Figures 110 and 111). The bainite regions formed in the different alloys was further examined under the scanning electron microscope (SEM) and Figure 112 shows its typical appearance under the SEM.

It is not possible, however, to determine whether there are no carbides in the microstructure using the scanning electron microscope due to limitations in magnification. Transmission Kikuchi diffraction and transmission electron microscopy techniques were used to study the bainite further, as will be discussed in the following section.

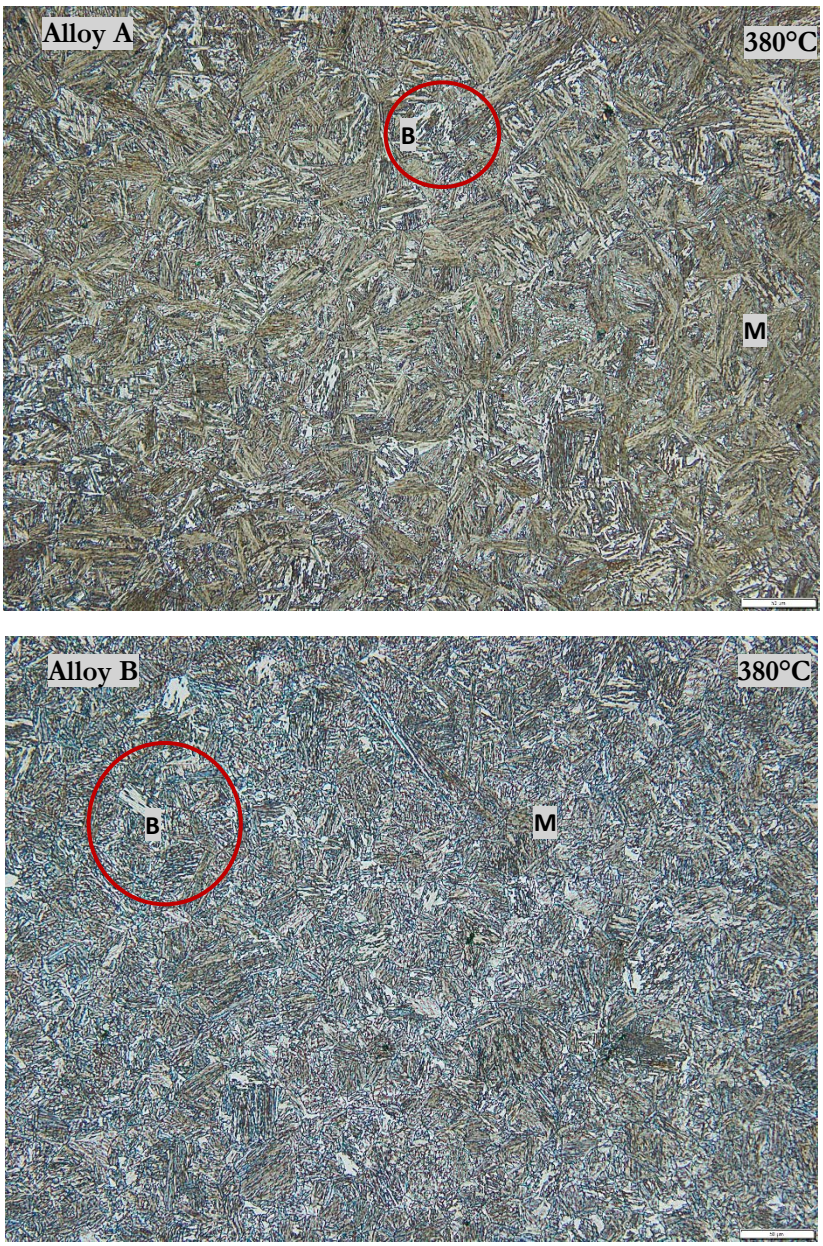

Figure 110. Microstructures of Alloys A and B isothermally heat treated in a salt bath, showing a mixture of bainite (B) and martensite (M) both heat treated at 380°C

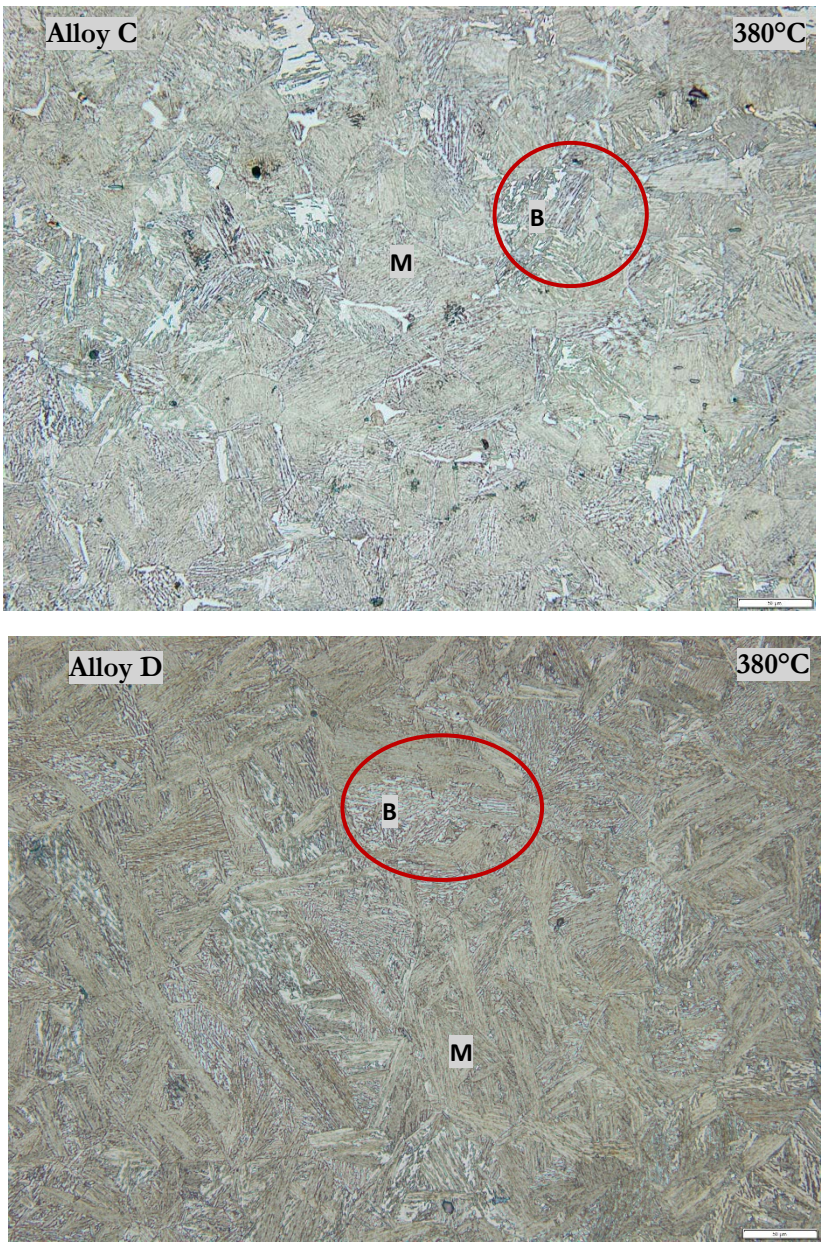

Figure 111. Microstructures of Alloys C and D isothermally heat treated in a salt bath, showing a mixture of bainite (B) and martensite (M) both heat treated at 380°C

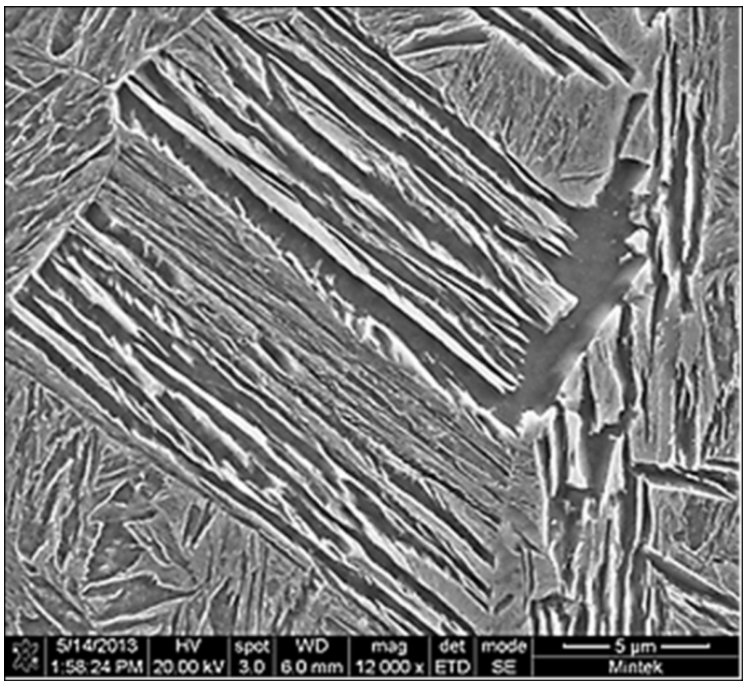

Figure 112. Scanning electron microscopy (SEM) micrograph of a bainitic region found in Alloy D showing bainite heat treated at 380°C

4.5. Transmission Kikuchi Diffractometry (TKD) and Transmission Electron Microscopy (TEM) Analysis

Samples from Alloys A and D, after heat treatment, were milled using the focused ion beam scanning electron microscope (FIBSEM) at the Nelson Mandela University. The milled samples were then studied under the transmission electron microscope (TEM) and the results are given in Figure 113 to 116. The TEM micrograph show that Alloys A to D have a plate-like structure. Alloy B showed some precipitates in the microstructure and these were identified as aluminium-rich precipitates by EDS, as shown in Figure 114. There was no evidence of carbides in the microstructure.

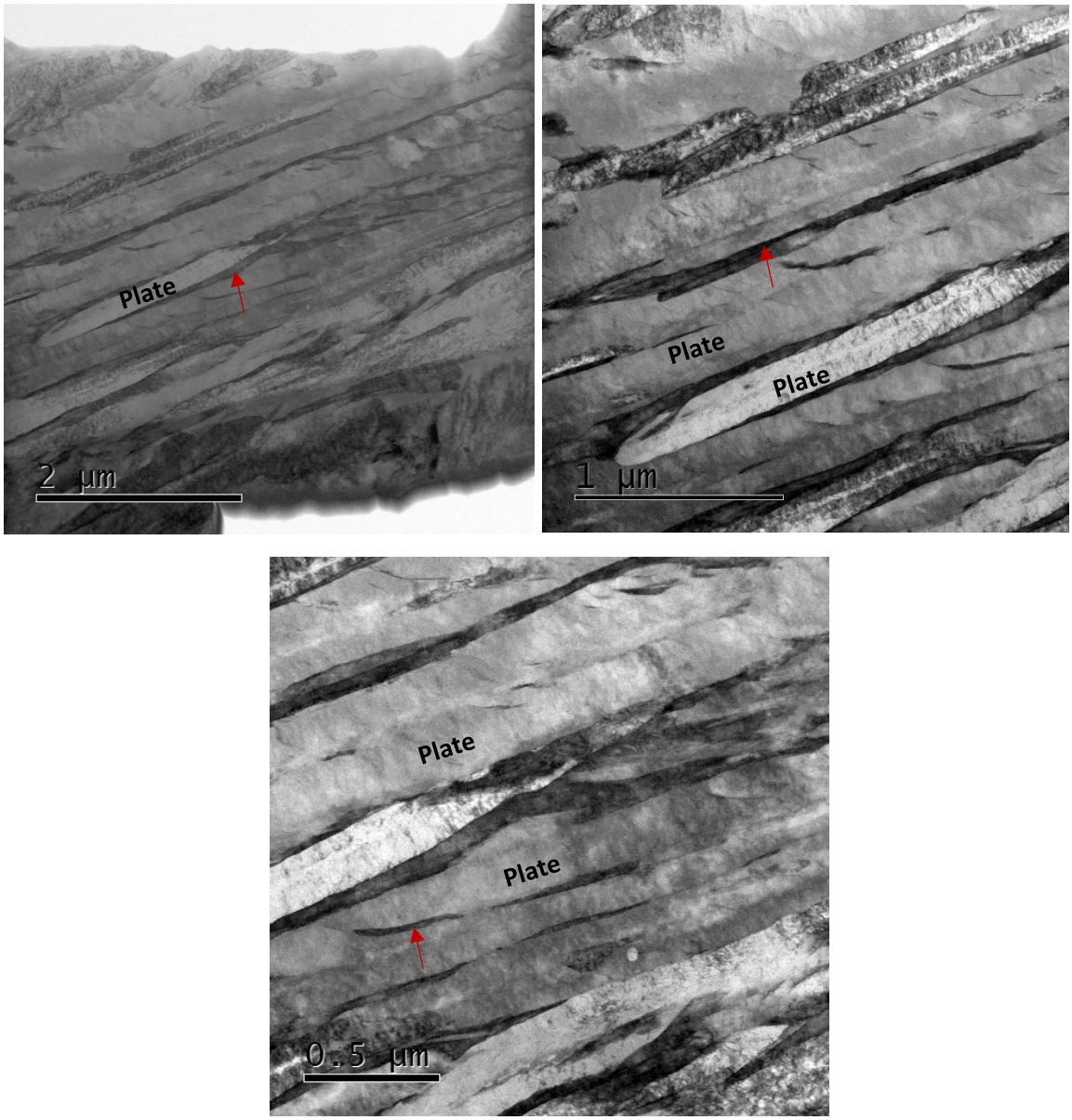

Figure 113. TEM micrographs of experimental bainitic Alloy A showing a plate like morphology of the bainitic ferrite. The alloy was heat treated at 400°C

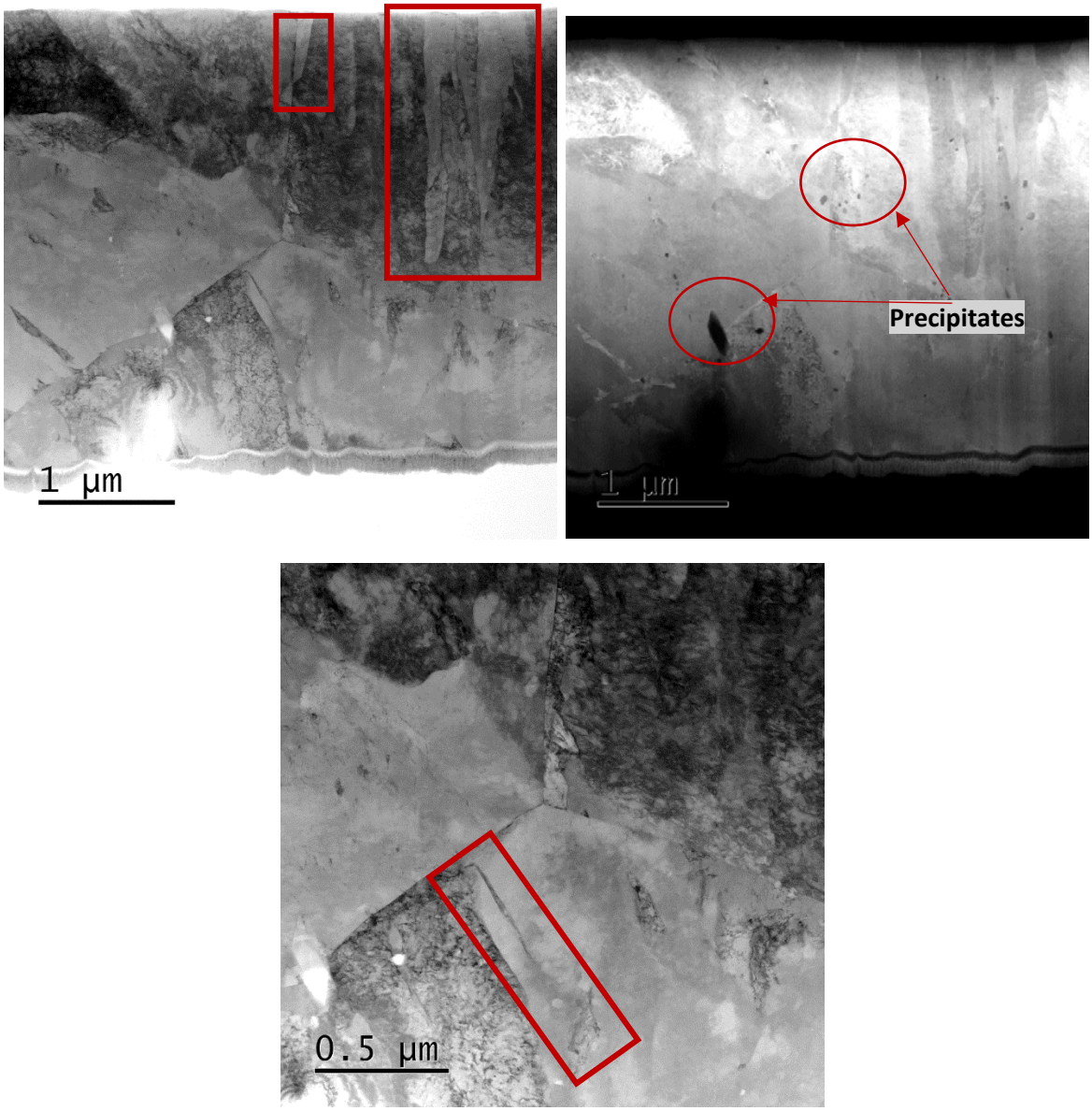

Figure 114. TEM micrographs of experimental bainitic Alloy B showing a plate-like structure, shown inside the rectangular regions, and some precipitates heat treated at 400°C

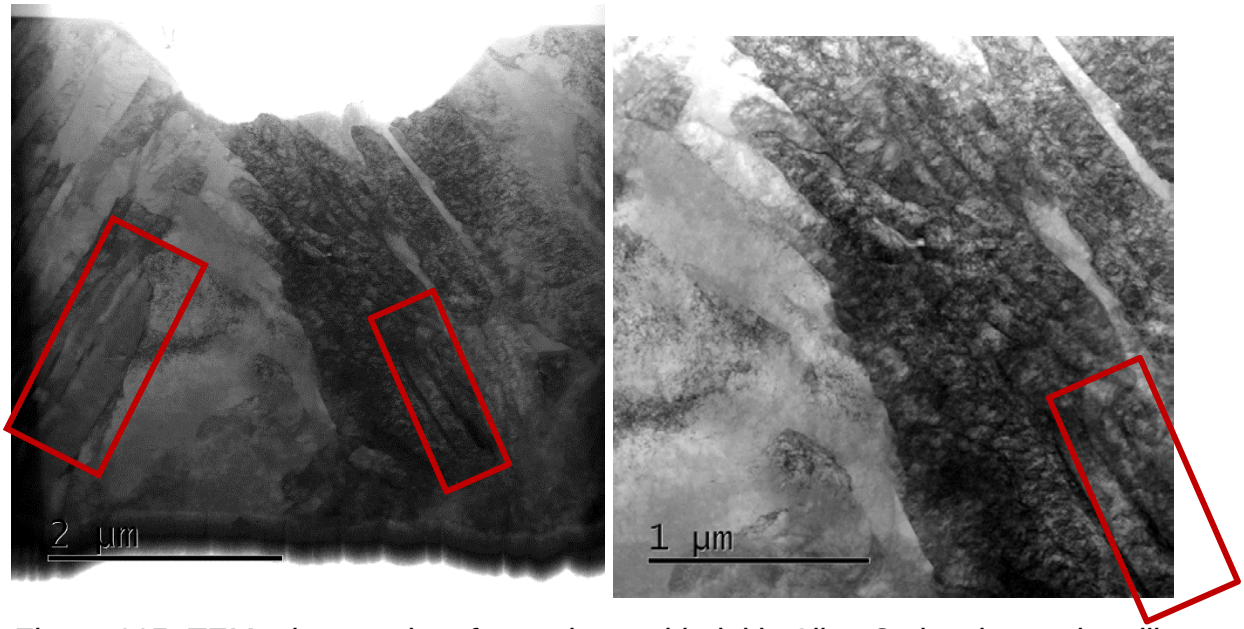

Figure 115. TEM micrographs of experimental bainitic Alloy C showing a plate-like structure inside the rectangular regions heat treated at 400°C

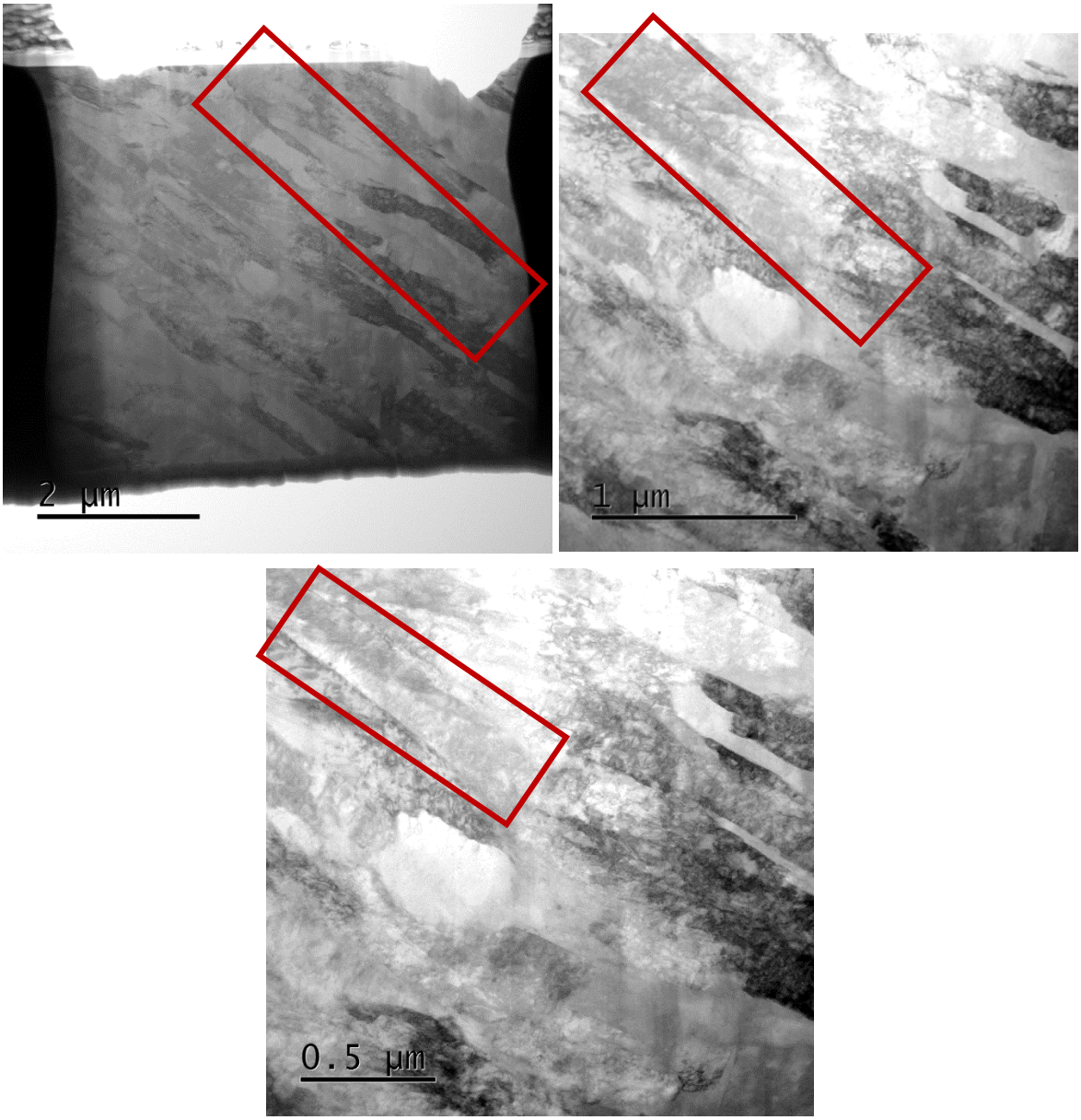

Figure 116. TEM micrographs of experimental bainitic Alloy D showing a plate-like structure inside the rectangular regions heat treated at 400°C

Figures 117 to 120 show the transmission Kikuchi diffraction (TKD) micrographs for Alloys A to D. These are obtained by examining the FIB-milled samples under the SEM using electron backscatter diffraction (EBSD). EBSD identifies the different phases in the steel based on their structures, i.e. face centred cubic (FCC) for austenite and body centred cubic (BCC) for ferrite. The results show that the blue phase is FCC-austenite and the red phase is BCC-ferrite. The microstructures of Alloys A to D are thus comprised of ferrite (bainite) with retained austenite in-between the bainite plates. Again, there was no indication of carbides in the microstructures. The TKD samples were milled from the bainite region only.

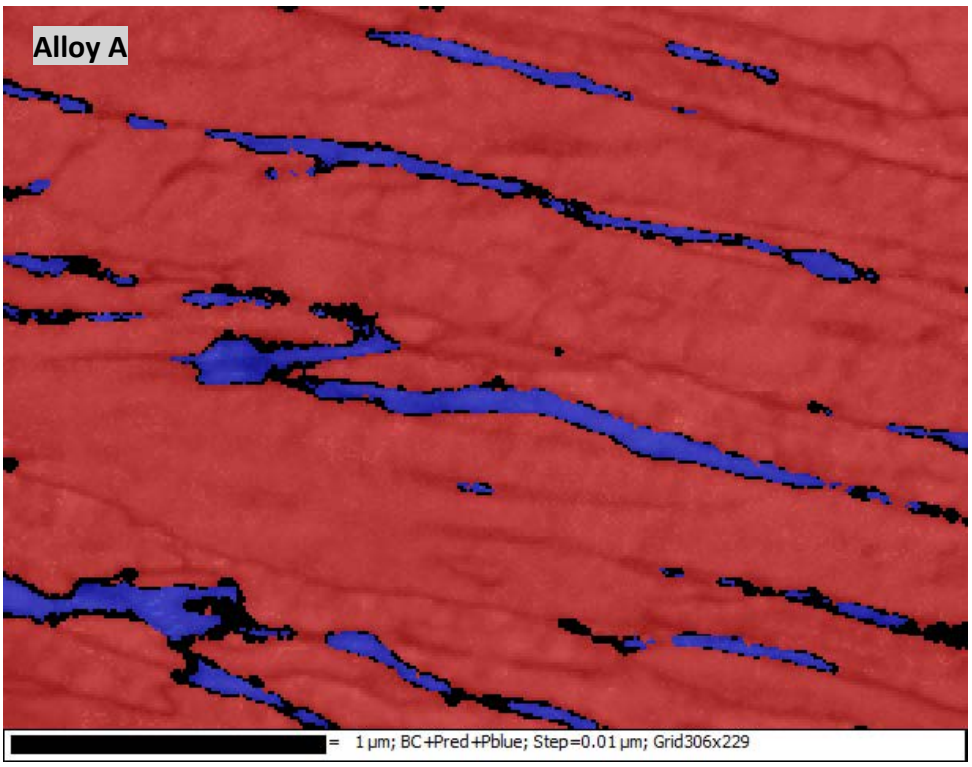

Figure 117. TKD Micrographs of experimental bainitic Alloy A (heat treated at 400°C) showing the FCC-austenite (blue) and BCC-ferrite (red) phases. The black areas are not a phase but regions in the sample that were not well resolved

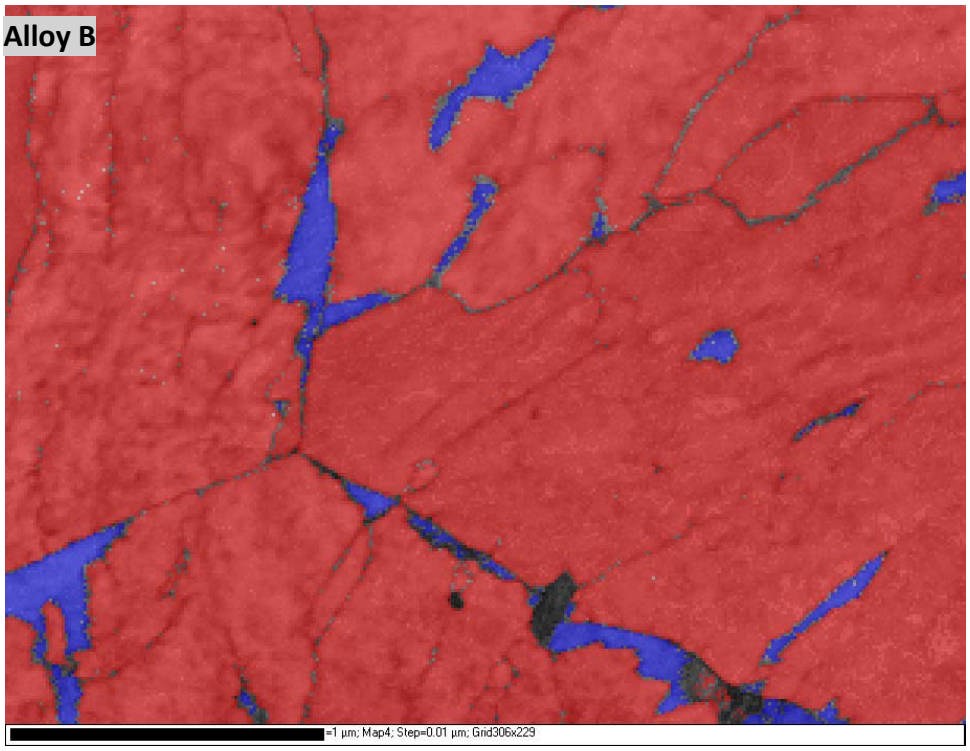

Figure 118. TKD Micrographs of experimental bainitic Alloy D (heat treated at 400°C) showing the FCC-austenite (blue) and BCC-ferrite (red) phases. The black areas are not a phase but regions in the sample that were not well resolved

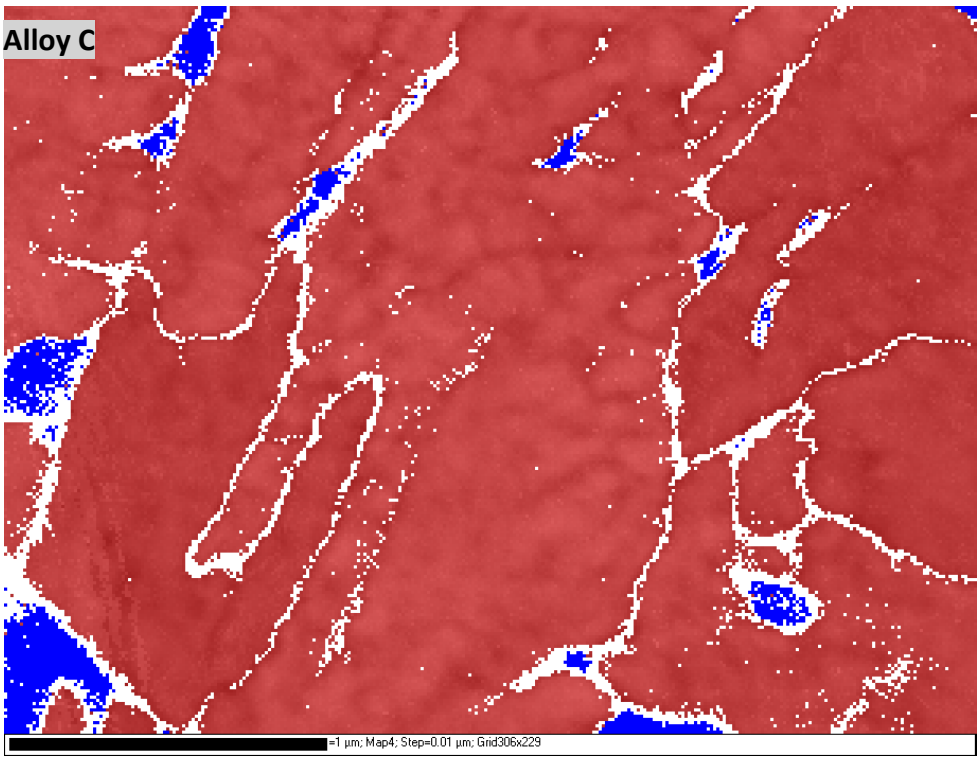

Figure 119. TKD Micrographs of experimental bainitic Alloys B and C (both heat treated at 400°C) showing the FCC-austenite (blue) and BCC-ferrite (red) phases. The white areas are not a phase but regions in the sample that were not well resolved

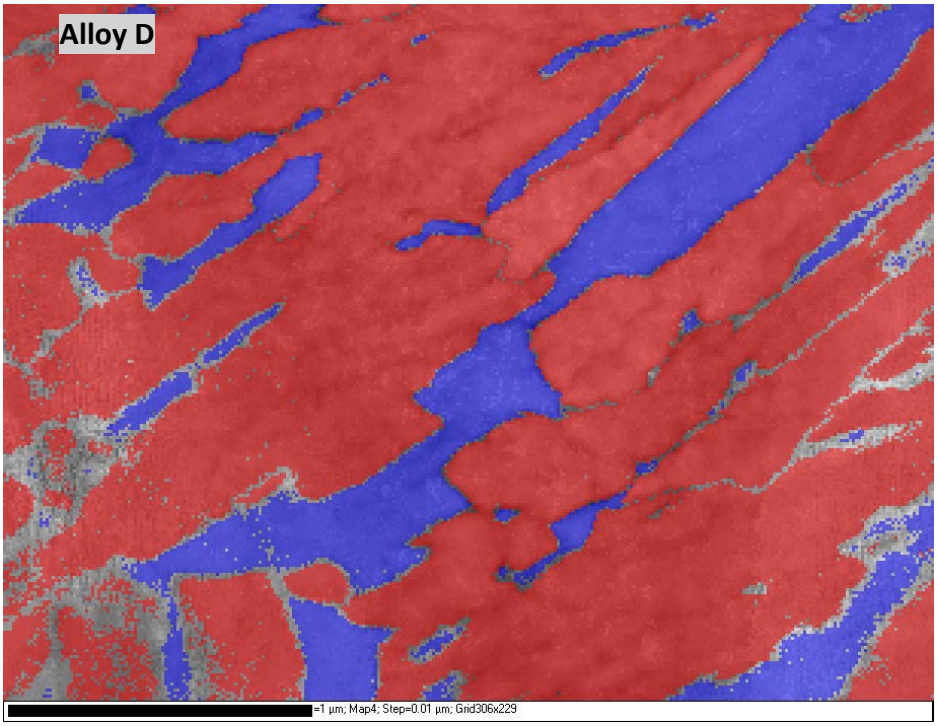

Figure 120. TKD Micrographs of experimental bainitic Alloys D (heat treated at 400°C) showing the FCC-austenite (blue) and BCC-ferrite (red) phases. The grey areas are not a phase but regions in the sample that were not well resolved

From the results of the tests conducted on Alloys A to D it was found that Alloys A and D's chemical compositions are suitable for isothermal heat treatment but because of its higher hardenability, Alloy D is better suited to heat treat large steel components, such as railway wheels, which usually experience slower cooling rates. New Series 2 Alloys E to H were produced to test for the mechanical properties of carbide-free alloys. The new alloys were based on Alloy D composition (wt%) of: C: 0.3±0.2, Mn: 1.5.± 0.5, Cr: 0.5.± 0.5, Mo: .0.2 ± 0.1, Si: 0.3-2.

5. Series 2 Alloys (Alloys E to H)

5.1. Chemical Composition of Alloys E to H

Four new alloys, largely based on Alloy D composition but with variations in silicon contents, were manufactured to study the tensile and impact properties of the carbide-free alloys. Table 21 gives the chemical compositions of the experimental alloys. One alloy (Alloy E) was made with a low silicon content of 0.36 wt% and three alloys (Alloys F-H) had a high-silicon content between 1 wt%- 1.9 wt%. These high silicon contents were added to retard carbide formation. Manganese (Mn), chromium (Cr) and molybdenum (Mo) were added for hardenability.

Table 21. Chemical composition of experimental Alloys E to H after casting and hot rolling

Alloy	C	Si	Mn	P	S	Cr	Mo	Al	B	Ni
E	0.19	0.36	1.41	0.017	0.009	0.5	0.26	0.003	0.0003	0.056
F	0.26	1.85	1.37	0.018	0.010	0.6	0.18	0.009	0.0007	0.056
G	0.29	1.47	1.38	0.016	0.011	0.5	0.17	0.018	0.0008	0.064
H	0.28	1.00	1.57	0.024	0.012	0.5	0.23	0.006	0.0003	0.069

The martensite start (M_s) and bainite start (B_s) temperatures for Alloys E to H were calculated using the MUCG38 programme (Table 22). The transformation temperature (T_1) used to heat treat the alloys were chosen to be, ~10°C above the M_s temperature, to maximise the volume fraction of bainite produced. The alloys were austenitised at temperature T_A, which was ~50°C above the A_{C3} temperature calculated using dilatometry, and then quenched into a salt bath to a temperature T_1 to form bainite.

Table 22. The heat treatment temperatures for Alloys E to H

	MUCG83 °C		Kasatkin °C	Transformation °C	
Alloy	**M_s**	**B_s**	**A_{C3}**	**T_A**	**T_1**
E	405	549	836	900	415
F	374	529	844	900	380
G	358	519	835	900	365
H	352	511	830	900	370

There is a large difference in the B_s temperature because of the differences in the chemical composition of Alloys E to H. Alloying elements have a depressing effect on the Bs temperature, particularly the carbon content. A higher alloying content results in a lower B_s temperature.

5.2. Metallography of Heat Treated Alloys E to H

5.2.1. As-Polished Microstructures of Alloys E to H

Alloys E to H were examined under the optical microscope in the as-polished condition to analyse for any inclusions in their microstructures, see Figure 121. The microstructures show inclusions in the microstructures of Alloys E to H. Analysis of the inclusions using energy dispersive spectroscopy (EDS) of the scanning electron microscope (SEM) found the inclusions in the alloys to be a mixture of oxides and manganese sulphides. These inclusions are common in castings, particularly those cast in air, as is the case with these alloys, and affect the tensile and impact toughness properties negatively. According to ASTM E45 the cleanliness of the alloys is thin series globular oxides with an index number of i= 2 for Alloys A and H and thick series globular oxides with an index number of i= 1.5 for Alloys F and G. this is acceptable according to the South African rail steel standards.

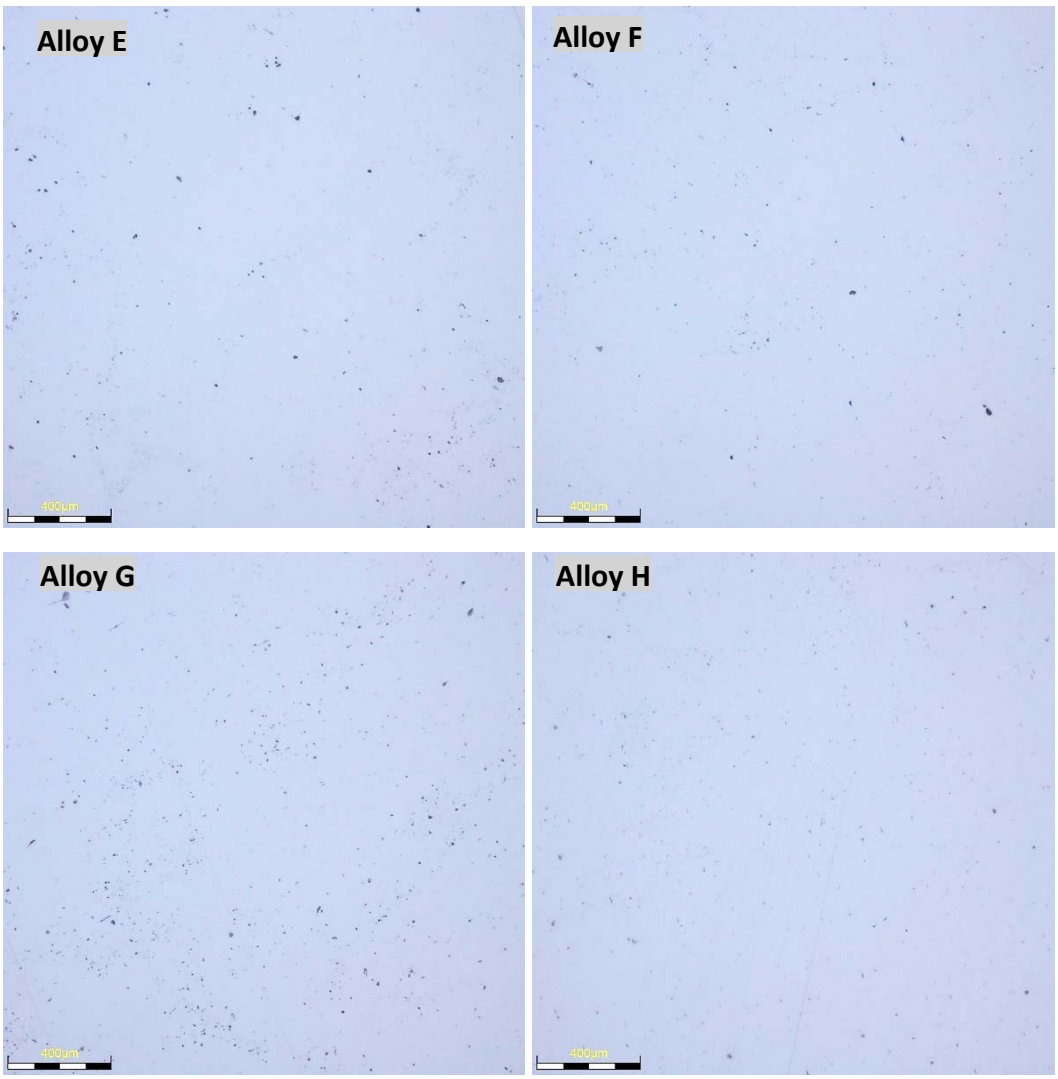

Figure 121. As-polished microstructure of Alloys E to H taken at 10x magnification, showing inclusions

Different etchants were used to etch the experimental alloys to determine which one best reveals their microstructures. Table 23 lists the different etchants used and the method followed to etch the alloys. Figures 122 and 123 show the microstructures obtained with the different etchants. From the results methods 4 and 6 gave the best distinction between bainite and martensite.

Table 23. Different Etchants used to reveal the microstructure of Alloys E to H

	Etchant	method	Microstructure
1.	2% Nital (2 ml Nitic Acid + 198 ml Ethanol)	Polish an unmounted sample and etch with 2% Nital. Place in a furnace at 260°C for 2.5 hrs, then cool to room temperature	Colours bainite dark blue and martensite light blue
2	10% $Na_2S_2O_5$ (10g $Na_2S_2O_5$ + 100ml H_20)	Immerse polished sample for 15 seconds	Colours bainite blue and martensite brown
3	4% Picral (4g Picric Acid + 100ml Ethanol)	Immerse polished sample for 60s, oscillate continuously	Bainite appears darker than the martensite
4	1% $Na_2S_2O_5$ (1g $Na_2S_2O_5$ + 100ml H_20) + 4% Picral (4g Picric Acid + 100ml Ethanol)	Mix solutions in a 1:1 ratio just before etching. Immerse polished sample for 10s-15s, oscillate continuously	Colours bainite brown or blue and martensite white
5	(a) 4% Picral (4g Picric Acid + 100ml Ethanol) (b) 10g $Na_2S_2O_5$ + 3g $K_2S_2O_5$ +100ml H_20	Pre-etch polished sample with 4% Picral. Immerse polished sample for 60s, oscillate continuously. Then etch with solution b by immersion for ~30s, oscillate continuously	Colours bainite blue-purple and martensite brown
6	(a) 4% Picral (4g Picric Acid + 100ml Ethanol) (b) 10% $Na_2S_2O_5$ (10g $Na_2S_2O_5$ + 100ml H_20)	Pre-etch polished sample with 4% Picral. Immerse polished sample for 60s, oscillate continuously. Then etch with solution b by immersion for 15 seconds	Colours bainite white and martensite white
7	2% Nital (2 ml Nitic Acid + 198 ml Ethanol)	Swab the polished sample with the Nital until etched.	Colours bainite blue and martensite brown

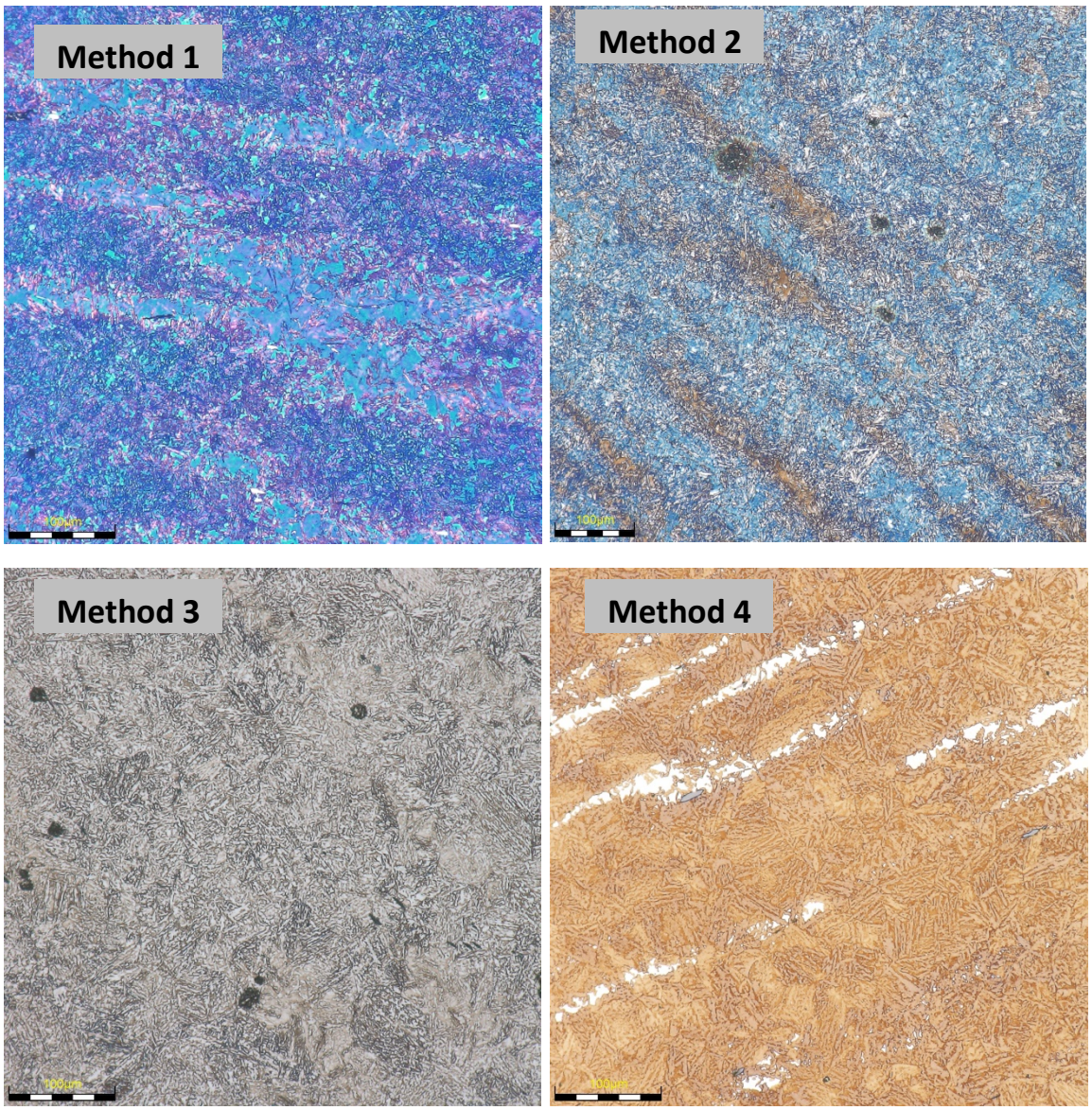

Figure 122. Microstructures revealed after etching with different etchants (methods 1 to 4)

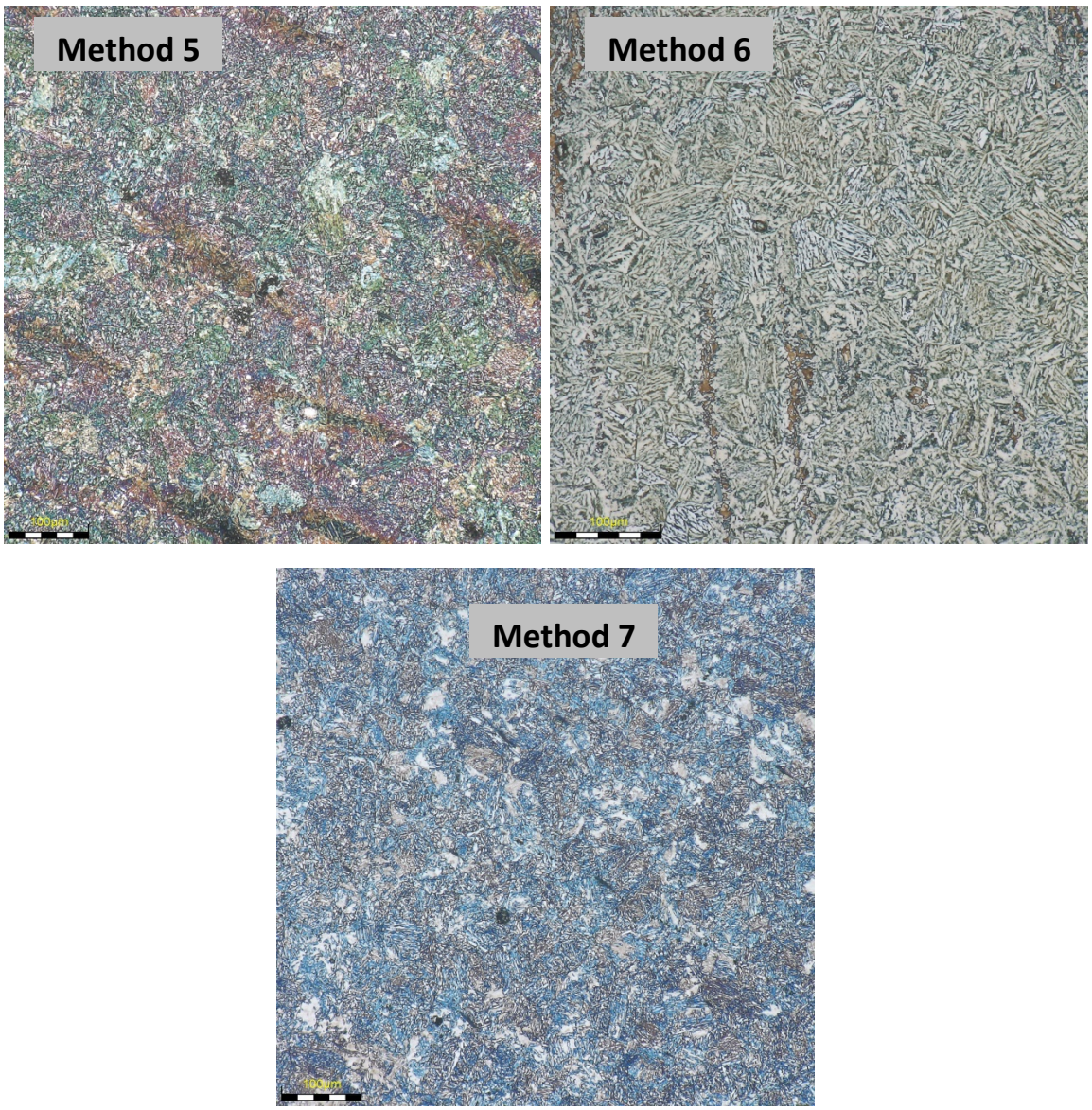

Figure 123. Microstructures revealed after etching with different etchants (methods 5 to 7)

5.2.2. The Volume Fraction of the Different Phases in the Microstructures of Alloys E to H

The alloys were etched using Method 4 and Figure 124 shows the microstructures attained for Alloys E to H. Their microstructures are banded, comprising bainite (B) with some patches of martensite (M). EDS analysis of the bainite and martensite phase are given in Table 24. The martensite has a higher alloy content of silicon, chromium, molybdenum and manganese.

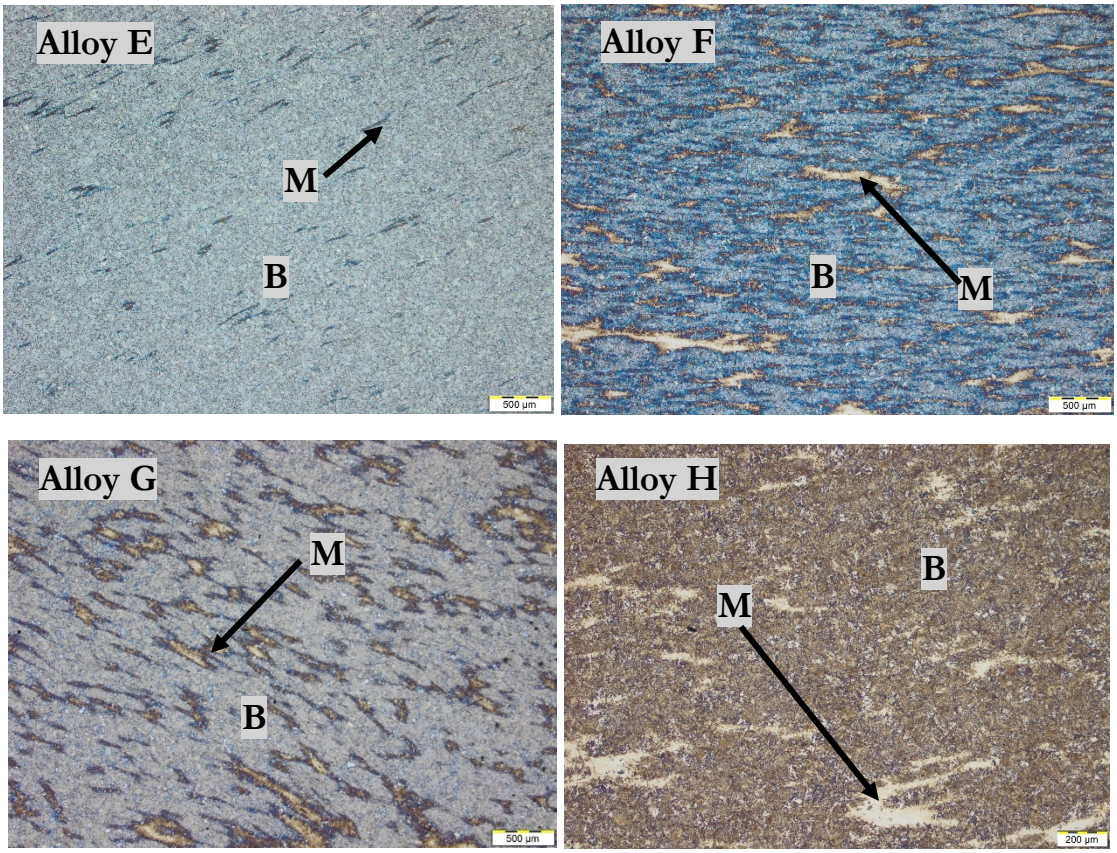

Figure 124. Microstructures of Alloys E to H after etching using Method 6, taken at 2.5X magnification showing a banded microstructure of bainite and martensite

Table 24. Composition analysis of the martensitic and bainitic phases in Alloys E to H

Sample	Phase	Si	Cr	Mn	Mo
E	Bainite	0.34	0.48	1.44	0.15
E	Bainite	0.41	0.55	1.57	0.28
E	Bainite	0.36	0.49	1.35	0.16
E	Bainite	0.33	0.47	1.32	0.12
E	Bainite	0.40	0.55	1.61	0.19
E	Bainite	0.34	0.46	1.36	0.16
E	Bainite	0.37	0.44	1.37	0.17
E	Bainite	0.34	0.48	1.36	0.15
E	Bainite	0.37	0.43	1.40	0.18
E	Martensite	0.53	0.77	1.96	0.51
E	Martensite	0.51	0.77	1.98	0.63
E	Martensite	0.53	0.71	1.91	0.43
F	Bainite	1.75	0.55	1.54	0.13
F	Bainite	1.73	0.52	1.53	0.05
F	Bainite	1.72	0.56	1.51	0.13
F	Bainite	1.77	0.51	1.40	0.07
F	Bainite	1.76	0.48	1.50	0.03
F	Bainite	2.09	0.64	1.75	0.25
F	Bainite	1.77	0.54	1.54	0.15
F	Martensite	2.43	0.83	2.11	0.46
G	Bainite	1.26	0.44	1.26	0.04
G	Bainite	1.31	0.46	1.42	0.13
G	Bainite	1.31	0.47	1.44	0.11
G	Bainite	1.31	0.48	1.40	0.15
G	Bainite	1.28	0.46	1.39	0.09
G	Bainite	1.32	0.50	1.36	0.15
G	Martensite	2.16	0.92	2.45	0.97
G	Martensite	1.86	0.76	2.10	0.48
H	Bainite	0.90	0.48	1.45	0.12
H	Bainite	0.95	0.46	1.42	0.12
H	Bainite	0.99	0.47	1.51	0.12
H	Bainite	0.91	0.49	1.57	0.12
H	Bainite	0.93	0.46	1.48	0.16
H	Bainite	1.02	0.52	1.54	0.14
H	Martensite	1.31	0.73	2.12	0.54
H	Martensite	1.28	0.76	2.17	0.39

To determine the volume fraction of the bainite and martensite in the microstructures of Alloys E to H, point counting was used, and the results are given in Table 25. From the point counting results it can be seen that the alloys have a high volume

fraction of the bainite (B) phase between 87%-98%. Neutron diffraction was used to measure the ferrite (BCC) and austenite (FCC) phases in the microstructures of Alloys E to H. This method cannot distinguish between bainite and martensite (M), as they are both BCC in structure, but the combined volume fraction of bainite and martensite (both BCC in structure) was between 74%-97%. Neutron diffraction however measures retained austenite (FCC) quite accurately and the retained austenite results show that Alloy E with the lowest silicon content had a very low retained austenite of 2.6%. Alloys F and H had high retained austenite contents of 20% and 25% respectively and Alloy G had a retained austenite content of 9%.

The average Vickers hardness results for Alloys E to H are between 284-412. Microvickers hardness indents were made in the martensite and bainite phases in the microstructure as shown in Table 25. The martensite was found to have a hardness higher than the bainite.

MUGC83 predicts higher volume fraction of bainite but lower retained austenite values.

Table 25. Point counting, neutron diffraction and hardness measurements for Alloys E to H, M = martensite and B = bainite.

	Point Counting		Neutron Diffraction		Average Hardness (Hv)	Microvickers, Hv martensite	Microvickers, Hv bainite	MUCG83	
Alloy	**M**	**B**	**BCC**	**FCC**				**B**	**FCC**
E	12	88	97.4	2.6	284±6	508±51	277±21	95	4.7
F	13	87	80.0	20.0	412±41	592±56	396±41	94	5.7
G	2	98	90.6	9.4	352±7	359±48	316±14	94	5.6
H	10	90	74.5	25.5	295±2	433±99	324±60	94	6.2

5.3. Transmission Kikuchi Diffraction (TKD) for Alloys E to H

TKD results for Alloys E to H are given in Figures 125 to 128. The Microstructure of Alloy E, with a low silicon content of 0.3 wt%, showed evidence of cementite in the microstructure along the boundaries of the bainite plates (Figure 125). Alloys E to H showed a microstructure of bainite and retained austenite with no cementite, see Figures 126-128.

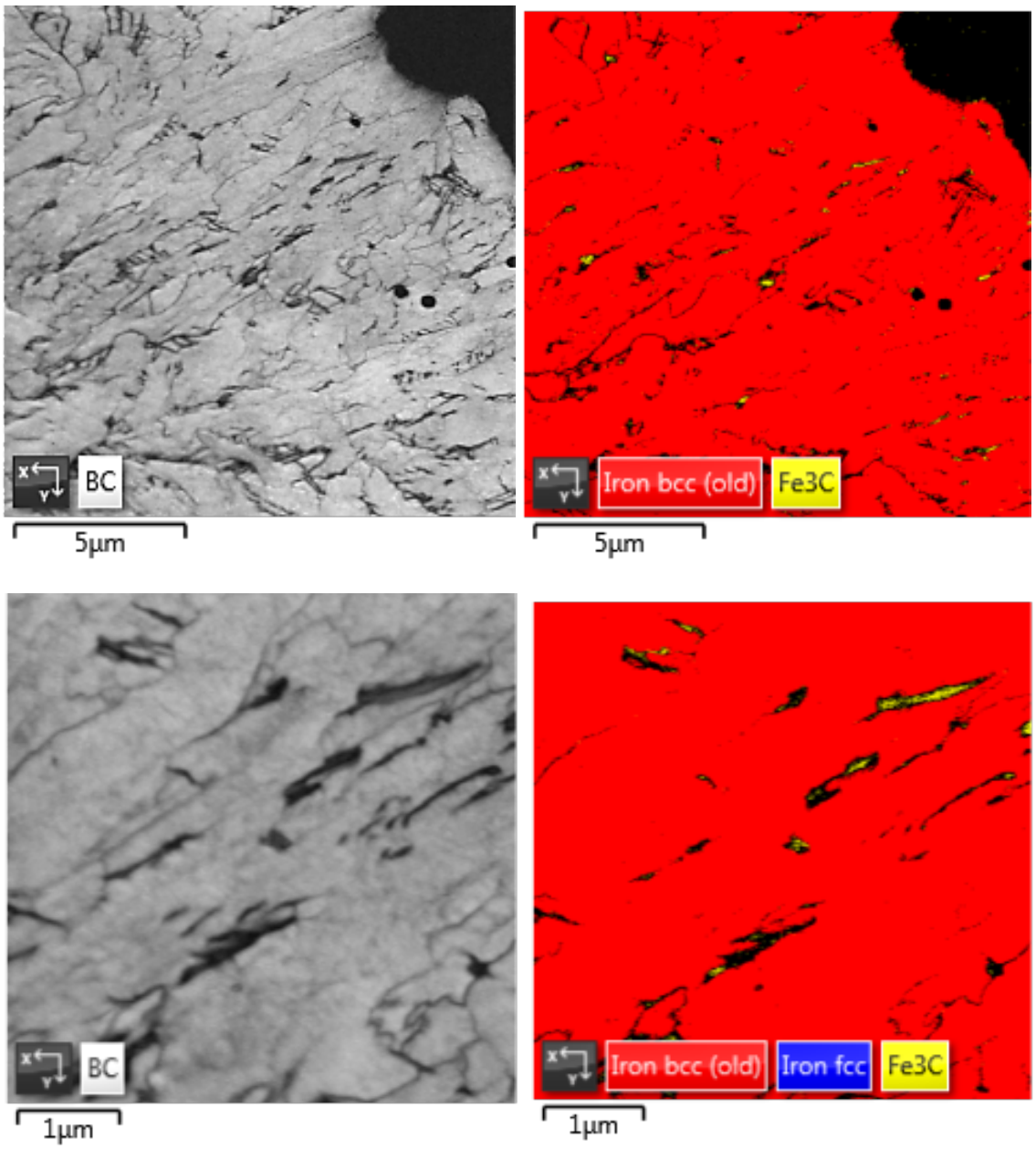

Figure 125. TKD Micrographs of experimental bainitic Alloy E showing the bainite-BCC (red) and cementite (Fe_3C) (yellow) phases

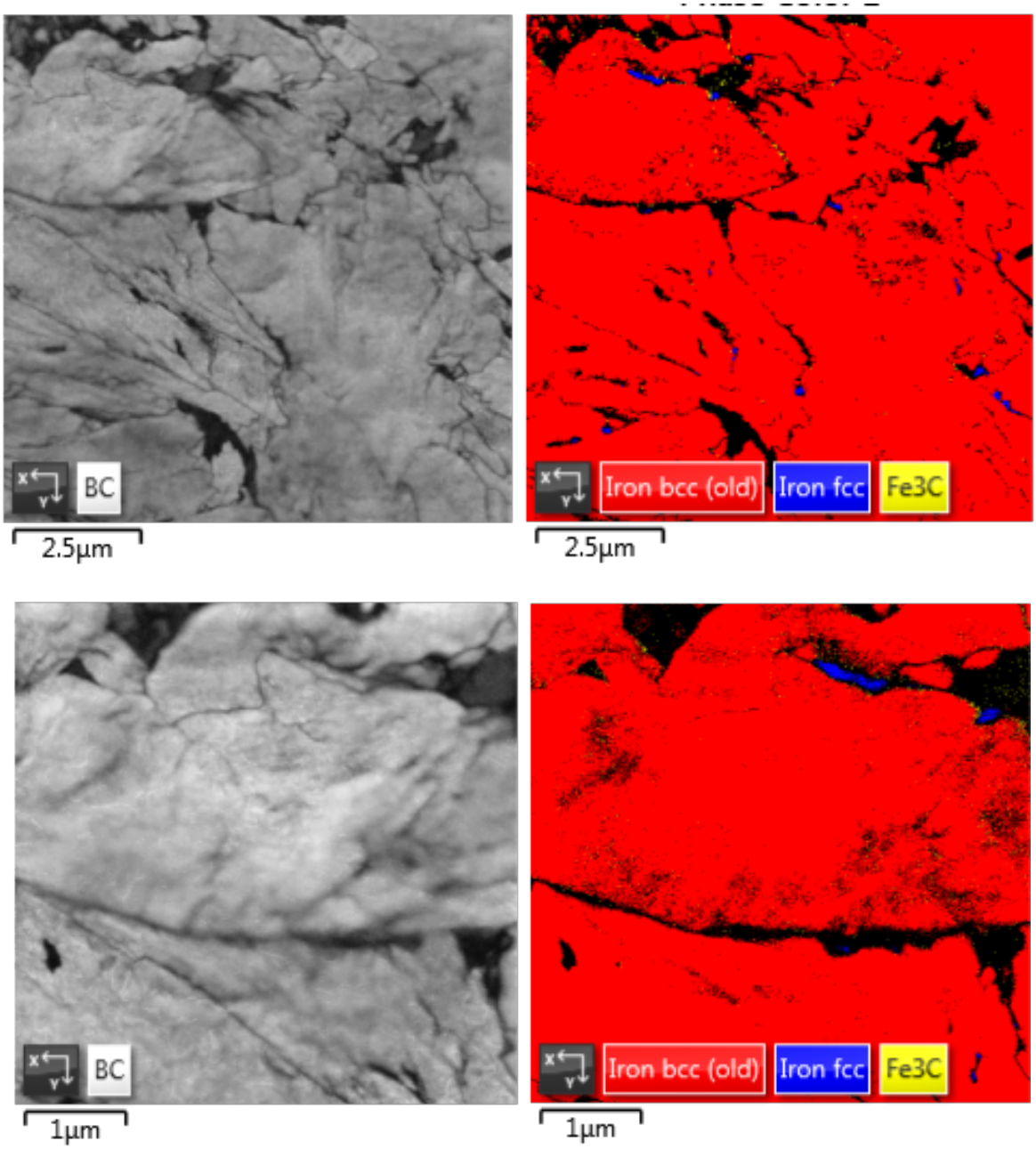

Figure 126. TKD Micrographs of experimental bainitic Alloy F showing FCC-austenite (blue) and BCC-ferrite (red phases. The black area is not a phase but regions in the sample that were not well resolved

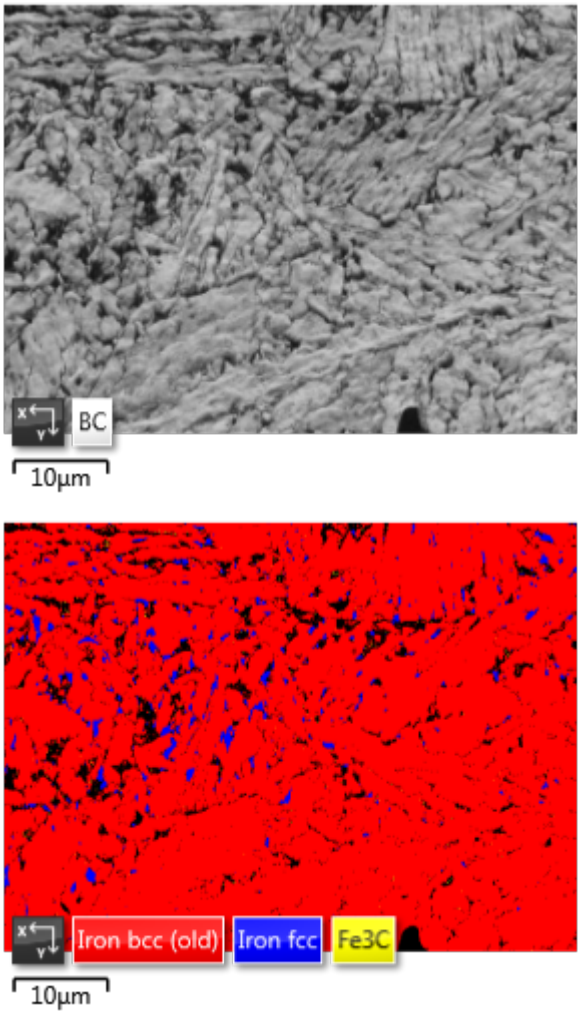

Figure 127. TKD Micrographs of experimental bainitic Alloy G showing the FCC-austenite (blue) and BCC-ferrite (red) phases. The black area is not a phase but regions in the sample that were not well resolved

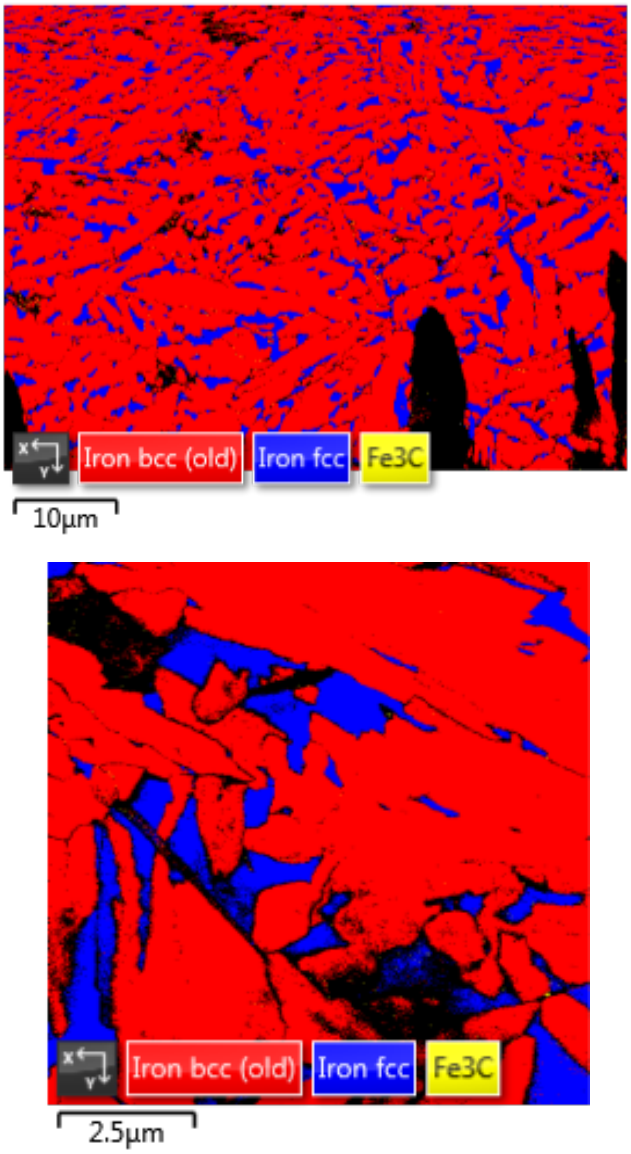

Figure 128. TKD Micrographs of experimental bainitic Alloy H showing the FCC-austenite (blue) and BCC-ferrite (red) phases. The black area is not a phase but regions in the sample that were not well resolved

5.4. Tensile Test Results

Tensile tests were conducted on Alloys E to H after heat treatment and the results are given in Table 26. AAR Class C rail steel was used as the reference alloy. The AAR standard for Class C does not stipulate any requirements for the yield strength properties. Alloys E to F had a yield strength ranging from 714-829 MPa. The tensile strength for AAR Class C is required to be >1050 MPa and Alloy F achieved a tensile strength of 1224 MPa while the other alloys had a lower tensile strength, see Figure 129. Alloy F also showed the highest yield strength. The hardness of Alloys F is higher than the hardness range stipulated for the AAR Class C alloy in the rim. The

elongation of Alloys E to F is higher than the 7% stipulated for the AAR Class C alloy (Figure 130). Alloy F showed the lowest elongation

Figure 130 shows an increasing trend with an increase in retained austenite up to 20%, after which the strengths decrease. The elongation and reduction in area decreases up to 20% RA, thereafter increasing. In Figures 131 and 132 the yield and tensile strengths and hardness increase at a martensite volume fraction of >12% martensite, while the elongation and reduction in area shows a decreasing trend. At a bainite volume fraction >87% the tensile and yield strength and hardness decreased and the elongation and reduction in area increases, see Figure 133 and 134.

From the results Alloy F shows the better tensile and hardness properties, with good elongation.

Table 26. Tensile properties (yield strength (YS), ultimate tensile strength (UTS), elongation, reduction in area (RIA) of Alloys E to H and AAR Class C (forged) rail wheel steels

Alloy	0.2% YS (Mpa)	UTS (Mpa)	Elongation (%)	RIA (%)	Hardness (Hv) average	Neutron Diffraction		Point Counting	
						% Retained austenite	BCC	M	B
E	722±18	919±29	13.7±0.88	20.0±5	284±6	2.6	97.4	12	88
F	829±9	1224±44	9.4±0.6	9.1±0.8	412±41	20	80	13	87
G	738±58	978±53	10.5±2.1	17.3±6.5	352±7	9.4	90.6	2	98
H	714±45	960±54	11.9±1.5	18.1±11.8	295±2	25.5	74.5	10	90
AAR Class C	-	>1050	7	-	320-376 (Rim)	-	-		

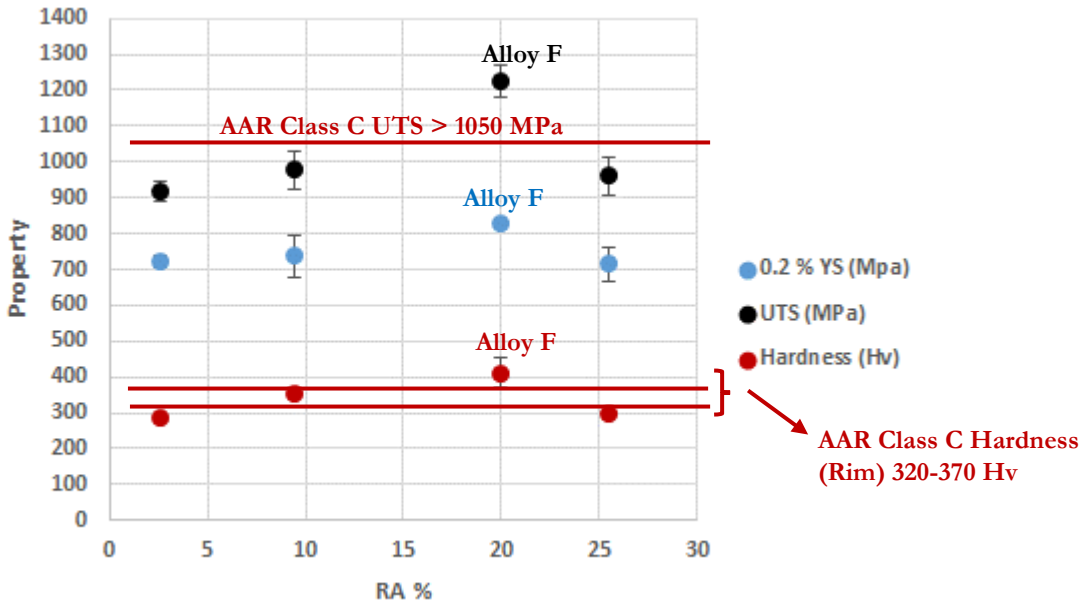

Figure 129. 0.2% yield (YS), ultimate tensile strength (UTS) and hardness versus retained austenite (%RA) results for Alloys E to G compared to AAR Class C alloy

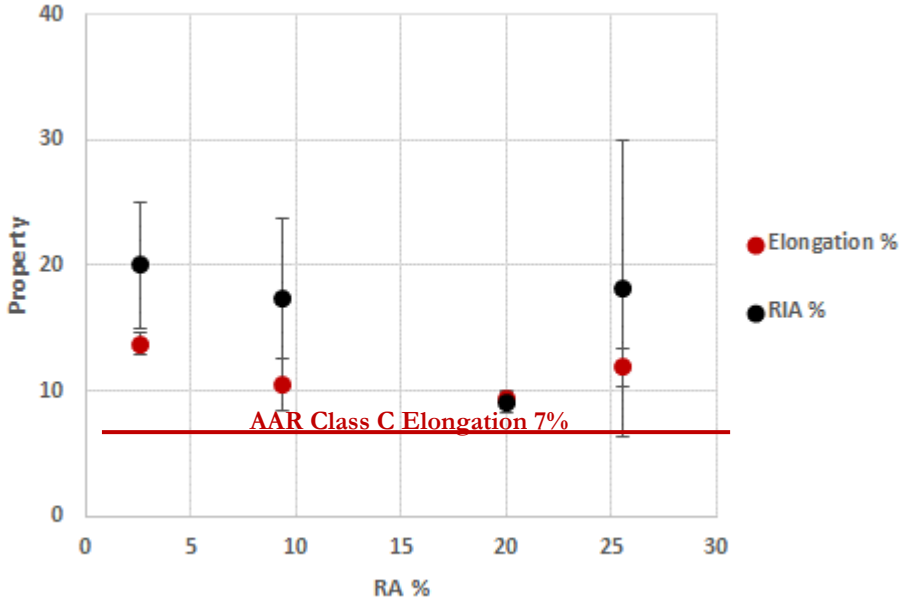

Figure 130. Elongation and reduction in area (RIA) versus retained austenite (%RA) results for Alloys E to G compared to AAR Class C alloy

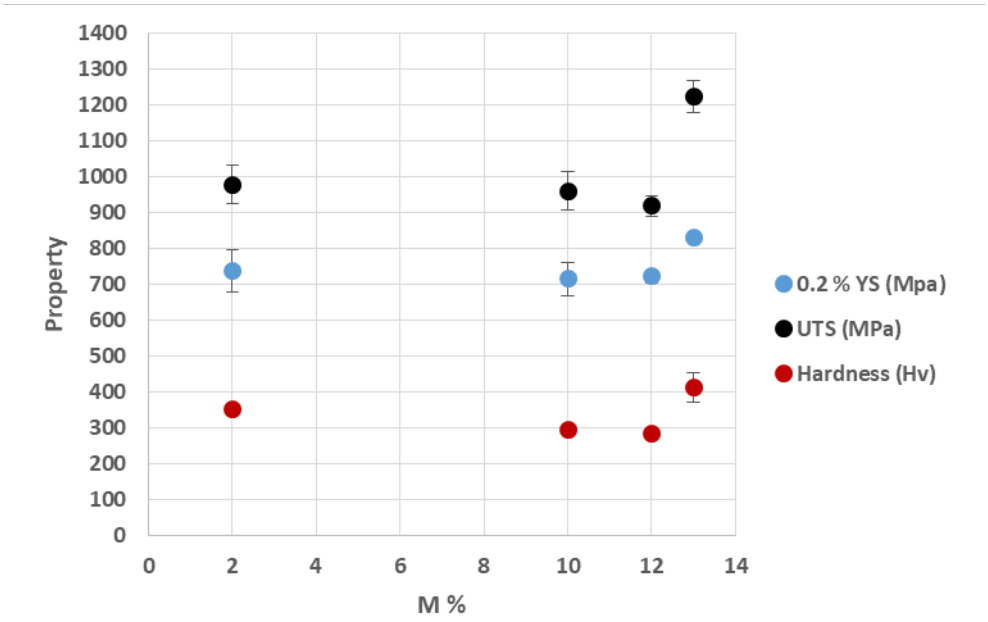

Figure 131. 0.2% yield (YS), ultimate tensile strength (UTS) and hardness versus martensite content (%M) results for Alloys E to G

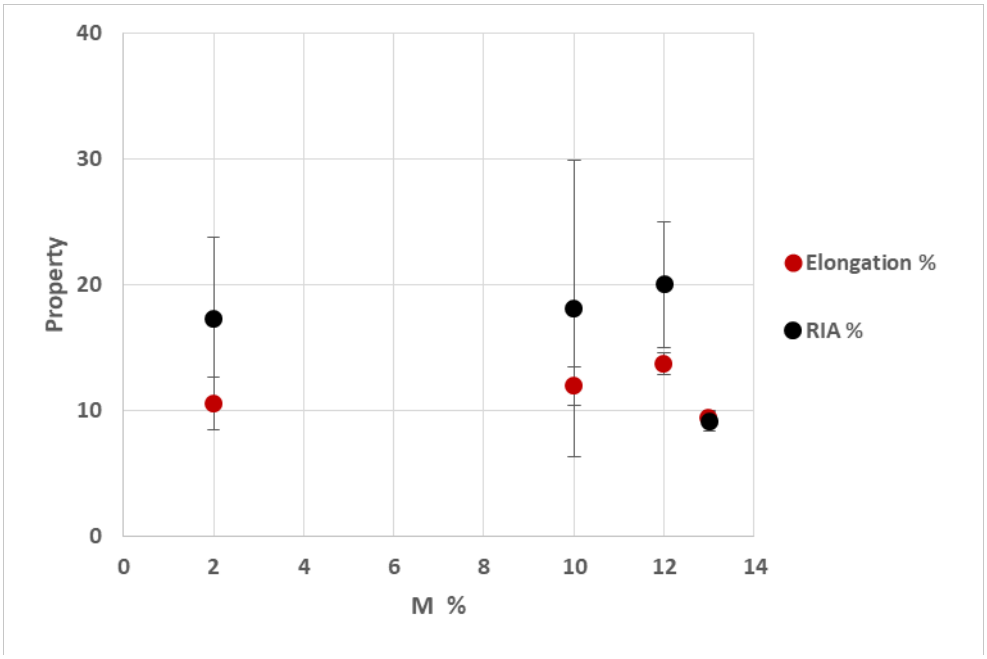

Figure 132. Elongation and reduction in area (RIA) versus martensite content (%M) results for Alloys E to G

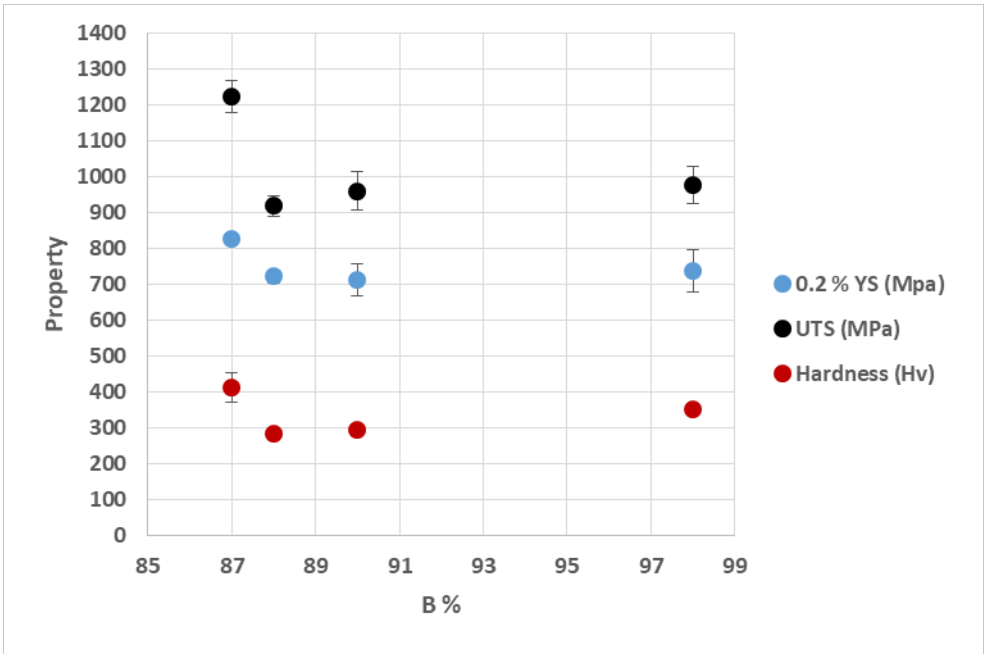

Figure 133. 0.2% yield (YS), ultimate tensile strength (UTS) and hardness versus bainite content (%B) results for Alloys E to G

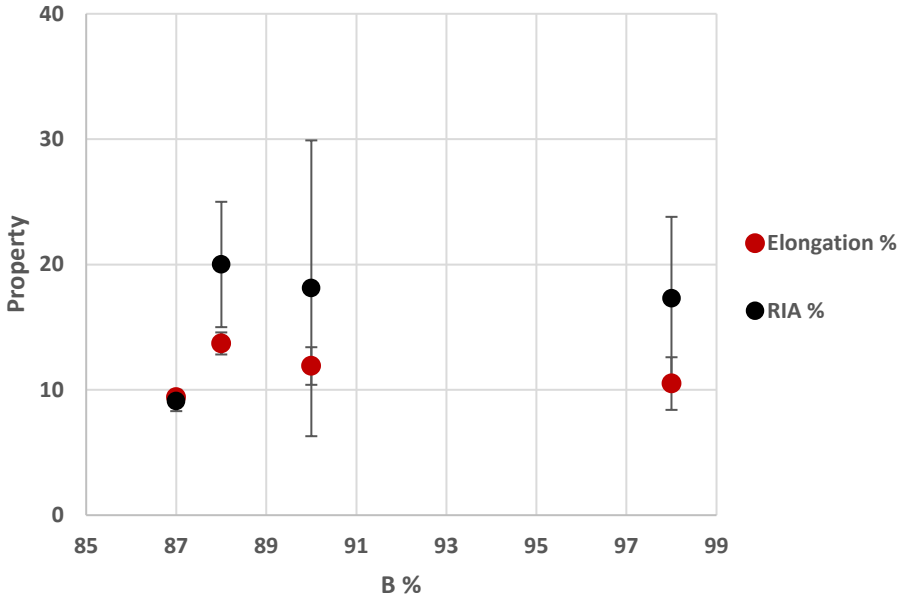

Figure 134. Elongation and reduction in area (RIA) versus bainite content (%B) results for Alloys E to G

5.5. Charpy V-Notch Impact Testing

The results for the charpy v-notch impact testing conducted on Alloys E to H are given in Figure 135. Alloys E and F show the lowest impact energy absorbed,

followed by Alloy G. Alloy H shows the highest impact energy absorbed. Alloys E, F and G show a low impact energy of ≤ 5J up to 100°C, whilst Alloy H shows an impact energy of ~6J up to 50°C, after which its impact energy increases drastically. The ductile to brittle transition temperature (DBTT) for Alloys E, F and G is at high temperatures > 120°C, but Alloy H has a DBTT at ~80°C.

Samples from AAR Class C wheel alloy, in the rim, were tested at room temperature and the results are shown in Table 27. Alloy H showed similar energy absorbed at room temperature as AAR Class C. Alloy H has the highest retained austenite of 25% and, from previous results, showed the highest elongation and reduction in area but lowest hardness.

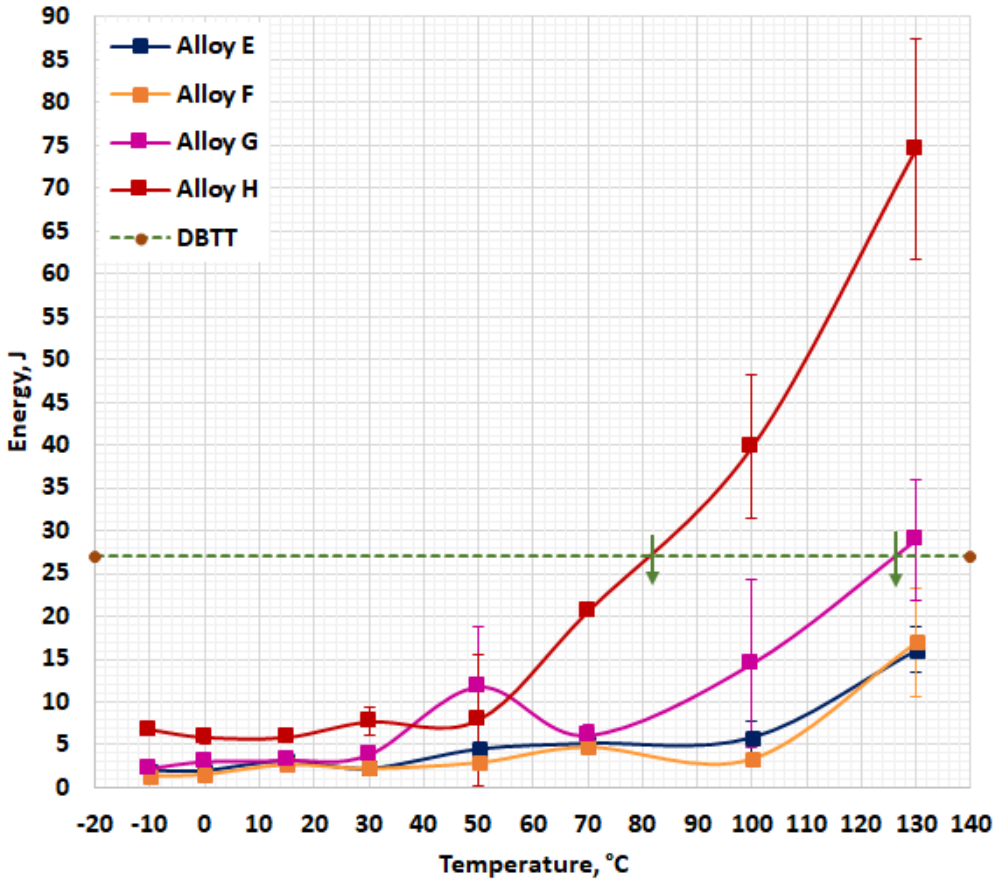

Figure 135. Impact toughness results for Alloys E to H, showing the ductile to brittle transition temperature (DBTT) calculated at 27J

Table 27. Impact Properties of Alloys E to H and AAR Class C at room temperature (RT)

Alloy	Average Impact energy absorbed at room temperature (J)	Retained Austenite
AAR Class C Forged Wheel	6.6*	-
Alloy E	2.3±0.4	2.6
Alloy F	2.3±0.5	2.0
Alloy G	3.8±0.6	9.4
Alloy H	7.7 ±0.7	25.5

*A. Kapito, J.Jonck and G. Maruma [126]]

The typical fracture surfaces found for Alloys E to H, after testing were similar. Figure 136, shows an example of the typical fracture surfaces obtained after testing and examination under the SEM. At low temperatures the metal behaves in a brittle manner and the fracture surface shows river markings or cleavage facets. At higher temperatures, the metal fails in a ductile manner and the fracture surface is dimpled. At intermediate temperatures both river markings and dimples may be found in the microstructure due to a mixed mode of failure.

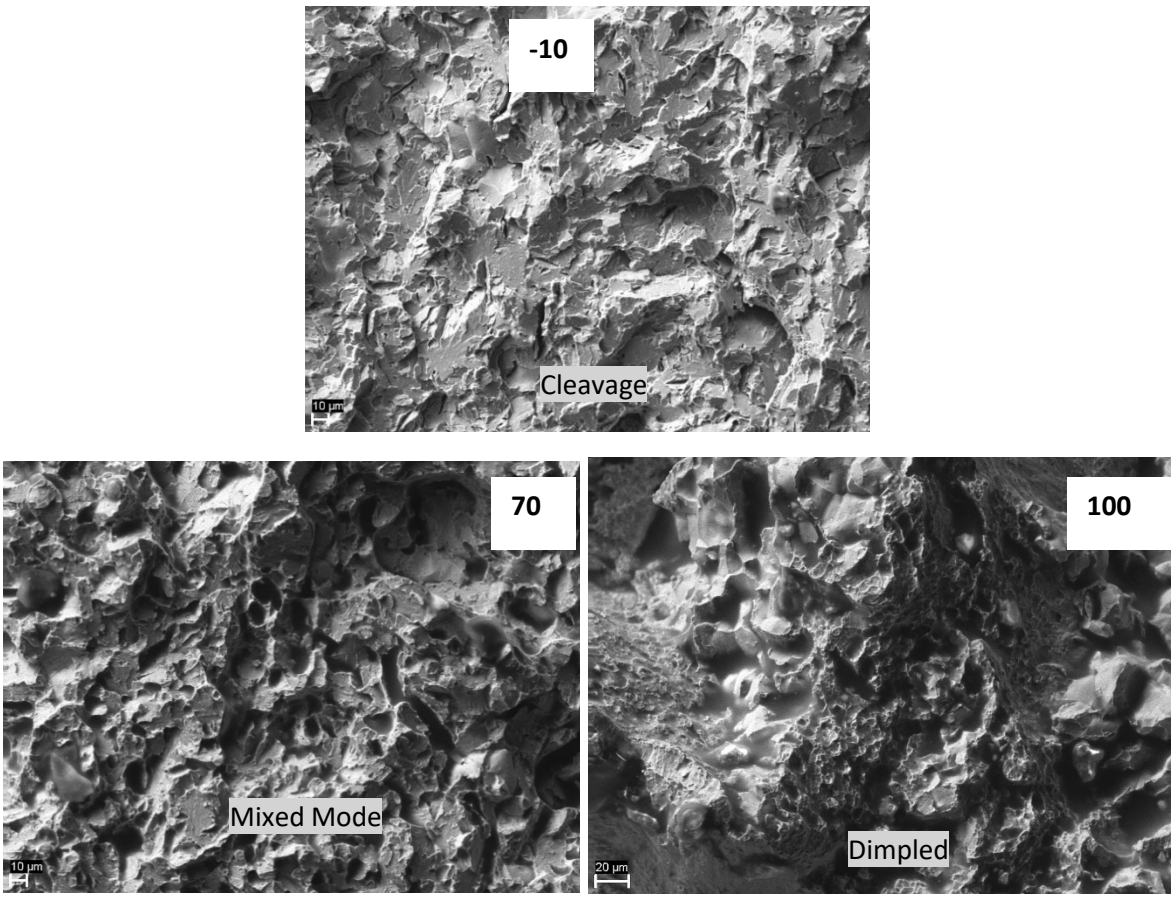

Figure 136. Fracture surfaces of Alloy H after impact testing

5.6. Temper Treatment

Rail wheels are tempered after rim quenching to relieve residual stresses. Tempering is a heat treatment of steels where the steel is isothermally heated at a temperature where austenite cannot form [48]. If there is metastable austenite in the microstructure it will transform and form carbides. In carbide-free bainite hardening is caused by the transformation of retained austenite to cementite. At this point the microstructure will no longer be carbide-free. Generally bainite is known to experience autotempering as it is transformed at higher temperatures where the diffusion of carbon is favoured [53]. Tempering was done on the alloys to show the temperatures where loss of hardness would occur in the carbide-free Alloys F to H.

Alloys F to H were tempered at temperatures between 200°C and 600°C and the results are given in Figure 137 (the heat treatment to form bainite is given in Table 22).

The formation of carbides will cause an increase in the hardness of the microstructure, i.e. a peak in hardness will appear on the hardness curve. Alloy G shows peak hardness values at 300°C and Alloys F and H at 400°C. Alloy H shows softening at 300°C, probably due to the stress relief, but the hardness increases again at 400°C.

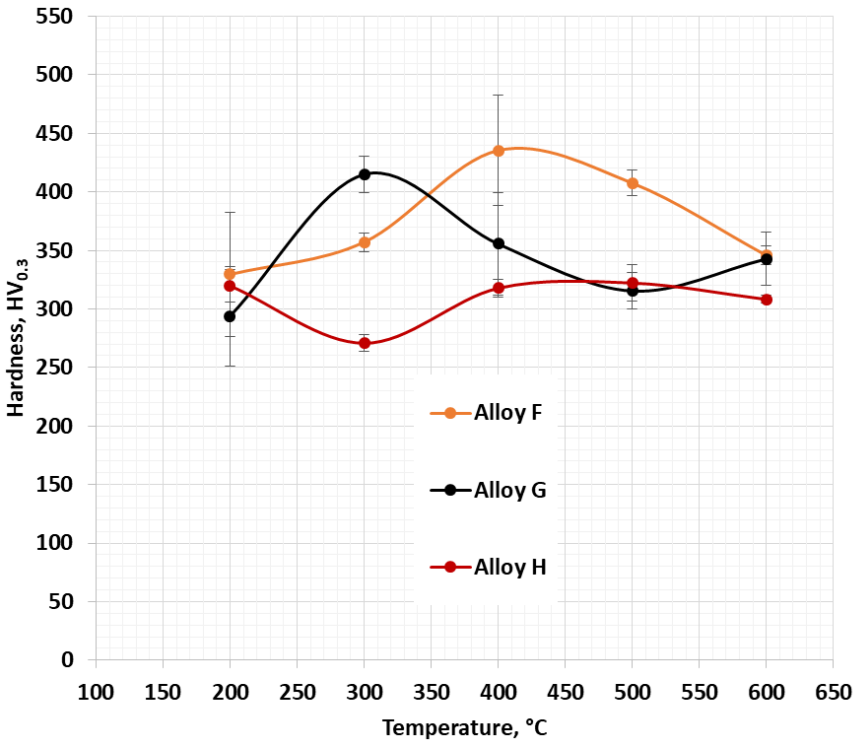

Figure 137. Hardness (HV) versus temperature (°C) curve for Alloys E to H after tempering. The solid lines represent hardness results after tempering while the dashed lines show the average hardness before tempering

From the results it can be seen that:

- Alloy F showed the highest tensile strength and hardness properties
- All Alloys showed elongation > 7%
- All Alloys showed low impact toughness , except for Alloy H which showed impact properties similar to AAR Class C

Based on all the results a new carbide-free Alloy I (Series 3) was produced based on the composition of Alloy F, due to its high hardness, for wear testing.

6. Chemical Composition for Series 3, Alloy I

Alloy I (Alloy Series 3) was produced to test for the wear properties of a carbide-free alloy under sliding conditions. A test rig, built at the University of Pretoria, was used to testing.

Experimental Alloy I, with an actual chemical composition shown in Table 28, was produced to study its wear behaviour. The alloy was a low manganese, boron variation of Alloy F with a silicon content of ~2 wt%. The boron addition was made to aid with the bainite formation and molybdenum was included for hardenability.

Table 28. Chemical Composition of Alloy I

Alloy	Element (wt. %)								
	C	Si	Mn	Cr	Mo	Al	B	P	S
I	0.30	1.78	0.71	0.62	0.16	0.022	0.002	0.018	0.011

6.1.1. Heat Treatment of Alloy I

Alloy I was heat treated in a salt bath at two temperatures of 400°C and 435°C in the salt bath for an hour before quenching in water. The two temperatures were chosen to produce two different bainite volume fractions for wear testing (Table 29). The Bs and Ms temperatures were calculated using MUCG83.

Figure 138 shows the microstructures for Alloy I after heat treatment. Visually, the bainite volume fraction at 435°C appears less than at 400°C. This is to be expected as it was also found in the literature that as the temperature decreases below the B_s, the amount of bainite formed increases.

The volume fractions of the phases in the microstructure were measured using ImageJ, a java-based image processing program used to analyse phases in microstructures [125].It was indeed found that Alloy I, heat treated at 400°C had a higher volume fraction of bainite than that heat treated at 435°C.

The hardness of Alloy I after heat treating at 435°C was higher than that attained after heat treatment at 400°C, due to the higher amount of martensite in the alloy AAR Class B rail steel was used as the reference for the wear testing.

Table 29. Bainite volume fraction, hardness and retained austenite for Alloy I heat treated at 400°C and 435°C

	Transformation °C		**MUCG83**		**IMAGEJ %**		**Hardness**
Alloy	**T_A**	**T_1**	**M_s**	**B_s**	**VB**	**VM**	**H_{V10}**
H-400	1050	400	383	383	94	8	327±9
H-435	1050	435	545	545	79	21	352±7
Class B	Commercial Alloy		-	-	Pearlitic Rail Steel		230±10

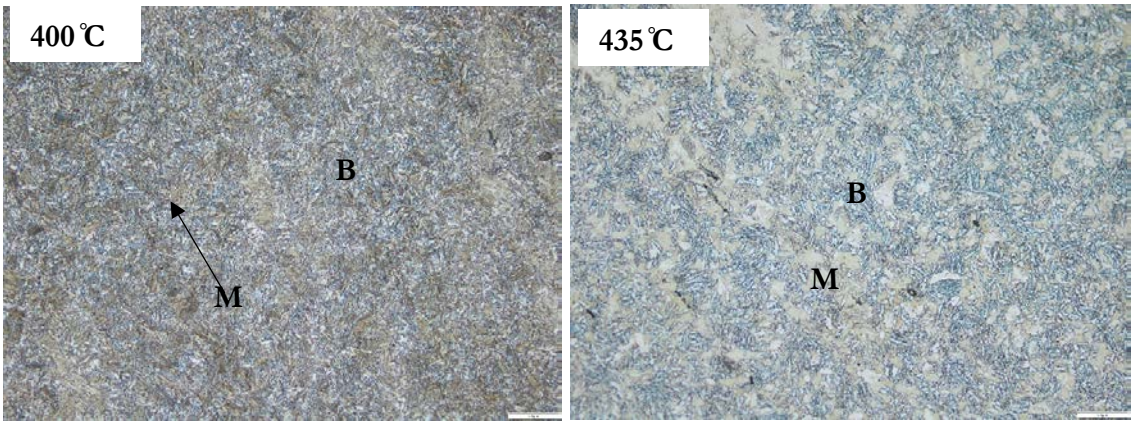

Figure 138. Microstructures of Alloy H after heat treatment at 400°C and 435°C showing bainite (B) and martensite (M)

6.1.2. Test Rig and Test Specimen

Pin-on-disk wear testing is a method commonly used to determine the wear properties of rail steels during sliding [123, 124]. During this test, a pin rotates against a flat disc while a constant load is applied. A circular wear path is formed on the flat disc. Figure 139 is a schematic of the pin-on disc test rig that was used in this study.

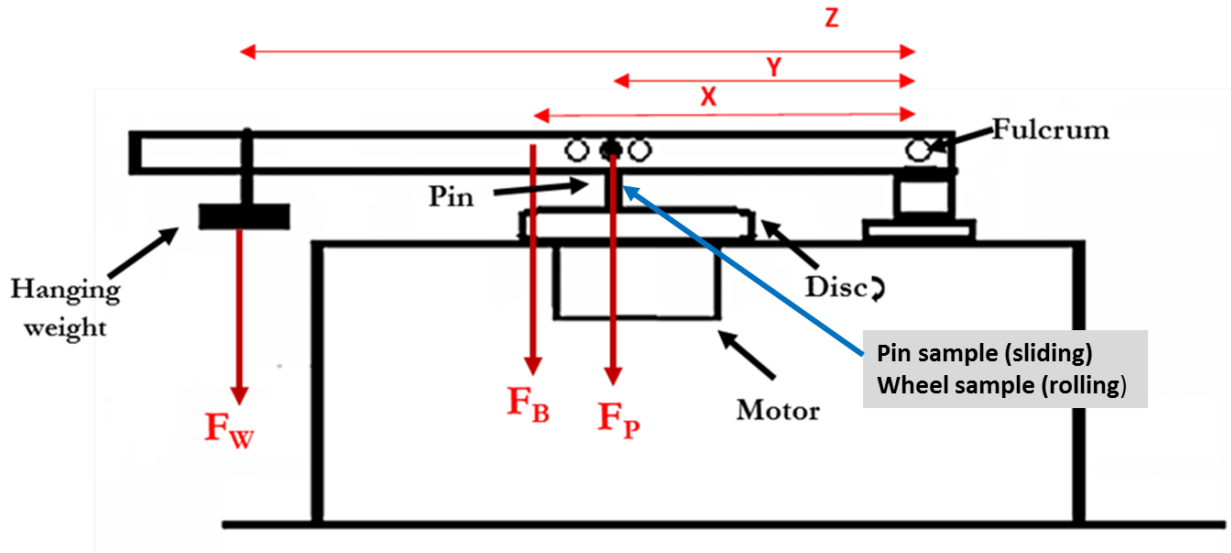

Figure 139. Schematic cross-section of the pin-on-disc test rig built at the University of Pretoria (UP)

Figure 140 shows the pin specimen used to test for pure sliding wear. To simulate a bainitic wheel running on a pearlitic rail, the set-up was such that the bainitic pins were made from experimental Alloy I and the discs were made of Class B rail steel which is most commonly used for rail tracks and wheels in South Africa.

Different hanging weights (with varying masses) were used to apply different forces on pin samples. The pins were rounded with a very small tip radius. This was done to maximise the contact pressure achievable by the rig, see Figure 141. It can be seen in Figure 141 that a pin with a smaller tip radius experiences a higher contact pressure with a hanging weight that has a lower mass. A radius of 0.5 mm was chosen for the tip of the pin samples.

The pin samples were prepared using wire cutting. The contact pressure was calculated using Equation A, in Figure 142, based on the contact between a sphere and a flat surface with a circular contact area [113].

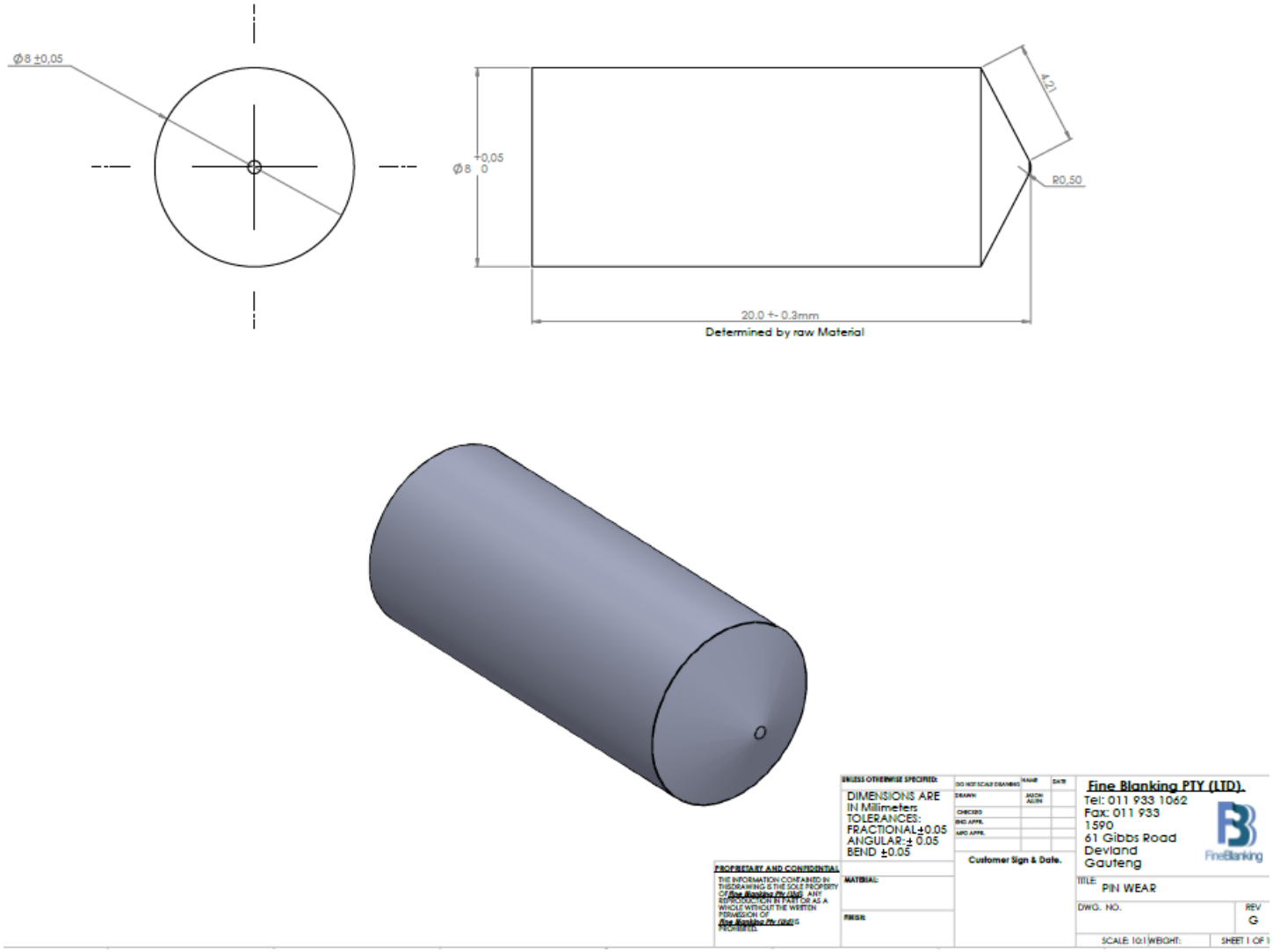

Figure 140. Rounded pin test specimen machined by FineBlanking to be used for sliding wear testing

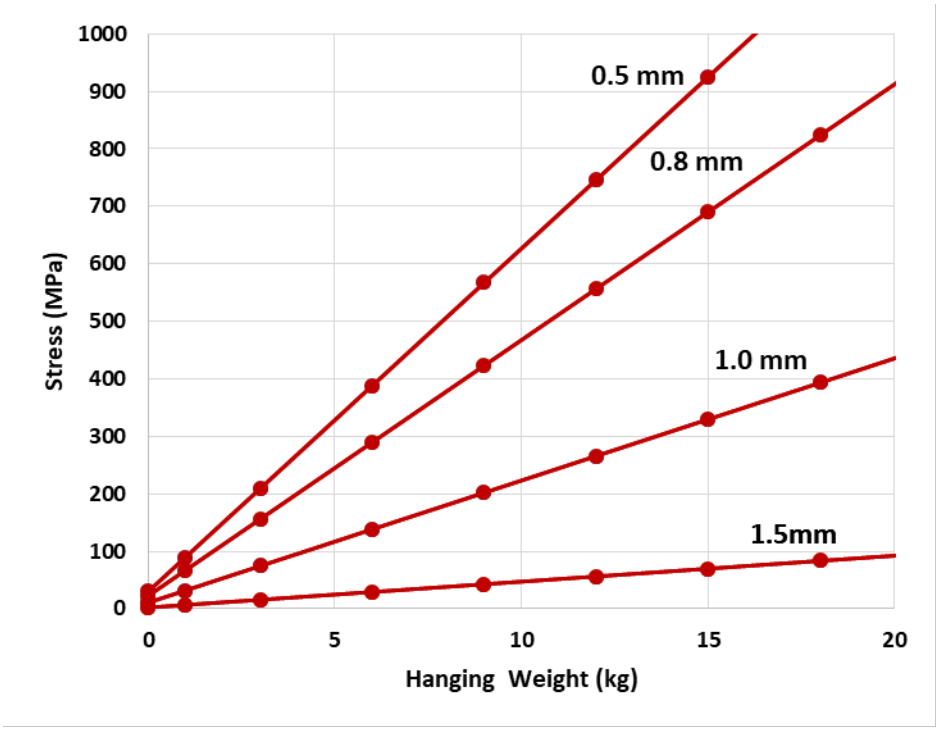

Figure 141. The contact stress achievable at different hanging weights with test pins with different rounded diameters.

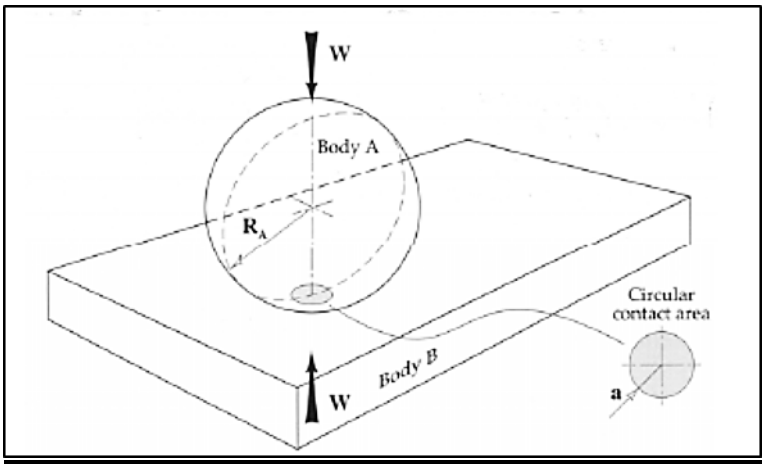

$$\textbf{\textit{Equation A}}: \; P_{max} = \frac{3W}{2\pi r^2}$$

Figure 142. The contact between a sphere and a flat surface with a circular contact area [113]

6.1.2.1. Force on the Pin Due to the Mass of the Pin

The test rig is not digitised and forces on the pin were calculated by measuring bending moments (M) around the fulcrum in Figure 139.

The moments (M) around the fulcrum due to the mass of the sample carrier beam only are:

$M_1 = F_B \times X$ where $F_B = m_B \times g$

$M_2 = F_{P1} \times Y$ but $M_1=M_2$

Thus $F_{P1} = (F_B \times X)/Y = (0.895\ kg)\ (9.81)\ (220.5 \times 10^{-3})/\ (122.5 \times 10^{-3}) = 15.8\ N$

Where F_B = force of the beam due to its mass, F_{F1}= force on the pin, X = 220.5 mm and Y = 122.5 mm and are distances from the centre of the beam and the pin, respectively, to the fulcrum.

The moments around the fulcrum due to the added hanging weight

$M_3 = F_W \times Z = F_W \times 390 \times 10^{-3}$ where $F_B = m_B \times g$

$M_4 = F_{P2} \times Y = F_{P2} \times 122.5 \times 10^{-3}$ but $M_3=M_4$

$F_{P2} = (F_W \times 390 \times 10^{-3})/122.5 \times 10^{-3} = 3.18 \times F_W = 3.18 \times 9.81 \times W\ (kg) = 31.2 \times W\ (N)$

Where F_W = force due to the mass of the hanging weight, F_{F2}= force on the pin, Y=122.5 mm and Z= 390 mm and are distances to the pin and the hanging weight, respectively, from the fulcrum and W is the mass of the hanging weight in kg.

The total forces acting on the pin thus is: $F_{tot} = F_{P1} + F_{P2} = 15.8 + 31.2W\ (N)$, where W is in kg

The stress (Pa) on the pin was calculated using Archards Equation for stress for a rounded specimen as follows:

$$\sigma = \frac{3 \times F_{total}}{2 \times \pi \times a^2} \left(\frac{N}{mm^2}\right)$$ where a is the pin tip diameter

6.1.3. Sliding Mass Loss Test Results

Alloy I was tested using the pin-on-disc test rig and different hanging weights were used to apply different stresses on the pin, see Table 30. The mass of the hanging weight that can be added to the test rig is limited ~1kg. Table 30 also shows the four different stresses applied to the pins during testing. Class B pins were also tested as a reference. The pins were tested for 15 minutes per test in duplicate.

Table 30. Hanging weights, forces and stresses used to test pin samples

Hanging Weight (g)	Hanging Weight (kg)	F_{tot}(N)	σ_{pin} (MPa)
0	0.0	15.8	30.2
200	0.2	22.0	42.1
500	0.5	31.4	60.0
993.9	1.0	46.8	89.4

Figure 143 shows the mass loss results for the pin samples tested with the mass loss of the pins increased with increasing stress applied. The wear rate of Alloy I heat treated at 400°C was similar to that of Class B. Alloy I heat treated at 435°C also had a similar wear rate to Class B up to an applied stress of about 20 KPa, at higher applied stresses, the wear rate increased drastically. The volume mass loss was calculated according to ASTM G 99 – 95a.

The rail disc, made from Class B alloy, used as the counterface upon which the pins were rotated also wore during testing, see Figure 144. The counterface showed more volume loss when a Class B pin was rotated on it at applied stresses >15KPa. At lower stresses the counterface showed similar wear rates irrespective of the pin used to test. Figure 145 shows that the pins wore much less than the discs.

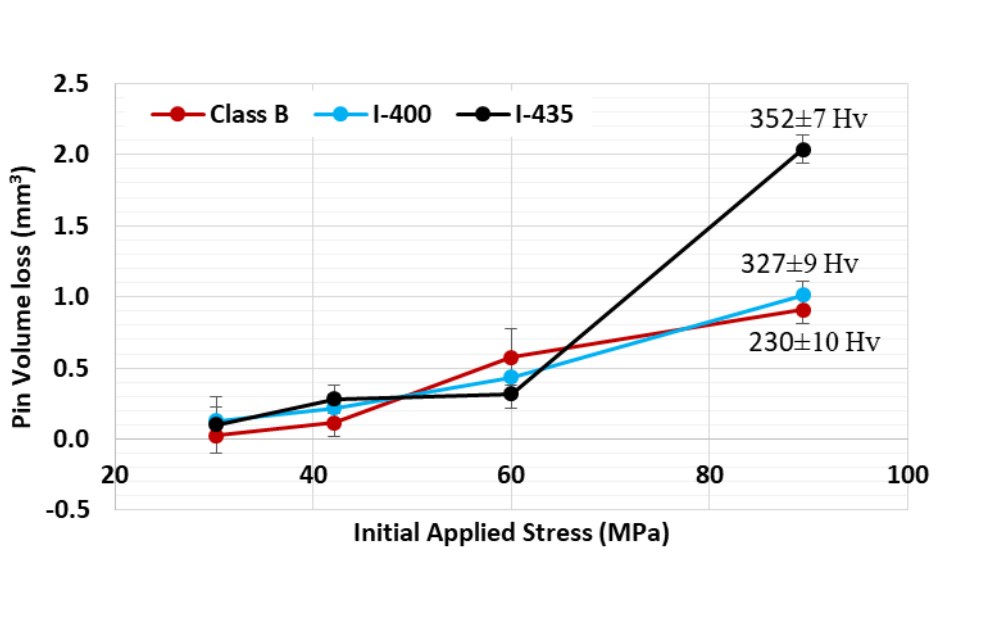

Figure 143. Mass loss of bainitic Alloy I pins, heat treated at 400°C and 435°C, and Class B pins after sliding wear testing at different initial applied stresses

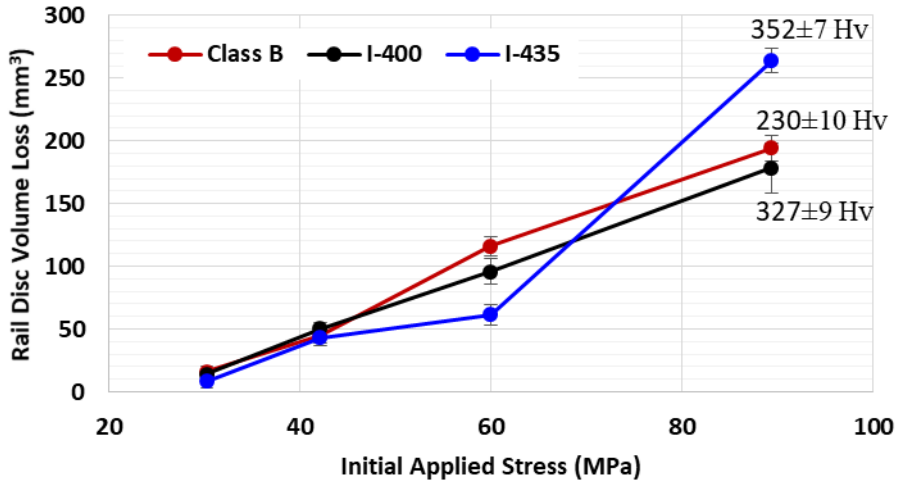

Figure 144. Mass loss of pearlitic rail discs after wear testing with pins, heat treated at 400°C and 435°C, and Class B pins at different initial applied stresses

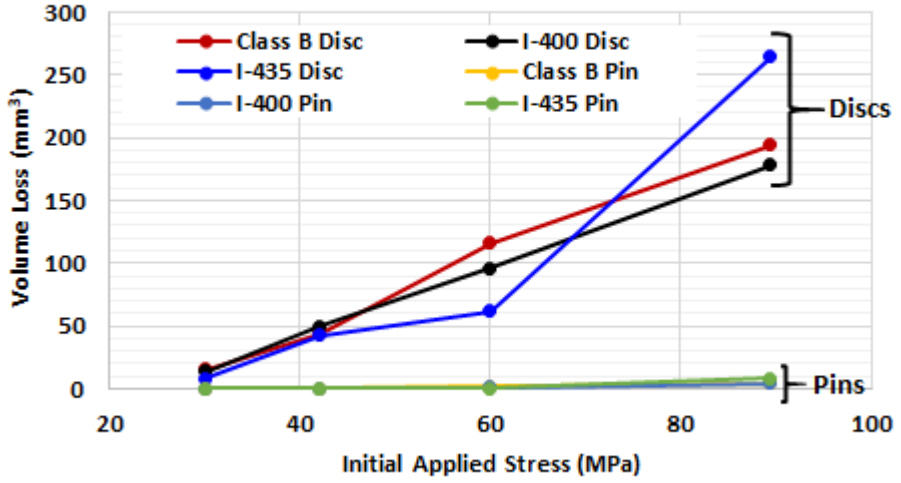

Figure 145. Rail disc, made from Class B, volume loss after testing with pins made from Alloy I, heat treated at 400°C and 435°C, and Class B at different initial applied stresses

The hardness of the tested alloys was taken near and away from the worn surface, see Figure 146, and for Alloy I-400 the hardness at the wear surface increased up to ~60MPa, before decreasing. The hardness near the wear surface was much harder than that away from it. This could be increasing its wear resistance. For Alloy I-435 the hardnening at the surface decreased throughout the test, particularly at ~60MPa, the point at which the volume loss also increased drastically. The hardness

difference near and away from the wear surface also decreases throughout the test, especially at□60MPa. Class B shows increasing hardness at the wear surface

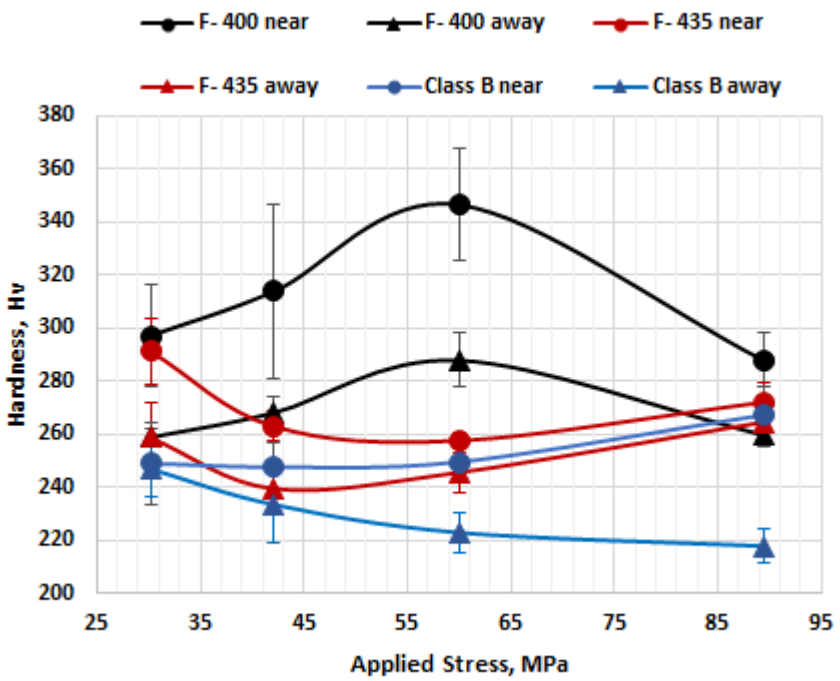

Figure 146. Hardness versus applied stress curve for Alloy I pin samples, heat treated at 400°C and 435°C, and for Class B. The dashed lines represent the average hardness, taken away from the worn surface, for Alloy I and Class B

The worn surfaces for pins are shown in Figure 147. The pin worn surfaces show grooving after testing due to plastic deformation. The grooving is more pronounced in the Class B alloy than in the bainitic alloy. The diameter of the pin wear surface increases with increasing applied stress. Three dimensional images of the pin wear surfaces are shown in Figure 148, and the results again show that the surface of the pins was grooved during testing. The wearing was not uniform over the surface of the pins, as indicated by the step on the pin worn surface. The height of the grooves on the Class B worn surfaces were higher than those on the bainitic alloy, indicating that Class B experienced higher deformation during testing than Alloy I.

The same grooving effect can be seen on the worn surfaces of the rail discs (Figure 149) but the rail discs also showed some pitting and gouging, after testing. The wear track diameter on the discs increases with increasing applied stress.

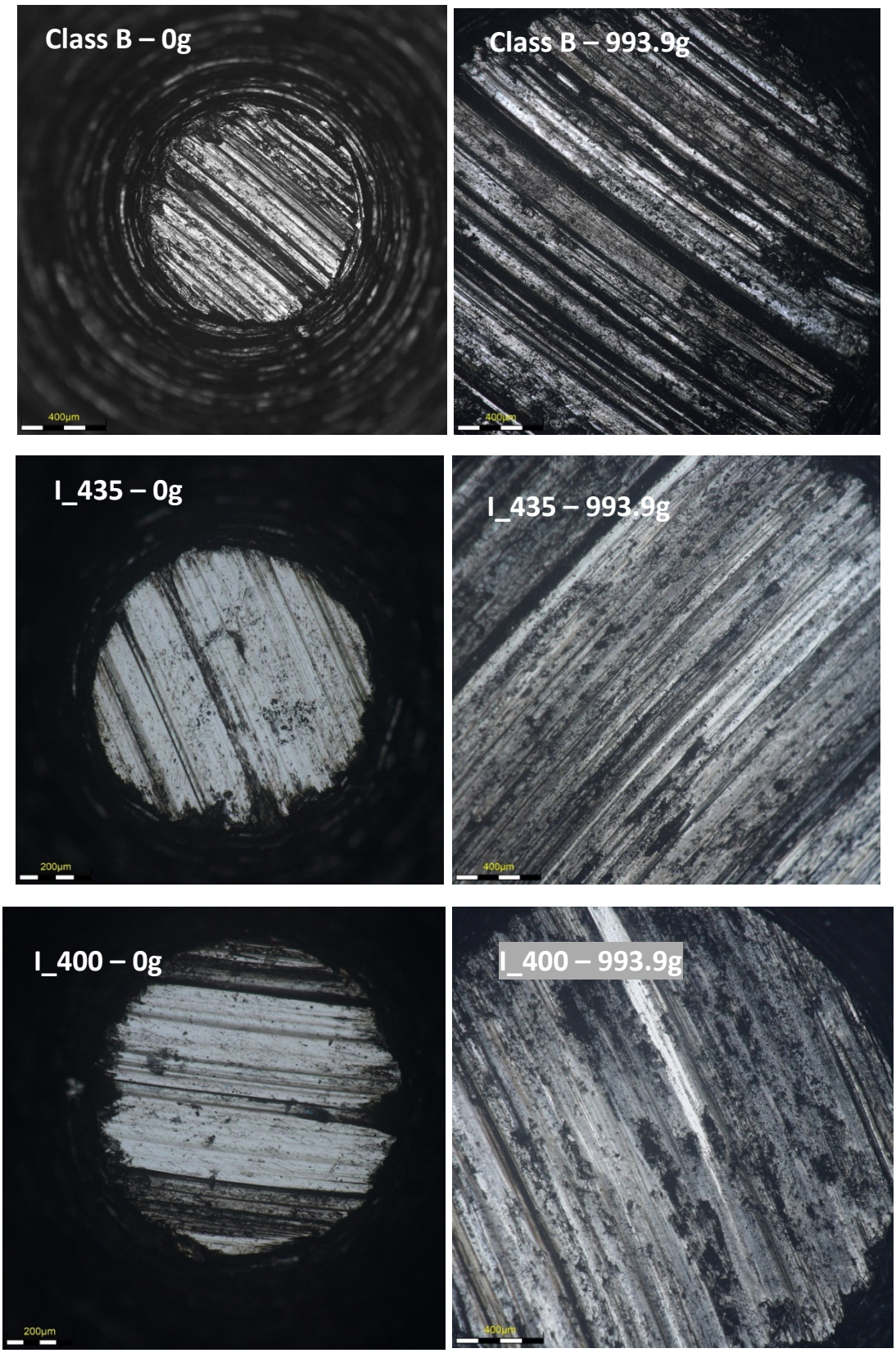

Figure 147. Worn surfaces of the pins for Alloy I, after heat treatment at 400°C and 435°C respectively, and for Class B, after sliding wear testing. The masses (g) are for the hanging weights used during testing.

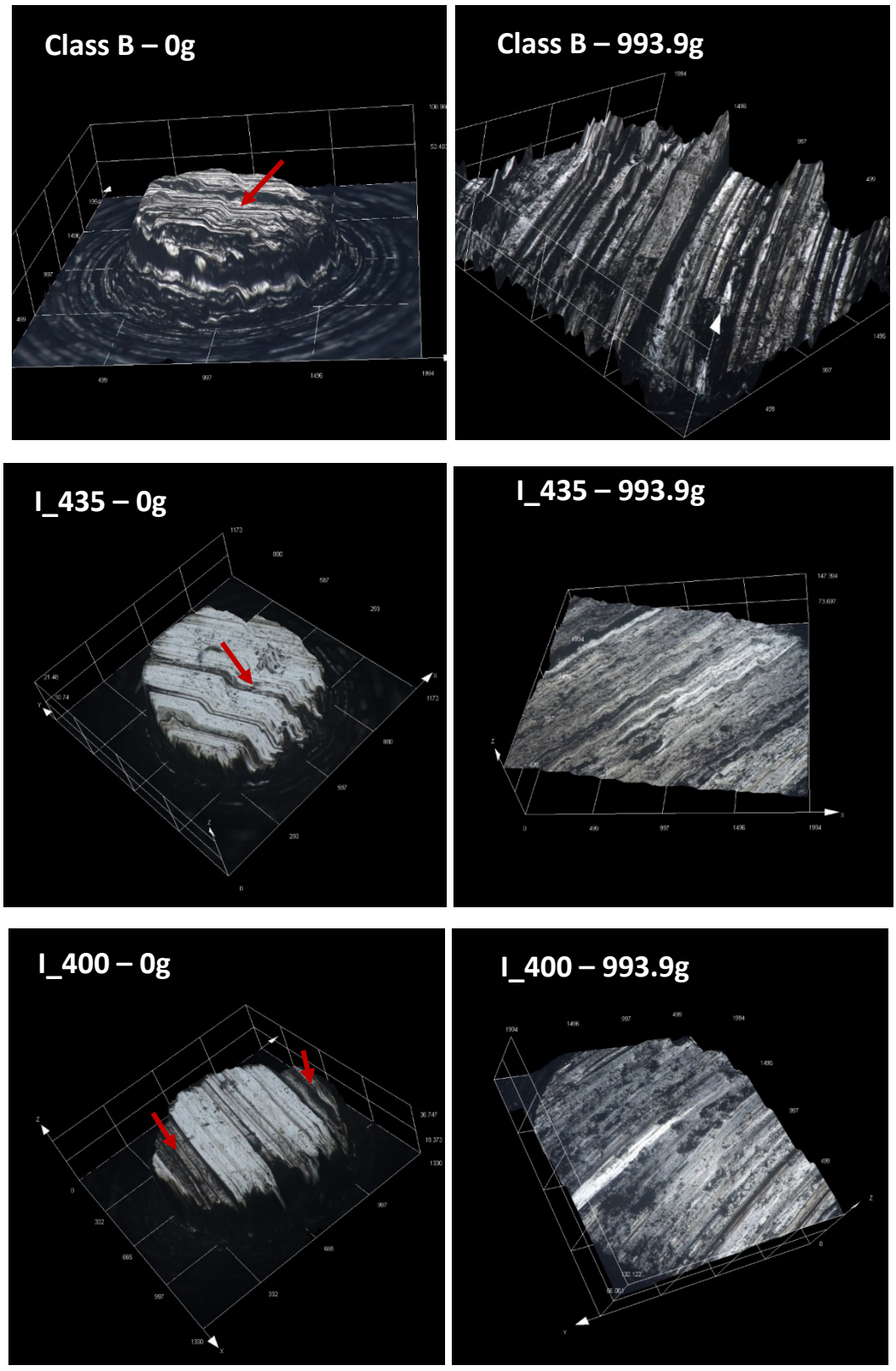

Figure 148. Three dimensional (3D) images of the worn surfaces of the pins for Alloy I, after heat treatment at 400 and 435 C respectively, and for Class B, after sliding wear testing. The arrows indicate where there is a step on the worn surfaces. The masses (g) are for the hanging weights used during testing.

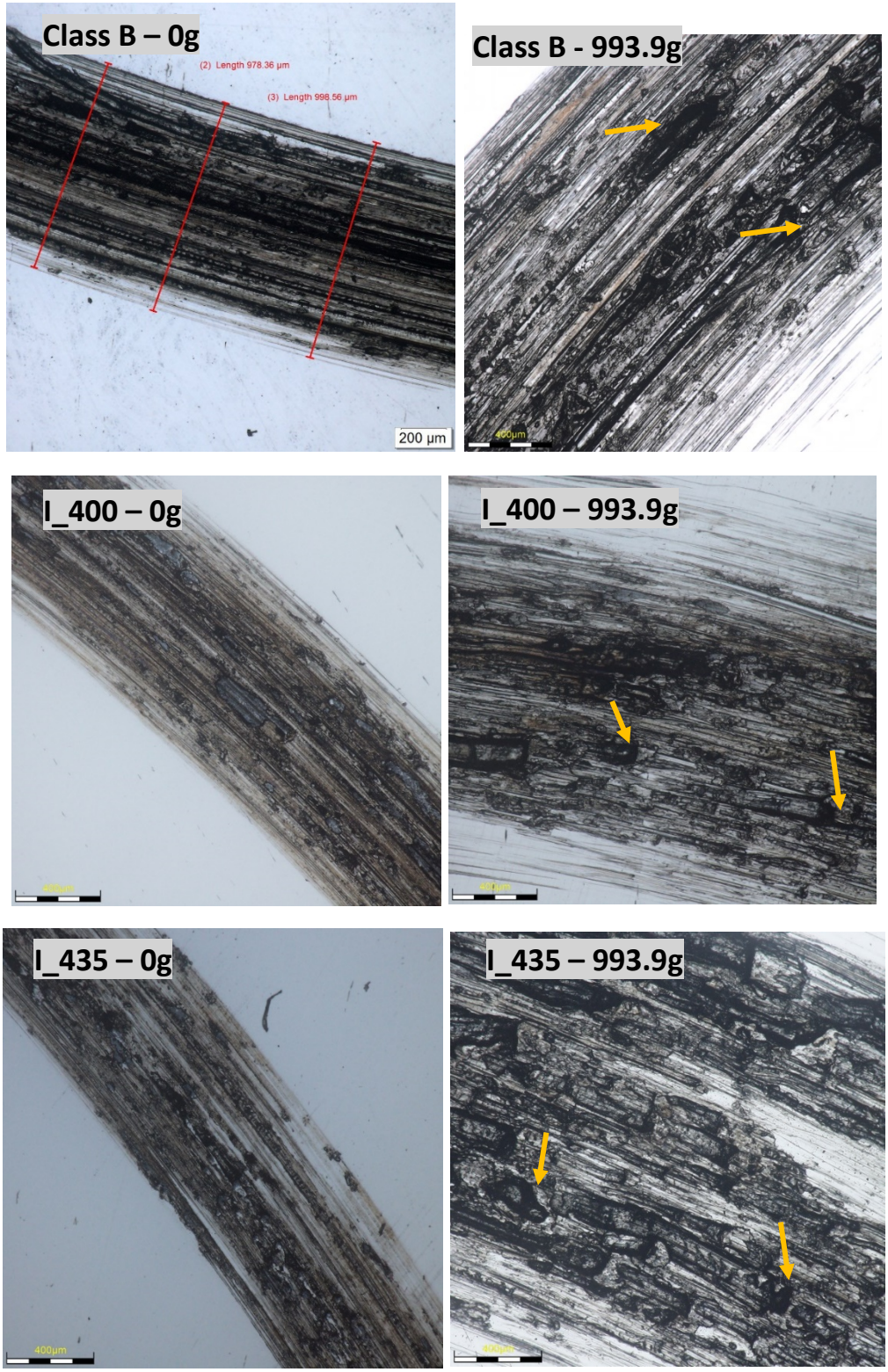

Figure 149. Typical features on the worn disc rail surfaces *after testing with a pin made from Class B and Alloy I-heat treated at 400°C and 435°C. The yellow arrows point at regions of pitting. The masses (g) are for the hanging weights used during testing.*

6.1.4. Cross-Sections of Worn Surfaces

After wear testing the pin samples were cross-sectioned to examine the microstructures under the SEM. Pins tested at the highest stress achievable of 27KPa, were examined under the SEM. There is evidence of significant deformation on the cross-sections of the Class B pin samples after testing, see Figure 150. There is also evidence of cracking at the wear surface and coarse inclusions in the microstructure that have been pulled out during testing, leaving voids. These inclusions act as crack initiation points and diminish the wear resistance of the Class B steel.

Alloy I, heat treated at 400°C, shows an undulating wear surface due to deformation (Figure 151). The worn surface also shows cracking. There is evidence of inclusions in the microstructure, but not as significant as in the Class B alloy. These inclusions again act as crack initiation points.

Alloy I, heat treated at 435°C, also shows an undulating wear surface due to deformation (Figure 152). The worn surface did not show cracking and there were minor inclusions in the microstructure.

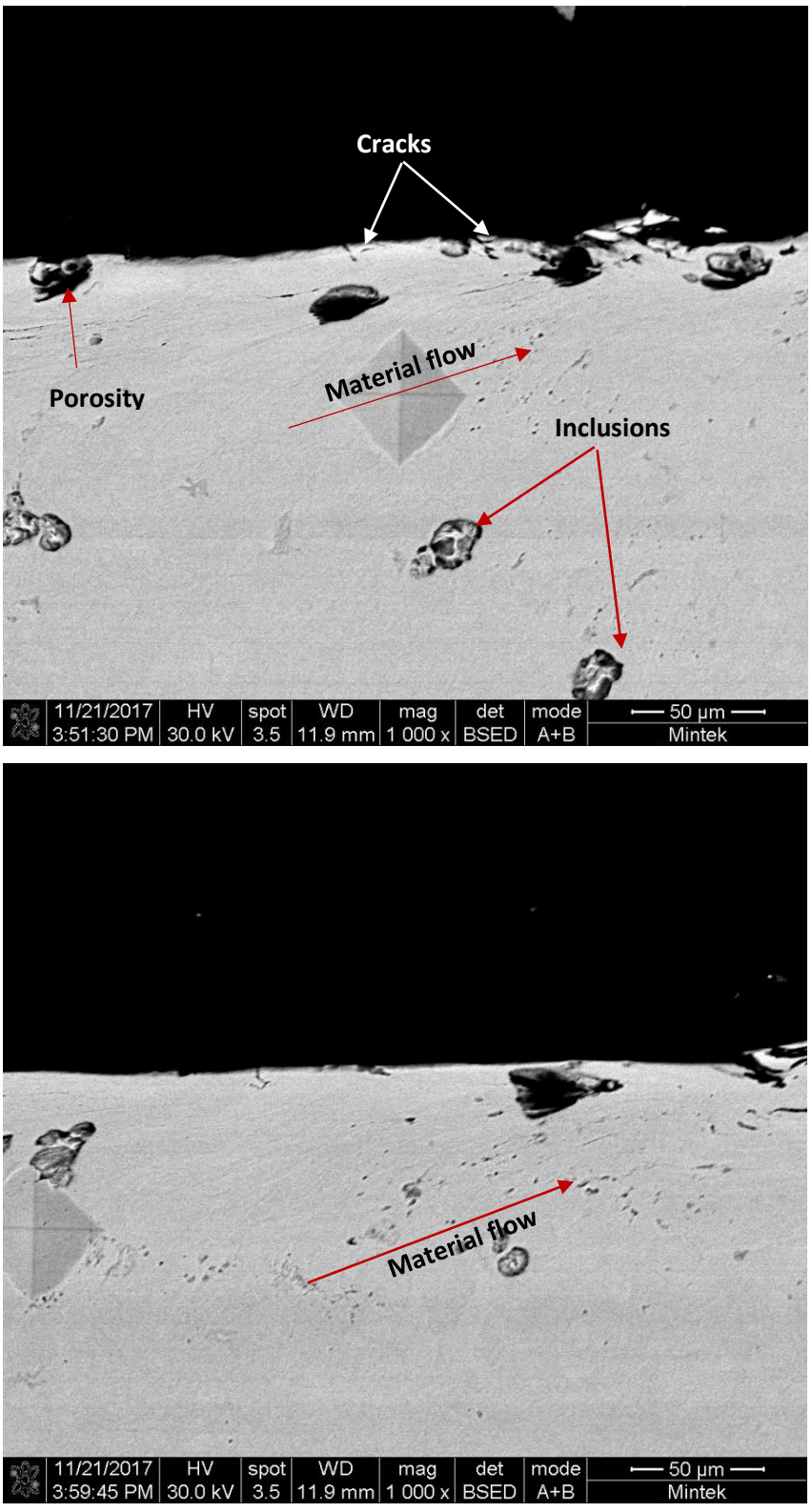

Figure 150. SEM micrograph of the cross- section of the worn surface for Class B after testing at 89.4 MPa, showing deformation (material flow), porosity, inclusions (casting defects) and cracking

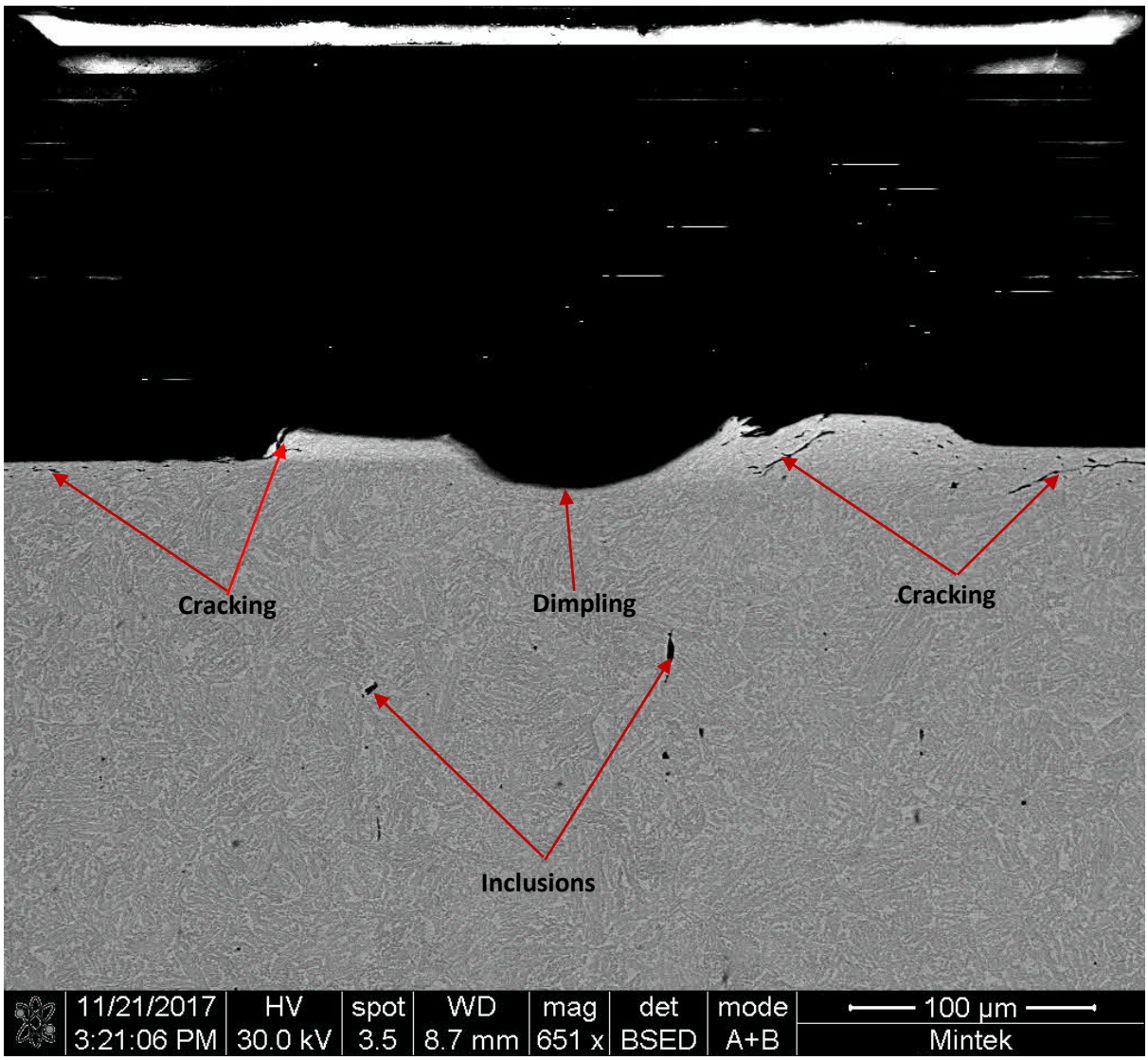

Figure 151. SEM micrograph of the cross- section of the worn surface for Alloy I - 400°C after testing at 89.4 MPa, showing dimpling, cracking and inclusions (casting defects)

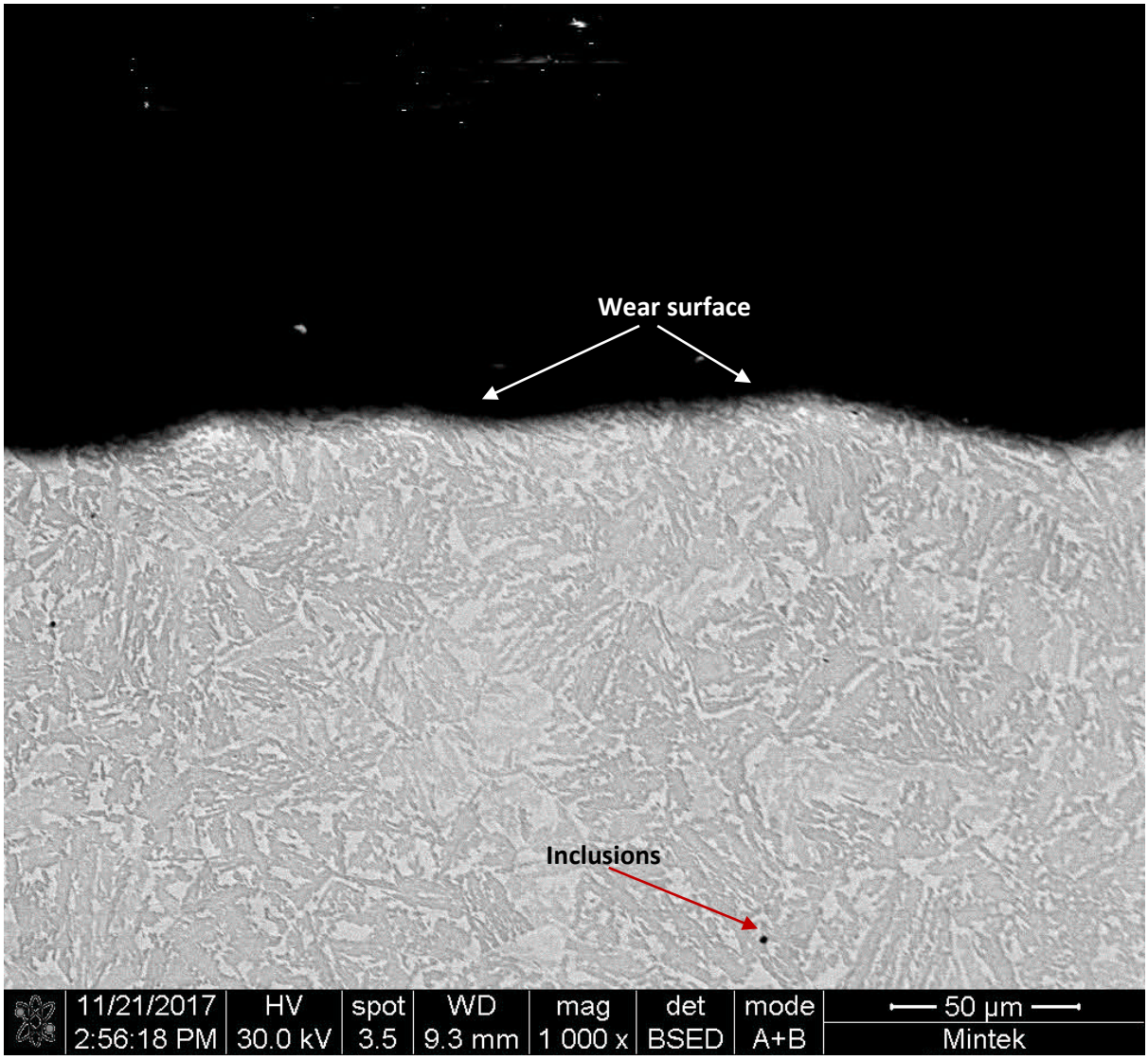

Figure 152. SEM micrograph of the cross- section of the worn surface for Alloy I - 435°C after testing at 89.4 MPa, showing an undulating wear surface

7. Discussion

High carbon pearlitic alloys are the commonly used steels for the production of rail steels today. These alloys have a high wear resistance and with the advanced accelerated cooling technology available today, can be produced with very small interlamellar spacings. The small interlamellar spacing results in high yield strengths, hardness and wear resistance. The higher hardness however results in lower ductility. Wear resistance in rail steels is well monitored and managed in industry, but a major concern is rolling contact fatigue (RCF) resistance. RCF is generally cracking that occurs in the rail steel during service. To have high resistance to RCF a material should have a high resistance to crack initiation and propagation i.e. a high fracture toughness

The interlamellar spacing achievable in modern rail steels is very close to the theoretical minimum and this is limiting the further development of pearlitic rail steels. An alternative steel that has received much attention for rail applications is the bainitic steel. This steel is intrinsically harder than pearlitic steels. Carbide-free bainitic steels comprises a microstructure of bainitic ferrite and retained austenite, but no large brittle carbides. The absence of the carbides gives this microstructure a certain toughness, i.e. resistance to crack initiation and propagation.

The carbide-free bainite alloys need tailored compositions and heat treatments and the addition of high silicon contents. In this study Alloys A to I with compositions listed in Table 31 were studied.

A number of alloy compositions and heat treatments were used to produce a carbide-free bainitic microstructure. In this study the behaviour of the carbide-free bainitic microstructure was studied under different test conditions. Three different Alloy Series 1 to 3 were thus produced as follows:

- Series 1 alloys (Alloys A to D) were produced to study the effect of alloying elements and heat treatment (isothermal and continuous cooling) on the carbide-free microstructure
- Series 2 alloys (Alloys E to H) were used to study the mechanical properties (hardness, tensile and impact) of the carbide-free bainitic microstructure
- Series 3 (Alloy I) was used to study the wear behaviour of the carbide-free microstructure

Isothermal heat treatment

A thermodynamic study of the alloy composition showed that lower carbon contents increased the bainite volume fraction formed. The results also showed that the addition of alloying elements such as manganese, chromium and molybdenum increased the hardenability of the steels by pushing the upper C-curve of the time temperature transformation (TTT) diagram to the right. High silicon alloys with 0.1 wt% carbon were produced in the laboratory but it was difficult to avoid ferrite formation during heat treatment and so alloys with 0.3 wt% carbon were studied in this project.

MUCG83 software was used to study the TTT diagrams for Alloys A to D and Alloy A showed the highest hardenability with a wide range of cooling rates, >0.1°C/s available to avoid ferrite formation.

The T'_0 curve results showed that Alloy C would form the highest volume fraction of bainite, but the TTT curve showed that very high cooling rates >100°C/s are required to avoid ferrite formation. Alloy A therefore is ideal for isothermal heat treatment. An ideal heat treatment procedure for Alloy A would then be as shown in Figure 153.

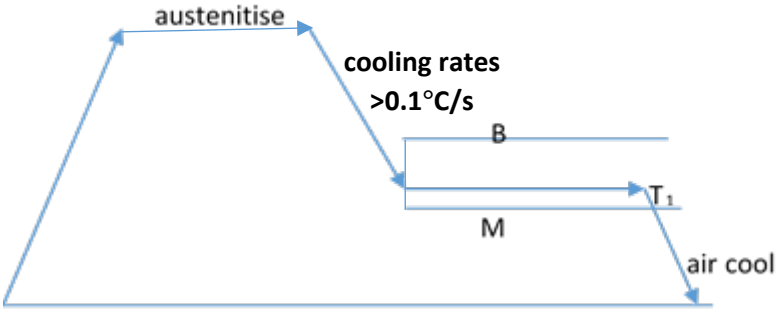

Figure 153. Isothermal heat treatment for Alloy A

Continuous cooling heat treatment

The CCT diagrams showed that Alloy A had an isolated bainite region between 2.5-5°C/s. due to the addition of 30ppm of boron. The bainite regions for Alloys B and C are shielded by the ferrite region. In Alloy D the bainite region is found at slow cooling rates of <1°C/s, due to the addition of 0.2 wt% molybdenum and 0.2 wt% vanadium. This is ideal for thick components that cool slowly, like railway wheels. The ideal heat treatment for Alloy D then would be as shown in Figure 154.

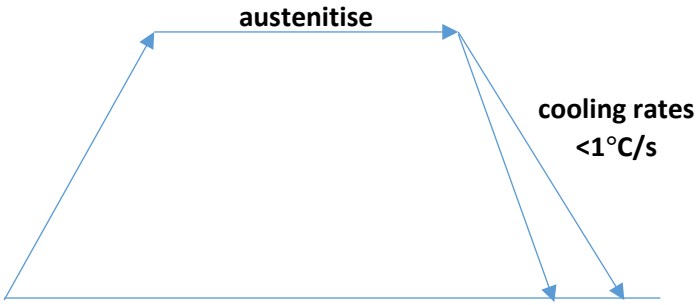

Figure 154. Continuous cooling heat treatment for Alloy D

Table 31. Summary of the composition, phases and mechanical properties of the alloys studied in this project. RA=retained austenite, Hv = Vickers hardness, YS=yield strength, UTS = ultimate tensile strengths, ETF = elongation to failure, DBTT=dustile to brittle transition

Alloy	Chemical Composition, wt%								Temp/ time	phase	RA %	Hv	YS	UTS	ETF	DBTT (27J)
	C	Si	Mn	Cr	Mo	B	V	Al								
A	0.30	1.4	1.9	0.5	0.02	0.003	0.001	0.27	380°C 1hr	CFB (0.23)	-	-	-	-	-	-
B	0.25	1.0	1.5	0.6	0.02	0.0005	0.002	0.24	380°C 1hr	CFB (0.12)	-	-	-	-	-	-
C	0.27	2.0	0.9	0.7	0.00	0.002	0.003	0.24	380°C 1hr	CFB (0.12)	-	-	-	-	-	-
D	0.24	2.0	1.6	0.5	0.18	0.0003	0.20	0.22	380°C 1hr	CFB (0.12)	-	-	-	-	-	-
E	0.19	0.4	1.4	0.5	0.26	0.0003	0.0074	0.003	415°C 1hr	UB	3	284	722	919	14	>130
F	0.26	1.9	1.4	0.6	0.18	0.0007	0.011	0.009	380°C 1hr	CFB	20	412	829	1224	9	>130
G	0.29	1.5	1.4	0.5	0.17	0.0008	0.019	0.018	365°C 1hr	CFB	9	352	738	978	11	>130
H	0.28	1.o	1.6	0.5	0.23	0.0003	0.025	0.006	370°C 1hr	CFB	26	295	714	960	12	82
I-400	0.30	1.78	0.71	0.62	0.16	0.002	0.001	0.022	400°C 1hr	CFB	-	327	-	-	-	
I-435	0.30	1.78	0.71	0.62	0.16	0.002	0.001	0.022	435°C 1hr	CFB	-	352	-	-	-	
Class C [86]	0.67 - 0.77	0.15 - 1.00	0.60 - 0.90	<0.25	-	-	-		-	F+P	7	320-376	-	-	-	
Class B	0.60	0.6	0.7	0.2	-		-	0.05	-	F+P	8	285-351	-	-	-	

Alloys E to F were tested for their tensile properties and the results showed that in the experimental alloy with <20% retained austenite, >12% martensite and ~87% bainited showed the highest yield and tensile strengths and hardness. At higher fractions of retained austenite the elongation and reduction in area increased. The temper results showed that a temperatures >400°C softens the hardness of Alloy F. The elongation of the alloys however were greater than those for AAR Class C. Figure 155 shows that the carbide-free alloys fall in the advanced high strength steel (AHSS) grade of alloys on the elongation vs tensile strength graph for steels. Alloy E is not carbide-free but showed carbides in the microstructure due to its low silicon content. Alloys F-H show a combination of high strength and moderate ductility, the ductility a result of the high retained austenite. The high strength emanating from the combination of fine bainite and martensite in the microstructure.

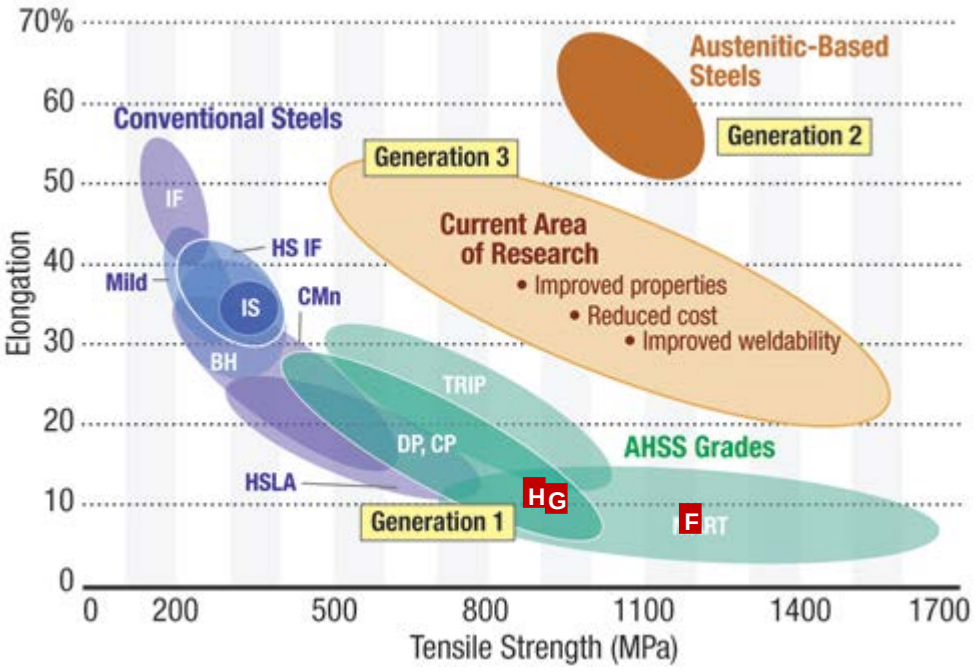

Figure 155. Elongation (%) vs tensile strength (MPa) data for conventional, advanced high strength and austenitic-based steels. The current area of research is also shown for the development of new generation steels [127]

The impact energy results showed that Alloy H with the higher retained austenite of 25% showed the better impact properties. The experimental alloys studied in this project generally showed poor impact properties. Figure 156 shows the measurements of the bainite sub-unit thickness as a function of the transformation temperatures found in literature [53]. Alloys A to D were found to have a thickness of 0.1 µm - 0.2µm, as indicated by the red block on the figure. To improve impact

properties the reduction of the sub-units i.e. grain refinement could be explored by the addition of alloying elements to lower the transformation temperatures.

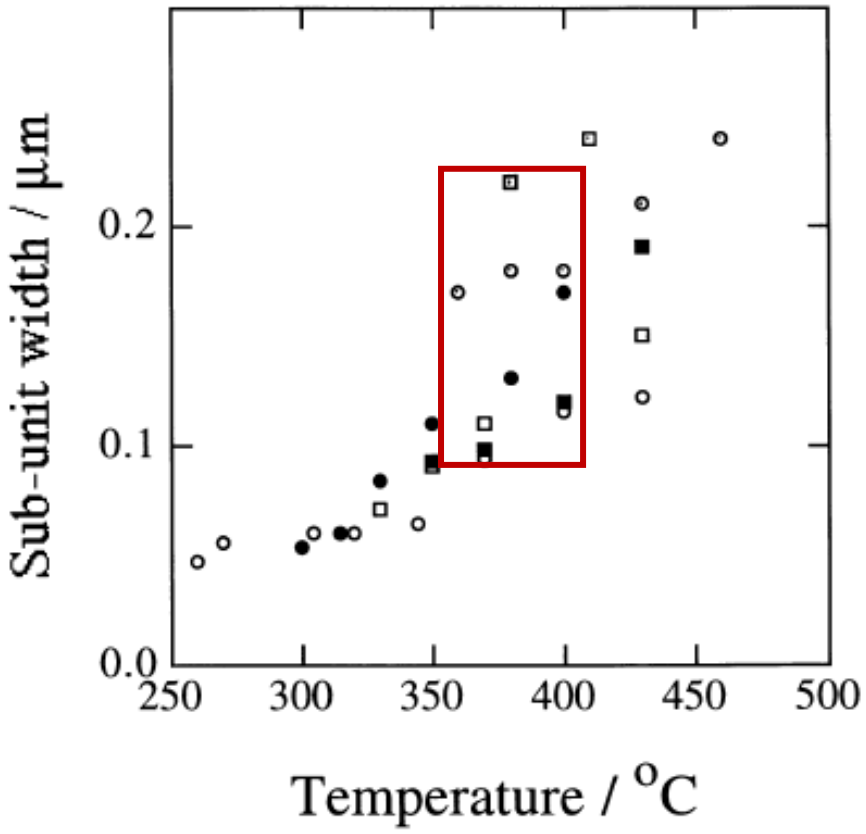

Figure 156. Measurements of the bainite sub-unit thickness as a function of the transformation temperatures [53]. Alloys A to D were found to have a thickness of 0.1 µm - 0.2µm, as indicated by the red block on the figure.

Alloy I, was tested for sliding wear resistance and the parameters used to test the samples on the pin-on-disc wear test rig can be compared to that of the conditions where the rail head/wheel tread contact, see Figure 160. This is limitation of the rig. These conditions are not as severe as the rail gauge/ wheel flange contact conditions. The sliding velocity and contact pressure parameters for the wear test rig place the conditions at the bottom left corner of Figure 157.

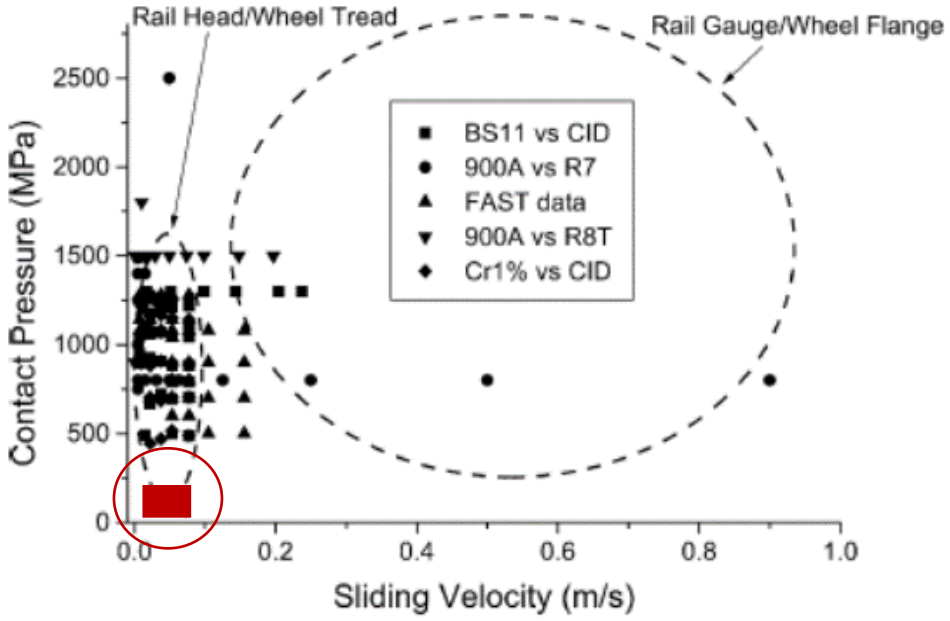

Figure 157. Contact pressure (MPa) and sliding velocity (m/s) for rail steels, with the red square indicating the contact conditions achieved by the wear test rig used in this study.

Generally bainitic steels have been found to have poorer wear resistance than pearlitic alloys. In this study the bainitic alloy heat treated at 400°C showed the better wear properties, similar to that of AAR Class B. the alloys had higher hardness than AAR Class B but showed similar work hardening of the wear surface to that of AAR Class B.

A summary of the best performing alloys for each alloy series tested is given in the Table 32.

Table 32. The best performing alloys for each alloy Series 1 to 3 (Alloys A to I)

Series	Alloy	Comment
Series 1	A	This alloy shows the highest hardenability under isothermal cooling conditions. The TTT curve showed the ferrite curve pushed to the far right. The bainite region in this alloy was also well isolated from the ferrite curve for a wide range of cooling rates.
	D	This alloy shows the highest hardenability under continuous cooling conditions. The CCT curve showed the ferrite curve pushed to the far right. The bainite region in this alloy was also well isolated from the ferrite curve.
Series 2	F	This alloys shows the highest tensile and yield strength and is ideal for components than require good mechanical strength
	H	This alloy shows the highest impact strength resistance
Series 3	I-400	This alloy shows better wear resistance

8. Conclusions

The carbide-free bainitic alloys can be developed to be alternative alloys for rail wheel applications in South Africa. Composition specifications for carbide-free bainitic alloys for rail applications, developed based on this study are given in Table 33. These alloys can be used to satisfy different requirements such as: high impact resistance, high tensile strength, good wear resistance and whether isothermal or continuous cooling will be used.

Table 33. Composition specification for carbide-free bainitic alloys to be used for rail wheel applications

Alloy	Chemical Composition, wt%								Comment	Heat Treatment
	C	Si	Mn	Cr	Mo	B	V	Al		
A	0.30	1.4	1.9	0.5	0.02	0.003	0.001	0.27	Ideal for isothermal heat treatment	Austenitise at 850 and cool at <0.1°C/s to 380°C
D	0.24	2.0	1.6	0.5	0.18	0.0003	0.20	0.22	Ideal for continuous cooling heat treatment	Austenitise at 950 and cool at >1°C/s to romm temperature
F	0.26	1.9	1.4	0.6	0.18	0.0007	0.011	0.009	Ideal for high tensile properties and high hardness	Austenitise at 950°C and cool quickly to 365°C and temper at <400°C
H	0.28	1.o	1.6	0.5	0.23	0.0003	0.025	0.006	Ideal for moderate impact properties	Austenitise at 950°C and cool quickly to 365°C and temper at 200°C
I-400	0.30	1.78	0.71	0.62	0.16	0.002	0.001	0.022	-Ideal for good wear resistance- -	Austenitise at 1050°C and cool quickly to 400°C

- The hardness and tensile properties of carbide-free bainitic alloys are higher for lower retained austenite contents, apart from the elongation which increases with higher retained austenite
- The retained austenite for carbide-free bainite again influenced the impact properties with higher impact resistance as the retained austenite increases
- The wear resistance of carbide-free bainite depends on the work hardening rate of the wear surface

9. Future Work

The following future work is envisioned for this project:

- Produce cleaner carbide-free bainitic alloys and optimise the continuous cooling heat treatment process
- Determine the minimum silicon content required to produce carbide-free bainite
- Study the transformation of retained austenite to martensite during wear testing

10. Publications

Relevant Publications

- A. Kapito, W. Stumpf, M.J. Papo, On the Development of Bainitic Alloys for Railway Wheel Applications, Advanced Metals Initiative ZrTa2011 New Metals Development Network Student Conference Proceedings, October 2011.
- A. Kapito, W. Stumpf, M.J. Papo, Bainite as an Alternative for Railway Wheel Applications, Microscope Society of Southern Africa, Vol 41, 2011, pp. 59

Conference Presentations

- **A. Kapito**, W. Stumpf, M.J. Papo, Bainite as an Alternative for Railway Wheel Applications, Microscope Society of Southern Africa, Pretoria Conference, December 2011.
- **A. Kapito**, W. Stumpf, M.J. Papo, On the Development of Bainitic Alloys for Railway Wheel Applications, ZrTa2011 Conference, Mount Grace, Magaliesburg, September, 2011.

On the development of bainitic alloys for railway wheel applications

by A. Kapito*, W. Stumpf†, and M.J. Papo*

Transaction Paper

Synopsis

The ferrite-pearlite microstructure is the most popular microstructure for alloys used in structural applications, including railway wagon wheels. These alloys have been designed through alloying and thermo-mechanical processing to have a refined microstructure. Ferrite-pearlite alloys are low cost, weldable, have good fabricability, and are reliable under extreme conditions. Given these performance attributes, it seems unlikely then that their dominant position as structural steels would ever be challenged by alternative microstructures. One major achievement in the development of ferrite-pearlite steels has been in the refinement of their interlamellar spacing to very fine distances of the order of < 0.3 µm. A refined microstructure increases the hardness of the alloy, thus increasing its life under wear conditions. The interlamellar spacing in pearlitic steels has, however, been refined almost to its theoretical limit. The increasing demand for speed and increased axle loading on railway wagons requires the use of stronger, tougher, and more durable materials. This has opened the window for the development of novel bainitic steels.

Bainitic alloys have a higher level of microstructural refinement than pearlitic ones. They have shown to have good wear resistance and rolling-contact fatigue resistance, and high toughness. This paper will discuss the progress to date on the development of bainitic railway wheel alloys. Four alloy chemistries have been chosen for possible further development.

Keywords
Bainite, railway wheel, Class B, ferrite-pearlite, Brinell hardness.

Introduction

Railway wagon wheels experience a tremendous amount of wear and fatigue cracking[1–4]. The current ferrite-pearlite alloys are the dominant choice for railway wheel applications. In South Africa, railway wheels are made from medium-high carbon grade steels with 0.57-0.77 wt% carbon, and have a ferrite-pearlite microstructure. These steels, however, have a low yield strength (~680 MPa) and resistance to rolling contact fatigue (RCF). Typical tensile strengths of these alloys range between 900–1 072 MPa, depending on alloy chemistry, with elongations in the range of 7–17 percent. Typical hardness values are 255–363 BHN.

Attempts to improve mechanical properties of ferrite-pearlite steels have focused on increasing the hardness to increase wear resistance and service life. Increased hardness has been achieved through micro-alloying with vanadium (V) and niobium (Nb), production of cleaner steels, and the refinement of the microstructure through the reduction of the interlamellar spacing to values ~0.3 µm[3–6]. Premium Rail steels have been developed for high axle loads, with tensile strengths of ~1 300–1 400 MPa and hardness range of 340–390 BHN.

Despite these developments, the ferrite-pearlite steels are limited in that there is a threshold limit to the hardness that can be achieved, making it difficult to push their wear performance further, owing to the fact that the lamellar spacing has been refined close to its limit[4,7]. In an attempt to develop rail steels with higher hardness, alternative microstructures such as bainite are being explored[8]. Bainitic rail steels are attractive because of their lower carbon contents and finer microstructure, resulting in higher strengths, hardness, toughness, and better weldability[5]. Bainite, like pearlite is a mixture of ferrite and cementite but in a non-lamellar morphology. There are generally two types of bainite: upper and lower[5]. Upper bainite forms at temperatures between 400–500°C and is made up of ferrite laths with carbides between the laths. Lower bainite forms at temperatures between 250–400°C and is also made up of ferrite laths, but the carbides form within the laths.

It is the aim of this ongoing project to develop a bainitic alloy that has better mechanical and wear properties than the current ferrite-pearlite alloys used to make railway wagon wheels. The alloy must be cost-effective and produced locally using existing technology. The development of a new bainitic

* *Advanced Materials Division, Mintek.*
† *Department of Materials Science and Metallurgical Engineering, University of Pretoria.*

 SA ISSN 2225-6253. This paper was first presented at the ZrTa2011 New Metals Development Network Conference, 12–14 October 2011, Mount Grace Country House & Spa, Magaliesburg.

rail wheel steel needs to be considered in the context of the existing bainitic alloys, and Table I lists the chemical composition and mechanical properties of a number of bainitic steels that have been developed for rail applications.

Both upper and lower bainite have potential for railway applications; however, focus has been on the upper bainitic microstructure, particularly on the development of carbide-free alloys. The presence of brittle carbides in the microstructure of bainitic alloys has, to a large extent, hindered their commercialization potential[1,7]. The addition of silicon (~2 wt%) to the steel chemistry suppresses the formation of carbides in upper bainite[1,5]. This results in a microstructure that comprises bainitic ferrite, ductile high-carbon retained austenite (γ), and possibly some martensite (α'). The carbide-free bainitic alloys can attain hardness values of >400 BHN, ultimate tensile strength (UTS) ~1215 MPa, and yield strength ~860 MPa with elongations of up to 15 percent. All the bainitic alloys listed in Table I, with the exception of Micralos, were found to have higher hardness values and better RCF resistance than ferrite-pearlite alloys; however, their wear resistance was poorer[9–12]. In general, therefore, the currently developed bainitic alloys have better RCF resistance but their wear resistance seems questionable.

Experimental procedure

Production and heat treatment of experimental alloys

Three alloys, namely a conventional Class B ferrite-pearlite alloy and bainitic V1 and V2 alloys, were melted in an induction furnace open to the atmosphere, with a target composition as listed in Table II.

The critical heat treatment temperatures for the alloys were calculated using Equations [1–5] as listed below[13].

$$A_{c1} = 723 - 20.7Mn - 16.9Ni + 29.1Si + 16.9Cr + 290As + 6.38\,W \quad [1]$$

$$A_{c3} = 910 - 203\sqrt{C} - 15.2Ni + 44.7Si + 104V + 31.5Mo + 13.1W \quad [2]$$

$$M_s = 539 - 423C - 30.4Mn - 17.7Ni - 12.1Cr - 11.0Si - 7.0Mo \quad [3]$$

$$B_s = 630 - 45Mn - 40V - 35Si - 30Cr - 25Mo - 20Ni - 15W. \quad [4]$$

$$CE = C + \frac{Mn}{6} + \frac{Cr + Mo + V}{5} + \frac{Cu + Ni}{15} \quad [5]$$

The critical heat treatment temperatures are the temperatures at which ferrite begins to transforms to austenite (A_{c1}), the temperature at which the steel becomes fully austenitic (A_{c3}), the martensite start temperature (M_s), and the bainite start temperature (B_s). These temperatures were used to choose the annealing, tempering, homogenizing, and the salt bath temperatures.

After casting, the Class B alloy was solution annealed at 870°C for two hours and then quenched in a spray of water. It was then allowed to cool in air before tempering at 580°C.

Table I

Commercial bainitic rail alloys

Name	Chemical composition (wt %)				
	C	Mn	Si	Ni	Cr
J6	0.3	2	1.8		1.9
LB	-	-	-	-	-
CF-B	-	-	-	-	-
Micralos	0.4	1		0.5	0.4
Low-medium carbon Si-Mn-Mo-V steel	0.2	2	1.4	0.2	0.1

Name	Mechanical Properties				
	Hardness	UTS (MPa)	Yield (MPa)	Elongation (%)	
J6	42-46HRC	-	-	9	
LB	>430BHN	-	-	9	
CF-B	>400BHN	-	-	-	
Micralos	386BHN	1215	1135	15	
Low-Medium Carbon Si-Mn-Mo-V steel	310BHN	1090	860	15	

Table II

Target composition of experimental alloys

Sample	Element (wt %)					
	C	Mn	Si	Al	Cr	B
Class B	0.57-0.67	0.60-0.90	0.15 min	0.08 max	0.3 max	-
V1	0.3-0.4	1.5-2	2-3	0.02-0.03	0.5-0.6	0.0015-0.003
V2	0.3-0.4	1.5-2	0.5-1	0.02-0.03	0.5-0.6	0.0015-0.002

Table III

Actual chemical compositions of experimental alloys

Sample	Element (wt %)					
	C	Mn	Si	Al	Cr	B
Class B	0.59	0.72	0.4	0.07	0.3	-
V1	0.41	1.99	2.8	0.02	0.5	0.003
V2	0.40	1.79	0.8	0.02	0.5	0.002

Alloys V1 and V2, after casting, were homogenized for 2 hours at 1 000°C and air-cooled. These alloys were then forged and hot-rolled at 1 000°C into plates with dimensions of 300 mm × 70 mm × 15 mm. The plates were then austenitized (A_{c3} +50°C) and immediately quenched in a salt bath at 400°C for 1 hour to allow for bainite transformation.

Characterization and mechanical testing of experimental alloys

Cross-sections of the as-cast, homogenized, and heat-treated alloys were cut and tested for composition using spark emission spectroscopy. Additional cross-sections were ground, polished to a 1 µm finish, and etched with 2% Nital to reveal the microstructure. A Nikon optical microscope was used to study the microstructures. The scanning electron (SEM) microscope was also used to study the microstructure in the backscatter (BSE) mode.

Brinell hardness measurements using a load of 750 kg were performed on cross-sections of the as-cast, homogenized, and heat treated ingots.

Tensile specimens with 6 mm diameter and 25 mm gauge length were used for tensile tests. The tests were carried out in accordance with the requirements of ASTM E8-99. In this test, the specimens were subjected to a continually increasing uniaxial tensile force using a tensile test machine while measurements of the elongation of the specimen were simultaneously recorded.

Charpy impact samples were machined from the heat-treated ingots. These were tested at room temperature in accordance with ASTM E23-72. The machined specimens had dimensions of 10 mm × 10 mm × 55 mm and contained a 45° V notch, 2 mm deep with a 0.25 mm root radius along the base. The energy absorbed during impact was measured.

Results and discussion

Chemical composition

Table III lists the actual chemical compositions of the experimental alloys.

Alloys V1 and V2 had varying silicon (Si) contents to determine its effects on the formation of bainite. Manganese (Mn) and chromium (Cr) were added for hardenability. Boron (B) was added to suppress the formation of allotriomorphic ferrite and to increase the hardenability of bainite.

Metallography

The microstructures for the alloys produced in the as-cast, homogenized, and heat-treated conditions are shown in Figures 1 to 3. Figure 1 shows the microstructures for the Class B alloy, and Figures 2 and 3 for V1 and V2 alloys, respectively.

The microstructures for the Class B alloy in both the as-cast and solution-treated condition were ferrite-pearlite (see Figure 1). The solution annealing and tempering refined the pearlitic microstructure.

The microstructure of V1 in the as-cast condition is ferrite-pearlite (Figure 2a). After homogenization, the pearlite is refined as shown in Figure 2b. The final microstructure after heat treatment is that of upper bainite and untempered martensite. The martensite is formed during water quenching after the salt bath quench, which implies that the

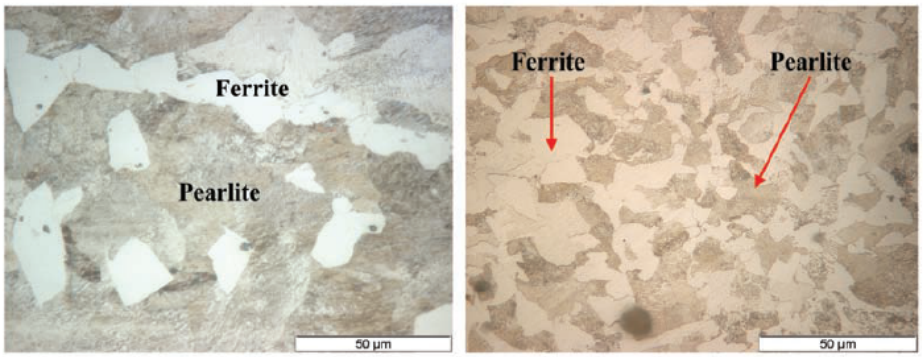

Figure 1—The microstructure of the Class B alloy showing (a) ferrite-pearlite in the as-cast and (b) the solution-treated and tempered condition

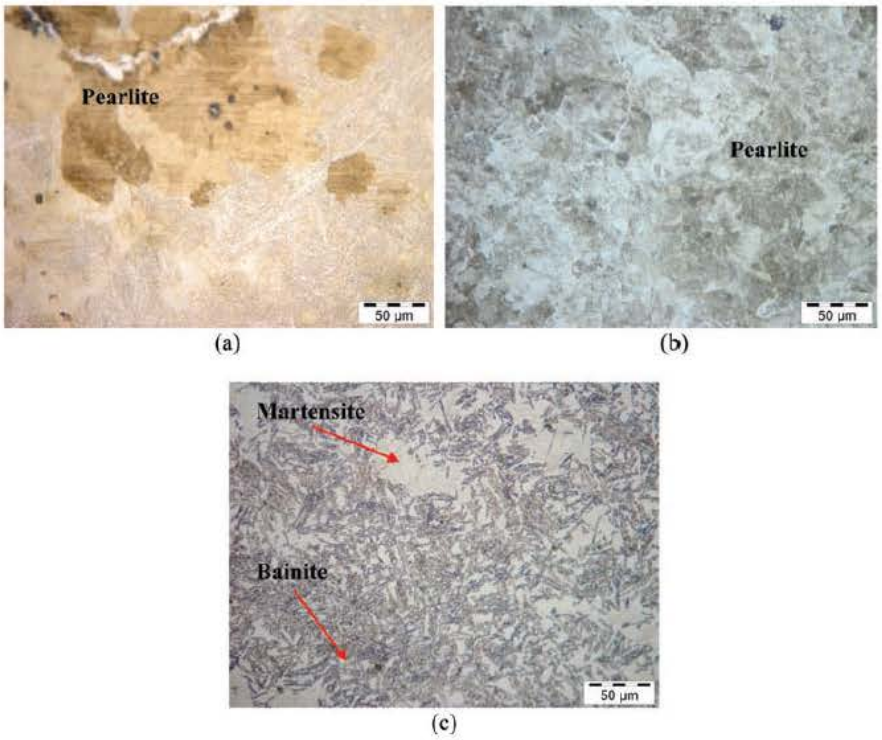

Figure 2—The microstructure of alloy V1 showing (a) pearlite in the as-cast condition, (b) refined pearlite in the homogenized condition, and (c) upper bainite and martensite in the heat-treated condition

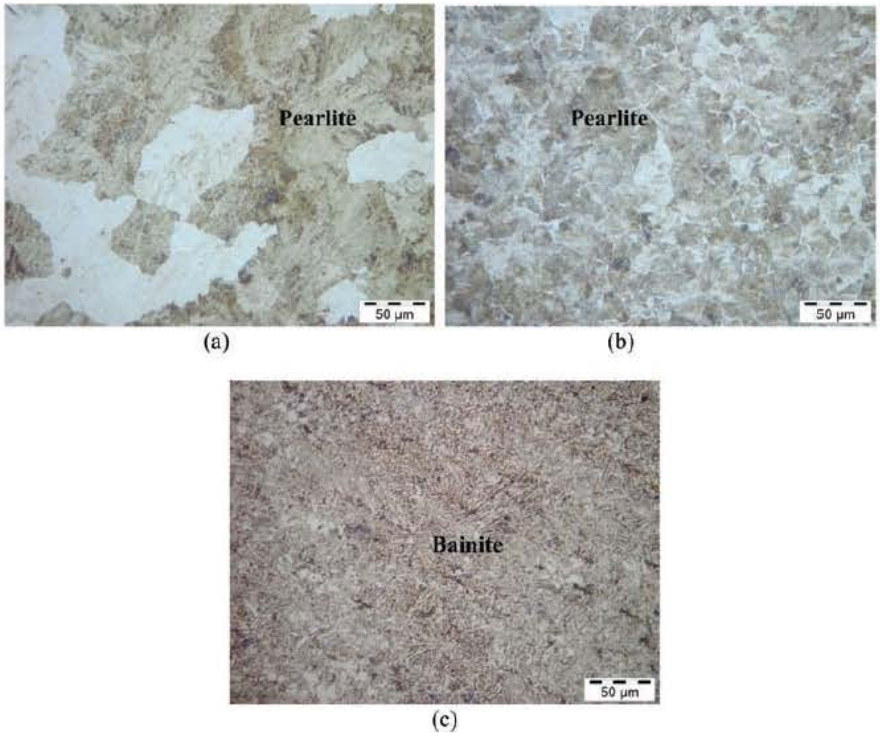

Figure 3—The microstructure of alloy V2 showing (a) pearlite in the as-cast condition, (b) refined pearlite in the homogenized condition, and (c) upper bainite in the heat-treated condition

microstructure after the salt bath treatment was bainite and retained austenite. Alloy V1 has a high Si content of ~3 wt%. Silicon enriches the austenite (γ) with carbon and stabilizes it to lower temperatures.

Similarly, the microstructures of alloy V2 in the as-cast and homogenized conditions were pearlitic, with a finer microstructure after homogenization. The amount of upper bainite formed during the salt bath quench, however, was greater than that formed in V1, due to the lower silicon content of V2. It is ideal to increase the amount of bainite formed when developing alloys for railway wheel applications. This is because the transformation of retained austenite into martensite during operation embrittles the railway wheel and causes cracking. A silicon content of <3 wt% is thus ideal for the production of the experimental bainitic alloys; in fact, 2 wt% is usually used to produce carbide-free bainite[1,5,7,12].

Scanning Electron Microscopy (SEM)

Figure 4 shows the SEM micrographs of the bainitic alloys. SEM imaging was used to study the features of the microstructure at higher magnifications than those possible with optical microscopy. SEM imaging revealed the presence of martensite in alloy V2, whereas this was not clear with optical microscopy (Figure 4a). Both alloys V1 and V2 were composed of bainite ferrite and martensite. There seems to be no evidence of carbides in the microstructure. However, to verify this result, transmission electron microscopy (TEM) will need to be utilized as this has an even higher magnification capability than the SEM. The SEM was also unable to resolve the individual bainite-ferrite laths. The maximum resolution that could be achieved with the SEM without affecting the clarity of the image was 0.5 µm. With TEM, resolutions of 0.2 µm can be achieved.

Hardness

The hardness values of the alloys are listed in Table IV. Class B had a typical hardness value of 255–269 BHN in the as-cast and tempered condition. V1 has a high hardness of 490 BHN, probably due to the martensite in its microstructure. V2 in the heat-treated condition had a hardness of 363 BHN, higher than Class B. A higher hardness translates into a higher wear resistance.

Tensile tests

The tensile tests results for the alloys as listed in Table V showed that V1 was very brittle, with an elongation of only 0.8%. This is because of the martensite present in its microstructure. Testing this alloy in the tempered condition could improve the results. Alloy V2 had a tensile (1131 MPa) and yield (700 MPa) strength higher than Class B, but with good ductility of ~15%. Compared to alloy V1 it had better ductility and higher strengths. The higher yield strengths of alloys V1 and V2, compared to the Class B alloy, implies that these alloys should have superior resistance to RCF.

Table IV

Brinell hardens results for the experimental alloys

Condition	Brinell (BHN)		
	Class B	V1	V2
As-cast	255	397	304
Homogenized	-	279	263
Heat-treated	269	490	363

Table V

Tensile test results for the experimental alloys

Sample identity	UTS (MPa)	Yield Stress (MPa)	Elongation (%)
Class B	730	463	23.0
V1	925	862	0.8
V2	1131	700	14.9

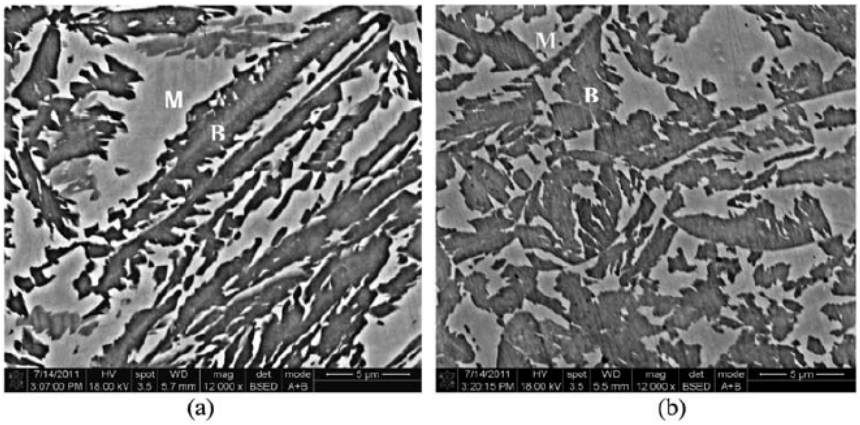

(a) (b)

Figure 4—SEM micrographs of (a) V1 and (b) V2 bainitic alloys showing martensite (M) and bainite (B)

Table VI
Charpy V-notch results for the experimental alloys

Sample identity	Impact energy (J)
Class B	21.0
V1	3.4
V2	4.1

Charpy V-notch tests

The conventional Class B alloys are expected to have a minimum impact energy of 16 J. From the Charpy impact test results Class B was found to have an impact energy of 21 J, which is within specification. High-silicon bainitic steels with retained austenite have been found to have an impact energy of ~25 J. However, the presence of martensite in the experimental is detrimental to their impact toughness. Alloys V1 and V2 had very low impact toughness values of 3–4 J. Although alloy V2 had good ductility results from the tensile test, this did not translate to good impact toughness.

Conclusions

According to previous studies[5], the mixed microstructures consisting of bainite and martensite have been found to be a consequence of inadequate heat-treatment or the use of steels with inadequate hardenability. Early research has indicated that bainite-martensite microstructures have poor ductility, toughness, and strength. As the amount of bainite increases the mechanical properties should improve. It is therefore vital to determine the correct heat treatment for the steel alloys to avoid martensite formation and maximize bainite transformation.

From the preliminary results, the following conclusions can be drawn:

- A high silicon content of ~3 wt% stabilizes the austenite during transformation and decreases the amount of bainite transformation significantly
- Bainite has higher tensile and yield strengths than pearlite, but with good ductility
- The toughness of the experimental bainitic alloys was very low compared to that of pearlitic alloy. This is believed to be due to the presence of martensite in the microstructure. Tests with retained austenite or tempered martensite should show better toughness results.

Future work

In the near future the following aspects need to be addressed:

- TEM analysis of the bainitic alloys to determine the presence/absence of carbides in the microstructure
- Wear testing of the produced alloys will benchmark the bainitic alloys V1 and V2 against the conventional ferrite-pearlite Class B rail grade. Wear is vital in determining the life of railway wheels
- Dilatometry testing to determine the correct heat treatment for the alloys so that continuous cooling and transformation (CCT) diagrams can be determined. CCT diagrams will allow for the selection of correct cooling temperatures and rates to achieve a bainitic microstructure and avoid martensite and ferrite formation.

Acknowledgement

We would like to thank Mintek and AMI-FMDN for their financial support and permission to publish this work. We also thank the University of Pretoria and Professor Waldo Stumpf for his technical support.

References

1. Bhadeshia, H.K.D.H. Improvements in and relating to carbide-free bainitic steels and methods of producing such steels. *International Publication Number: WO 96/22396*, 11 January 1996. International Patent Classification: C21D 9/04, 1/20, 1/02, C22C 38/00.
2. Ueda, M., Uchino, K., Matsushita, K. and Kobayashi, A. Development of HE rails with high wear and damage resistance for heavy haul railways. *Nippon Steel Technical Report No. 85*, January 2002. pp. 167–172.
3. Lee, K.M. and Polycarpou, A.A. Wear of Conventional pearlitic and improved bainitic rail steels. *Wear,* vol. 259, 2005. pp. 391–399.
4. Zhang, M. and Gu, H. Microstructure and mechanical properties of railway wheels manufactured with low-medium carbon Si-Mn-Mo-V steel. *Journal of University of Science and Technology Beijing*, vol. 15, no. 2, April 2008. pp. 125.
5. Bhadeshia, H.K.D.H. Bainite in Steels, 2nd edn. London, IOM Communications Ltd. 2001. pp. 347.
6. Yates, J.K. Innovation in Rail Steels. www.msm.cam.ac.uk/phase-trans/parliament,html. Accessed May 2010.
7. Bhadeshia, H.K.D.H. Novel Steels For Rails, *Encyclopedia of Materials Science:* Science and Technology. Pergamon Press, Elsevier Science, 2002. pp. 1–7.
8. Lee, K.M. and Polycarpou, A.A. Wear of Conventional pearlitic and improved bainitic rail steels. *Wear,* vol. 259, 2005. pp. 391–399.
9. Clarke, M. Wheel rolling contact fatigue (RCF) and rim defects investigation. *Wheel Steels Handbook*. Research Programme Engineering Rail Safety and Standards Board. pp.1–20.
10. Stock, R. and Pippan, R. RCF and wear in theory and practice—the influence of rail grade on wear and RCF. *Wear*, vol. 271, no. 1–2, 18 May 2011. pp. 125–133.
11. Gianni, A., Ghidini, A., Karlsson, T., and Ekberg, A. Bainitic steel grade for solid wheels: metallurgical, mechanical, and in-service testing. Proceedings of the Institution of Mechanical Engineers, Part F: Journal of Rail and Rapid Transit March 1, 2009. p. 223. *Special Issue Paper*, vol. 163. pp. 163–171.
12. Zhang, M. and Gu, H. Microstructure and mechanical properties of railway wheels manufactured with low-medium carbon Si-Mn-Mo-V steel. *Journal of University of Science and Technology Beijing*, vol. 15, no. 2, April 2008. pp. 125.
13. Stumpf, W. University of Pretoria, heat treatment of steels. Part of the postgraduate course NHB 700, University of Pretoria, August-September 2010. ◆

BAINITE AS AN ALTERNATIVE MICROSTRUCTURE FOR RAILWAY WHEEL APPLICATIONS

A. Kapito[1], W. Stumpf [2] and M.J. Papo[1]

[1]Advanced Materials Division, Mintek, South Africa, [2]Dept. of Materials Science and Metallurgical Engineering, University of Pretoria, South Africa

The majority of railway wheels are manufactured from steel grades that have a carbon content of 0.65-0.82 wt% and have a pearlitic microstructure[1]. Pearlite is a lamellar mixture of ferrite and carbides. Pearlitic rail steels have been developed over the years to have a very fine microstructure through alloying and heat treatment. This has produced pearlitic rail steels with high hardness values of 380-400HB, yield strengths of 896MPa and good wear resistance[1,2]. The pearlitic steels, however, have low rolling contact fatigue resistance, a major failure mode in railway wheels. In addition, they form brittle martensite during sliding/braking. Their development in terms of hardness and microstructural refinement has also peaked[2,3]. The demand for higher speeds and axle loads on railway wheels, however, requires stronger and tougher alternative microstructures for railway wheels. The bainitic microstructure is being developed as an alternative to pearlite for railway wheel applications.

Bainite is a mixture of non-lamellar carbides and lath-shaped ferrite but in a much finer structure than pearlite. There are two types of bainite, upper and lower. Upper bainite consists of elongated cementite (Fe_3C) particles on its ferrite lath boundaries while lower bainite consists of heavily dislocated ferritic laths with Fe_3C precipitating inside the laths [1,4].

Bainitic steels are being developed mainly for high speed and heavy haul operations[4,5]. Laboratory tests have shown the bainitic steels to have better tensile strength, impact toughness, resistance to rolling contact fatigue and comparable wear resistance to pearlitic steels, particularly the high silicon (~2wt%) grades. These steels typically have a chemical composition of 0.3-0.4wt% C, 1-2wt% Si, 2wt% Mn and 0.5wt% Cr.

It is the aim of this work to develop a bainitic steel alloy for railway wheel applications. This alloy should be cast locally and be used as an alternative to the locally-produced pearlitic railway wheel grades, for example Class B.

Two alloys, one with a composition typical of a Class B and the other typical of a high silicon bainitic grade, were cast in an induction furnace. The alloys were homogenized at 1200°C and air cooled. The bainite was formed in a salt bath at 400°C after austenitization. Cross-sections of the as-cast, homogenized and heat treated samples were taken, polished and etched with a potassium metabisulphate ($K_2S_2O_5$) solution to reveal the microstructure. The microstructures were examined using an Olympus Optical Microscope.

Figure 1 shows the pearlitic microstructure of the homogenized bainitic alloy and Figure 2 shows the bainitic microstructure formed. The bainitic alloy was found to have higher strength (1131MPa) than the Class B (807MPa) grade but with a good ductility of 15%. Impact test results (~4J), however, were poor for the bainitic alloy. This was unexpected and further tests are required to determine the cause.

References

1. Bhadeshia, H.K.D.H. (1992) Bainite in Steels: Transformations, Microstructures and Properties, London, IOM Communications Ltd.
2. Olivares, O. *et al.* (2011) Wear 271, 364.
3. Robles Hernandez, F.C. *et al.* (2010), J. Rail Rapid Transit, 224(5), 413.
4. Chang, L.C. (2005) Wear 258, 730.
5. Caballero, F. G. and Bhadeshia, H. K. D. H. (2004) Int. J. ISSI 1(1), 15.

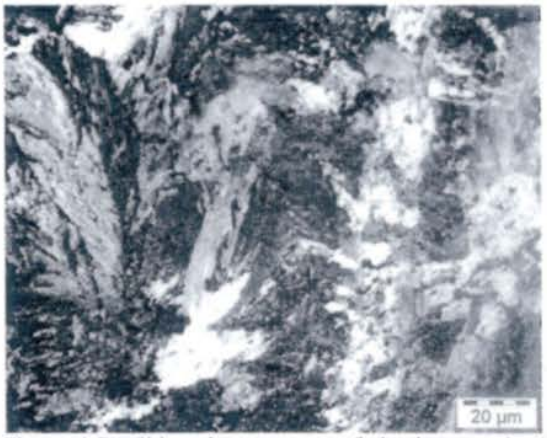

Figure 1.Pearlitic microstructure of the homogenized bainitic alloy.

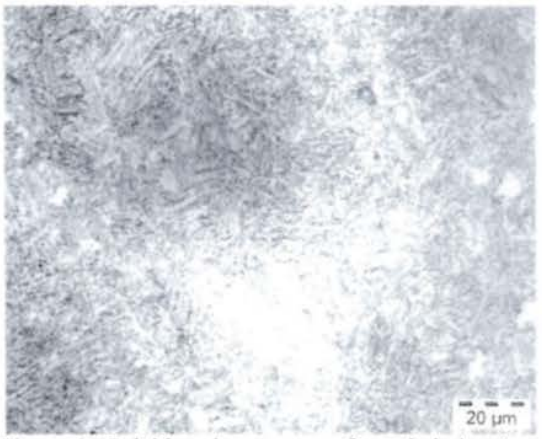

Figure 2. Bainitic microstructure formed during heat treatment in a salt bath at 400°C.

Corresponding author: *AsimenyeK@mintek.co.za*

11. References

1. Transnet, Market Demand Strategy, http://www.transnetfreightrail-tfr.net/MDS/Pages/Overview.aspx, visited November 2016
2. Transnet, Transnet Annual Results Presentation March 2016, https://www.slideshare.net/TransnetPortTerminals/transnet-annual-results-presentation-march-2016, visited November 2016
3. I. Venter, Italian group invests R200m in local railway wheel plant, Creamer Media's Engineering News, 2 June 2017, http://www.engineeringnews.co.za/article/italian-group-invests-r200m-in-local-railway-wheel-plant-2017-06-02, visited September 2018
4. International heavy Haul Association, Guidelines to Best Practices for Heavy Haul Railways Operations: Wheel and Rail Interface Issues, https://www.scribd.com/document/355255964/ihha-guidelines-to-best-practices-for-heavy-haul-railways-operations-wheel-rail-interface-issues-pdf, visited November 2016
5. N. Ridley, A Review of the Data on the Interlamellar Spacing of Pearlite, Metallurgical Transactions A Volume 15a, June 1984, pp. 1019-1036
6. B. Bramfitt, *A Metallurgical Perspective of the Role of Rail Steel in the Growth of America*, 2011 AIST Adolf Martens Memorial Steel Lecture, A Publication of the Association for Iron & Steel Technology, January 2012, pp. 158-172
7. Agico Group, How Rails are Made, http://www.railway-fasteners.com/news/how-rails-are-made.html, visited July 2018
8. B. Talamini, J.E. Gordon and A.B. Perlman, Finite Element Estimation of the Residual Stresses in Roller-Straightened Rail, Copyright @ 2004 ASME https://www.researchgate.net/figure/Schematic-of-the-steps-of-the-rail-manufacturing-process_fig1_266095612, visited July 2018
9. Nippon Steel and Sumitomo Metal, Structural Steel, https://www.nssmc.com/en/product/construction/process/, visited August 2018
10. Arcelormittal, Steelton Steel Making and Processing Flow Chart, http://rails.arcelormittal.com/ckeditor_assets/attachments/648/rail-mill-steelton-.jpg, visited August 2018

11. M Diener and A Ghidini, *Materials for Heavy Haul Solid Wheels: New Experiences*, Special Issue Paper, Proc. IMechE Vol. 224 Part F: J. Rail and Rapid Transit, JRRT356, 19 April 2010, 421-428
12. D.B. Williams and E.P. Butler, Grain boundary discontinuous precipitation reactions, Int Met Reviews: No 3 (1981) p153 (Review)
13. P.R Howell, The pearlite reaction in steels: Mechanisms and crystallography. Part 1: From H. C. Sorby to R. F. Mehl, Materials Characterization; Journal Volume: 40; Journal Issue: 4-5, pp. 227
14. L. Xiao-Fei, P. Langenberg, S. Münstermann, W. Bleck, R*ecent Developments of Modern Rail Steels,* http://www.metal.citic.com/iwcm/UserFiles/img/cd/2005-HSLA-NB/HSLA-034.pdf, cited June 2014
15. J.N Hobstetter, "Decomposition of Austenite by Diffusional Processes", Ed V.F Zackay and H.I. Aaronson, Publ Interscience NY (1962)p1
16. A. Hultgren, Isothermal transformation of austenite. Trans. ASM. 1947;39:915–1005.
17. S.S. Sahay, G. Mohopatra and G.E. Totten, *Overview of Pearlitic Rail Steel: Accelerated Cooling, Quenching and Mechanical Properties*, Journals of ASTM International, Vol.6, No.7, pp. 1-26
18. R. Kuziak and T. Zygmunt, A New Method of Rail Head Hardening of Standard-Gauge Rails for Improved Wear and Damage Resistance, Steel Research Int. 84 (2013) No. 1, pp. 13-19
19. R.J. Ackert; R.W. Witty; P.A. Crozier Method For The Production of Improved Railway Rails by Accelerated Cooling in Line With the Production Rolling Mill, Patent Number: 4,486,248, Date of Patent: Dec. 4, 1984
20. K. Tokunaga, T. Arimura, M. Yamaguchi, M. Yamaguchi, H. Fukuda, M. Honjo, R. Matsuoka and M. Takemasa, 7Development Of SP4 Rail with High Wear Resistance for Heavy Haul Railways, http://seaisi.org/seaisi2017/file/file/full-paper/10B-6%20Development%20of%20SP4%20Rail%20with%20High%20Performance%20Pearlitic%20for%20Heavy%20Haul%20Railways.pdf, visited July 2018

21. K. Saeki And K. Iwano, Progress and Prospects of Rail for Railroads, Technical Review, Nippon Steel & Sumitomo Metal Technical Report No. 105 December 2013
22. .H. Yokoyama, S. Mitao and M. Takemasa, Development of High Strength Pearlitic Steel Rail (SP Rail) with Excellent Wear and Damage Resistance, NKK TECHNICAL REVIEW No.86 (2002), pp 1- 7
23. H. Yoshitake, Y. Makino, K. Suc1no, H. Kageyama, T. Suzuki, K. Fukuda, And T. Miyata, Manufacture and Properties of Deep Head Hardened Rail, Transportation Research Record 1174, pp. 50-56
24. A. Moser And P. Pointner, Head-Hardened Rails Produced from Rolling Heat, Transportation Research Record 1341, pp 70-74
25. ASM International, *High-Carbon Steels: Fully Pearlitic Microstructures and Applications*, http://www.asminternational.org/documents/10192/1849770/Chapter_15_WEB.pdf, cited August 2015
26. G. Gersh and R. Heyder, *Advanced Pearlitic and Bainitic High Strength Rails Promise to Improve Rolling Contact Fatigue Resistance*, https://www.researchgate.net/publication/266035565_Advanced_pearlitic_and_bainitic_high_strength_rails_promise_to_improve_rolling_contact_fatigue_resistance, visited June 2017
27. I. Poschmann, E. Tschapowetz and H. Rinnhofer, *Heat Treatment for Railway Wheels, Tyres and Rings*, http://www.presstrade.eu/downloads/aft/AFT_WBER_E.pdf, cited January 2012
28. V.J. Matjeke, Reliability studies of cast and forged railway wheels, MSc Thesis, University of the Witwatersrand, 2017
29. M. Clarke, Wheel rolling contact fatigue (RCF) and rim defects investigation to further knowledge of the causes of RCF and to determine control measures, RSSB Wheel Steel Guide, https://www.scribd.com/doc/30796881/T672-Wheel-Steel-Handbook-Final, visited August 2018
30. M.S. Shirley, *Method for Casting Objects with an Improved Riser Arrangement*, US 6 932144 B2, August 23, 2005

31. L.V. Chuprina, G.A. Pol'skii, Y .N. Grishchenko, and A.D. Rozhkova, *Current Trends in the Production of Railroad Wheels and the Effect of Out-Of-Furnace Treatment of the Steel on Their Properties*, Metallurgist, Vol. 50, Nos. 7–8, 2006.

32. Rail Wheel Factory (Indian Railways), http://www.docstoc.com/docs/46726713/Rail-Wheel-Factory-(Indian-Railways) accessed March 2011.

33. K. Wang and R. Pilon, *Investigation of Heat Treating of Railroad Wheels and its Effect on Braking Using Finite Element Analysis,* Griffin Wheel Company, http://simplorer.com/staticassets/ANSYS/staticassets/resourcelibrary/confpaper/2002-Int-ANSYS-Conf-116.PDF, visited Dec 2011

34. C. Lonsdale and D. Stone, *Some Possible Alternatives for Longer-Life Locomotive Wheels*, Proceedings of IMECE02, 2002 ASME International mechanical Engineering Congress & Exposition, November 17-22, New Orleans, Louisiana, pp. 239-244

35. M. Alessandroni, A.M. Paradowska, E. Perelli Cippo, R. Senesi, C. Andreani, G. Gorini, P. Montedoro, F. Chiti, D. Sala and D. Spinelli, *Investigation of Residual Stress Distribution of Wheel Rims using Neutron Diffraction*, Materials Science Forum Vol. 681 (2011) pp 522-526

36. S. Nabeshima, H. Nakato, T.Fujl, T. Fujimura, K. Kushida And H. Mizota, Control of Centerline Segregation in Continuously Cast Blooms by Continuous Forging Process, ISIJ International. Vol. 35 (1995), No. 6, pp. 673-679

37. C.H. Moon, K.S. Oh, J.D Lee, S.J. Lee And Y. Lee, Effect of the Roll Surface Profile on Centerline Segregation in Soft Reduction Process, ISIJ International, Vol. 52 (2012), No. 7, pp. 1266–1272

38. O. Haida, H. Kitaoka, S. Kakihara, H. Bada, S. Shiraishi and Y. Habu, Macro- and Semi-macroscopic Features of the Centerline Segregation in CC Slabs and their Effect on Product Quality, Transactions ISIJ, Vol. 24, 1984, pp. 891-898

39. C. Mapelli, M. Vedani and A. Zambon, On Microstructure Development And Inclusion Generation In A Continuously Cast Resulphurised Steel, http://www.scielo.org.ar/img/revistas/laar/v32n3/html/v32n3a02.htm

40. Lucchini RS Group, Wheels, http://lucchinirs.com/railway-products/wheels/, visited August 2018
41. N. Singh, Wheels, https://www.slideshare.net/nishanrupial/wheel-defects, visited September 2018
42. C.P. Lonsdale and R.D. Swartzell, Recent Improvements in Wrought Railroad Wheel Production at Standard Steel, http://www.standardsteel.com/rdpapers/wroughtwheel.pdf, visited September 2018
43. V. Angadia and H.A. Shivappa, Determination of Effect of Residual Stresses Induced in Railway Wheels using Finite Element Approach, International Journal for Ignited Minds (IJIMIINDS), Volume: 03 Issue: 10, | Oct-2016, pp. 166-174, Available @ www.ijiminds.co, visited September 2018
44. M. Milošević, A. Miltenović, M. Banić and M. Tomić, Determination of Residual Stress in Rail Wheel During Quenching Process with FEM Simulation, XVII International Scientific-Expert Conference on Railways, RAILCON '16, Serbia, Niš, October 13-14, 2016, pp. 65-68
45. G. Donzella, S. Granzotto, G. Amici, A. GhidinP and R. Bertelli, Microstructure and residual stress analysis of a 'rim chilled' solid wheel for rail transportation system, Transactions on Engineering Sciences, vol 8, 1995, WIT Press, www.witpress.com, ISSN 1743-3533, pp. 293-300, visited September 2018
46. G. Vander Voort, The Interlamellar Spacing of Pearlite, April 9, 2015 https://vacaero.com/information-resources/metallography-with-george-vander-voort/1437-the-interlamellar-spacing-of-pearlite.html, visited September 2017
47. G.F. Vander Voort and A. RoószMeasurement of the interlamellar spacing of pearlite, Metallography, Volume 17, Issue 1, February 1984, Pages 1-17
48. W.E. Stumpf, *Phase Transformations in Metals and their Alloys*, The University of Pretoria, Materials and Metallurgical Engineering, Course NFM 700, 2010
49. R. Ordóñez Olivares, C.I. Garcia, A. DeArdo and S. Kalay, *Advanced Metallurgical Alloy Design and Thermomechanical Processing for Rails*

Steels for North American Heavy Haul Use, Wear, Vol. 217, issues 1-2, 18 May 2011, pp. 364-373

50. E. Magel, P. Sroba, K. Sawley and J. Kalousek, *Control of Rolling Contact Fatigue of Rails*, Center for Surface Transportation Technology, National Research Council Canada,
51. U. Zerbst, *Applications of Fracture Mechanics to Railway Components – An Overview*, http://www.gruppofrattura.it/ocs/index.php/ICF/ICF11/paper/viewFile/10672/10018, visited July 2016
52. C. Mesplont, *Phase Transformation and Microstructure-Mechanical Properties Relations in Complex Phase High Strength Steels*, Gent University, PhD Thesis
53. H.K.D.H. Bhadeshia, *Bainite in Steels*, Second Edition, Institute of Materials, March 2001, ISBN 1 86125 112 2 (H)
54. H.K.D.H. Bhadeshia, *POSCO Lectures on Bainite*, www.youtube.com, visited March 2014
55. H.K.D.H. Bhadeshia and J.W. Christian, *Bainite in Steels*, Metallurgical Transaction A, Volume 21A, April 1990, pp. 767-797
56. B.L. Bramfitt and J.G. Speer, *Perspective on the Morphology of Bainite*, Metallurgical Transaction A, Volume 21A, April 1990, pp. 817-829
57. D.V. Edmonds and R.C. Cochrane, *Structure-Property Relationships in Bainitic Steels*, Metallurgical Transactions A, Volume 21A, June 1990, pp. 1527-1540
58. K.P. Rice, R.H. Geiss, R.R. Keller, Transmission Electron Backscatter Diffraction In The Sem: Specimen Thickness Effects, Applied Chemicals and Materials Division, National Institute of Standards and Technology (NIST), Boulder, CO 80305, https://www.nist.gov/sites/default/files/documents/pml/div683/conference/TU-03-2.pdf
59. X. Zhang, G. Xu, X. Wang, D. Embury, O. Bouaziz, G. R. Purdy and H. S. Zurob, Mechanical Behaviour of carbide-Free Medium Carbon Bainitic Steels, The Minerals, metals & materials Society and ASM International 2013

60. L. Morales-Rivas, H. Roelofs, S. Hasler, C. Garcia-Mateo, F.G. Caballero, Detailed Characterisation of Complex banding in Air-Cooled Bainitic Steels, J. Min. Metall. Sect. B-Metall. (51) 1 (B) 2015 25-32
61. R.A. Jaramillo, M.T. Lusk and M.C. Mataya, Dimensional anisotropy during phase transformations in chemically banded 5140 steel. Part I: Experimental investigation, Acta Materialia 52 (20014) 851-858
62. L. Morales-Rivas, H. Roelofs, S. Hasler, C. Garcia-Mateo, F.G. Caballero, Complex Microstructural Banding of continuously Cooled Crabide-Free Bainitic Steels, Materials Science Forum, Vols. 783-786, pp 980-985
63. , F.G. Caballero, J. Chao, J. Cornide, C. Garcia-Mateo, M.J. Santofomia and C. Capdevila, Toughness Deterioration in Advanced High Strength Bainitic Steels, Materials Science and Engineering, A 525 (2009) 87-95
64. M.J. Santofimia, S.M.C van Bohemen, J. Sietsma, *Combining Bainite and Martensite in Steel Microstructures for Lightweight Applications*, The journal of the Southern African Institute of Mining and Metallurgy, Vol. 113, pp.143 - 148
65. P. Pointner, *High Strength Rail Steels-The Importance of Material Properties in Contact Mechanics Problems*, Wear 265 (2008) 1373–1379
66. J. Pacyna, *The Microstructure and Properties of New Bainitic Rail Steels*, Journal of Achievements in materials and manufacturing Engineering, Vol. 28, Issue 1, 2008, pp. 19-22.
67. L.C Chang, *Bainite Transformation and Novel Bainitic Rail Steels*, PhD Thesis Department of Materials and Metallurgy, Cambridge, March 1995,
68. *Lower Bainite*, http://www.msm.cam.ac.uk/phase-trans/bainitec.html, visited April 2014
69. H.K.D.H Bhadeshia, *High Performance Bainitic Steels*, Materials Science Forum Vols. 500-501, November 2005, pp. 63-74
70. H.K.D.H. Bhadeshia, *New Bainitic Steels by Design*, University of Cambridge, University of Cambridge, www.msm.cam.ac.uk/phase-trans, visited June 2013
71. L. Fielding, *The Bainite Controversy*, M.Eng, Materials Science and Technology, Volume 29, Number 4, April 2013, pp. 383-399

72. H.K.D.H. Bhadeshia and D. V. Edmonds, *The Bainite Transformation in a Silicon Steel*, Metallurgical Transactions A, Volume 10A, July 1979, pp. 895-907
73. B.P.J. Sandvik, *The Bainite Reaction in Fe-Si-C Alloys: The Primary Stage*, Metallurgical Transaction A, Volume 13A, May 1982, pp. 777-787
74. P. Kolmskog, *Does Bainite Form With or Without Diffusion*, PhD Thesis in Materials Science and Engineering, Stockholm 2013, ISBN 987-91-7501-755-6, http://www.diva-portal.org/smash/get/diva2:618512/FULLTEXT01.pdf
75. H.K.D.H. Bhadeshia, *Developments in Martensitic and Bainitic Steels: Role of The Shape Deformation*, Materials Science and Engineering A, Vol. A378, 2004, 34–39
76. J. Cornide, C. Garcia-Mateo, C. Capdevila and F.G. Caballero, *An Assessment of the Contributing Factors to the Nanoscale Structural Refinement of Advanced Bainitic Steels*, Journal of Alloys and Compounds 577S (2013) S43–S47
77. T. Yokota, C. Garcıa Mateo and H.K.D.H. Bhadeshia, *Formation of Nanostructured Steels by Phase Transformation*, Scripta Materialia 51 (2004) 767–770
78. L.C. Chang, *Microstructures and Reaction Kinetics of Bainite Transformation in Si-Rich Steels*, Materials Science and Engineering A368 (2004) pp. 175-182
79. H. Amel-Farzad, H.R. Faridi, F. Rajabpour, A. Abolhasani, Sh. Kazemi and Y. Khaledzadeh, *Developing Very Hard Nanostructured Bainitic Steel*, Materials Science and Engineering A559 (2013) 68-73
80. F.G. Caballero, M.K, Miller, S.S. Babu and C. Garcia-Mateo, *Atomic Observations of Bainite Transformation in a High Carbon High Silicon Steel*, Acta Materialia 55 (2007) 381-390
81. C. Garcia-Mateo, F. G. Caballero and H.K.D.H. Bhadeshia, *Development of Hard Bainite*, ISIJ International, Vol. 43 (2003), No. 8, pp. 1238 -1243
82. S. Khare, K. Lee and H.K.D.H. Bhadeshia, *Carbide-Free Bainite: Compromise between Rate of Transformation and Properties*, Metallurgical and Materials Transactions A, Volume 41A, April 2010, pp. 922-928

83. F. Caballero, M. Santofimia, C. Capdevila, C. García-Mateo and C. García De Andrés, *Design of Advanced Bainitic Steels by Optimisation of TTT Diagrams and T_0 Curves*, ISIJ International, Vol. 46 (2006), No. 10, pp. 1479–1488

84. Cambridge University, Phase transformation Group, MUGC83, Materials Algoriths Project Program Library, https://www.phase-trans.msm.cam.ac.uk/map/steel/programs/mucg83.html, visited October 2016

85. F. Han, H. Byoungchul, D.W. Suh, Z. Wang, Z. and S.J.Kim, (2008) *Effect of Molybdenum and Chromium on Hardenability of Low-Carbon Boron-Added Steels*, Metals and Minerals International, Vol. 14, No. 6, pp. 667-672.

86. M. Zhou, G. Xu, J. Tian, H. Hu and Q. Yuan, Bainitic Transformation and Properties of Low Carbon Carbide-Free Bainitic Steels with Cr Addition, Metals 2017, 7, 263; doi:10.3390/met7070263 www.mdpi.com/journal/metals, visited June 2018

87. H.K.D.H. Bhadeshia, *Properties of Fine-Grained Steels Generated by Displacive Transformation*, Materials Science and Engineering A 481–482 (2008) 36–39

88. E. Kozeschnik and H.K.H.D. Bhadeshia, *Influence of Silicon on Cementite Precipitation in Steels*, Materials Science and Technology, 2008, Vol. 24, No.3, pp. 343-347S.

89. V. I. Kalikmanov, Classical Nucleation Theory, Nucleation Theory, Springer, Dordrecht, 978-90-481-3642-1, pp 17-41

90. R. W. K. Honeycombe Some Aspects of Micro-Alloying, Transactions of the Japan Institute of Metals, 1983, Volume 24 Issue 4 Pages 177-189

91. H.A. Aglan, and M. Fateh, *Fracture and Fatigue Crack Growth Analysis of Rail Steels*, Mechanics of Materials and Structures, Volume 2, No. 2, February 2007.

92. A. Gianni, A. Ghidini and A. Ekberg, *Bainitic Steel Grade for Solid Wheel: Metallurgical*, *Mechanical and In-Service Testing*, Proc, IMechE Vol. 223 Part F: J. Rail and Rapid Transit, pp 163-171, www.ndt.net, visited 28 September 2014.

93. F.C. Zhang, B. Lv, C.L. Zheng, Q. Zou, M., Zhang, M. Li, and T.S. Wang, *Microstructure of the Worn Surfaces of a Bainitic Steel Railway Crossing*, Wear, 268, 2010, 1243-1249

94. S. Ahmed and A. Zervos, *Railway Ballast*, Engineering and the Environment, University of Southampton, http://www.southampton.ac.uk/~muvis/case_studies/06_Railway_ballast.html, visited September 2014

95. , J. Zuspan, Track Guy Consultants, Trackwork 101© Training http://www.trackguy.com/trackwork_101.htm, visited September 2014

96. R.P.B.J. Dollevoet, *Design of an Anti-Head Check Profile Based on Stress Relief*, PhD Thesis, University of Twente, Enschede, The Netherlands

97. U.S. Department of Transportation*, Rolling Contact Fatigue: A Comprehensive Review*, DOT/FRA/ORD-11/24, Final Report November 2011, U.S. Department of Transportation, Federal Railroad Administration, Office of Railroad Policy and Development Washington, DC 20590, http://ntl.bts.gov/lib/43000/43400/43400/TR_Rolling_Contact_Fatigue_Comprehensive_Review_final.pdf, visited September 2014

98. *Transport Safety Board of Canada*, Railway Investigation Report No. R11D0099, Non-Main-Track Derailment, Agence Métropolitaine de Transport, Commuter Train No. 805, Mile 73.84, Saint-Hyacinthe Subdivision, Montreal, Quebec, 09 December 2011, http://www.tsb.gc.ca/eng/rapports-reports/rail/2011/r11d0099/r11d0099.pdf, visited September 2014

99. M.R. Zhang and H.C. Gu, *Microstructure and Properties of carbide Free Bainite Railway Wheels Produced by Programmed Quenching*, Materials Science and Technology, Vol. 23, No. 8, 2007, pp. 970-974

100. *U.S. Department of Transportation, Fracture and Fatigue Damage Tolerance of Bainitic and Pearlitic Rail Steels*, Research Results, U.S Department of Transportation, Federal Railroad Administration, RR06-02, February 2006, www.fra.dot.gov/Elib/Document/2136, visited September 2014

101. H.A. Aglan, Z.Y. Liu, M.F. Hassa and M. Fateh, *Mechanical and Fracture Behaviour of Bainitic Rail Steel,* Journal of materials Processing Technology, 151, 2004, 268-274.

102. V.V. Pavlov, L.A. Godik, L.V. Korneva, N.A. Kozyrev and E.P. Kuznetsov, *Railroad Rails Made of Bainitic Steel*, Metallurgist, Vol.51, Nos 3-4, 2007, pp.209-212

103. H.K.D.H. Bhadeshia and J. Vijay, *Improvements in and Relating to carbide-Free Bainitic Steels and Methods of Producing Such Steels*, Patent No. WO 96/22396, 25 July 1996

104. H. Kageyama, M. Ueda and K. Sugino, *Process for Manufacturing High-Strength Bainitic Steel Rails with Excellent Rolling-Contact Fatigue Resistance*, Patent No. US 5382307, 17 January 1995

105. M. Ueda, K. Uchino, K. Iwano and A. Kobayashi, *Bainite Type Rail Excellent in Surface Fatigue Damage Resistance and Wear Resistance*, Patent No. AU 737977 B2, 6 September 2001

106. J. Jaiswal, P. Sécordel and F. Fau, *Corus Premium Grades to Adress Wear And Rolling Contact Fatigue,* https://www.arema.org/files/library/2010_Conference_Proceedings/Corus_Premium_Grades_to_address_Wear_and_Rolling_Contact_Fatigue.pdf, visited September 2014

107. I. Poscmann, E. Tschapowetz and H. Rinnhofer, *Heat Treatment Process and Facility for Railway Wheels, Tyres and Rings,* Advanced Forging Technologies, www.werkstoff-service.de, accessed 12 April 2014.

108. R. Zhou, Y. Jiang, D. Lu, R. Zhou and Z. Li, *Development and Characterization of a Wear Resistant Bainite/Martensite Ductile Iron by Combination of Alloying and a Controlled Cooling Heat-Treatment*, Wear*,* 250, 2001, 529-534.

109. CQU University Australia, Centre for Railway Engineering, http://www.cre.cqu.edu.au/projects/rail_grinding.htm, visited 11 May 2014.

110. R. Lewis and U.Olofsson, *Mapping Rail Wear Regimes and Transitions*, Wear 257 (2004) 721-729

111. Rail, 2nd Edition, Eurailscout Inspection and Analysis, http://www.google.co.za/url?sa=t&rct=j&q=&esrc=s&source=web&cd=4&cad=rja&uact=8&ved=2ahUKEwiw2tTK-bLdAhVqBsAKHShkB50QFjADegQIBxAC&url=http%3A%2F%2Fwww.eurailscout.nl%2Fglobal%2Feurailscout%2Fafbeeldingen%2Ffactsheets%2Ffact%2520sheet_schiene_2014_en_aktuell%2520din-2.pdf&usg=AOvVaw3mHibijmGAMgjbuNb1QsUz, visited September 2017

112. Chinese Patent WO2018006843A1, Low cost lean production bainitic steel wheel for rail transit, and manufacturing method therefore, https://patents.google.com/patent/WO2018006843A1/en, visited September 2018

113. S. Sharma, S. Sangal, and K. Mondal, Development of New High-Strength Carbide-Free Bainitic Steels, Metallurgical And Materials Transactions A, Volume 42a, December 2011, pp. 3921-3933

114. X.Y. Long a, J. Kang a, B. Lvb, F.C. Zhang, Carbide-free bainite in medium carbon steel, Materials and Design 64 (2014) 237–245

115. I.M. Hutchings, *Tribology Friction and Wear of Engineering Materials*, Arnold, 1992, ISBN 0 340 56184X

116. R. Lewis, E. Magel, W-J Wang, U. Olofsson, S. Lewis, T. Slatter and A. Beagles, Towards a Standard Approach for the Wear Testing of Wheel and Rail Materials, Proceedings of the Institution of Mechanical Engineers, Part F: Journal of Rail and Rapid Transit, 231 (7) pp. 760-774, ISSN 0954-4097, http://doi.org/10.1177/0954409717700531, visited September 2018

117. Designation: G 99 – 95a (Reapproved 2000), Standard Test Method for Wear Testing with a Pin-on-Disk Apparatus

118. P. Clayton and N. Jin, *Unlubicated Sliding and Rolling/Sliding Wear Behaviour of Continuously Cooled, Low/Medium Carbon Bainitic Steels*, Wear 200 (1996) 74 -82

119. S. Das Bakshi, A. Leiro, B. Prakash, H.K.D.H. Bhadeshia, *Dry Rolling/Sliding Wear of Nanostructured Bainite*, Wear 316 (2014) 70-78

120. C.C. Viafara, M.I. Castro, J.M. Velez and A. Toro, *Unlubricated sliding wear of Pearlitic and Bainitic Steels*, Wear 259 (2005) 405-411

121. X.Y. Feng, F.C. Zhang, J. Kang, Z.N. Yang and X.Y. Long, *Sliding Wear and Low Cycle Fatigue Properties of New Carbide Free Bainitic Rail Steel,* Materials Science and Technology, 2014, Vol 30, No 12, 1410-1418

122. A. Leiro, E.Vuorinen, K.G.Sundin, B.Prakash, T.Sourmail, V.Smanio, F.G.Caballero, C. Garcia-Mateo, R. Elvira, *Wear of Nano-Structured Carbide-Free Bainitic Steels Under Dry Rolling–Sliding Conditions,* Wear 298–299 (2013) 42–47

123. M. Federici, G. Straffelini and S. Gialanella, Pin-on-Disc Testing of Low-Metallic Friction Material Sliding Against HVOF Coated Cast Iron: Modelling of the Contact Temperature Evolution, Tribol Lett (2017) 65: 121. https://doi.org/10.1007/s11249-017-0904-y, visited September 2018

124. A. Shebani and C. Pislaru, Wear Measuring and Wear Modelling Based on Archard, ASTM, and Neural Network Models, http://eprints.hud.ac.uk/id/eprint/23886/1/Amer_ICAR_2015.pdf

125. Image J, Scriptable Java App for Scientific Image Processing, https://imagej.en.softonic.com/, cited January 2018

126. A. Kapito, G. Maruma and J. Jonck, Metallurgical Characterisation of 34-Inch Advanced Casting Technique (ACT) Class B Cast and Forged Rail Wheel from Transnet Engineering Koedospoort, Mintek Internal Report No. 42228, 18 December 2015

127. S. Keeler, The Science of Forming- Automotive Steels--Online Technical Resources, 1 May 2012, https://www.metalformingmagazine.com/enterprise-zones/article/?//2012/5/1/Automotive_Steels--Online_Technical_Resources, visited January 2019